

# **Heat Transfer in Window Frames with Internal Cavities**

Arild Gustavsen

Department of Building and Construction Engineering  
Faculty of Civil and Environmental Engineering  
Norwegian University of Science and Technology  
Trondheim, Norway

September, 2001



# Abstract

Heat transfer in window frames with internal air cavities is studied in this thesis. Investigations focus on two- and three-dimensional natural convection effects inside air cavities, the dependence of the emissivity on the thermal transmittance, and the emissivity of anodized and untreated aluminium profiles. The investigations are mostly conducted on window frames which are the same size as real frames found in residential buildings.

Numerical and experimental investigations were performed to study the effectiveness of one commercial Computational Fluid Dynamics (CFD) program for simulating combined natural convection and heat transfer in simple three-dimensional window frames with internal air cavities. The accuracy of the conjugate CFD simulations was evaluated by comparing results for surface temperature on the warm side of the specimens to results from experiments that use infrared (IR) thermography to map surface temperatures during steady-state thermal tests. In general, there was good agreement between the simulations and experiments.

Two-dimensional computational fluid dynamic and conduction simulations are performed to study the difference between treating air cavities as a fluid and as a solid when calculating the thermal transmittance of window frames. The simulations show that traditional software codes, simulating only conduction and using equivalent conductivities for the air cavities, give U-values that compare well with results from fluid flow simulations. The difference between the two models are mostly limited to the temperature distribution inside air cavities. It is also found that cavities with an interconnection less than about 7 mm can be treated as separate cavities.

Three-dimensional natural convection effects in simple and custom-made PVC and thermally broken aluminum window frames with one open internal cavity were studied, with the use of CFD simulations and thermography experiments. Focus was put on corner effects and heat transfer rates. From the results it appears that the thermal transmittance of a four-sided section can be found by calculating the average of the thermal transmittance of the respective single horizontal and vertical sections. In addition, it was found that two-dimensional conduction heat

transfer simulation software agrees well with three-dimensional CFD simulations if the natural convection correlations used for the internal cavities are correct.

Numerical simulations were done with natural convection in three-dimensional cavities with a high vertical aspect ratio and a low horizontal aspect ratio. The cavities studied had vertical aspect ratios of 20, 40, and 80 and horizontal aspect ratios ranging from 0.2 to 5. It was shown that three-dimensional cavities with a horizontal aspect ratio larger than five can be considered to be a two-dimensional cavity to within 4 % when considering heat transfer rates. Nusselt number correlations for the different horizontal aspect ratios are presented for cavities with vertical aspect ratios of 20 and 40. Complex multicellular flow was studied for the case where the vertical and horizontal aspect ratios were 40 and 2, respectively.

Experimental studies included the normal spectral and total emissivity of specimens from six meter long untreated and anodized aluminum profiles. Specimens facing the internal cavities (thermal break cavity and all aluminum cavity) were measured. Some masking tapes often used in hot box experiments were also measured. The normal total emissivity was found to be is fairly constant (between 0.834 and 0.856) for exterior parts of the anodized profile and for surfaces facing the thermal break cavity. The normal total emissivity of the all-aluminum internal cavities was found to vary between 0.055 and 0.82. The experiments were performed with a Fourier transform infrared spectrometer in the wavelength interval from 4.5 to 40  $\mu\text{m}$ .

# Preface

The work presented in this thesis has been made possible by financial support from Hydro Aluminium through the strategic doctorate program “Aluminium in Buildings and Energy Systems”. The financial support was obtained by Professor Øyvind Aschehoug at the Department of Building Technology, NTNU. Most of the work has been carried out at the Department of Building and Construction Engineering at the Norwegian University of Science and Technology, NTNU.

I would like to thank my supervisor Professor Jan Vincent Thue for always being available when I had questions to ask. Sivert Uvsløkk at the Norwegian Building Research Institute (NBI) deserves my thanks for helping out with technical problems in the laboratory.

I would also like to thank Dariush Arasteh, Brent T. Griffith, Paul Berdahl, and Mike Rubin for valuable discussions and for letting me use their laboratories during a six month stay from July 1999 to January 2000 at Lawrence Berkeley National Laboratory (LBNL) in Berkeley, California, USA. I also extend thanks to Howdy Goudey (LBNL) for help in the laboratory, and Christian Kohler (LBNL) and Dragan Curcija (Carli, Inc.) for valuable discussions and comments to my work.

I acknowledge the English editing assistance from Stewart Clark, NTNU.

Last but not least I would like to thank my fiancée Marit and my family for always being supportive and encouraging.



# Contents

<b>Abstract</b>	<b>iii</b>
<b>Preface</b>	<b>v</b>
<b>Contents</b>	<b>vii</b>
<b>List of Papers</b>	<b>ix</b>
<b>Nomenclature</b>	<b>xi</b>
<b>Chapter 1 Introduction</b>	<b>1</b>
1.1 Background . . . . .	1
1.2 Objectives and Limitations . . . . .	4
1.3 Thesis Outline . . . . .	6
<b>Chapter 2 Heat Transfer in Fenestration Products</b>	<b>9</b>
2.1 General Heat Transfer Relations . . . . .	9
2.1.1 Conduction . . . . .	9
2.1.2 Convection . . . . .	9
2.1.3 Thermal Radiation . . . . .	11
2.1.4 Thermal Resistance . . . . .	11
2.1.5 Thermal Transmittance, U-value . . . . .	12
2.2 Fenestration Components . . . . .	12
2.3 Calculating the Overall Thermal Transmittance . . . . .	14
2.3.1 Thermal Transmittance of Entire Windows . . . . .	15
2.3.2 Thermal Transmittance of Glazing . . . . .	16
2.3.3 Thermal Transmittance of Frames . . . . .	17
<b>Chapter 3 Heat Transfer in Frame Cavities</b>	<b>25</b>
3.1 Introduction . . . . .	25
3.2 Problem Description . . . . .	26
3.3 Important Dimensionless Groups . . . . .	27
3.4 Correlations for Frame Cavities . . . . .	34
3.4.1 Three-dimensional Effects . . . . .	35
3.4.2 Boundary Condition Effects . . . . .	35
3.4.3 Convection in Enclosures with Simple Boundary Conditions . . . . .	36

3.4.4	Correlations for Complex and Realistic Boundary Conditions . . . . .	39
3.4.5	Correlations from International Standards . . . . .	41
3.5	Comparison of Correlations . . . . .	44
3.5.1	Natural Convection Correlations . . . . .	44
3.5.2	Radiation Heat Transfer Correlations . . . . .	47
3.6	Conclusions . . . . .	48
<b>Chapter 4</b>	<b>Air Flow in and U-values of Window Frames</b>	<b>51</b>
4.1	Introduction . . . . .	51
4.2	Frame Sections . . . . .	52
4.3	Numerical Procedure . . . . .	53
4.4	Results and Discussion . . . . .	56
4.4.1	Stream and Temperature Contours . . . . .	56
4.4.2	U-value Comparison . . . . .	61
4.5	Conclusions . . . . .	64
<b>Chapter 5</b>	<b>Radiation Heat Transfer Properties - Emissivity of Aluminum Surfaces</b>	<b>65</b>
5.1	Introduction . . . . .	65
5.2	Radiation Intensity and Emissive Power . . . . .	65
5.3	The Blackbody in Radiation Heat Transfer . . . . .	66
5.4	Radiation Properties of Real Surfaces . . . . .	67
5.4.1	Emissivity . . . . .	68
5.4.2	Absorptivity . . . . .	68
5.4.3	Reflectivity . . . . .	69
5.4.4	Relationships between the Radiation Properties . . . . .	69
5.5	Thermophysical Properties of Aluminum Surfaces . . . . .	70
5.5.1	Radiative Properties by Classical Electromagnetic Theory . . . . .	70
5.5.2	Emissivity of Selected Materials Relevant for Aluminum Frames . . . . .	75
5.5.3	Material Properties of Selected Materials . . . . .	80
5.6	Sensitivity Study . . . . .	80
5.7	Conclusions . . . . .	84
<b>Chapter 6</b>	<b>Conclusions</b>	<b>87</b>
<b>Chapter 7</b>	<b>Suggestions for Further Work</b>	<b>91</b>
<b>References</b>		<b>93</b>

# List of Papers

**I.** Gustavsen, A., Griffith, B.T. and Arasteh D. (2001). Three-Dimensional Conjugate Computational Fluid Dynamics Simulations of Internal Window Frame Cavities Validated Using Infrared Thermography, *ASHRAE Transactions*, Vol. 107, Pt. 2.

**II.** Gustavsen, A., Griffith, B.T. and Arasteh D. (2001). Natural Convection Effects in Three-Dimensional Window Frames with Internal Cavities, *ASHRAE Transactions*, Vol. 107, Pt. 2.

**III.** Gustavsen, A. and Thue, J.V. (2001). Numerical Simulation of Natural Convection in Three-dimensional Cavities with a High Vertical Aspect Ratio and a Low Horizontal Aspect Ratio, *International Journal of Heat and Mass Transfer*, submitted.

**IV.** Gustavsen, A. and Berdahl, P. (2001). Spectral Emissivity of Anodized Aluminum and the Thermal Transmittance of Aluminum Window Frames, *Nordic Journal of Building Physics*, submitted.



# Nomenclature

Symbol	Description	Unit
$A$	area	$\text{m}^2$
$A_f$	contact area between fluid and hot plate (excludes $A_w$ )	$\text{m}^2$
$A_w$	contact area between hot plate and walls	$\text{m}^2$
$b$	wall thickness	$\text{m}$
$b_f$	projected width of frame section	$\text{m}$
$b_p$	visible width of insulation panel	$\text{m}$
$c_0$	speed of electromagnetic radiation propagation in vacuum	
$c_p$	specific heat capacity at constant pressure	$\text{J kg}^{-1} \text{K}^{-1}$
$d$	thickness of material layer	$\text{m}$
$e$	emissive power	$\text{W m}^{-2} \text{sr}^{-1} \text{m}^{-1}$
$E$	intersurface emittance	-
$F$	view factor correction coefficient	-
$g$	acceleration due to gravity	$\text{m s}^{-2}$
$G$	incident radiation	$\text{W}$
$Gr_L$	Grashof number, $\beta\Delta TgL^3/\nu^2$	-
$h$	Planck's constant	
$h_a$	convective heat transfer coefficient	$\text{W m}^{-2} \text{K}^{-1}$
$h_r$	radiative heat transfer coefficient	$\text{W m}^{-2} \text{K}^{-1}$
$h_R$	blackbody radiative heat transfer coefficient, does not include the intersurface emissivity	$\text{W m}^{-2} \text{K}^{-1}$
$H$	height of enclosure	$\text{m}$
$i$	radiant intensity	$\text{W m}^{-2} \text{sr}^{-1} \text{m}^{-1}$
$k$	Boltzmann constant	

**xii** *Nomenclature*

$l_{\Psi}$	perimeter of glazing area	m
$L$	length of enclosure	m
$L^{2D}$	thermal conductance	$\text{W m}^{-1} \text{K}^{-1}$
$M_g$	molar weight	$\text{kg mol}^{-1}$
$n$	refractive index; $n_2/n_1$ in some equations	-
$\bar{n}$	complex refractive index	-
$Nu$	Nusselt number	-
$N_{RC}$	radiation conduction interaction parameter, $\sigma T_H^4 L/k\Delta T$	
$P$	pressure	Pa
$Pr$	Prandtl number, $\nu/\alpha$	-
$q$	heat flux	$\text{W m}^{-2}$
$Q$	heat flow or linear density of heat flow	W or $\text{W m}^{-1}$
$Q_f$	heat transfer from the hot plate to the fluid	W
$Q_{f0}$	heat transfer from the hot plate to the fluid when the fluid is stationary	W
$Q_{f0}^0$	heat transfer from the hot plate to the fluid when the fluid is stationary (no radiation and conduction effects in the surrounding walls)	W
$Q_r$	radiative heat transfer from the hot plate to the fluid	W
$Q_{r0}$	radiative heat transfer from the hot plate to the fluid when the fluid is stationary	W
$Q_w$	heat transfer into the area $A_w$ of the wall from the hot plate	W
$Q_{w0}$	value of $q_w$ when the fluid is stationary	W
$R$	general gas constant	-
$R$	thermal resistance	$\text{m}^2 \text{K W}^{-1}$
$Ra_L$	Rayleigh number, $Gr_L Pr$	-
$T$	temperature	K
$T_R$	temperate ratio, $T_C/T_H$	-
$U$	thermal transmittance	$\text{W m}^{-2} \text{K}^{-1}$
$W$	width of enclosure	m
$x, y$	Cartesian coordinates	

*Greek symbols*

$\alpha$	absorptivity	-
$\alpha$	thermal diffusivity, $k/\rho c_p$	$\text{m}^2 \text{s}^{-1}$
$\beta$	thermal coefficient of expansion	$\text{K}^{-1}$
$\varepsilon$	emissivity	-
$\phi$	circumferential angle	
$\kappa$	extinction coefficient	
$\lambda$	conductivity	$\text{W m}^{-1} \text{K}^{-1}$
$\lambda$	wavelength	m
$\mu$	dynamic viscosity	$\text{kg m}^{-1} \text{s}^{-1}$
$\nu$	kinematic viscosity	$\text{m}^2 \text{s}^{-1}$
$\rho$	density	$\text{kg m}^{-3}$
$\rho$	reflectivity	-
$\sigma$	Stefan-Boltzmann constant	
$\theta$	angle from the surface normal	
$\theta$	tilt angle of enclosure	
$\tau$	transmittance	-
$\Psi$	linear thermal transmittance	$\text{W m}^{-1} \text{K}^{-1}$

*Subscripts*

<i>air</i>	refers to air
<i>b</i>	blackbody
<i>B</i>	bottom plate
<i>c</i>	center of glass
<i>C</i>	cold plate
<i>d</i>	divider
<i>de</i>	divider edge
<i>e</i>	edge
<i>ext</i>	external
<i>f</i>	frame
<i>fr</i>	frame (ASHRAE calculated)

#### xiv Nomenclature

$H$	hot plate
$in$	in, warm side
$\lambda$	wavelength dependent
$m$	mean
$n$	normal
$out$	outside, cold side
$proj$	projected
$r$	radiation
$T$	top plate
$t$	total (ASHRAE calculated)
$tot$	total
$w$	wall
$window$	refers to window surface
$x, y$	directional dependent quantity
$\parallel$	parallel component
$\perp$	perpendicular component

#### *Superscripts*

'	directional quantity
''	bidirectional quantity

# Chapter 1

## Introduction

### 1.1 Background

In northern climates the construction of well-insulated buildings is important for reducing the energy use for heating, especially in small residential buildings. Even in larger commercial buildings where internal gains may exceed the transmission losses, well-insulated buildings are desirable. This is because well-insulated buildings have less transmission losses during the night, they are more easily controlled with respect to energy use, and because thermal discomfort due to badly insulated constructions can be avoided (Hanssen et al. 1996). Because of this, focus has been put on the insulating capabilities of building sections for years. In Norway for instance the requirements for the thermal transmittance (U-value) of new building sections like roofs, external walls and windows were last restricted in 1997 (NBC 1997). Table 1.1 shows the U-value requirements and also the evolution of the U-value requirements for different building sections according to the Norwegian building code. From 1969 to 1997 the thermal transmittance requirements of new outer walls were reduced from  $0.45 \text{ W/m}^2\text{K}$  to  $0.22 \text{ W/m}^2\text{K}$ . For windows the reduction has been from  $3.14$  to  $1.6 \text{ W/m}^2\text{K}$ . If we assume a residential house with base area of  $10 \times 10 \text{ m}^2$  and height of  $2.4 \text{ m}$  having 30 % of the walls covered by windows, and that the building envelope sections of that building comply to the U-value requirements in the second column from the right in Table 1.1, we find that about 50 % of the total energy loss through the building envelope of that building will be through the windows. If the window area is reduced to 20 % the corresponding percentage is 40 %. Thus, decreasing the U-value of windows can be an important factor in reducing energy use for heating in residential buildings.

The frame region is an important part of a fenestration product. Looking at a window with a total area of  $1.2 \times 1.2 \text{ m}^2$  and a frame with a width of 10 cm, the area occupied by the frame is 30 % of the total. If the total area of the window is increased to  $2.0 \times 2.0 \text{ m}^2$  the percentage is 19 % (still using the same frame). In rating fenestration products engineers area weight the ther-

**Table 1.1.** Thermal transmittance ( $\text{W}/\text{m}^2\text{K}$ ) requirements according to Norwegian building codes<sup>a</sup>.

Building Sections	Norwegian building code 1969 (NBC 1969)	Norwegian building code 1987 (NBC 1987)		Norwegian building code 1997 (NBC 1997)	
		> 18 °C	10-18 °C	≥ 20 °C	15-20 °C
Outer Wall	0.46	0.3	0.6	0.22	0.28
Window	3.14	2.4	3.0	1.6	2.0
Door	3.14	2.0	2.6	1.6	2.0
Roof	0.41	0.2	0.4	0.15	0.20
Floor on Ground	0.46	0.3	0.5	0.15	0.20

a. This table simplifies the U-value requirements for some building sections and building codes. Please refer to the different building codes for detailed information.

mal performance of the different parts to find one number describing the entire product. Thus, to be able to accurately calculate a product's thermal performance, we need accurate models describing the thermal performance of each part, or to be able to accurately measure the thermal performance of each section. Because experiments are expensive accurate models are required.

Until now most of the work, that is searching for accurate models describing heat transfer in fenestration products has focused on the glazing cavity. The goal of this work has mostly been to develop accurate correlations for natural convection effects inside multiple pane windows (see e.g. Batchelor 1954, Eckert and Carlson 1961, Hollands et al. 1976, Raithby et al. 1977, Berkovsky and Polevikov, 1977, Yin et al. 1978, ElSherbiny et al. 1982a, Shewen et al. 1996, Wright 1996, or Zhao 1998). Most of these papers study natural convection between two high vertical isothermal walls separated by two horizontal adiabatic or perfectly conducting walls (a two-dimensional cavity). Studies of heat transfer in multiple pane windows also include findings of which Rayleigh numbers there will be secondary (or multicellular) flow (see e.g. Korpela et al. 1982 Lee and Korpela 1983, Zhao et al. 1997, Lartigue et al. 2000). Secondary flow enhances heat transfer through glazing cavities. Some researchers (see e.g. Curcija 1992, Curcija and Goss, 1993, Schrey et al. 1998, Branchaud et al. 1998, and Griffith et al. 1998) have also studied heat transfer effects on the exterior and interior side of fenestration products.

Much work has not been conducted on heat transfer in window frames. In solid window frames the heat flow is carried out by conduction, which can be simulated with standard conduction simulation software (like e.g. Blomberg 1991, Enermodal 1995 or Finlayson et al. 1998). In window frames with internal cavities the heat transfer process is more complex, involving

combined conduction, convection and radiation. Ideally, to fully describe heat transfer through such window frames there is a need to simulate fluid flow to find the convection effects and to use either view-factors or ray-tracing techniques to find the radiation effects inside the cavities. But because of computational resources and the additional modelling efforts these simulations often require, such simulations still are rare. Instead air cavities are transformed into solid materials with an effective conductivity; that is, the conduction, convection and radiation effects are combined into an effective conductivity. Then, like for solid window frames without internal cavities, standard conduction simulation software can be used to find how well such sections insulate, or the thermal transmittance (U-value). Some studies have, however, been performed with focus on heat transfer effects in window frames with internal cavities. Standaert (1984) studies the U-value of an aluminum frame with internal cavities. The cavities are treated as solids and effective conductivities are assigned to each cavity. The effective conductivities of cavities not completely surrounded by aluminum are calculated from a fixed thermal resistance of  $R = 0.37 \text{ m}^2\text{K/W}$  ( $\lambda_{eq} = L/R$  where  $\lambda_{eq}$  is the equivalent conductivity and  $L$  is the length of the cavity in the heat flow direction). Cavities completely surrounded by aluminum are assigned an effective conductivity of  $0.1 \text{ W/mK}$ . Jonsson (1985) and Carpenter and McGowan (1989) also treat air in window frame cavities as solids and use equivalent conductivities to calculate heat flow. In their studies the effective conductivity concept was formulated as

$$\lambda_{eq} = \lambda_{air} \times Nu + \frac{h_R \times L}{[1/\epsilon_H + 1/\epsilon_C - 1]}, \quad (1.1)$$

where  $\lambda_{eq}$  is the equivalent conductivity,  $\lambda_{air}$  is the conductivity of air,  $Nu$  is the Nusselt number,  $L$  is the length of the air cavity, and  $\epsilon_H$  and  $\epsilon_C$  are the emissivities of the warm and cold sides of the cavity walls, respectively.  $h_R$  is the black-body radiative heat transfer coefficient, which depends on temperatures of the interior walls of the cavity and also on cavity geometry. Jonsson (1985) used  $h_R = 3.3 \text{ W/m}^2\text{K}$  for different cavity geometries while Carpenter and McGowan (1989) report different  $h_R$  values, depending on cavity height to length aspect ratios. Other studies on heat transfer in window frames are performed by Griffith et al. (1998) and Carpenter and McGowan (1998). Both studies are on curtain-wall aluminum frames. However, their work focused more on the effect of the bolts on the heat flow and the temperature distribution on the warm side surface rather than the convection effects inside the cavities of the frames. In another study the effect of air leakage on the conductive heat transfer in window frames was studied (Hallé et al. 1998). They used computational fluid dynamic (CFD) techniques to simu-

late air leakage effects, but the frame cavities themselves were treated as solids. In a recent study Svendsen et al. (2000) studied the effect of dividing air cavities in one complex aluminum frame, and the use of different radiation models when calculating the U-value. They found that different ways of doing the calculations influence the final U-value considerably. In addition to the above-mentioned articles, two masters theses have been written on heat transfer in window frame cavities. Roth (1998) compared the thermal transmittance calculation methods based on ASHRAE and CEN/ISO standards. Haustermans (2000) performed both experiments and numerical simulations and studies the thermal transmittance of different window frames. Both theses include results from CFD simulations. Some of the studies mentioned above are discussed further in Chapters 2, 3 and 4.

## 1.2 Objectives and Limitations

The interest in window frames with internal cavities in this project is due to window frames made of aluminum. The aluminum alloy used in window frames (usually 6061-T6; see e.g. TAA (1994) for a description of this and other aluminum alloys) has a conductivity of about 160 W/mK. Comparing this conductivity to the conductivity of other typical window frame materials like hardwood, softwood and PVC, that have conductivities of 0.18, 0.13 and 0.17 W/mK, respectively, we understand that window frames made of aluminum need special care to insulate well. Since aluminum is such a poor insulator of heat, it is used together with other materials such as polyamide (nylon) to increase the insulation capabilities of the frame. Together these materials form complex geometries with several air cavities (see Figure 1.1). Determining the natural convection and radiation heat transfer effects inside frame cavities will therefore be an important part of finding the thermal transmittance of such window frames. The natural convection and radiation effects will depend on cavity geometry and frame orientation. We also have to remember that a complete window frame is usually a collection of two horizontal and two vertical sections, joined at the edges (usually, because there also can be other frame parts dividing the window, and because a window does not need to be vertically mounted).

In this thesis the following topics will be addressed:

1. Previous research on convection and radiation heat transfer in window frame cavities will be examined. Are the natural convection correlations used for calculating the equivalent conductivities of air cavities accurate?

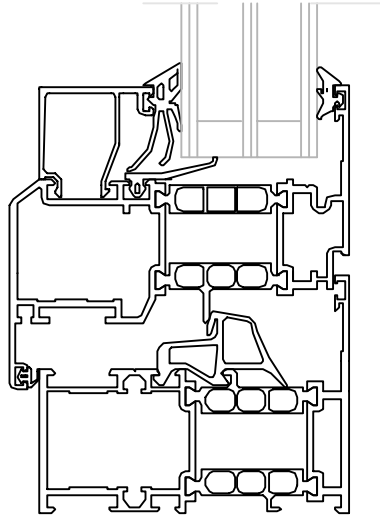


**Figure 1.1.** Example of a complex aluminum window frame with thermal break (from the WICLINE S80.1 series from WICONA).

2. The generic CFD code FLUENT (Fluent 1998) will be used in this thesis to simulate fluid flow and heat transfer. The effectiveness of the CFD code for simulating combined natural convection and heat transfer in window frames with internal cavities will be evaluated.
3. Are the calculation procedures for non-rectangular cavities accurate? Non-rectangular frame cavities having gaps or interconnections less than a certain dimension are split at the gap opening or the interconnection. The dimension at which this division of cavities is to take place differs from standard to standard. This area therefore merits research.
4. Can traditional two-dimensional conduction heat transfer simulation codes be used to accurately predict the complex conjugate heat transfer process taking place in three-dimensional window frames with internal cavities?
5. Can the thermal transmittance of a complete window frame with joined, open internal cavities be found by area-weighting the thermal transmittance of the respective horizontal and vertical profiles, of which the complete window frame is made up?
6. There is a lack of heat transfer correlations for natural convection in three-dimensional cavities with a high vertical aspect ratio and a low horizontal aspect ratio. Thus, numerical simulations of heat transfer in such cavities will be performed and correlations developed. New correlations are important for finding the thermal transmittance of vertical frame sections. The numerical simulations will also show for which horizontal aspect ratios high three-

dimensional cavities can be treated as two-dimensional and if multicellular flow is found in high cavities with a low horizontal aspect ratio.

7. Determining the thermal transmittance of window frames involves radiation heat transfer simulations. An important parameter in radiation simulations is the emissivity. Literature studies and measurements will be performed to find the emissivity of anodized and untreated aluminium profiles. Numerical simulations will also be conducted to find the dependence of the emissivity on the thermal transmittance of a window frame. Today, it is usual only to separate between 0.2 for shiny metallic surfaces (since aluminum oxidizes with time) and 0.9 for treated (e.g painted or anodized) surfaces.

The investigations are mostly conducted on window frames where the size is comparable to real frames found in residential buildings. Further, experiments and numerical simulations are limited to window frames where the main heat flow direction is perpendicular to gravity. The numerical simulations of heat transfer through the window frames are conducted with fixed warm and cold surface heat transfer coefficients. Air leakage effects are not addressed. Although the interest in window frames with internal cavities was due to aluminum window frames, the results developed also are applicable to window frames with internal cavities made of other materials, such as PVC.

### **1.3 Thesis Outline**

This thesis is divided in two parts, where the first part consist of seven chapters and the second part of four papers. Related to natural convection the following division is selected: Calculation procedures for thermal transmittance of window frames are reviewed in Chapter 2. In Chapter 3 we present and compare natural convection correlations for the internal cavities of window frames. Three-dimensional conjugate computational fluid dynamics simulations of internal window frame cavities are validated by infrared thermography experiments in Paper I. Chapter 4 presents two-dimensional numerical CFD and conduction simulations of heat transfer in complex window frames. Corner effects and heat transfer rates for complete three-dimensional window frames with internal cavities are presented in Paper II. Paper III contains the work on natural convection in vertical cavities with a small horizontal aspect ratio and a high vertical aspect ratio.

Related to emissivity the following division is chosen: Chapter 5 reviews radiation properties and the emissivity of untreated and treated aluminum. In addition, Chapter 5 includes a discus-

sion on how accurately the emissivity of aluminum needs to be determined. Paper IV presents measurements of the normal spectral and normal total emissivity of different parts of an anodized aluminum window frame profile and some tapes used in determination of the thermal transmittance of window frames.

Chapter 6 concludes this thesis and Chapter 7 gives suggestions for further work.

All the of the papers were written with other researchers. Paper I and Paper II were written with Brent T. Griffith and Dariush Arasteh. This means that the research plan for the work conducted in Paper I was developed by all the authors. The experimental work (including data analysis) was done by me, but with Brent T. Griffith as a supervisor in the beginning. All numerical work was conducted by me. The paper was mainly written by me, with valuable comments and suggestions from Brent T. Griffith and Dariush Arasteh. Paper II was proposed by me. Beyond that, the work for Paper II was distributed between the co-authors as for Paper I.

Paper III was written with Jan Vincent Thue. The idea for the paper was put forward by me and I conducted the numerical work and wrote the paper. Jan Vincent Thue came with valuable comments during the writing process.

Paul Berdahl was a co-author for Paper IV, which was proposed by me. I conducted most of the experimental work and wrote the paper. Paul Berdahl helped with the experimental work in the beginning, and was a valuable discussion partner during the writing process.



# Chapter 2

## Heat Transfer in Fenestration Products

### 2.1 General Heat Transfer Relations

Heat transfer in fenestration components is due to the three different heat transfer modes, conduction, convection and radiation. Conduction occurs in solid materials and fluids at rest. Convection and radiation occur in air cavities and at the indoor and outdoor faces of fenestration products.

#### 2.1.1 Conduction

Conduction is heat transfer due to molecular/atomic vibrations. If one side of a body is at a higher temperature than the other side, the molecules or atoms on the warm side will vibrate more than the surrounding molecules/atoms, setting the neighbor molecules/atoms in movement. This way heat will move from the warm side of the body to the cold side. The parameter of interest when studying conduction heat transfer is the conductivity,  $\lambda$ , which is a material property that has the dimension W/mK. For certain types of materials, like wood, the conductivity may have different values depending on the heat flow direction. The conductivity may also depend on temperature and pressure, however for building applications it is mostly considered a constant. Knowing the conductivity and the temperature distribution within a body enable us to calculate heat flow through the body. For the one-dimensional case we have

$$q = -\lambda \frac{dT}{dx} . \quad (2.1)$$

#### 2.1.2 Convection

Convection is heat transfer because of fluid motion. If for instance cold air blows across the exterior face of a window having a higher temperature than the air, heat will be transferred from the window to the air because of convection. The rate at which this heat is transferred depends

on the wind speed and the temperature difference between the air and the window's exterior face. Higher temperature difference and wind speed give a higher rate of heat flow. An analysis of convection is more involved than conduction heat transfer because the motion of fluid must be studied simultaneously with the energy-transfer process. The continuity equation, the Navier-Stokes equations and the energy equation need to be solved. This is normally done numerically. However, in building physics applications the most common way to find the convection heat transfer is to use simplified equations. Heat flux from the exterior surface of a window to the air outside can for instance be found from

$$q = h_a(T_{window} - T_{air}) , \quad (2.2)$$

where  $h_a$  is the convection heat transfer coefficient which has the dimension  $W/m^2K$ .  $T_{window}$  and  $T_{air}$  are the temperatures of the exterior surface of the window and air, respectively.  $h_a$  is found from correlations emanating from experiments or numerical simulations. For a rectangular cavity with two isothermal vertical walls separated by two horizontal adiabatic walls, like that shown in Figure 2.1, we use the following equation to find the heat flux

$$q = \frac{Nu \cdot \lambda \cdot (T_H - T_C)}{L} . \quad (2.3)$$

Here  $Nu$  is the dimensionless Nusselt number,  $\lambda$  is the conductivity of the cavity fluid, and  $L$  is the length of the cavity in the heat flow direction.  $T_H$  and  $T_C$  are the temperatures of the hot and cold walls, respectively. The Nusselt number is a positive number larger or equal to one. If  $Nu$  takes the value one, we have pure conduction. Nusselt number correlations exist for a vast number of geometries, ranging from shallow rectangular cavities to tall slots (like glazing cavities), and also for specific geometries for special applications. The correlations are usually found from numerical simulations and experiments. The square cavity problem has received a lot of attention (e.g. de Vahl Davis and Jones 1983, de Vahl Davis 1983, Zhong et al. 1985, Kuyper et al. 1993, Henkes and Hoogendoorn 1995, and Tian and Karayiannis 2000) and serves as a reference case against which numerical and experimental results are compared. Chapter 3 presents Nusselt number correlations that can be used for heat transfer calculations on window frames with internal cavities.

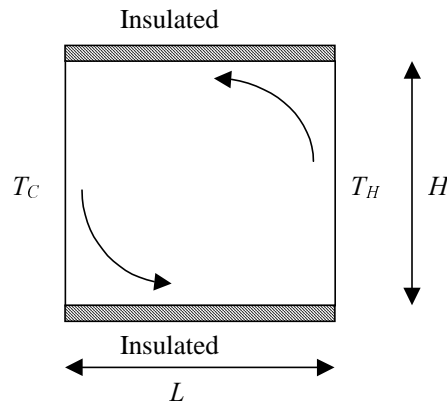


**Figure 2.1.** Schematic of flow in an enclosed cavity with two isothermal and two insulated walls.

### 2.1.3 Thermal Radiation

Thermal radiation is due to energy transfer from electromagnetic waves. In contrary to conduction and convection, which both require a medium to transfer heat, radiation can also take place in vacuum. For most building applications, radiation heat transfer occurs directly from surface to surface, without interacting with the medium that separates the surfaces. This is because air usually is the medium, and air is almost transparent to radiation in the wavelength area relevant for heat transfer inside building components. Several different properties are important when working with radiation heat transfer. These include the emissivity,  $\epsilon$ , and the reflectivity,  $\rho$ . The first property describes how well a body emits radiation compared to an ideal blackbody, and the latter how well a body reflects energy. These depend on wavelength, temperature and the direction of the radiation and are described in more detail in Chapter 5.

### 2.1.4 Thermal Resistance

The thermal resistance in heat transfer calculations is analogous to the electrical resistance in electricity calculations. A large thermal resistance means less heat flow, and vice versa. Also, similar to electricity resistances, the thermal resistances can be drawn in network diagrams to visualize the thermal situation (see e.g. Claesson and Hagentoft 1994). For a solid material we find the thermal resistance,  $R$ , from

$$R = \frac{d}{\lambda}, \quad (2.4)$$

where  $\lambda$  is the conductivity of the material and  $d$  is the thickness of the material in the heat flow direction. For air cavities the thermal resistance includes both radiation and convection effects, and are found from correlations. The dimension of  $R$  is  $\text{m}^2\text{K}/\text{W}$ . The thermal resistance is additive and can be added to other resistances to find a total resistance of a wall if there are several parallel layers with different materials.

### 2.1.5 Thermal Transmittance, U-value

The thermal transmittance, or U-value, is an aggregate parameter that is used to describe the total heat flow through a building section. It is defined as

$$U = \frac{Q}{A \cdot (T_{in} - T_{out})}, \quad (2.5)$$

where  $Q$  is the total heat flow through the building section,  $A$  is the area of the section, and  $T_{in}$  and  $T_{out}$  is the inside and outside air temperatures, respectively. If we know the total thermal resistance,  $R_{tot}$ , of a building section including the warm side and cold side surface resistances, the U-value can be found from

$$U = \frac{1}{R_{tot}}. \quad (2.6)$$

## 2.2 Fenestration Components

The word fenestration refers to any aperture in a building. Fenestration components include opaque door slabs, glazing material, framing, mullions, external and internal shading devices and integral (between-glass) shading systems (ASHRAE 1997). In this thesis we focus mostly on the framing of windows and façades. Below and in Figure 2.2 we name and describe some of the most important parts of a window (from CEN 1996):

- Casement - A movable lockable component of a window characterized by a rotational connection to the frame. In some cases this may also include some degree of sliding movement.
- Casement window - A window containing one or more casements.
- Frame - A case or border enclosing a door or forming a perimeter of a window.
- Glazing - An infill in a door or window which will admit light but will resist the passage of air or other elements.

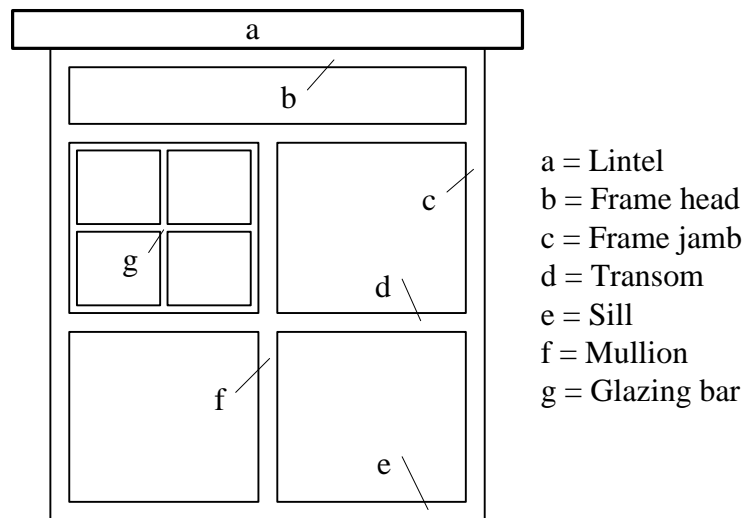


**Figure 2.2.** Figure showing some of the different parts of a window (based on figure in CEN 1996).

- Sash - A moveable component of a window that is moved by sliding to create an opening in the window.
- Window - Building component for closing an opening in a wall that enables the passage of light and may provide ventilation.

In this thesis we use the word frame for the parts of a window surrounding the glazing; that is, frame is used for window parts like casement, sash, frame jamb, transom, sill, mullion, and frame head.

Other parts of a window also need to be named. These are the spacer and sealant, shown in Figure 2.3. The spacer keeps the glazing panes apart at a specified distance and the sealant makes the edge of the glazing air and moisture tight. This is important to avoid condensation inside the glazing cavity. The glazing cavity is filled with dry air or another gas, usually krypton or argon.

Figure 2.4 shows examples of different types of frames and casements with glazing. From left to right we see a thermally broken aluminum frame, a wooden frame and a PVC frame with steel reinforcement. All these frames have cavities, either partly open to the exterior environment or not. There are also other types of window frames like glass fiber (which also has internal cavities) and all wooden window frames. Although, the interest in window frames with internal cavities was due to aluminum window frames, studies of such frames will also be of relevance for frames made in other materials.

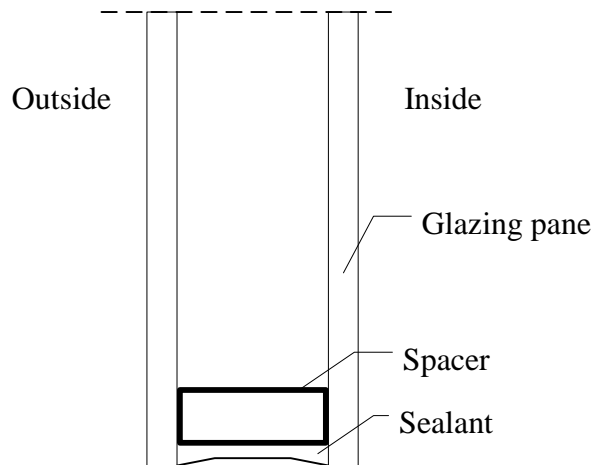


**Figure 2.3.** Schematic of double glazing, spacer, and sealant.

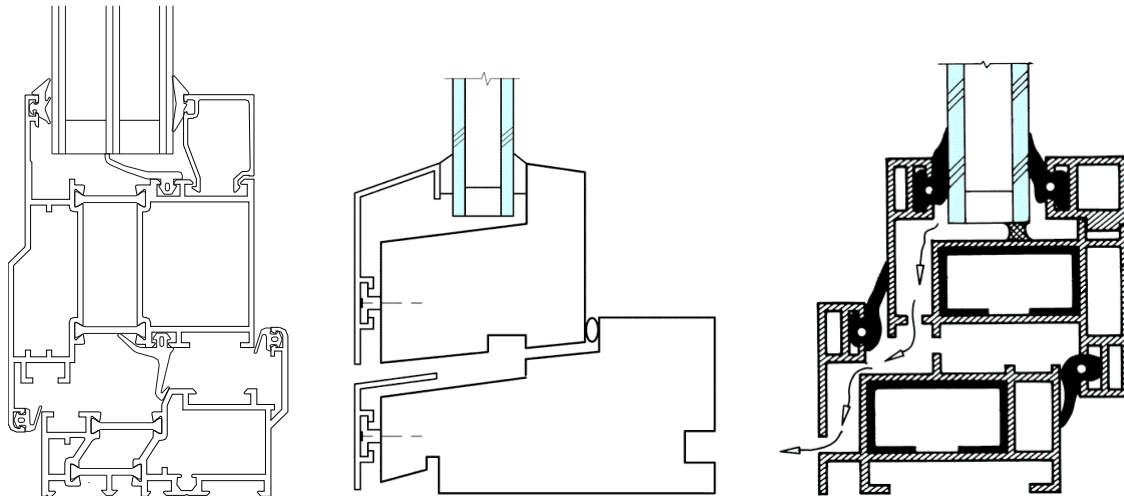


**Figure 2.4.** Different frame sections. From left to right we see an aluminum frame with a thermal break (test frame from WICONA), a wooden frame with aluminum cladding, and a PVC (PVC = polyvinyl chloride) frame with steel reinforcement (BKS 2000). The arrows in the figure of the PVC frame indicate typical drainage openings inside the frame. Similar openings are also found in aluminum frames.

### 2.3 Calculating the Overall Thermal Transmittance

The thermal transmittance, or U-value, is used for rating fenestration products and other building sections. Experiments and numerical simulations can be performed to find the U-value of parts of building sections, like for instance the frame of a window, and entire building sections, like entire windows. Because numerical simulations easily become too involved they are usually limited to building components. Experiments, on the other hand, tend to be performed for the

larger sections. This section deals with how calculations are performed to find the thermal transmittance of fenestration products.

### 2.3.1 Thermal Transmittance of Entire Windows

The U-value of a window can either be found by measuring the entire window (including the glazing and frame) or by measuring or simulating the U-value of the individual parts a window is made up of. If the latter approach is used we find one U-value for the glazing (valid for the central area, and does not include the effect of the glass spacer), one for the frame, and corrections are made for the interaction between glazing and frame, for the so-called edge of glass area. Then area weighting is used to find the U-value of the entire window. Thus, according to ISO (2000a), the thermal transmittance of a window,  $U_{tot}$ , is to be calculated from

$$U_{tot} = \frac{\sum A_g \cdot U_g + \sum A_f \cdot U_f + \sum l_\Psi \cdot \Psi}{A_{tot}}, \quad (2.7)$$

where  $A_g$  and  $A_f$  are the projected vision and frame area, respectively, and  $A_{tot}$  is total area of the entire fenestration section.  $U_g$  and  $U_f$  are the glazing and frame thermal transmittances, respectively.  $\Psi$  is the linear thermal transmittance which accounts for the interaction between the frame and the glazing, and  $l_\Psi$  is the perimeter of the glazing area. The summations included in the equation are to account for the various sections of one particular component. For instance, the sill, head and the side jambs of a window may have different U-values. A similar approach to the one described above, with respect to the total window thermal transmittance, is also described in CEN (2000). There U-values are given directly for different glazing widths, glazing cavity gases and glass coatings. In addition, CEN (2000) also includes calculation procedures for double and coupled windows. This thesis is focused mostly on the thermal transmittance of the frame,  $U_f$ , and the calculation procedures performed to find this value are presented in Section 2.3.3.

ASHRAE (1996) prescribes a different approach for finding the thermal transmittance of fenestration products. The total fenestration U-value,  $U_t$ , is calculated from

$$U_t = \frac{\sum A_c \cdot U_c + \sum A_{fr} \cdot U_{fr} + \sum A_e \cdot U_e + \sum A_d \cdot U_d + \sum A_{de} \cdot U_{de}}{A_t}. \quad (2.8)$$

$U_c$ ,  $U_{fr}$ , and  $U_d$  are the thermal transmittances of the center of glass, frame sections (jamb, sill, and head), and dividers (e.g. mullions and transoms), respectively.  $U_e$  is the edge of glass thermal transmittance and  $U_{de}$  is the divider edge of glass thermal transmittance. The calculation procedures of  $U_{fr}$  and  $U_e$  are further described in Section 2.3.3.  $A_c$  is the center-glass area, which is defined as the glazed area not within 63.5 mm of frames or dividers.  $A_{fr}$  and  $A_d$  are the frame and divider areas projected to the plane of the glazing, respectively.  $A_e$  is the glazed area within 63.5 mm of the frame, and  $A_{de}$  is the glazed area within 63.5 mm of dividers but not within 63.5 mm of the frame. It should be noted that the Eq. (2.8) also is included in ISO (2000a) as an alternate approach for finding the thermal transmittance of fenestration products, however, the exact dimension of the edge of glazing area is not explicitly stated there. Roth (1998) compared the two calculation procedures, Eq. (2.7) and Eq. (2.8), and found that they give almost identical overall window U-values, when using the same boundary conditions and material properties. With respect to the ASHRAE (1996) procedures Roth (2000) recommends the use of a 100 mm wide edge of glass area (instead of 63.5 mm wide).

Experimental procedures also exist for finding the thermal transmittance of entire fenestration products,  $U_{tot}$ , and parts of fenestration products like for instance the frame. Information about these procedures can for instance be found in ISO (2000b) and CEN (2001b) and will not be discussed further here.

### 2.3.2 Thermal Transmittance of Glazing

The thermal transmittance of the glazing will vary over the glazing surface because of warm and cold side surface heat transfer variations and also because of the convection effects inside multiple glazings. However, when rating glazing and fenestration products idealized conditions are assumed. The thermal transmittance of the glazing may be calculated from (ISO 1994)

$$\frac{1}{U_g} = \frac{1}{h_{out}} + \frac{1}{h_t} + \frac{1}{h_{in}}, \quad (2.9)$$

where  $h_{out}$  and  $h_{in}$  are the external and internal heat transfer coefficients, respectively. These depend on wind speed and surface emissivity but for rating purposes fixed values are used.  $h_t$  is the conductance of the glazing unit and is calculated from

$$\frac{1}{h_t} = \sum^N \frac{1}{h_s} + \sum^M d_m r_m . \quad (2.10)$$

$N$  is the number of spaces,  $M$  is the number of glass panes,  $d_m$  is the total thickness of each glass pane, and  $r_m$  is the thermal resistivity of glass, usually equal to 1 mK/W.  $h_s$  is the glazing cavity conductance which again is found from

$$h_s = h_g + h_r . \quad (2.11)$$

$h_g$  is the convection conductance and  $h_r$  is the radiation conductance for each cavity. The convection part depends on the Nusselt number, width of the glazing cavity and the conductivity of the gas inside the glazing cavity. The radiation part depends on the emissivities of the glazing panes,  $\varepsilon_1$  and  $\varepsilon_2$ , and the mean temperature,  $T_m$ , of the glazing system.

CEN (1997) describes an approach identical to ISO (1994) with respect to calculation procedures for finding glazing U-values. ISO (2000a) also deals with calculations of the thermal transmittance of the glazing area, however, these calculations are more detailed.

### 2.3.3 Thermal Transmittance of Frames

The thermal transmittance of window frames are usually found from two-dimensional numerical simulations. Software packages often used are for instance FRAME (Enermodal 1995) and THERM (Finlayson et al. 1998). There are also other software packages available. Both packages are conduction simulation programs, meaning that they only consider heat transfer in solid materials, and do not simulate fluid flow. Still, it is possible to use them on problems involving convection and radiation. Then convection and radiation correlations are used (THERM also includes an option for radiation simulations using view-factors).

When two-dimensional studies are performed to find the thermal transmittance of window frames the differential equation needed to be solved is

$$\frac{\partial}{\partial x} \left( \lambda_x \frac{\partial T}{\partial x} \right) + \frac{\partial}{\partial y} \left( \lambda_y \frac{\partial T}{\partial y} \right) + q(x, y, t) = \rho \cdot c_p \cdot \frac{\partial T}{\partial t} , \quad (2.12)$$

where  $T$  is the temperature and  $q$  is the rate of internal heat generation.  $\lambda_x$  and  $\lambda_y$  are the thermal conductivities in the  $x$ - and  $y$ -directions, respectively,  $\rho$  is the material density, and  $c_p$  is the specific heat capacity of the material. Usually the internal heat generation term and the transient

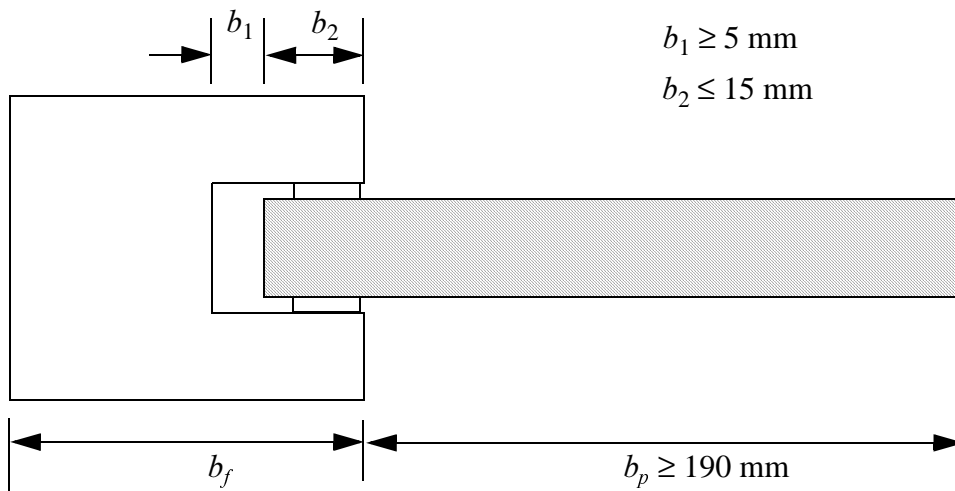


**Figure 2.5.** Window frame section with insulation panel installed.

terms are zero. Also, usually  $\lambda_x$  is equal to  $\lambda_y$ . Discretization of this equation gives a set of algebraic equations that can be solved numerically on a computer. Specification of boundary conditions and material properties (thermal conductivities) then need to be done. The boundary conditions used the most are the convection/radiation boundary conditions and the adiabatic boundary condition. For the convection/radiation boundary conditions the heat flux to the wall is found from

$$q = h_{ext}(T_{ext} - T_{wall}) , \quad (2.13)$$

where  $h_{ext}$  is the combined convection and radiation heat transfer coefficient, and  $T_{ext}$  and  $T_{wall}$  are the external and wall temperatures, respectively. Here, external means either warm side or cold side. The adiabatic boundary condition means that there is no heat flux across the boundary.

Figure 2.5 shows the cross-section to be modeled when the thermal transmittance of only the frame is to be determined according to CEN (2001a) and ISO (2000a). Instead of the actual glazing system the frame is to be completed by an insulation panel with a thermal conductivity of  $\lambda = 0.035 \text{ W/mK}$ . The panel is pushed into the frame up to a clearance of 5 mm, but not more than 15 mm. The visible part of the panel is to be 190 mm at least, and the thickness is to be the same as the thickness of the replaced glazing system. The equation used to find the thermal transmittance of the frame,  $U_f$ , can then be written

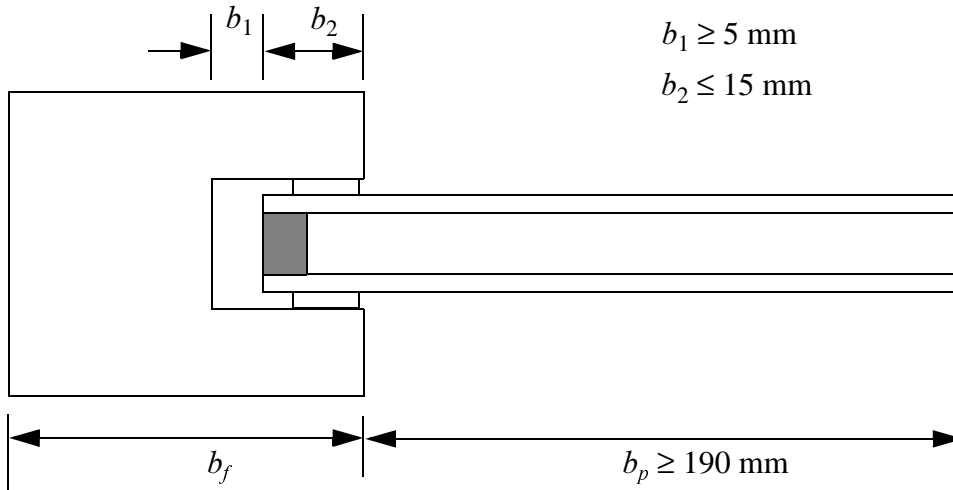


**Figure 2.6.** Window frame section with glazing installed.

$$U_f = \frac{L_f^{2D} - U_p \cdot b_p}{b_f} . \quad (2.14)$$

$U_p$  is the thermal transmittance of the center of the insulation panel,  $b_f$  is the projected width of the frame section, and  $b_p$  is visible width of the insulation panel.  $L_f^{2D}$  is the thermal conductance of the entire section shown in Figure 2.5, and is calculated from the total heat flow rate per unit length through the section divided by the temperature difference between the indoor and the outdoor. The linear thermal transmittance,  $\Psi$ , which accounts for the interaction between the frame and the glazing, can be calculated from

$$\Psi = L_\Psi^{2D} - U_f \cdot b_f - U_g \cdot b_g , \quad (2.15)$$

where  $L_\Psi^{2D}$  is the thermal conductance with the insulating panel in Figure 2.5 replaced with the original glazing, like that shown in Figure 2.6.  $U_g$  is the thermal transmittance of the glazing (central area and excluding the effect of glass spacer) and  $b_g$  is the visible width of the glazing.  $U_f$  is found from Eq. (2.14). Thus, two simulations of the frame are required if the thermal transmittance of a window is to be found from Eq. (2.7).

If the thermal transmittance of the window is to be calculated according to ASHRAE (1996), Eq. (2.8), the frame and edge of glass  $U$ -values are found from

$$U_{fr} = \frac{Q_{fr}}{b_f \cdot (T_{in} - T_{out})}, \text{ and} \quad (2.16)$$

$$U_e = \frac{Q_e}{b_e \cdot (T_{in} - T_{out})}. \quad (2.17)$$

$Q_{fr}$  and  $Q_e$  are heat flow rates per unit length through the frame and edge of glass areas. Here the frame is simulated with the actual glazing, and therefore  $Q_{fr}$ , and hence  $U_{fr}$ , include the effect of glass and spacer.  $b_e$  is the projected width of the edge of glass (equal to 63.5 mm by definition) and  $b_f$  is the projected width of the frame, the same as above.  $T_{in}$  and  $T_{out}$  are the indoor and outdoor temperatures, respectively. This approach for finding frame U-values is similar to an alternate approach described in ISO (2000a), however, an explicit width of the edge of the glass area is not specified there.

In the numerical simulations solid materials are easily assigned a conductivity. Typical conductivity values for frame materials can for instance be found in CEN (2001a). However, knowing that there are a vast number of window frames with even more air cavity geometries, there is a need for rules about how to transform air cavities to solids. For instance, we would not expect the same convection and radiation effects in the two cavities shown in Figure 2.7. This is because convection and radiation depend on cavity geometry. We also have to remember that the orientation of the frame, vertical, horizontal or a combination (like for complete window frames), also influences the heat flow (see Figure 2.8).

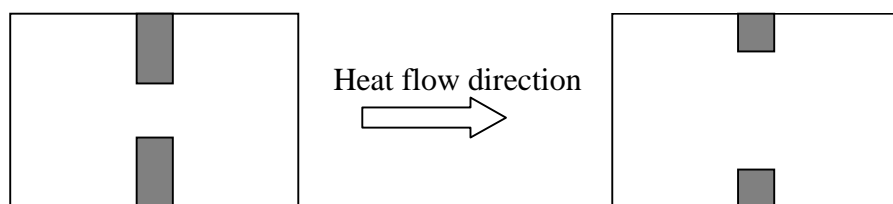


**Figure 2.7.** Schematic diagram of two simple frame cavities.

International standards use different approaches to transform air cavities to solids. Some consider heat transfer in vertical frames only and others consider heat transfer in horizontal and vertical frames. There are also differences in the way non-rectangular cavities are treated. However, the different standards (ASHRAE 1996, ISO 2000a, and CEN 2001a) agree about the first basic

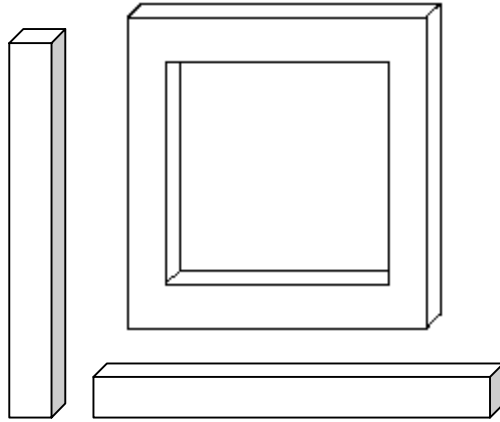


**Figure 2.8.** Schematic diagram of horizontal and vertical parts of a window frame and a complete frame.

steps; the first two equations that are used to transfer the air cavities to a solid. The equivalent conductivity assigned to an air cavity is expressed as

$$\lambda_{eq} = \frac{L}{R}, \quad (2.18)$$

where  $L$  is the dimension of the cavity in the heat flow direction.  $R$  is the thermal resistance, and can be found from

$$R = \frac{1}{h_a + h_r}. \quad (2.19)$$

$h_a$  and  $h_r$  are the convective and radiative heat transfer coefficients, respectively. Correlations for  $h_a$  and  $h_r$  are presented and discussed in Chapter 3.

Because the correlations for  $h_a$  and  $h_r$  are usually developed for rectangular cavities, special care is needed for irregular cavities. CEN (2001a) transform a non-rectangular cavity to a rectangular cavity like that shown in Figure 2.9. Notice that CEN (2001a) calculates the thermal transmittance for vertical frames. In addition, cavities with one direction not exceeding 2 mm or cavities with an interconnection not exceeding 2 mm are to be considered as separate.

In North America thermal transmittance of window frames are determined according to procedures prescribed by the National Fenestration Rating Council (NFRC). According to Mitchell et al. (2000) the convection heat transfer coefficient of a frame cavity is to be determined based on the bounding rectangle of the cavity (illustrated in Figure 2.10). Also, cavities that are separated

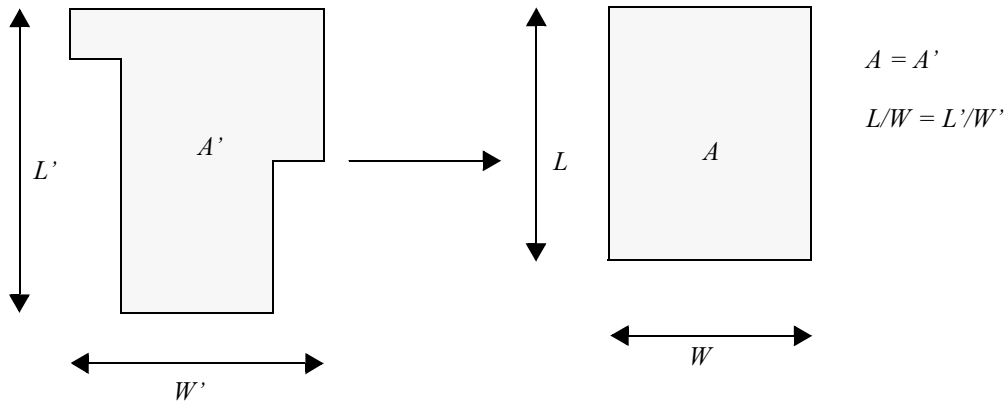


**Figure 2.9.** Figure describing how non-rectangular cavities are treated in CEN (2001a). Note that CEN (2001a) calculates the thermal transmittance of vertical frames. The heat flow direction is from bottom of the page to the top.

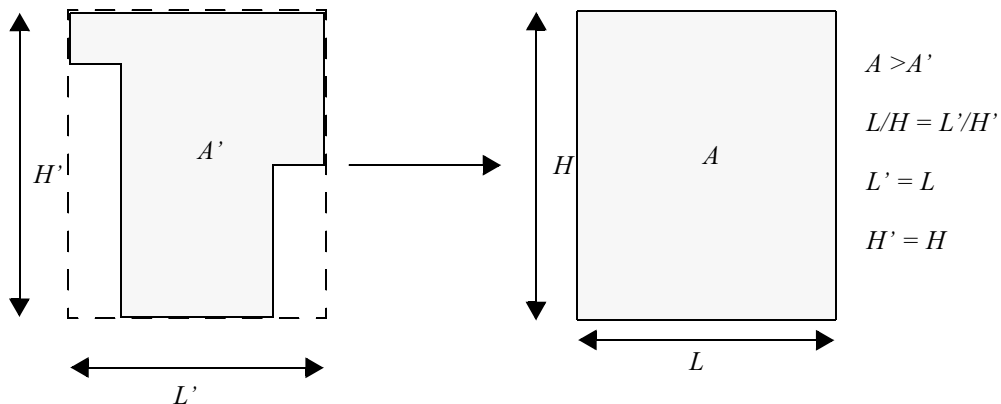


**Figure 2.10.** Figure describing how non-rectangular cavities are treated according to NFRC procedures. The heat flow direction is from left to right.

by a connection less than 0.25 inches (6.35 mm) are to be broken up. However, if a frame cavity has a Nusselt number less than or equal to 1.20, it is not necessary to break up the cavity into smaller cavities. According to NFRC procedures the fenestration product is to be divided into its cross sections, and thermal transmittances are to be found for each component (sill, head, jamb, meeting rail, and divider), see Mitchell et al. (2000).

ISO (2000a) prescribes that irregular air cavities are to be converted into equivalent rectangular cavities according to the procedures in CEN (2001a). If the shortest distance between two opposite surfaces is smaller than 5 mm the frame cavity is to be split at this “throat” region. This standard also specifies when heat flow is considered horizontal and vertical, and which surfaces of the irregular cavity that belongs to the vertical and horizontal surfaces of the equivalent rectangular cavity. The heat transfer correlation is to be selected based on the orientation of the frames, e.g. for jamb sections, correlations usable for aspect ratios,  $H/L$ , larger than 5 are to be used (also see Chapter 3).



# Chapter 3

## Heat Transfer in Frame Cavities

### 3.1 Introduction

Heat transfer by natural convection and conduction in enclosures has received considerable attention. This is largely due to the many applications, which include solar collectors, cooling of electronic equipment, nuclear reactor technology and building technology. Building technology applications include for example heat transfer in hollow walls, hollow window frames and double glazed windows. More recently, radiation heat transfer effects have also been included when numerically analyzing the heat transfer for the above-mentioned applications.

Ideally, to fully incorporate convection heat transfer in the cavities when calculating the thermal transmittance of window frames, we need to do computational fluid dynamic simulations. Solving the equations involved are time consuming, especially if we model the full three-dimensional problem. An alternative approach is to use the simpler numerical correlations for the convection and radiation interaction in the cavities. These are used for finding equivalent conductivities for the cavities.

When correlations are found they are usually developed for special applications. And because of the diversity of the applications, resulting in cavities of all types of shapes, correlations are also found for various types of enclosures. Because of this the engineer needs to find the right correlation for each problem and also be aware of the limitations of each correlation. This chapter summarizes some of the most used correlations for convection and radiation heat transfer in cavities with air, and is not a complete review of the literature covering heat transfer in enclosures. Here, the focus is put on correlations that can be used for the numerical calculation of heat transfer in window frame cavities and cavities of multiple glazing windows. First, we review the dimensionless numbers relevant for the convection heat transfer inside the cavities, with a discussion of the range applicable for the above defined applications. Different ways of defining the Nusselt number are also discussed. Second, we summarize some of the correlations found in

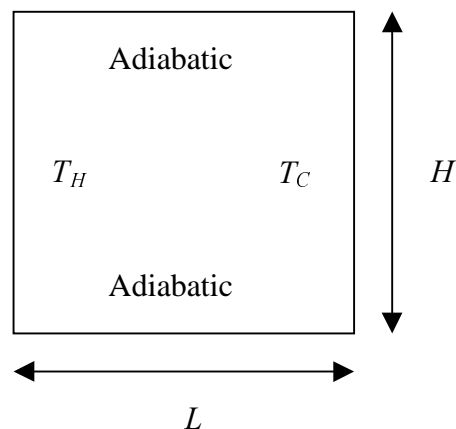


**Figure 3.1.** Rectangular cavity with two isothermal ( $T_H > T_C$ ) and two insulated walls.

the literature and also in some international standards that discuss heat transfer in cavities. Both correlations for cavities with simple (adiabatic and perfectly conducting walls) and more realistic boundary conditions will be discussed. Finally, we compare the correlations.

## 3.2 Problem Description

Correlations for heat transfer in enclosures found in the literature usually are for geometries like the ones shown in Figure 3.1 and Figure 3.2. The sections consist of two isothermal plates separated by walls which are usually assumed to be adiabatic or perfectly conducting. The latter boundary condition imposes a linear temperature rise from the cold plate to the hot one, regardless of the convective strength. Further, the correlations are developed for different angles  $\theta$  and aspect ratios;  $H/L$  and  $W/L$  for three-dimensional geometries, and  $H/L$  only for two-dimensional geometries. In this chapter we focus on correlations developed for situations where  $\theta = 90^\circ$ , which is the angle usually found for cavities in building walls.

Figure 3.3 shows a cross section of a complex window frame made in aluminum with thermal breaks. Based on this figure and other figures of facade systems and window frames (Wicona 1998a and Wicona 1998b) we find that the typical cavity dimensions range from approximately  $1 \text{ mm} \times 1 \text{ mm}$  within rubber gaskets, via  $7.5 \text{ mm} \times 6.5 \text{ mm}$  within thermal breaks to  $150 \text{ mm} \times 60 \text{ mm}$  within aluminum extrusions. The first number is the length  $L$  between the supposed isothermal plates in the simplified structures shown in Figure 3.1 and Figure 3.2. More specifically we therefore have  $H/L \sim 1$  and  $W/L > W_{min}/L_{max} \approx 1 \text{ m} / 0.15 \text{ m} \approx 6$  for the horizontal sections and likewise  $W/L \sim 1$  and  $H/L > 6$  for vertical sections. However, we have to remember that

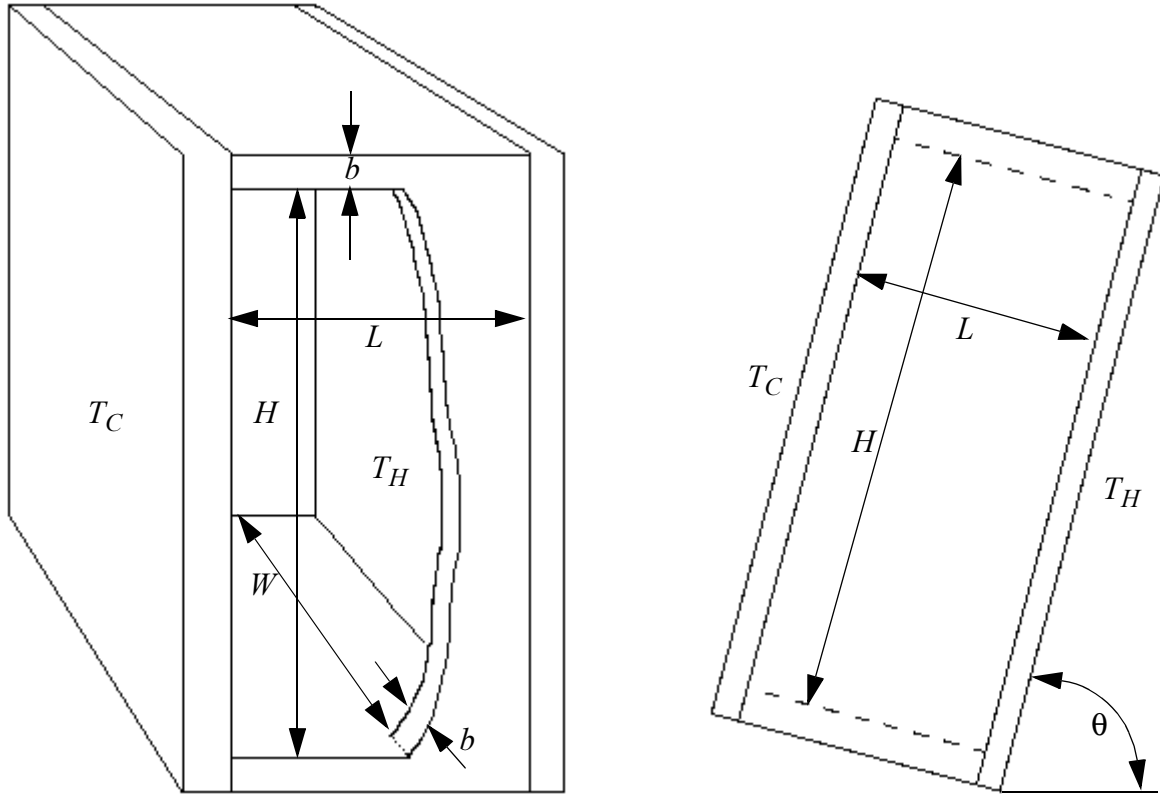


**Figure 3.2.** Typical geometry configuration for Nusselt number correlations.

most of the cavities in real facade systems not only extend either in the horizontal or vertical direction, but that cavities extend both vertically and horizontally (see Figure 2.8). Drainage openings in the sections and cavities that are open to the exterior environment also complicate the situation.

### 3.3 Important Dimensionless Groups

When dealing with convection heat transfer one often run into dimensionless groups. We can now describe the most used groups and also give their range relevant for natural convection heat transfer in frame cavities.

First we introduce the Prandtl number, which may be thought of as the ratio of the momentum and thermal diffusivities

$$Pr = \frac{c_p \mu}{\lambda} = \frac{\nu}{\lambda / \rho c_p} = \frac{\nu}{\alpha} . \quad (3.1)$$

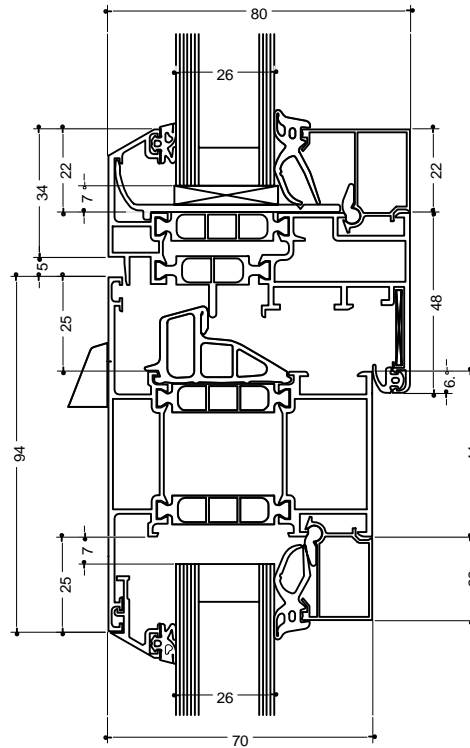


**Figure 3.3.** Figure of window frame from WICONA Bausysteme GmbH. This frame is from the WICLINE 70.1 series (Wicona 1998a).

There are three broad groups of the Prandtl number which are worth mentioning. These are liquid metals, with  $Pr \ll 1$ ; gases, with  $Pr \sim 1$ ; and oils, with  $Pr \gg 1$ . For air  $Pr \approx 0.7$  for the temperature range relevant for heat transfer in building sections.

The second dimensionless number is the Grashof number,

$$Gr_L = \frac{\beta \Delta T g L^3}{\nu^2}, \quad (3.2)$$

which represents the ratio of buoyant forces to viscous forces. This number is used when we consider natural convection flow. For the configuration shown in Figure 3.1,  $\Delta T = T_H - T_C$ .  $L$  is usually taken to be the distance between the two isothermal walls.

Next, we present the Rayleigh number  $Ra_L$  which is the product of Grashof number and Prandtl number

$$Ra_L = Gr_L \cdot Pr = \frac{\beta \Delta T g L^3}{\nu \alpha}. \quad (3.3)$$

For natural convection problems, the Rayleigh number has the same role as the Reynolds number for forced convection. The transition from laminar to turbulent flow occurs at  $Ra_x \sim 10^9$  for natural convection along a vertical plate, with  $Ra_x$  evaluated at a distance  $x$  from the leading edge. For vertical cavities, the configuration in Figure 3.1, circulation occurs for  $Ra_L > 0$  (that is  $\Delta T > 0$ ), however, heat transfer is essentially by heat conduction as long as  $Ra_L < 10^3$ . As the Rayleigh number increases circulating flow develops and cells are formed. At  $Ra_L \sim 10^4$  the flow changes to a boundary layer type with a boundary layer flowing downward on the cold side and upward on the hot side, while the fluid in the core remains relatively stationary. At  $Ra_L \sim 10^5$  vertical rows of horizontal vortices develop in the core (Mills 1995). The change between different flow regimes alter with the aspect ratio. Figure 3.4 shows how the transition from laminar to turbulent flow changes with the aspect ratio  $H/L$ , and that cavities with  $H/L > 10.7$  experience secondary flow (or multicellular flow) for some Rayleigh numbers. Figure 3.5 (a) shows an example of secondary flow in a two-dimensional cavity with two isothermal vertical walls and two adiabatic horizontal walls. Figure 3.5 (b) shows a cavity without secondary flow. In each figure the left-hand wall has a higher temperature than the right-hand side. See e.g. Batchelor (1954), Eckert and Carlson (1961), or Ostrach (1988) for a more detailed description of the different flow regimes in enclosures.

We now study what range of Rayleigh numbers we can expect for window frame cavities. From Eq. (3.3) we see that the size of the Rayleigh number is mainly determined by the dimension  $L$  of the cavity and by the temperature difference between the hot and the cold walls,  $\Delta T = T_H - T_C$ . This is because the other parameters in Eq. (3.3) are approximately unchanged over the temperature range relevant for building applications (excluding fire scenarios). Figure 3.6 shows the Rayleigh number as a function of  $\Delta T$  and  $L$ .  $Ra_L$  ranges from approximately 1 to  $10^7$ , and most of the cavities will experience a Rayleigh number  $Ra_L < 10^6$ . This is because the larger cavities is surrounded by aluminum only and therefore will have a small  $\Delta T$ . Further,  $Ra_L$  is influenced most by the length separating the two isothermal plates. The mean temperature for the calculations where  $T_m = 283\text{K}$ , and the other parameters in Eq. (3.3) were evaluated for this temperature.

Another important dimensionless number is the Nusselt number,  $Nu$ , which is a dimensionless heat transfer coefficient.  $Nu$  is usually defined as the ratio of the heat transfer coefficient  $h$  to the conductive term  $\lambda/L$  of the fluid ( $\lambda$  is the conductivity of the fluid)

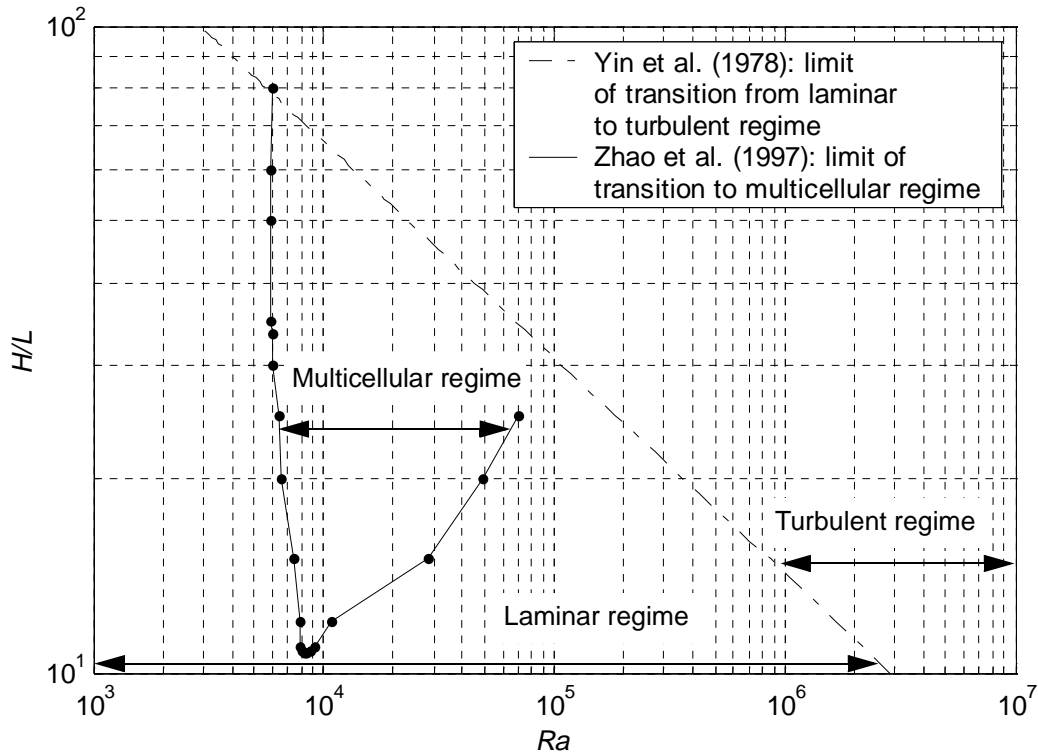
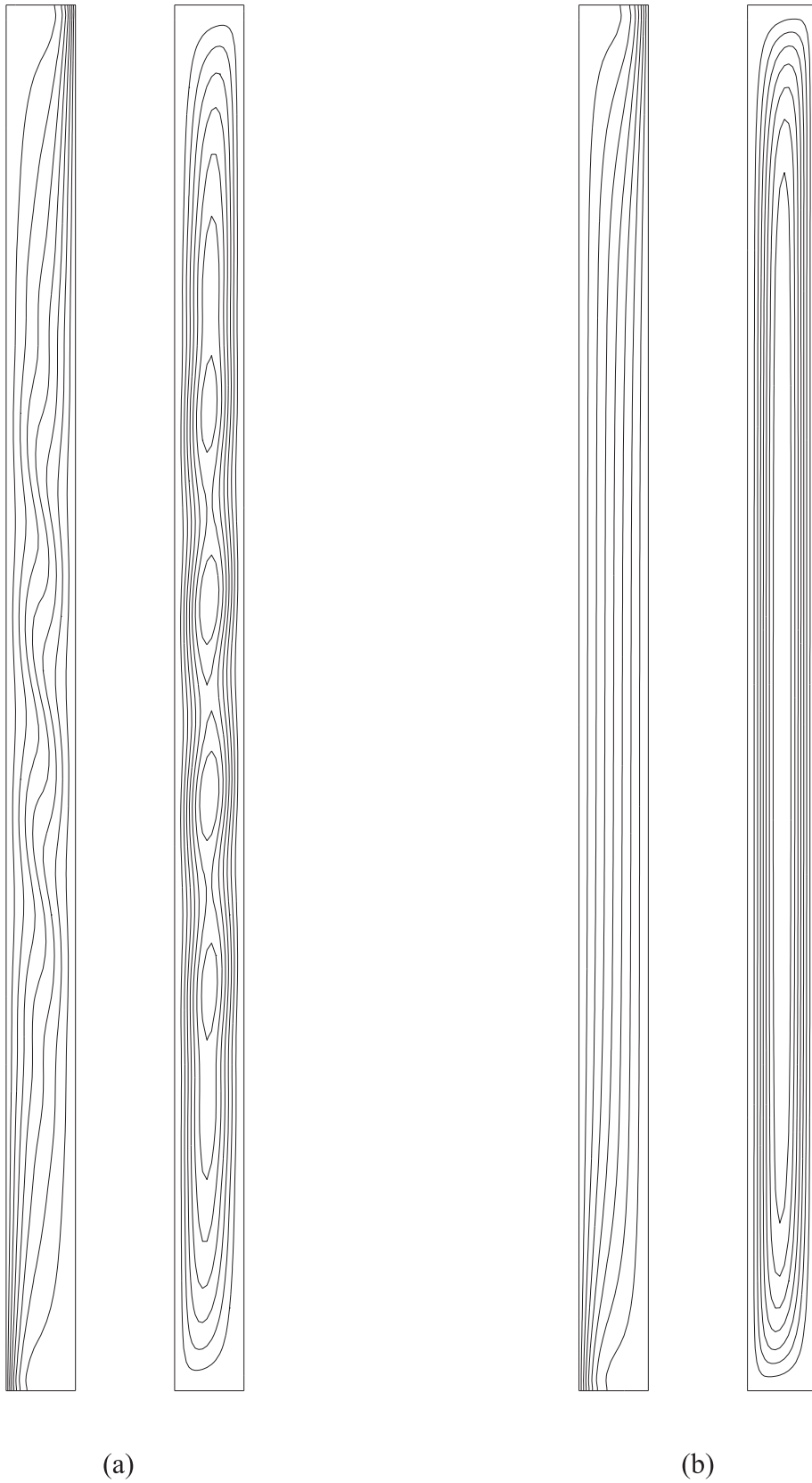


Figure 3.4. Flow regimes in cavities with high aspect ratios.

$$Nu_L = \frac{Q_f}{Q_{f0}^0} = \frac{A \cdot h(T_H - T_C)}{A \cdot \lambda(T_H - T_C)/L} = \frac{h}{\lambda/L}. \quad (3.4)$$

$Q_{f0}^0$  is the heat transfer from the hot plate to the fluid when the fluid is stationary (no radiation and conduction effects in the surrounding walls, see Figure 3.2), and  $Q_f$  is non-radiative heat transfer from the hot plate to the fluid.  $Nu_L = 1$  if the fluid is stationary and if we exclude radiation and conduction effects in the walls separating the two isothermal plates. However, when radiation and conduction also interact in an enclosure, Hoogendoorn (1986) points out that  $Nu$  from this definition can be greater than 1 even for cases where there are no flow and  $\Delta T > 0$  (occurs for cavities where  $\theta \neq 90^\circ$ ). This is because the radiative coupling increases the conduction near the hot and cold walls compared to the conduction alone situation. Thus, some other definition of  $Nu$  is used in situations where we want  $Nu$  only to include the additional convection heat transfer due to fluid motion. Raithby and Hollands (1985) discuss such a definition, and Hoogendoorn (1986) compares their definition to a definition made by Linthorst (1985). Before we can refer to these Nusselt numbers we have to define some areas for the configuration in Figure 3.2, for which  $Nu$  correlations are found in experiments, and also make some assump-



**Figure 3.5.** Possible flow patterns in a glazing cavity where the height to width aspect ratio is 20: (a)  $Ra = 10^4$ ; (b)  $Ra = 5 \times 10^3$ . In each figure the left-hand diagram displays temperature contours, and the right-hand diagram displays streamlines.

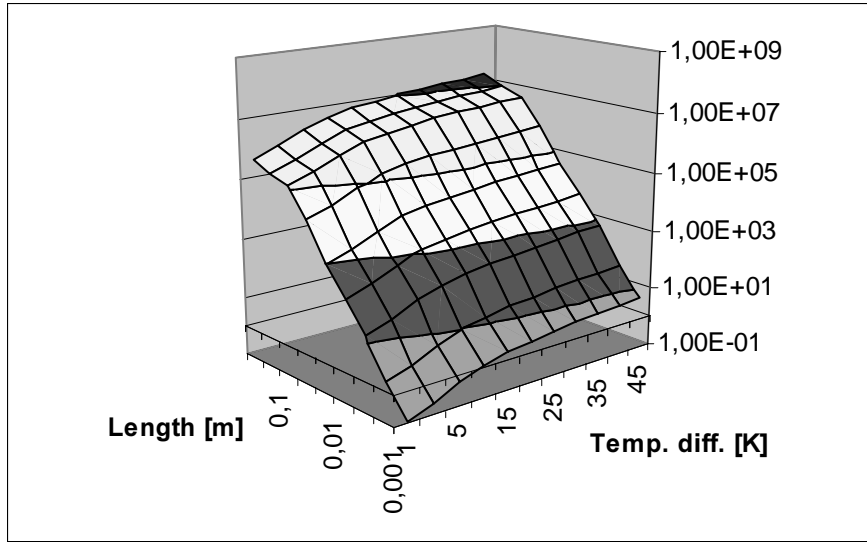


**Figure 3.6.** The figure shows Rayleigh number as function of temperature difference  $\Delta T = T_H - T_C$  and length  $L$  of the cavity. The kinematic viscosity, thermal diffusivity and the thermal coefficient of expansion are constant.

tions about the properties included. The *plate* area  $A_f = HW$  is the area over which the fluid has contact with each isothermal plate, and the *wall* area  $A_w = (2b + H)(2b + W) - HW$  is the area the isothermal plates contacts the wall. The wall is assumed to have uniform thickness  $b$  and thermal conductivity  $\lambda_w$ . See Figure 3.2 for a definition of  $H$  and  $W$ . Further the fluid is assumed to have conductivity  $\lambda$  and to be either transparent or opaque to radiation.

According to Raithby and Hollands (1985) the Nusselt number may be evaluated from two equations, depending on what situations we consider. The first is defined by

$$Nu_1 = 1 + \frac{(Q_f - Q_{f0})}{A_f \cdot \lambda (T_H - T_C) / L} = 1 + \frac{(Q_f - Q_{f0})}{Q_{f0}^0}, \quad (3.5)$$

and the second by

$$Nu_2 = 1 + \frac{[Q_f + Q_r + Q_w - (Q_{f0} + Q_{r0} + Q_{w0})]}{A_f \cdot \lambda (T_H - T_C) / L} = 1 + \frac{(Q_{tot} - Q_{tot0})}{Q_{f0}^0}, \quad (3.6)$$

where  $Q_f$  is the non-radiative heat transfer rate from the inner area  $A_f$  of the hot plate,  $Q_r$  is the net radiant heat transfer from the same area into the cavity, and  $Q_w$  is the heat conducted from the area  $A_w$  of the hot plate and into the wall.  $Q_{f0}$ ,  $Q_{r0}$  and  $Q_{w0}$  are the respective heat transfers

when the fluid is stationary. If the fluid is transparent  $Q_{f0}$ ,  $Q_{r0}$  and  $Q_{w0}$  must be determined from a combined radiation-conduction analyses. The fluid motion usually alters the temperature distribution in the wall from what was the case when the fluid is stationary. In doing this, it alters not only  $Q_f$  but also  $Q_r$  and  $Q_w$ . This alteration is incorporated into Eq. (3.6) but not in Eq. (3.5). Therefore, Raithby and Hollands (1985) recommend Eq. (3.6). Eq. (3.5) can be used if we measure the convective heat transfer only, which is possible for interferometric experiments (Hoogendoorn 1986). However, this is not the case for caloric measurements where we cannot separate between  $Q_f$  and  $Q_r$ . Then the usual approach is to measure the total heat transfer for a stationary fluid situation ( $Q_{tot0}$ ) and compare this to a fluid-in-motion situation ( $Q_{tot}$ ). A stationary fluid situation can be achieved by tilting the enclosure such that the hot plate is above the cold plate ( $\theta = 180^\circ$  in Figure 3.2, see e.g. Leong et al. 1998) or by letting the air pressure inside the cavity be low (see Hollands and Konicek 1973 or Hollands 1973).

Note that the denominator in Eq. (3.5) and Eq. (3.6),  $Q_{f0}^0 = A_f \cdot \lambda(T_H - T_C) / L$ , indicate that heat transfers by pure conduction (no fluid motion and radiation-conduction interaction in the walls), while  $Q_{f0}$  is the non-radiative heat transfer from the inner area  $A_f$  of the hot wall to the cavity for a stationary fluid and for a situation where there can be both conducting walls and radiation in the enclosure. If we rewrite the commonly used definition given in Eq. (3.4), the difference between this definition and the definition of Raithby and Hollands (1985), Eq. (3.5), is easily seen

$$Nu = \frac{Q_f}{Q_{f0}^0} = 1 + \frac{(Q_f - Q_{f0}^0)}{Q_{f0}^0} . \quad (3.7)$$

The definition of the Nusselt number used by Linthorst (1985),

$$Nu_3 = \frac{Q_f}{Q_{f0}} = 1 + \frac{(Q_f - Q_{f0})}{Q_{f0}} , \quad (3.8)$$

is also different from the commonly used definition given in Eq. (3.4) or Eq. (3.7). Here the non-radiative heat flux leaving the hot isothermal plate is compared to the similar situation without convection (with the possibility of radiation in the cavity and conducting walls). Due to this different definitions of the Nusselt number, Hoogendoorn (1986) concludes that a comparison of experimental results from different authors on Nusselt numbers that give only convection effects is impossible if there are differences in radiative properties of the plates and walls. Further,

Hoogendoorn states that comparison with numerical data without the proper radiative boundary conditions cannot be made for such cases. ElSherbiny et al. (1982b) also discuss the effect of the boundary conditions on the total heat transfer, and specify the list of parameters that must be present when experimentalists are presenting their results. Raithby and Hollands (1985) enlarge this list and say that a dimensionless analyses in general reveals that

$$Nu = Nu\left(Ra, Pr, \theta, \frac{H}{L}, \frac{W}{H}, \frac{b}{L}, \frac{\lambda_w}{\lambda}, \frac{\sigma T_m L}{\lambda}, \varepsilon_w, \varepsilon_H, \varepsilon_C, \frac{T_H}{T_C}\right), \quad (3.9)$$

where  $\varepsilon_H$  and  $\varepsilon_C$  are the emissivities of the hot and the cold plates respectively and  $\varepsilon_w$  is the emissivity of the wall surrounding the fluid. Of special interest are the cases where the wall is treated as adiabatic and as perfectly conducting.

There are also differences in the temperature difference that is used when calculating the Nusselt number. Above all Nusselt numbers were calculated by dividing “some heat transfer” by the entire temperature difference across the cavity. In some places the Nusselt number is calculated by dividing the heat transferred by the temperature difference between the hot wall and the mean bulk temperature of the fluid (see e.g. Hsieh and Wang 1994).

### 3.4 Correlations for Frame Cavities

Several investigations have been conducted to find Nusselt number correlations for the geometries described in Figure 3.1 and Figure 3.2. Ostrach (1972) gives a review of early work within this area. Hoogendoorn (1986) and Ostrach (1988) present more recent reviews of articles discussing different aspects of natural convection in such enclosures. Natural convection heat transfer correlations from vertical and horizontal surfaces (also for enclosures) modified for building application are reviewed by Dascalaki et al. (1994). Further, textbooks like Gebhart et al. (1988), Mills (1995), and Kreith and Bohn (1997) also include correlations for convection heat transfer in enclosures. The present work is focused on correlations for situations relevant for air cavities in aluminum facade systems, window frames and multiple glazing for buildings. A full review of all the literature is not given, just the correlations that are recommended and most used. Because of the differences in the different Nusselt number definitions I have tried to specify under which conditions the experiments were conducted, and for what assumptions the numerical simulations were made. In addition, I have specified what form of Nusselt number that was used. Correlations from international standards will also be included. First,

some general remarks are given on three-dimensional effects on the Nusselt number and the boundary conditions usually found in numerical and experimental investigations.

### 3.4.1 Three-dimensional Effects

Most of the correlations for the Nusselt number are developed for situations where researchers can assume that the fluid flow is two dimensional. In relation to the three-dimensional geometry shown in Figure 3.2, we get a “two-dimensional cavity” when  $W/L$  approaches infinity. Some research has been done on the effect of  $W/L$  on the heat transfer. Fusegi et al. (1991) compared the overall Nusselt number for a three-dimensional cubical enclosure with the overall Nusselt number for the square two-dimensional enclosure. Their study was numerical and the walls were assumed to be adiabatic. They found that the Nusselt number for the three-dimensional cube was smaller than for the two-dimensional square for  $Ra < 10^5$ . The difference was about 8 % at most. At  $Ra = 10^6$  the difference was about 2 %.

ElSherbiny et al. (1982a) experimentally studied the effect of  $W/L$  for a cavity where  $H/L$  was held constant to 5. Heat transfer was measured along a strip (200 mm wide) lying midway between the two perfectly conducting edges. The total width  $W$  of the plates were 635 mm. For  $8 \times 10^3 < Ra_L < 2 \times 10^5$  the maximum difference between  $Nu$  for  $W/L = 5$  and  $Nu$  for  $W/L = 7.5$  was about 4.3 %. The corresponding difference in  $Nu$  for  $W/L = 7.5$  and  $Nu$  for  $W/L = 15$  was about 3 %. Outside this  $Ra_L$  range the differences in  $Nu$  caused by changes in  $W/L$  were negligible. Arnold et al. (1977) studied the effect of  $W/L$  on the heat transfer for multicellular array of rectangular parallelepiped cavities, an arrangement used for convection suppression in solar collectors. For  $H/L = 0.25$  they found that there were little effect of  $W/L$  on the heat transfer down to values of 0.5. Further, Raithby and Hollands (1998) report that Edwards et al. (1978) found that the Nusselt number was reduced substantially when the  $W/L$  was reduced from 0.5 to 0.25. Thus, for our case (heat transfer in window frame sections) the two-dimensional situation only can be utilized for horizontal mounted window frames and not vertical frames where  $W/L \sim 1$  and  $H/L > 6$ . For cavities in multiple glazed windows the two-dimensional situation can be utilized to some extent.

### 3.4.2 Boundary Condition Effects

Numerical and experimental investigations of heat transfer in enclosures with air are usually conducted by assuming the adiabatic or perfectly conducting wall boundary conditions. For numerical simulations both boundary conditions can easily be assumed and programmed. How-

ever, this is not the case for experimental investigations where the perfectly conducting wall boundary condition is the easiest one to obtain (ElSherbiny et al. 1982b and Leong et al. 1998). This can be done by using a metal sheet like aluminum or copper as the boundary. In order to use the adiabatic boundary condition we would need side walls bounding the air to have a conductivity of at least an order of magnitude less than the conductivity of air. This is not obtainable for practical application today.

Le Puetrec and Lauriat (1990) did a numerical investigation of the effect of side walls on heat transfer by natural convection in a three-dimensional cavity. The horizontal walls were adiabatic while conduction was allowed in the non-isothermal vertical side walls. There were two important parameters that characterized the heat losses at the side walls, the thermal conductance of the walls and the ambient temperature. For enclosures filled with low-conductivity fluids they found that heat losses have appreciable effects if the average temperature of the hot and cold walls not is kept very close to the ambient temperature. Further they found that their relative influence decreased when they increased the Rayleigh number and the longitudinal aspect ratio  $W/L$ . We now turn to the correlations for enclosures.

### 3.4.3 Convection in Enclosures with Simple Boundary Conditions

For vertical enclosures with air,  $5 < H/L < 40$ , and  $10^3 < Ra_L < 10^7$  Mills (1995) and Raithby and Hollands (1998) recommend the correlation of ElSherbiny et al. (1982a)

$$Nu_L = \max(Nu_1, Nu_2, Nu_3) , \quad (3.10)$$

where

$$Nu_1 = 0.0605 Ra_L^{1/3} , \quad (3.11)$$

$$Nu_2 = \left\{ 1 + \left[ \frac{0.104 Ra_L^{0.293}}{1 + (6310/Ra_L)^{1.36}} \right]^3 \right\}^{1/3} , \text{ and} \quad (3.12)$$

$$Nu_3 = 0.242 \left( \frac{Ra}{H/L} \right)^{0.272} . \quad (3.13)$$

For  $Ra_L \leq 10^3$  they found that  $Nu_L \approx 1$ , which is equivalent to treating the air as a solid with the conductivity of air. In their experimental setup  $W/L$  was greater than 7.5. They used a 0.5 mm thick copper sheet to separate the two vertical isothermal plates and therefore assumed a linear

temperature rise from the cold to the hot plate. The hot and the cold plates were also made of copper.

For  $H/L > 40$ ,  $Ra_L < 10^6$  and  $Pr \approx 0.7$  Raithby and Hollands (1998) recommend the correlation of Shewen et al. (1996)

$$Nu_L = \left\{ 1 + \left[ \frac{0.0665 Ra_L^{1/3}}{1 + (9000/Ra_L)^{1.4}} \right]^2 \right\}^{1/2}. \quad (3.14)$$

This correlation is based on experiments for aspect ratios of  $H/L$  equal to 40, 60 and 110. The air cavity was formed between two aluminum plates where the outside edges were closed by an aluminum foil covered by glassfiber insulation on the outside. This setup was chosen to ensure a linear temperature profile between the plates. The spacing between the plates  $L$  used was 18.97, 12.48 and 6.81 mm. The width  $W$  of the plates was 850, which gave  $W/L > 45$ . Shewen et al. (1996) also found that the data appeared to be nearly independent of  $H/L$  (there is a slight increase of  $Nu$  with  $H/L$ ), and points out that ElSherbiny et al. (1982a) made a similar observation for  $H/L > 20$ . Both the correlations of ElSherbiny et al. (1982a) and Shewen et al. (1996) were developed based on Eq. (3.6).

In vertical cavities of small aspect ratio Mills (1995) and Gebhart et al. (1988) suggest the correlations due to the two-dimensional numerical calculations of Berkovsky and Polevikov (1977) which can be used for cavities with insulated horizontal walls and for fluids with Prandtl numbers over a wide range. For  $Pr < 10^5$ ,  $2 < H/L < 10$  and  $Ra_L < 10^{10}$

$$Nu_L = 0.22 \left( \frac{Pr}{0.2 + Pr} Ra_L \right)^{0.28} \left( \frac{H}{L} \right)^{-1/4}, \quad (3.15)$$

and for  $10^{-3} < Pr < 10^5$ ,  $1 < H/L < 2$  and  $10^3 < \frac{Pr}{0.2 + Pr} Ra_L$

$$Nu_L = 0.18 \left( \frac{Pr}{0.2 + Pr} Ra_L \right)^{0.29}. \quad (3.16)$$

Hsieh and Wang (1994) also studied the Nusselt number for enclosures with aspect ratios in approximately the same range as Berkovsky and Polevikov (1977). However, their study was experimental, with the assumption of adiabatic walls. These walls were made of 10 mm plexi-glass with 10 mm polystyrene foam. For  $0.7 < Pr < 464$ ,  $W/L = 5$  and  $3 \leq H/L \leq 5$  they found

$$Nu_H = 0.321 \cdot Ra_H^{0.241} (H/L)^{-0.095} Pr^{0.053} \text{ for } 10^6 < Ra_H < 1.4 \times 10^7 \text{ and } \quad (3.17)$$

$$Nu_H = 0.133 \cdot Ra_H^{0.301} (H/L)^{-0.095} Pr^{0.053} \text{ for } 1.4 \times 10^7 < Ra_H < 2 \times 10^9 . \quad (3.18)$$

The data was not corrected for conduction through the gasket from the heated to the cooled plate, nor for radiation heat transfer from the hot to the cold plate. Still, the overall heat transfer measurements were expected to be within  $\pm 5\%$  of the actual convection heat transfer from each wall. For both correlations the temperature difference used to calculate the heat transfer coefficient is the difference between the wall temperature and the mean bulk temperature, equal to  $(T_H + T_C)/2$ .  $Ra_H$  was calculated based on the total temperature difference  $T_H - T_C$ .

Several numerical investigations have been conducted for the two-dimensional square cavity with adiabatic walls. This case is often referred to as the benchmark configuration, and benchmark solutions have both been found for laminar flow (de Vahl Davis and Jones 1983 and de Vahl Davis 1983) and turbulent flow (Henkes and Hoogendoorn 1995). However, none of these include general correlations for the Nusselt number. Most of the correlations developed for a square cavity are correlated using Eq. (3.19) where  $a$  and  $b$  are constants (subscripts for  $Nu$  and  $Ra$  are dropped for square enclosures because  $H=L$ )

$$Nu = a \cdot Ra^b . \quad (3.19)$$

Raithby and Hollands (1998) recommend the correlation of Kuyper et al. (1993) which was found for a square cavity with adiabatic walls. The standard  $k$ - $\epsilon$  model for turbulence was used in the prediction of turbulent flow.

$$Nu = 0.171 \cdot Ra^{0.282} \text{ for } 10^4 < Ra < 10^8 \quad (3.20)$$

$$Nu = 0.050 \cdot Ra^{0.341} \text{ for } 10^8 < Ra < 10^{12} \quad (3.21)$$

For cavities with  $H/L < 0.5$  and  $W/L \geq 5$  Gebhart et al. (1988) and Raithby and Hollands (1998) suggest the correlation of Bejan and Tien (1978)

$$Nu_L = 1 + \left\{ \left[ \gamma_1 Ra_L^2 \left( \frac{H}{L} \right)^8 \right]^m + \left[ \gamma_2 Ra_L^{1/5} \left( \frac{L}{H} \right)^{2/5} \right]^m \right\}^{1/m} , \quad (3.22)$$

where  $m = -0.386$ ,  $\gamma_1 = 2.756 \times 10^{-6}$ , and  $\gamma_2 = 0.623$ . This correlation is based on two-dimensional analytical analyses for laminar flow in a cavity with adiabatic walls. Hence, this equation is not recommended for  $Ra_H H^3/L^3 > 10^9$ . Further, because of the dominance of the walls in this problem, departures from the adiabatic wall conditions are expected to have a marked effect on  $Nu$ . Later Shiralkar and Tien (1981) further developed the correlation of Bejan and Tien (1978) since it was not sufficiently accurate for intermediate  $Ra$  range. However, Smart et al. (1980) found that Eq. (3.22) agreed well with their experiments, provided that they changed the constants  $\gamma_1$  and  $\gamma_2$ , even though an adiabatic wall boundary condition could not be utilized for their experiment. Smart et al. (1980) did an experimental investigation of heat transfer for multicellular array of rectangular parallelepiped cavities with  $3 < L/H < 10$  and  $W/H = 44$ . For the walls they used two types of polyethylene film, which gave different values for the wall conductivity. They also changed the emissivity of the walls and the isothermal plates. The working fluid was air. Smart et al. (1980) did not find a correlation covering the whole range of parameters studied, but gave a list of values for the constants  $\gamma_1$  and  $\gamma_2$ , which can be used for similar situations. These parameters can be found in both Smart et al. (1980) and Raithby and Hollands (1998). It is noted that there also will be heat transfer across wall boundaries for the experiment of Smart et al. (1980).

Both Gebhart et al. (1988) and Raithby and Hollands (1998) give a compilation of their referred Nusselt number correlations versus the aspect ratio,  $0.1 < H/L < 100$  (effect of  $W/L$  is excluded, because they assume two-dimensional flow). They find a maximum in  $Nu$  near  $H/L = 1$  and that this maximum moves to lower values of  $H/L$  as  $Ra$  is increased.  $Nu$  decreases fast towards 1 as  $H/L$  decreases from approximately 1 to 0.1. Further  $Nu$  also decreases as  $H/L$  increases from 1. However, this decrease is very slow. These comments are valid for  $10^3 < Ra_L < 10^5$ .

#### 3.4.4 Correlations for Complex and Realistic Boundary Conditions

Most of the above correlations have been for situations where the boundaries were assumed to be either adiabatic or perfectly conducting. There have also been some investigations of cases with more complex boundary conditions. Most of these investigations have been for square enclosures. Fusegi and Hyun (1994) have written a review covering different aspects of natural convections in enclosures with complex and realistic conditions, like non-idealized thermal boundary conditions, variable property effects and transient effects. Here we will focus on correlations for the Nusselt number that have emerged from such investigations.

Kim and Viskanta (1984) did experimental and numerical investigations of the wall conductance on natural convection in square cavities. The inside dimensions of the cavity test material were 3.6 cm by 3.6 cm ( $h \times l$ ) and the outside dimensions were 6 cm by 6 cm ( $H \times L$ ). The width  $W$  of the test cell was 19 cm, and the interior walls in the cavity was treated to give the surfaces an emissivity greater than 0.99. An interferometer was employed as a diagnostic tool for measuring the temperature distribution. The working fluid was air at atmospheric pressure. An empirical correlation of the average Nusselt Number was found from the numerical results to be

$$Nu = 0.410\phi^{0.93}(\lambda^*)^{0.138}(Ra^*)^{0.2}, \quad (3.23)$$

where  $0.3 < Pr < 50$ ,  $0.25 < \phi < 0.6$ ,  $10^5 < Ra^* < 10^7$  and  $3 < \lambda^* < 100$ .  $\phi$  which is called the void ratio is equal to  $l^2/L^2$ ,  $Ra^* = g\beta(T_H - T_C)l^3/\nu\alpha$ , and  $\lambda^* = \lambda_w/\lambda$ . The temperatures,  $T_H$  and  $T_C$ , are to be evaluated at the outer walls of the cavity, not at the boundary between fluid and material. The effect of radiation was excluded in the numerical calculations. They found good agreement between their numerical calculations and experiment, considering isotherms in the fluid.

More recently, there have been several numerical investigations of the radiation effect on natural convection for enclosures containing a fluid transparent to radiation (Behnia et al. 1990, Balaji and Venkateshan 1993, Balaji and Venkateshan 1994, Sen and Sarkar 1995, and Akiyama and Chong 1997). Common to most of them is the use of an energy balance between radiation and convection to determine the boundary conditions for the horizontal non-isothermal walls. Akiyama and Chong (1997) give a correlation of the total Nusselt number based on their numerical calculations of the heat transfer in a square enclosure (including both convection and radiation heat transfer)

$$Nu = 0.529Ra^{0.3065}\epsilon^{0.3497}, \quad (3.24)$$

which is valid for  $10^4 \leq Ra \leq 10^6$ ,  $0.02 \leq \epsilon \leq 1$ , and for  $T_0/(T_H - T_C) = 29.35$ , where  $T_0 = (T_H + T_C)/2$  is the reference temperature.

Balaji and Venkateshan (1994) give separate correlations for the radiation and the convection heat transfer. Their convection Nusselt number, which also is based on numerical calculations for a square cavity, is

$$Nu = 0.149Gr^{0.294}(1 + \varepsilon_H)^{-0.279}(1 + \varepsilon_C)^{0.182}(1 + \varepsilon_B)^{-0.135} \cdot (1 + \varepsilon_T)^{0.115} \left( \frac{N_{RC}}{N_{RC} + 1} \right)^{0.272} \quad (3.25)$$

where  $\varepsilon_H$ ,  $\varepsilon_C$ ,  $\varepsilon_B$ ,  $\varepsilon_T$  are the emissivities of the hot, cold, bottom and top walls of the cavity, respectively. The range allowed for the different parameters are  $10^3 \leq Gr \leq 10^6$ ,  $4 \leq N_{RC} \leq 22$ ,  $0.73 \leq T_R \leq 0.95$  ( $N_{RC} = \sigma T_H^4 L / k \Delta T$  and  $T_R = T_C / T_H$ ). All the emissivities can be varied from 0 to 1. The radiation Nusselt number was found to be

$$Nu_R = 0.657Gr^{-0.0093} \varepsilon_H^{0.808} \varepsilon_C^{0.342} (1 + \varepsilon_B)^{0.199} \cdot (1 + \varepsilon_T)^{-0.039} (1 - T_R^4)^{1.149} N_{RC}^{1.051} \quad (3.26)$$

### 3.4.5 Correlations from International Standards

Some international standards also deal with calculation of heat transfer in cavities. Here we review the correlations used to calculate heat transfer in unventilated cavities in window frames and other building sections. Focus is put on EN, ISO and ASHRAE-standards.

According to CEN (1998), which is a standard dealing with the determination of the thermal transmittance of frames of windows and doors, we can calculate the convection part of the heat transfer in an air cavity according to (the convective heat transfer coefficient)

$$h_a = \max\{C_1/L, C_2 \cdot (\Delta T/(1K))^{1/3}\}, \quad (3.27)$$

where  $C_1 = 0.025$  W/mK and  $C_2 = 0.73$  W/m<sup>2</sup>K.  $\Delta T$  is the temperature difference between the hot and the cold plates of the cavity. We see that the first term in Eq. (3.27) results from treating air as a stationary medium with  $C_1$  equal to the conductivity of air ( $\lambda_{air} = C_1$ ). Later this standard has been updated (CEN 2001a) and now, in addition to Eq. (3.27), cavities with smaller width  $W$  (see Figure 2.9) than 5 mm will have their convection heat transfer coefficients calculated according to

$$h_a = C_1/L. \quad (3.28)$$

That is, in cavities with a low horizontal aspect ratio,  $W/L$ , the heat flow (excluding radiation) is now assumed to be by conduction. According to CEN (1998) the radiative part of the heat transfer in an air cavity is calculated from (the radiative heat transfer coefficient)

$$h_r = E \cdot F \cdot 4\sigma \cdot T_m^3, \quad (3.29)$$

where

$$E = (\epsilon_C^{-1} + \epsilon_H^{-1} - 1)^{-1} \text{ and} \quad (3.30)$$

$$F = \frac{1}{2}(1 + \sqrt{1 + (L/H)^2} - L/H). \quad (3.31)$$

CEN (2001a) use another radiative heat transfer coefficient

$$h_r = \frac{4\sigma T_m^3}{\frac{1}{\epsilon_H} + \frac{1}{\epsilon_C} - 2 + \frac{1}{\frac{1}{2}\left(\sqrt{1 + \left(\frac{L}{H}\right)^2} - \frac{L}{H} + 1\right)}}. \quad (3.32)$$

This equation was originally developed by Roth (1998). Note that some conduction simulation tools still use the convection and radiation models described in CEN (1998) and not the models prescribed in the new version CEN (2001a).

Another standard dealing with heat transfer in cavities is ISO (1994). This standard considers the calculation of steady state U-values of multiple glazing (for the central area of the glazing). In this standard the Nusselt number is calculated from

$$Nu_L = 0.035 \cdot (Gr_L \cdot Pr)^{0.38}. \quad (3.33)$$

If  $Nu$  calculated from this formula is less than 1, the value of unity is supposed to be used. The radiative heat transfer coefficient is calculated according to Eq. (3.29), where corrected emissivities are used (these are calculated from the normal emissivities according to ISO 1994).

ISO (2000a) is a draft standard dealing with detailed calculations of the thermal properties of windows and doors. This standard gives several correlations for the Nusselt number in enclosures depending on what type of section the cavity is in (frame or glazing), the aspect ratio and the direction of heat flow. For horizontal heat flow in frame cavities where  $H/L < 0.5$  the correlation of Bejan and Tien (1978), Eq. (3.22), is to be used. For cavities where  $H/L > 5$  the correlation of ElSherbiny et al. (1982a), Eq. (3.10) - Eq. (3.13), are to be used. Interpolation between

the endpoints of the above correlations is to be used for  $0.5 < H/L < 5$ . For vertical glazing cavities the Nusselt number is to be calculated according to (originally from Wright 1996)

$$Nu_L = \max(Nu_1, Nu_2) , \quad (3.34)$$

where

$$Nu_1 = 0.0673838Ra^{1/3} \text{ for } 5 \times 10^4 < Ra < 10^6 , \quad (3.35)$$

$$Nu_1 = 0.028154Ra^{0.4134} \text{ for } 10^4 < Ra < 5 \times 10^4 , \quad (3.36)$$

$$Nu_1 = 1 + 1.17596678 \times 10^{-10} Ra^{2.2984755} \text{ for } Ra < 10^4 , \text{ and} \quad (3.37)$$

$$Nu_2 = 0.242 \left[ \frac{Ra}{H/L} \right]^{0.272} . \quad (3.38)$$

The radiative heat transfer coefficient for frame cavities is to be calculated from Eq. (3.32).

For natural convection in frame cavities ASHRAE (1996) uses the same approach as ISO (2000a). ASHRAE (1996) uses the following correlation to calculate the radiative heat transfer coefficient for frame cavities

$$h_r = \exp\left(1.53 - 0.194 \cdot \frac{L}{H}\right) \cdot \left(\frac{T_m}{273\text{K}}\right)^3 \cdot \frac{1}{\frac{1}{\epsilon_H} + \frac{1}{\epsilon_C} - 1} , \quad (3.39)$$

where  $T_m = (T_H - T_C)/2$ , in degrees Celsius.

Other international standards also dealing with heat transfer in enclosures in building sections are ISO (1996) (dealing with calculation methods of thermal transmittance of building components and building elements) and ISO (1995) (dealing with heat flow and surface temperatures in thermal bridges in building constructions). These standards give design values for the thermal resistance for unventilated air cavities with high emissivity surfaces. These values of the thermal resistance for the cavities are for discrete thicknesses of the air layer, that is the user has to refer to a specific table for each case to find the right thermal resistance of the air layer. In addition ISO (1996) also gives more general equations for calculating the thermal resistance of the air layer. For an unventilated airspace with width  $W$  and height  $H$  both more than 10 times the plate

spacing  $L$ , the conduction/convection coefficient is equal to the larger of  $1.25 \text{ W/m}^2\text{K}$  and  $0.025/L \text{ W/mK}$ . That is

$$h_a = \max\{0.025 \text{ W/mK}/L, 1.25 \text{ W/m}^2\text{K}\} . \quad (3.40)$$

The radiative coefficient is given by

$$h_r = E \cdot 4\sigma \cdot T_m^3 , \quad (3.41)$$

where  $E$  is given in Eq. (3.30). For small or divided unventilated cavities (width and height less than 10 times the isothermal plate spacing)  $h_a$  is the same and  $h_r$  is calculated from Eq. (3.29).

## 3.5 Comparison of Correlations

### 3.5.1 Natural Convection Correlations

The above Nusselt number correlations for different aspect ratios and application areas that have been presented were from papers and international standards. We can now compare the above correlations. The following calculations are based on a situation where  $T_H = 293 \text{ K}$ ,  $T_C = 273 \text{ K}$ , and where air properties are evaluated at  $T_m = 283 \text{ K}$ . From Figure 3.6 we find that there will be laminar flow for most of the frame cavities. Therefore, the plate spacing is varied between 0.01 m and 0.05 m. This results in  $10^3 < Ra_L < 10^6$ . The correlations from the international standards CEN (1998) and ISO (1996) give  $h_a$  rather than  $Nu$ . In order to compare these equations with the others, Eq. (3.4) was used to find  $Nu$ .  $L$  was used instead of  $Ra$  when comparing the different correlations because some of the correlations from international standards do not include the dimensionless number  $Ra$ . Keeping  $\Delta T$  fixed, results in  $Ra$  only depending on  $L$ , or rather  $L^3$ .

First, we compare the correlations that are suitable for air cavities in multiple glazing. The correlations compared are the ones from ISO (1994), Shewen et al. (1996), ElSherbiny et al. (1982a) and ISO (2000a), the one for glazing cavities.  $Nu$  from the correlations of ElSherbiny et al. (1982a) and ISO (2000a) were evaluated for  $H/L = 40$ . From Figure 3.7 we see that the correlations from Shewen et al. (1996) and ISO (2000a) give almost equal Nusselt numbers. Further, these correlations give a slightly larger value of the Nusselt number than the correlation from ISO (1994), with the correlation from ElSherbiny et al. (1982a) in between.

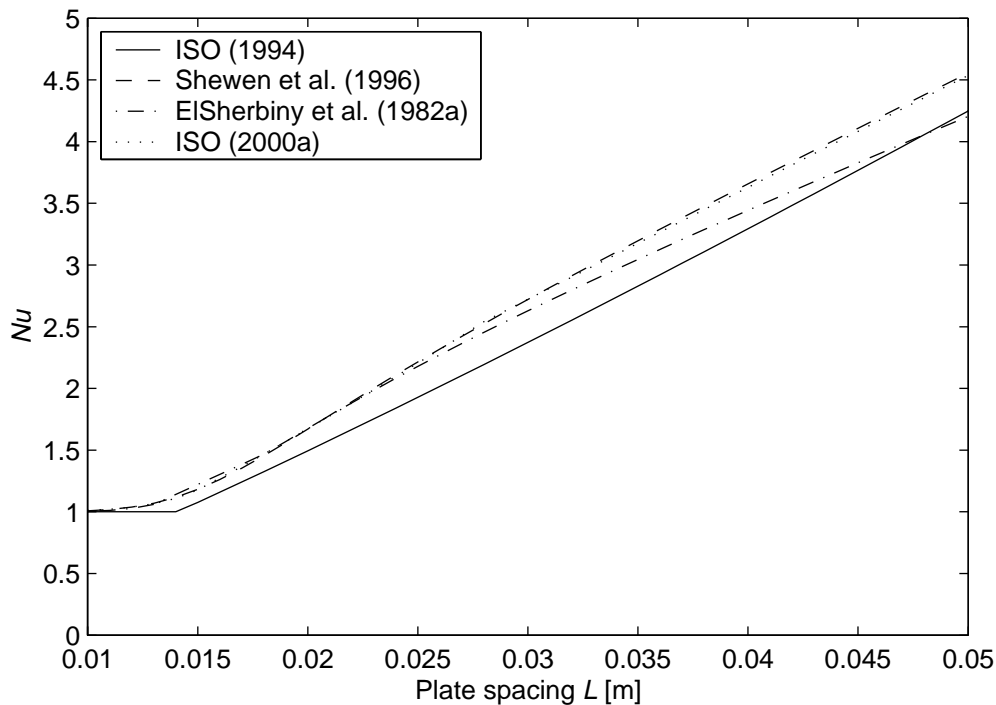


**Figure 3.7.** Comparison of Nusselt number correlations that is supposed to be usable for glazing cavities. For ElSherbiny et al. (1982a) and ISO (2000a)  $H/L$  was equal to 40.

Figure 3.8 shows  $Nu$  plotted from correlations that are supposed to be usable for square enclosures and window frame enclosures. We see that the correlations of Balaji and Venkateshan (1994), Kuyper et al. (1993) and Berkovsky and Polevikov (1977) compare well (all developed for  $H/L = 1$ ), and that the correlations from CEN (1998) and ISO (1996) run below. The Nusselt number calculated from the correlation in ISO (2000a), which is supposed to be used for window frames (using  $H/L = 1$ ) has a somewhat different trend than the other correlations. For  $H/L = 1$  linear interpolation between the correlations of Bejan and Tien (1978) at  $H/L = 0.5$  and ElSherbiny et al. (1982a) at  $H/L = 5$  is used. And as we see from the Figure 3.9, this trend is due to the correlation of Bejan and Tien (1978), which is the one having the most influence on the final result for  $H/L = 1$ . When calculating  $Nu$  from the correlation of Balaji and Venkateshan the emissivity of the plates and walls are among the parameters. Here, all emissivities were equal to 0.9. A decrease in the emissivity to 0.1 resulted in a slightly larger  $Nu$  (to the same level as  $Nu$  from Berkovsky and Polevikov 1977). This decrease in Nusselt number with increased emissivity is called the convective drop by Balaji and Venkateshan (1994).

In Figure 3.9 we compare  $Nu$  correlations supposed to be used for different aspect ratios. CEN (1998) can be used for vertical frame cavities ( $H/L$  large), Kuyper et al. (1993) can be used for

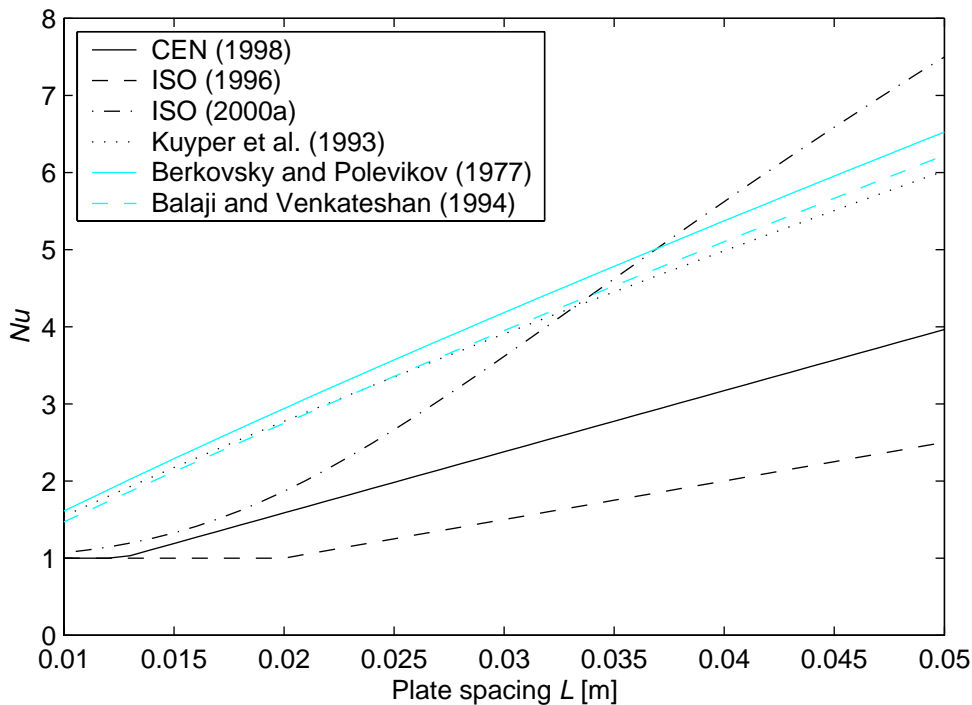


**Figure 3.8.** Comparison of Nusselt number correlations that is supposed to be usable for frame cavities. ISO (2000a) is calculated for  $H/L = 1$ .

cavities where  $H/L = 1$ , and ISO (1994) and Shewen et al. (1996) can be used for glazing cavities (high aspect ratio cavities). Figure 3.9 shows that the correlation from CEN (1998) lies close to correlations usable for glazing cavities. This is reasonable because the CEN (1998) correlation is supposed to be used for vertical frame cavities. However, we have to remember that  $Nu$  for a real three-dimensional cavity (vertical window frames have large  $H/L$  and  $W/L \approx 1$ ) probably will be smaller than for a two-dimensional cavity (glazing cavities have large  $H/L$  and large  $W/L$ ). Considering the correlation of Bejan and Tien (1978), we find that  $Nu$  lies below the square cavity correlations for  $L < 0.033$  m and above for  $L > 0.033$  m.  $H/L$  was equal to 0.5 for the calculation of  $Nu$  from Bejan and Tien (1978).

Figure 3.10 shows  $Nu$  plotted as a function of the aspect ratio  $H/L$  and Rayleigh number for the correlation from ISO (2000a) that is supposed to be used for frame cavities. The correlation is compared to other correlations (Kuyper et al. 1993 and Berkovsky and Polevikov 1977) within the interpolation area  $0.5 < H/L < 5$  to see how well this interpolation is. The figure shows that the interpolation seems to work well for  $Ra \sim 10^5$ , however for other Rayleigh numbers the interpolation does not compare well with the other correlations. Here we note that Roth (1998) compared natural convection correlations from ASHRAE (1996) (these are the same correla-

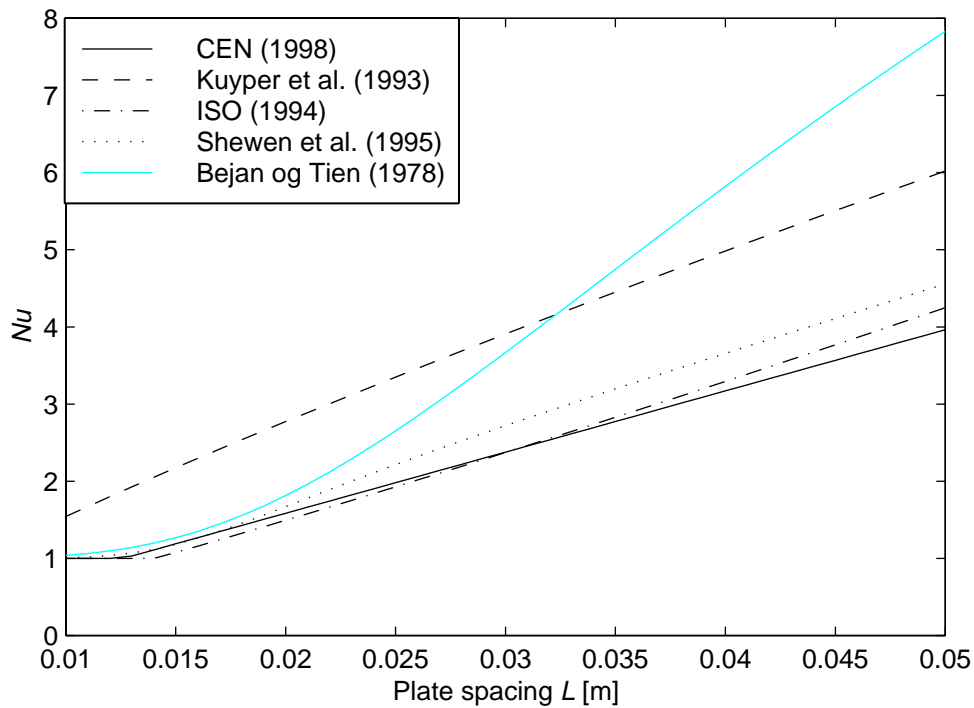


**Figure 3.9.** Comparison of correlations supposed to be used for different aspect ratios  $H/L$ . Bejan and Tien (1978) was calculated for  $H/L = 0.5$ .

tions as used in ISO 2000a, for frame cavities) and CEN (1998) for a number of cavities where the aspect ratio  $H/L$  ranged from 0.08 to 12.5. His results show that CEN (1998) over-predicts convection for  $H/L < 0.4$ . Further, for intermediate aspect ratios,  $0.4 < H/L < 10$ , CEN (1998) under-predicts natural convection heat transfer, and for large aspect ratios CEN (1998) seems to work well (like shown in Figure 3.9). However, Roth did not change the length,  $L$ , of all the cavities.  $L$  was kept constant at 25 mm for all the cavities having an aspect ratio between 0.08 and 1.0. Then  $L$  was decreased to 2 mm while  $H/L$  increased to 12.5. Since the natural convection correlation in CEN (1998) not depend on the aspect ratio, but rather on  $L$  and  $\Delta T$ , this conclusion would be different if the length,  $L$ , of the cavities had been different. In the CEN (1998) correlation,  $L$  and  $\Delta T$  seem to be more like the parameters used to change the Rayleigh number for high aspect ratio cavities. Also, as said previously, the CEN (1998) natural convection correlation is supposed to be used for high aspect ratio cavities.

### 3.5.2 Radiation Heat Transfer Correlations

Roth (1998) compares the different radiative heat transfer correlations, Eq. (3.29), Eq. (3.32) and Eq. (3.39), for different aspect ratios and reports that all  $h_r$  correlations compare fairly well

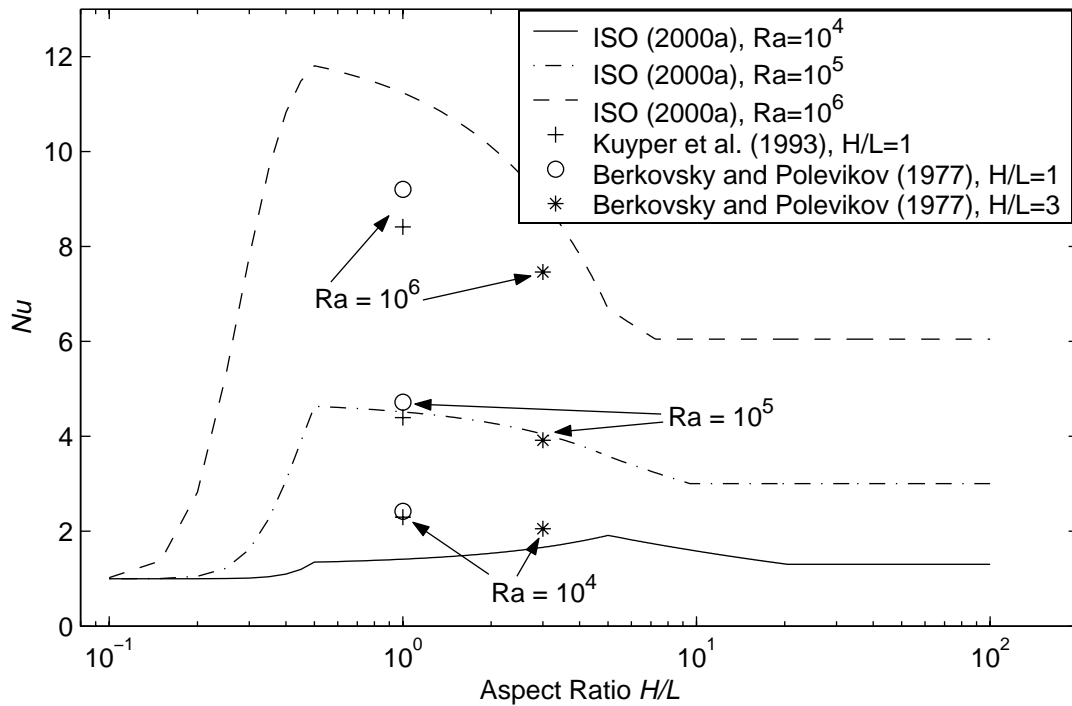


**Figure 3.10.** Nusselt number plotted as a function of aspect ratio  $H/L$ .

for cavities with aspect ratios,  $H/L$ , larger than 0.4. That is, the maximum deviation between the different correlations is about 15 %. Between  $H/L = 0.1$  and 0.4, the correlation from ASHRAE (1996) deviates from the other two correlations, CEN (1998) and ISO (2000a), which compare well for all aspect ratios considered here ( $0.1 \leq H/L \leq 13$ ). The radiative heat transfer correlations were compared for  $T_m = 283$  K and  $\epsilon_H = \epsilon_C = 0.9$ . The correlation developed by Roth (1998), Eq. (3.32), and now used in ISO (2000a) and CEN (2001a), is the one that is recommended today. This is because the correlation was developed from radiative heat transfer relations.

### 3.6 Conclusions

This chapter has presented the dimensionless numbers, Nusselt number correlations and theory considering the heat transfer in cavities relevant for the calculation of thermal transmittance of building sections like windows, facade systems and window frames. This was not a review covering all Nusselt number correlations found in the literature, but a compilation of Nusselt numbers relevant for the geometries found in the sections mentioned above. Focus was put on correlations which are recommended from other sources like general textbooks and review papers. Nusselt numbers from international standards were also included.

Some diversity was found between the Nusselt number calculated from international standards and articles. This difference may be justified in some of the cases due to the wide range of applications and geometries each correlation from an international standard is supposed to cover. The CEN (1998) natural convection heat transfer coefficient, which is supposed to be used for vertical frames, compares well to correlations suitable for high aspect ratio cavities. The ASHRAE (1996) and ISO (2000a) natural convection correlations for the simulation of natural convection heat transfer in frame cavities are usable for cavities having a low or a high vertical aspect ratio. However, in the interpolation area, between  $H/L = 0.5$  and  $H/L = 5$ , the correlation should be improved. Still, little research was found on the influence of the horizontal aspect ratio,  $W/L$ , on heat transfer in high vertical cavities.



# Chapter 4

## Air Flow in and U-values of Window Frames

### 4.1 Introduction

In Chapter 2 different ways of treating non-rectangular cavities were presented, and in Chapter 3 correlations for heat transfer in a cavity were presented and compared. Discrepancies were found both in the treatment of non-rectangular cavities and in the Nusselt number correlations. Previous research has shown that special care is needed when correlations for calculating the equivalent conductivity of air cavities are chosen. Haustermans (2000) measured and simulated two aluminum window frames. He found that the use of CEN (1998) correlations in numerical simulations gave results that compared well with experimental results for the same frame mounted vertically, and that ASHRAE (1996) correlations gave results that compared well to measured horizontal frames. Two-dimensional computational fluid dynamics (CFD) simulations also compared well to measured horizontal frames. He did not divide the air cavities in his numerical simulations. Svendsen et al. (2000) compared results from conduction simulations of heat transfer in one aluminum frame, using CEN (2001a) correlations, with the measured thermal transmittance of the same frame mounted vertically. They divided the air cavities at places where it seemed reasonable, and found that this made their results closer to the results from experiments. Using detailed radiation models increased the agreement even more.

In order to avoid the need for radiation and convection correlations and rules on how to treat air cavities in window frames the next step in the development of simulation software for finding window frame U-values might be to incorporate computational fluid dynamics (CFD) models into the codes. Since traditional simulation codes usually are two-dimensional, the simulation software will only be able to simulate heat transfer in horizontal frame sections (like frame sill and head). This chapter presents two-dimensional CFD and conduction simulations of four window frames with internal cavities, one PVC frame and three aluminum frames. These simulations are performed to see the size of the discrepancies between CFD and conduction

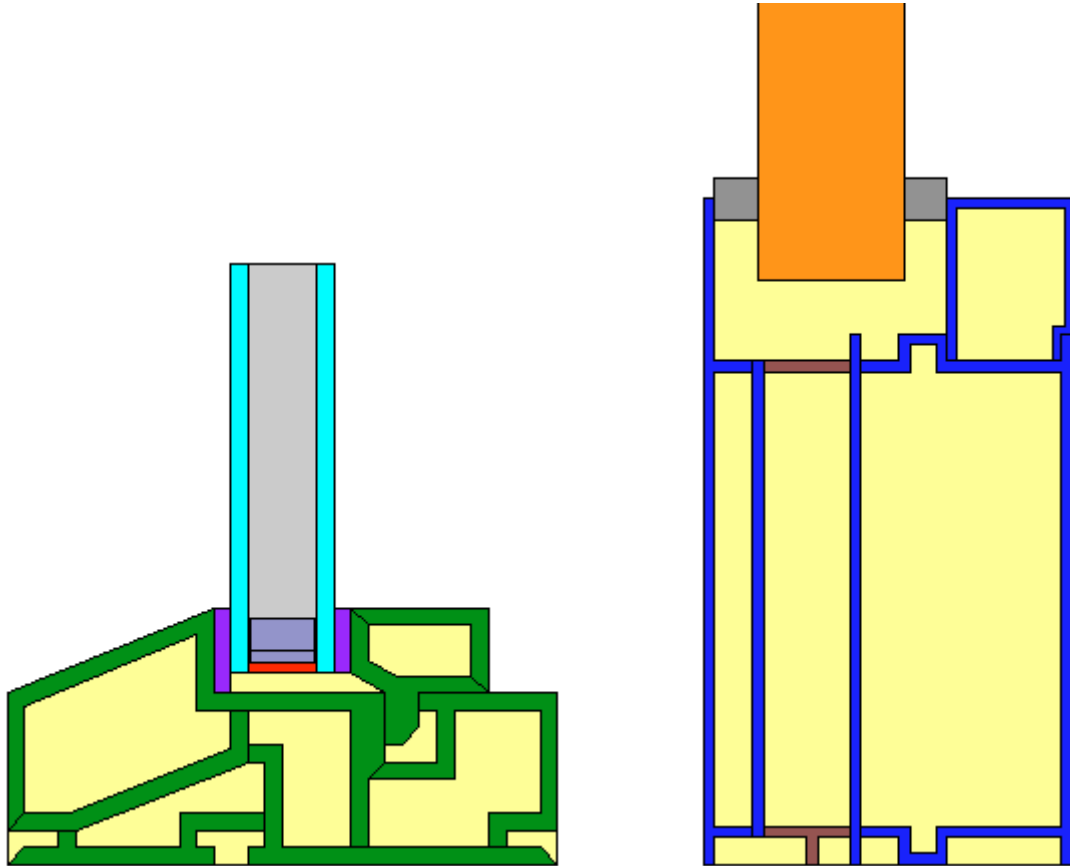


**Figure 4.1.** The figure to the left shows a PVC window frame (named S1) and the figure to the right a simple aluminum window frame (named S2).

simulations. This is done both by looking at temperature contour plots and also by comparing U-values. The CFD simulations are also studied to gain more insight into when air cavities should be divided. This is done by studying steam contours.

## 4.2 Frame Sections

Four window frames are simulated, one PVC frame and three aluminum frames, as shown in Figure 4.1 and Figure 4.2. These particular sections were chosen to include air cavities of various shapes, and limit the complexity of the drawing process. It should be noted that aluminum frames S3 and S4 are not well constructed with respect to having a low U-value, and that there are aluminum frames that have lower U-values. But then the frames usually are more complex.

The PVC frame was simulated with a glazing and the air cavity of the glazing was assumed to be solid, also in the CFD simulations (focus is on convection effects in the frame). The U-value reported for this section is  $U_{fr}$  from Eq. (2.16). The aluminum frames were simulated with insulation panels, like prescribed in ISO (2001a), and the U-values reported,  $U_f$ , are calculated

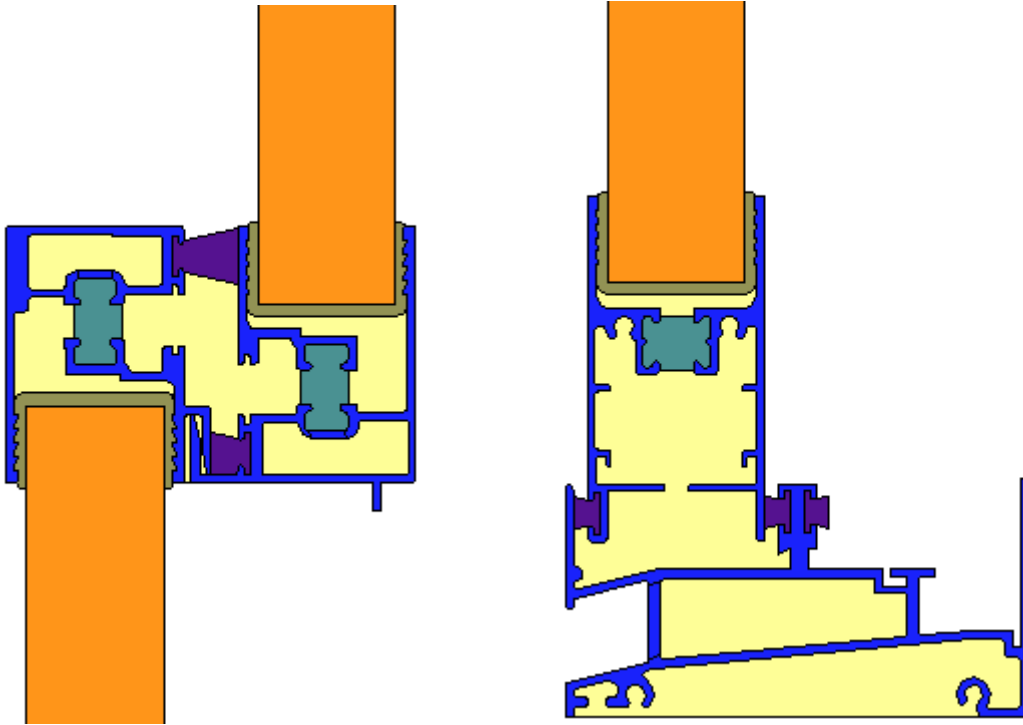


**Figure 4.2.** Figures of aluminum frames. The frame to the left is called S3 and the one to the right S4.

according to Eq. (2.14). The two sections shown in Figure 4.1, specimens S1 and S2, were drawn exactly identical in both simulation codes (see below), while the other two frames were drawn using CAD files as underlay. Therefore small differences may be found between the CFD code and conduction code models. The material properties used in the simulations are shown in Table 4.1, with color codes matching the colors in Figure 4.1 and Figure 4.2. The air properties used in the CFD simulations were evaluated at  $T = 10\text{ }^{\circ}\text{C}$ .

### 4.3 Numerical Procedure

The simulations were performed with THERM 2.1a (Finlayson et al. 1998) and FLUENT (Fluent 1998). Double precision was used for both codes. THERM uses a finite element approach to solve the conduction heat transfer equation. FLUENT uses a control volume method to solve the coupled heat and fluid flow equations. Incompressible and laminar flow is assumed, viscous dissipation is not addressed, and all thermophysical properties are assumed to be constant except for the buoyancy term of the  $y$ -momentum equation where the Boussinesq approximation is assumed. Semi-Implicit Method for Pressure-Linked Equations Consistent (SIMPLEC) was used to model the interaction between pressure and velocity. The energy and momentum variables at cell faces were found by using the Quadratic Upstream Interpolation for Convective

**Table 4.1.** Conductivity and emissivity of the materials used in the frame sections.

Material	Color	Conductivity [W/(mK)]	Emissivity
Air cavity		-	-
Aluminum		160	0.2
Buthyl rubber		0.24	0.9
Insulation panel		0.035	0.9
Foam rubber		0.03	0.9
Glass		0.9	-
Glazing cavity (solid)		0.032	-
Mohair		0.14	0.9
Polyamide (nylon)		0.25	0.9
Polysulphide		0.19	0.9
PVC		0.17	0.9
Spacer foam		0.2495	0.9
Urethane (liquid)		0.31	0.9
Vinyl (flexible)		0.12	0.9

Kinetics (QUICK) scheme. In addition, FLUENT uses central differences to approximate diffusion terms and relies on the PREssure Staggering Option scheme (PRESTO) to find the pressure values at the cell faces. PRESTO is similar to the staggered grid approach described by Patankar (1980). Convergence is determined by checking the scaled residuals and ensuring that they are less than  $10^{-6}$  for all variables except for the energy equation in which the residuals have to be less than  $10^{-11}$  (for some of the cases the energy residuals stopped at about  $5 \times 10^{-10}$ ). Radiation heat transfer was included in the simulations by the use of the Discrete Transfer Radiation Model (DTRM), which relies on a ray-tracing technique to calculate surface-to-surface radiation. The internal cavity walls are assumed to be diffuse gray, and air does not interact with the radiative process.

Some simplifications were made for the CFD model. That is, fluid flow was not simulated for all the air cavities. Instead, equivalent conductivities were assigned, and the cavities were

treated as solids. The conductivities assigned were the same as used in the conduction simulation program. Thus, differences between the two codes should not arise due to these simplifications. Also, due to the size of the cavities, large convection effects are not expected anyway. For the PVC frame the cavities treated in this way were three small cavities close to the bottom of the frame. For the aluminum frame in Figure 4.1, the four cavities close to the bottom of the frame were treated as solids. And for frame S3 (the one to the left in Figure 4.2) the two small cavities at the bottom of the aluminium frame and close to the right side of the lower insulation panel were treated as solids.

Prior to the final simulations some grid sensitivity tests were performed on the aluminum frame S2. For the CFD program grid sizes of 0.1 and 0.25 mm were tested. The first results in 865750 control volumes and the latter in 141436 control volumes. The simulations were carried out without including radiation. For a grid size of 0.1 mm a frame U-value of 1.9286 W/m<sup>2</sup>K was found, and for a grid size of 0.25 mm an U-value of 1.9247 W/m<sup>2</sup>K was found. This is only a difference of 0.2 %. Thus, a grid size of 0.25 mm was used in the final simulations (for all the frames). We also tested the effect of increasing the number of rays in the radiation heat transfer algorithm of the CFD code, and found that doubling the number of rays only resulted in a change of the frame U-value of 0.1 %. For THERM similar tests were performed. In the results section, Section 4.4, simulations where all cavities are treated as solids are performed in both programs to check the resemblance between the two codes.

The correlations used to find the equivalent conductivity of the air cavities are based on ASHRAE (1996), including using a bounding rectangle as shown in Figure 2.10. For the convection heat transfer coefficient, the correlation prescribed in ASHRAE (1996) is similar to the correlations used for window frames in ISO (2000a). However, the radiation correlation is different. The reason for using the ASHRAE correlations is that these are included in THERM and these convection correlations are those most suitable for horizontal window frame sections (of those available today). Horizontal frame sections can be simulated in two dimensions with a CFD code, simulating fluid flow in the cavities. Vertical sections have to be simulated in three dimensions.

In the process of finding an equivalent conductivity for the frame cavities, the surface temperature of the cavity walls is among the parameters. And when assigning the “air cavity material” to a cavity, the temperatures are set to predefined values, not necessarily right for the specified cavity. Therefore an iterative solution procedure was used where the wall temperatures were

updated. The temperatures of the walls had to be within 0.2 °C of the final simulated temperature.

CEN (2001a) boundary conditions were used for frames S2, S3 and S4. These are shown in Table 4.2. The table also includes the boundary conditions used for the PVC frame. These were selected since we wanted to have one case with a higher temperature difference across the frame. The boundary conditions for the frame are based on NFRC and can be found in Mitchell et al. (2000). The glazing boundary conditions are automatically calculated in THERM when a glazing system is imported. These are based on the center of glass surface temperatures, and will not be described further here.

**Table 4.2.** Boundary conditions used in the numerical simulations.

Description	$T$ [°C]	$h$ [W/m <sup>2</sup> K]
CEN inside boundary condition	20	7.692
CEN outside boundary condition	0	25
NFRC inside boundary condition (PVC frame only)	21.11	7.61
NFRC outside boundary condition (PVC frame only)	-17.78	29.03
Glazing inside boundary condition (valid for S1)	21.11	7.722
Glazing outside boundary condition (valid for S1)	-17.78	28.68

## 4.4 Results and Discussion

### 4.4.1 Stream and Temperature Contours

The different calculation procedures described in Chapter 2 include various ways of dividing non-rectangular cavities. NFRC (Mitchell et al. 2000) prescribes that cavities separated by a connection less than 6.35 mm are to be divided. According to ISO (2000a), cavities having walls that are separated by less 5 mm are to be separated. CEN (2001a) prescribes that cavities with one direction not exceeding 2 mm or cavities with an interconnection not exceeding 2 mm are to be considered as separate. These rules are presented without reference to any research papers and seem to be based on assumptions. Here, stream and temperature contour plots of the simulated frames are studied. This is done to see when the flow separates, and when it is reasonable to divide the air cavities when doing the conduction simulations.

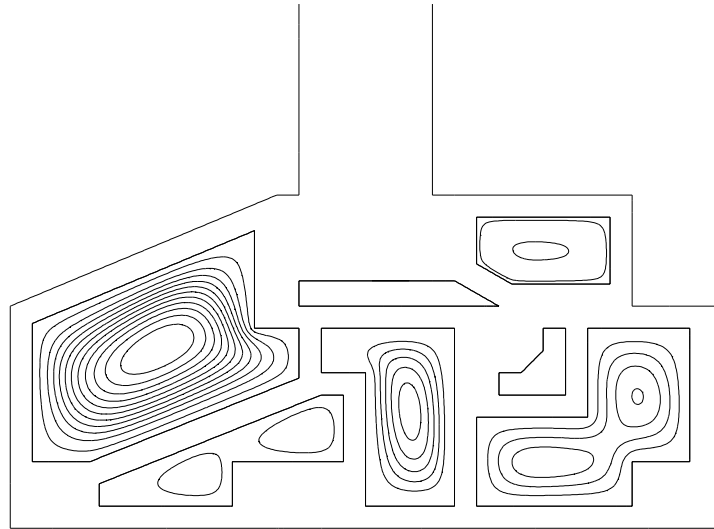


**Figure 4.3.** The figure shows velocity contours for the PVC frame (S1).

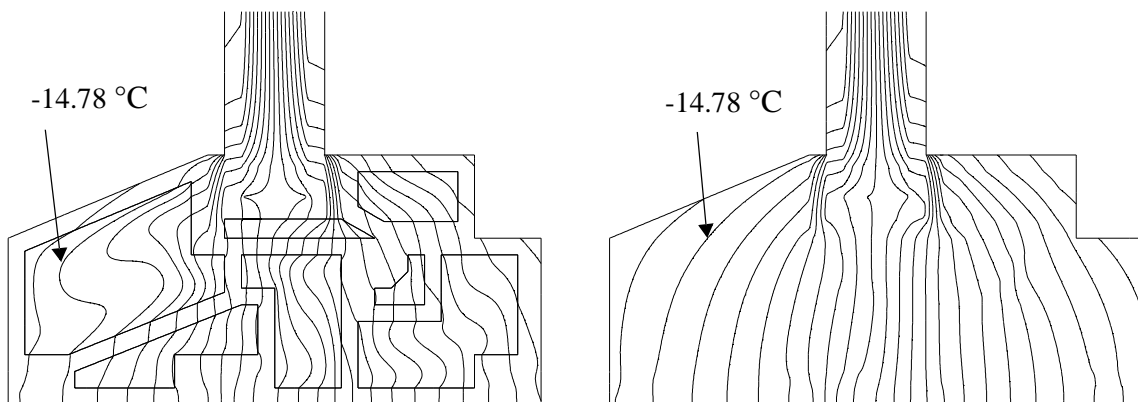
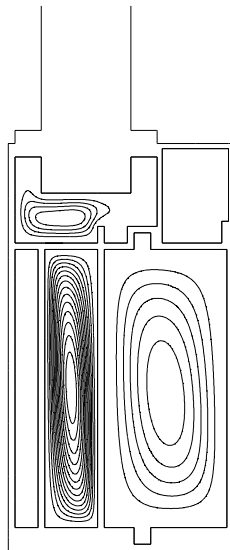


**Figure 4.4.** These figures display temperature contours for the PVC frame (S1). The figure to the left shows temperatures for the fluid flow simulation and the figure to the right displays temperatures for the solid cavity model. The temperature interval is about  $1.5\text{ }^{\circ}\text{C}$  ( $1.496\text{ }^{\circ}\text{C}$ ). The warm side is to the right and the cold to the left.

Figure 4.3 and Figure 4.4 show the velocity and temperature contours for the PVC frame (S1), respectively. With regard to the dividing of cavities there are three cavities of interest. For the bottom left cavity we see that two separate cells have developed. The length of the throat separating the two sub-cavities is 4.2 mm (here, the term “sub-cavity” is used for parts of a larger cavity that naturally can be separated from the larger cavity, based on studies of stream contours). For the lower middle cavity we see that the air flow turns to the right in the upper left corner and hardly enters the little pocket. The height of the pocket is 6.35 mm. However, the

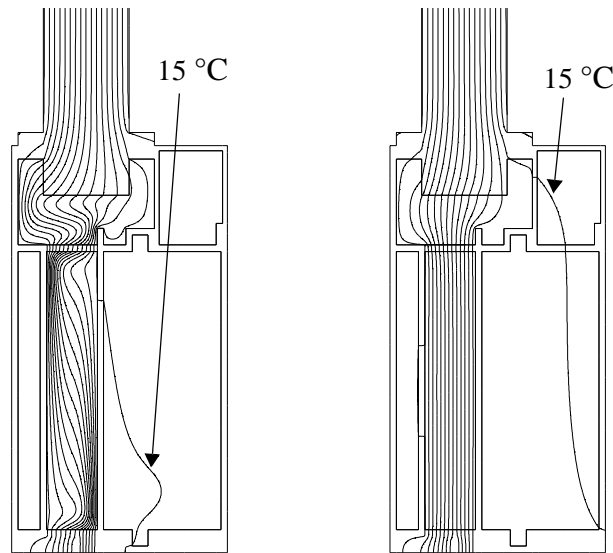
enclosure in the bottom right corner of the frame has a flow pattern that turns from one sub-cavity to the other. Thus, dividing is not necessary here. Here the shortest distance separating the sub-cavities is about 9 mm. Figure 4.4 shows that the temperature distribution in the two cases is quite different, but that the difference mostly is limited to the air cavities.

Figure 4.5 and Figure 4.6 present the velocity and temperature contours for the thermally broken aluminum frame S2. Here the upper cavity is of interest. Figure 4.5 shows that most of the circulation is within the lower left part of the cavity. The distance between the insulation panel and the left vertical aluminum profile is 8 mm and the length separating the insulation panel and the small vertical fin close to the thermal brake is 10 mm. Although there are not stream lines close to the bottom and top of the large right cavity of the frame, it makes sense to divide this. Then the small pockets at the top and at the bottom of the cavity are treated separately. As with the PVC frame, we see that the difference between the temperature patterns between the fluid flow case and the solid air cavity case is mainly limited to the air cavities.



**Figure 4.5.** The figure shows velocity contours for the thermally broken aluminum frame S2.

Figure 4.7 and Figure 4.8 are diagrams of the velocity and temperature contours for aluminum frame S3, and Figure 4.9 and Figure 4.10 shows the velocity and temperature contours for aluminum frame S4, respectively. Frame S3 has three enclosures that experience noticeable air circulation. We see that both the right and the left cavity do not experience circulation in the throats next to the flexible vinyl in which the insulation panel is inserted. Both throats have openings to



**Figure 4.6.** These diagrams display temperature contours for the aluminum frame S2. The figure to the left shows temperatures for the fluid flow simulation and the one to the right displays temperatures for the solid cavity model. The temperature interval is  $1\text{ }^{\circ}\text{C}$ . The warm side is to the right of each frame and the cold side to the left of each frame.

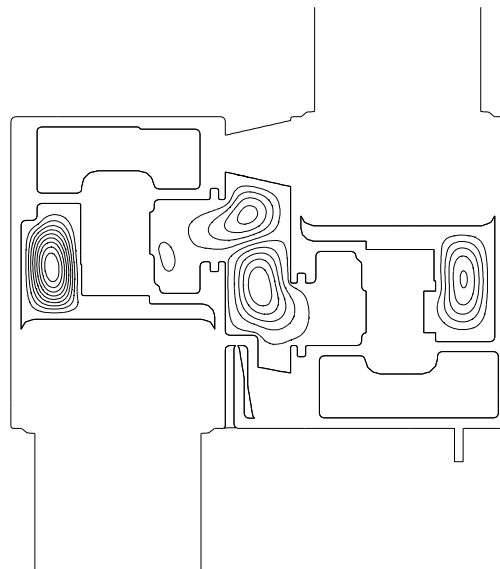


**Figure 4.7.** Diagram of the velocity contours for aluminum frame S3.

the larger parts of the cavities that are 3.6 mm wide. In the middle cavity there are two circulating cells. The upper cell circulates in the counterclockwise direction and the lower circulates in the clockwise direction. Unlike the other cavities studied in this chapter, this cavity has an

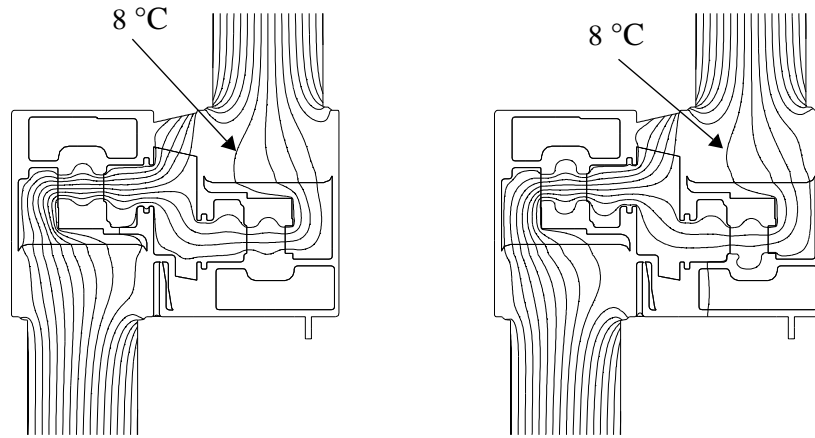


**Figure 4.8.** The figure to the left shows temperature contours for aluminum frame S3 simulated with fluid flow in air cavities and the one to the right shows temperature contours for the same frame simulated with solid air cavities. The temperature interval is 1 °C. The warm side is to the right of each frame and the cold side to the left.

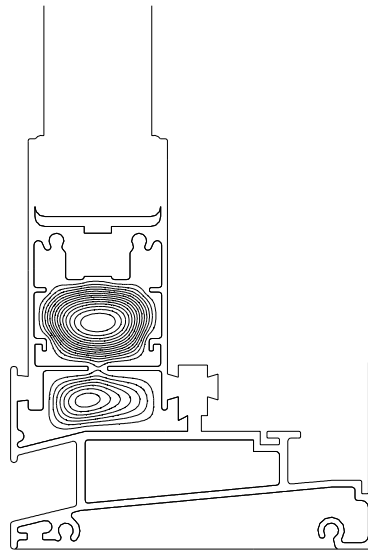


**Figure 4.9.** Velocity contours for aluminum frame S4.

upward vertical heat flow direction (the bottom side of the cavity is warm and the upper side of the cavity is cold). In Figure 4.9 we see the stream lines for aluminum frame S4. The cavity below the thermal brake has an horizontal interconnection that is 4.6 mm wide. The stream lines show that this cavity should be divided in two there. Close to the thermal brake there also are smaller sub-cavities that can be separated from the larger cavity. Here the length separating the two opposite walls are 5.3 mm, on both sides of the thermal brake. At each side of the bottom of

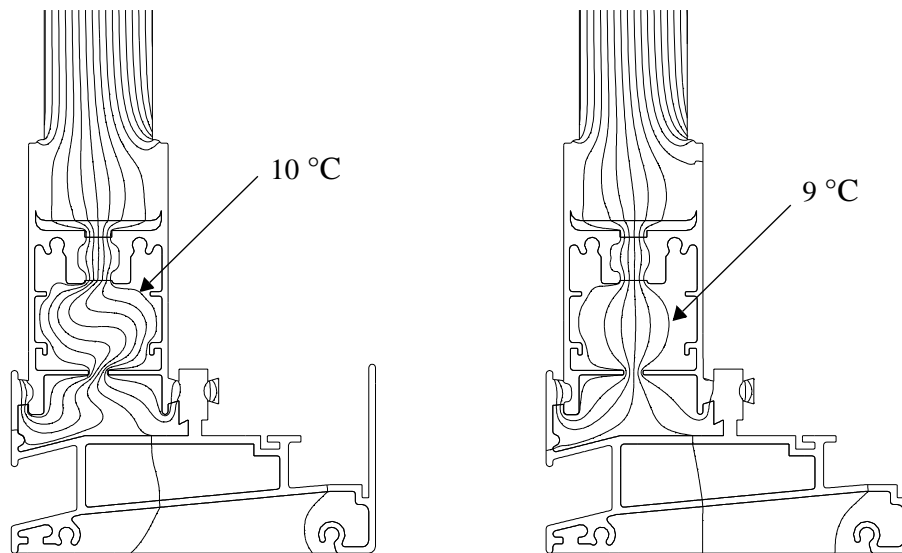


**Figure 4.10.** The diagram to the left shows temperature contours for aluminum frame S4 simulated with fluid flow in air cavities and the one to the right shows temperature contours for the same frame simulated with solid air cavities. The temperature interval is 1 °C. The warm side is to the right of each frame and the cold side to the left.

this cavity there likewise are two sub-cavities that can be separated from the larger cavity. On the left side the length separating the opposite parts are 7.4 mm apart, and on the right side the corresponding distance is 5 mm. In the bottom cavity we also find natural sub-cavities that can be separated from the larger cavity, even though there not are streamlines verifying this statement. With regard to the temperature contours for the two cases, Figure 4.10 shows that there are differences, but also here mostly limited within air cavities.

These simulations show that the current rules for dividing non-rectangular cavities are somewhat strict, being 6.35 mm according to NFRC (Mitchell 2000), 5 mm according to ISO (2000a) and 2 mm according to CEN (2001a). However, since the results presented in this chapter only are from a limited number of frames, strict rules are desirable. Other frames and other boundary conditions may produce different results. Still, based on the current simulations a 7-8 mm division rule seems to be reasonable. If a conservative approach is required a 7 mm division rule is recommended.

#### 4.4.2 U-value Comparison

The above discussion has pointed out where in the simulated frames air cavities can be divided. Now the U-values for the above cases are presented. The U-values are calculated from fluid

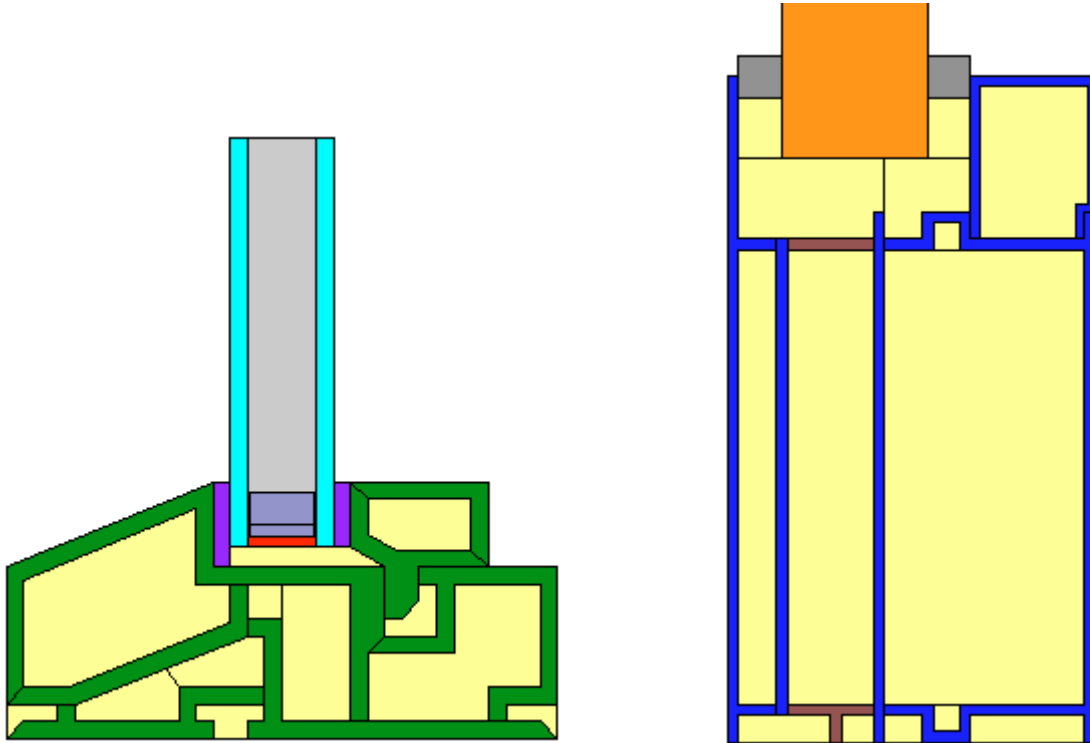


**Figure 4.11.** This figure shows which air cavities of frames S1 and S2 that have been divided and where they have been divided.

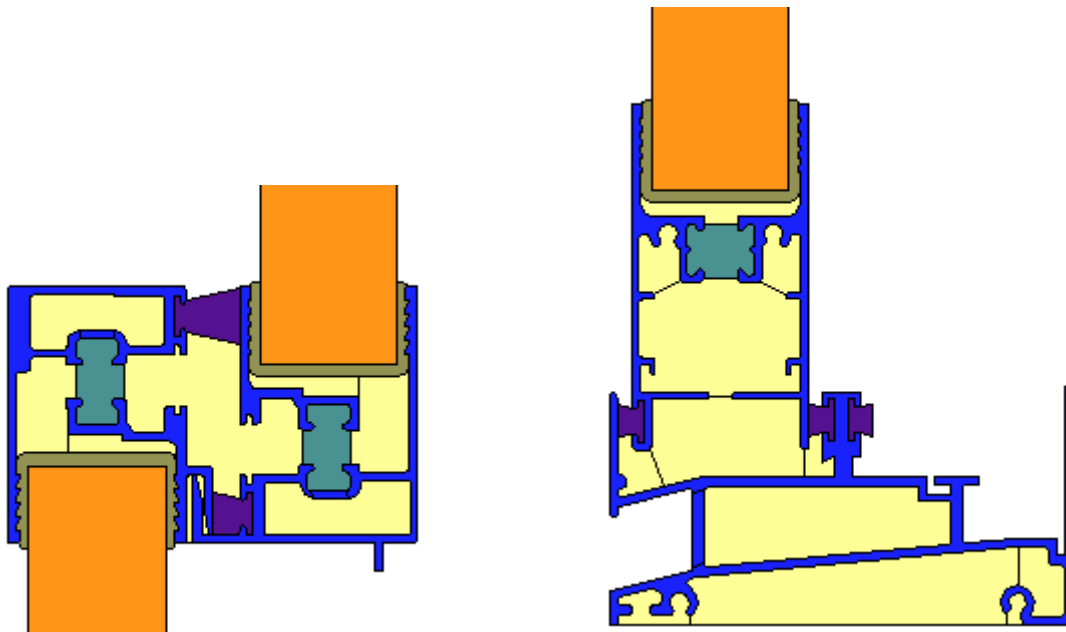


**Figure 4.12.** This figure shows where the air cavities have been divided for frames S3 and S4.

flow simulations and for solid air cavity simulations (using an equivalent conductivity for the air cavities). These simulations are performed with FLUENT and THERM. Based on the above

**Table 4.3.** Thermal transmittance (U-value) of simulated aluminum frames.

Case	Description	$U_f$ [W/m <sup>2</sup> K]
S1-1	THERM	1.7950
S1-2	THERM divided cavities	1.7020
S1-3	FLUENT fluid flow	1.5876
S1-4	FLUENT solid cavities	1.7899
S2-1	THERM	2.3278
S2-2	THERM divided cavities	2.1372
S2-3	FLUENT fluid flow	2.1912
S2-4	FLUENT solid cavities	2.3280
S3-1	THERM	7.8771
S3-2	THERM divided cavities	7.6144
S3-3	FLUENT fluid flow	7.5823
S3-4	FLUENT solid cavities	8.0513
S4-1	THERM	10.5022
S4-2	THERM divided cavities	10.3471
S4-3	FLUENT fluid flow	10.3146
S4-4	FLUENT solid cavities	10.4834

studies, results are also included where air cavities have been divided. These simulations are carried out with THERM. Figures 4.11 and 4.12 show which cavities that have been divided and where they were divided. Table 4.3 lists the U-values. First, the table shows that the FLUENT case where all cavities are treated as solids (case 4 for all frames) with the same conductivity as used in the THERM simulation (case 1 for all frames) compare well. The difference is only 0.3 % for the PVC frame (frame S1), 0.01 % for aluminum frame S2, and 0.2 % for aluminum frame S4. For frame S3 the difference is larger. The differences of 2.2 % may be attributed to differences between the simulated frames in the two programs. Frames S3 and S4 were created by using CAD files as underlay. Frames S1 and S2 were drawn from scratch in both codes and are therefore assumed to be identical with respect to geometry.

For all cases Table 4.3 shows that when air flow is simulated in the cavities, the result is a lower U-value than found in the conduction simulations (without dividing air cavities). Further, as expected, we find that dividing of air cavities reduces the U-value. For frames S2 to S4 the difference now at most is 2 %. For frame S1 the difference is 7 %. Even though the differences between the fluid cases and the solid cases with divided air cavities are small, we have to remember that the convection and radiation correlations used for finding the equivalent conductivity not necessarily are optimal for the various cavities (see Section 3.5).

## **4.5 Conclusions**

In this chapter conduction and fluid flow simulations have been carried out to study convection effects inside four horizontal window frames with internal cavities, and heat transfer rates through the same frames. By studying stream contours it seems that cavities having an interconnection less than about 7 mm can be treated as separate cavities. The simulations also show that traditional software codes, simulating only conduction and using equivalent conductivities for the air cavities, give results that compare well with the fluid flow simulations. CFD simulations of heat transfer in window frames may be valuable to gain more information about how the air flows in air cavities, and thus enable engineers to find better solutions for how to construct window frames with internal cavities. Still, more simulations of non-rectangular cavities should be carried out, to study if various cavity geometries (i.e. three-dimensional air cavities found in vertical frame sections) and other boundary conditions give different results.

# Chapter 5

## Radiation Heat Transfer Properties - Emissivity of Aluminum Surfaces

### 5.1 Introduction

Aluminum sections often consist of opaque sections and hollow sections with air. Heat transfer in hollow sections is due to conduction, convection and radiation. Conduction will occur if the air is at rest. Convection is heat transfer from the walls to the air because of air motion. Heat is transferred by radiation directly from one wall to another, and is not dependent on the fluid separating the walls, assuming a non-participating fluid.

This article presents the basic properties and relations used when calculating heat transfer by radiation. Further, it presents the emissivity of treated aluminum surfaces found in the literature. Focus is put on thermal radiation heat transfer properties in the wavelength-interval 4 - 70  $\mu\text{m}$ . This is because, as we will see later, radiation from a body at the temperature 283 K lies in this region. Visible light is in the range from  $\sim 0.4 - 0.7 \mu\text{m}$ . A study of how sensitive the numerical calculations of the thermal transmittance, U-value, are to different values of the emissivity is also included.

### 5.2 Radiation Intensity and Emissive Power

We need to define two quantities to understand the radiation properties of a real body. These quantities are the radiation intensity and the emissive power. The intensity,  $i'_{\lambda}(\lambda, T, \theta, \phi)$ , is defined as the radiant power (energy per unit time) per unit area perpendicular to the direction of travel (projected area), per unit solid angle and per unit wavelength interval (the notation used here is adopted from Siegel and Howell 1992)

$$[i'_{\lambda}(\lambda, T, \theta, \phi)] = \frac{\text{W}}{\text{m}^2 \cdot \text{sr} \cdot \text{m}} . \quad (5.1)$$

The emissive power,  $e'_{\lambda}(\lambda, T, \theta, \phi)$ , is unlike the intensity, evaluated for the elemental area on the surface of interest. Otherwise the emissive power is the same as the intensity. In equation form we get

$$e'_{\lambda}(\lambda, T, \theta, \phi) = i'_{\lambda}(\lambda, T, \theta, \phi) \cdot \cos \theta . \quad (5.2)$$

The prime indicates that the energy is evaluated per solid angle  $(\theta, \phi)$ , and the subscript  $\lambda$  indicates that the energy is evaluated per wavelength interval.

### 5.3 The Blackbody in Radiation Heat Transfer

When studying thermal radiation heat transfer and thermal radiation properties we have to describe the *blackbody*. This is because it serves as a standard to which real bodies are compared. A blackbody is defined as a body that absorbs all incident radiation, irrespective of wavelength or angle of incidence. No energy is transmitted or reflected. A consequence of this is that all energy leaving the surface is emitted by the surface. A blackbody is a perfect emitter in each direction and at every wavelength. This means that no surface can emit more radiation than a blackbody at a given temperature or wavelength. Planck's law gives the spectral distribution of hemispherical emissive power of a blackbody in vacuum (Siegel and Howell, 1992)

$$e_{\lambda b}(\lambda, T) = \pi i'_{\lambda b}(\lambda, T) = \frac{2\pi C_1}{\lambda^5 (e^{C_2/\lambda T} - 1)} . \quad (5.3)$$

Here,  $\lambda$  [m] is the wavelength of the radiation,  $T$  [K] is the temperature of the body,  $C_1 = hc_0^2$  and  $C_2 = hc_0/k$ , where  $h$  is Planck's constant,  $c_0$  is the speed of light in vacuum and  $k$  is the Boltzmann constant<sup>1</sup>. The spectral hemispherical emissive power is the power emitted into the hemisphere per unit wavelength interval centered around the wavelength  $\lambda$  and per unit surface area. The subscript  $b$  indicates that a blackbody is considered. To find the energy emitted into a specific unit solid angle, given by  $(\theta, \phi)$ , we apply

$$e'_{\lambda b}(\lambda, T, \theta) = \frac{e_{\lambda b}(\lambda, T) \cdot \cos \theta}{\pi} = i'_{\lambda b}(\lambda, T) \cdot \cos \theta . \quad (5.4)$$

From Eq. (5.4) we see that the emissive power of a blackbody,  $e'_{\lambda b}(\lambda, T, \theta, \phi) = e'_{\lambda b}(\lambda, T, \theta)$ , is independent of  $\phi$ . We also note that the intensity of a blackbody,  $i'_{\lambda b}(\lambda, T, \theta, \phi) = i'_{\lambda b}(\lambda, T)$ , is

1.  $h = 6.6260775 \times 10^{-34}$  J·s,  $k = 1.380658 \times 10^{-23}$  J/K, and  $c_0 = 2.99792458 \times 10^8$  m/s.

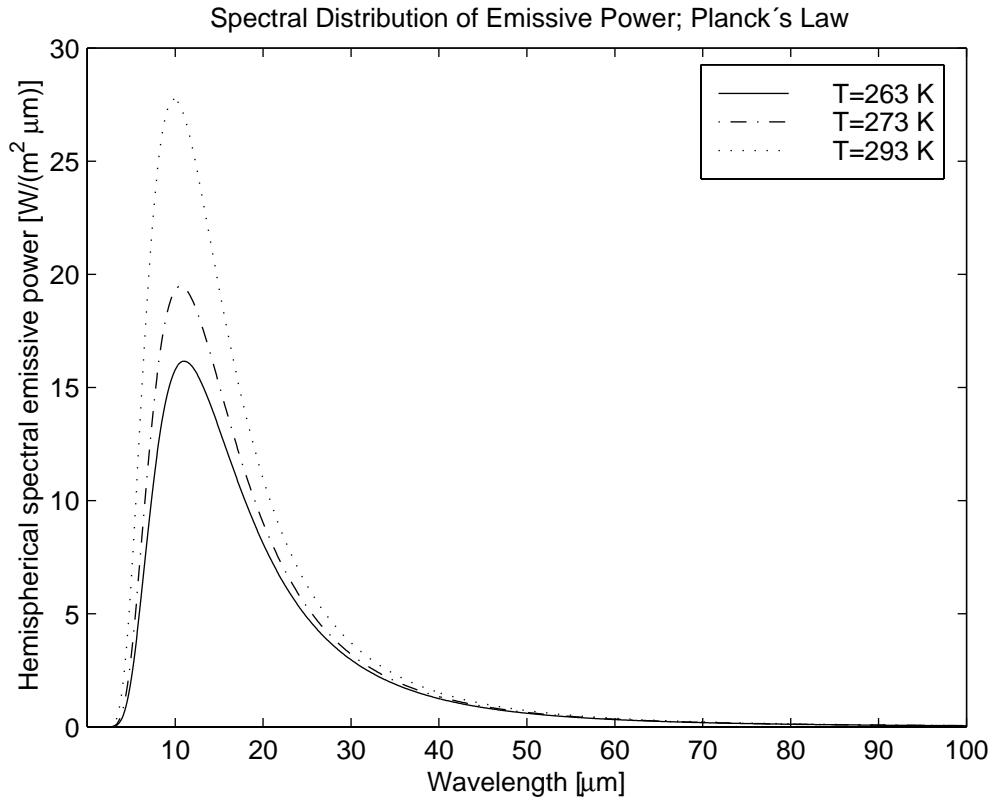


**Figure 5.1.** The spectral distribution of hemispherical emissive power.

independent of both  $\phi$  and  $\theta$ . However, for real surfaces this needs not be true. In Figure 5.1 the spectral hemispherical emissive power is plotted as a function of wavelength for some temperatures relevant for radiation heat transfer in building section cavities. Integrating Eq. (5.3) over all wavelengths ( $0 \rightarrow \infty$ ) gives the total hemispherical emissive power of a blackbody radiating into vacuum

$$e_b(T) = \pi i_b''(T) = \sigma T^4. \quad (5.5)$$

This equation is also called Stefan-Boltzmann law. We now turn to real surfaces.

## 5.4 Radiation Properties of Real Surfaces

Real surfaces neither emit nor absorb as much radiation as a blackbody. As described in the previous section all the energy incident on a blackbody will be absorbed, no energy will be reflected or transmitted. However, a real surface will reflect some of the incident energy and also transmit some energy if the material is transparent. For the surface shown in Figure 5.2 we get the following balance

$$G = \alpha G + \rho G + \tau G . \quad (5.6)$$

$G$  is the incident radiation,  $\alpha$  is the absorptivity,  $\rho$  is the reflectivity, and  $\tau$  is the transmittance. The transmittance is the ratio of the energy transmitted through the material to the energy incident on the surface.  $\alpha$  and  $\rho$  will be defined below. In addition we will define the emissivity  $\varepsilon$  of a surface. For a black surface we have  $\alpha = \varepsilon = 1$ , and  $\rho = \tau = 0$ .

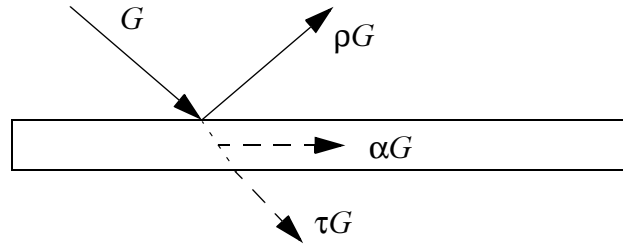


**Figure 5.2.** Energy balance for a real surface (radiation only).

### 5.4.1 Emissivity

The emissivity specifies how well a surface radiates energy as compared to a blackbody. In the most general case we denote the emissivity with  $\varepsilon'_{\lambda}(\lambda, \theta, \phi, T)$ . This is the directional spectral emissivity, and it depends on wavelength, direction and on the surface temperature. If we denote the emissive power leaving a real surface by  $e'_{\lambda}(\lambda, T, \theta, \phi)$  (energy emitted per unit time within a unit wavelength interval centered around the wavelength  $\lambda$ , per unit elemental surface area and per solid angle) we get

$$\varepsilon'_{\lambda}(\lambda, \theta, \phi, T) = \frac{e'_{\lambda}(\lambda, T, \theta, \phi)}{e'_{\lambda b}(\lambda, T, \theta, \phi)} . \quad (5.7)$$

The values usually reported in the literature are the normal emissivity,  $\varepsilon_n(T)$ , and the hemispherical total emissivity,  $\varepsilon(T)$ . The latter is obtained by integrating the energy relations in Eq. (5.7) both over the hemisphere and for all wavelengths ( $\lambda$  from 0 to  $\infty$ ).

### 5.4.2 Absorptivity

The spectral directional absorptivity,  $\alpha'_{\lambda}(\lambda, \theta, \phi, T)$ , is defined as the ratio of the spectral energy that is absorbed from a given direction to the spectral energy incident from that direction. In addition to being dependent on the spectral and directional characteristics of the incident energy the absorptivity is dependent on the temperature of the absorbing surface.

### 5.4.3 Reflectivity

The reflectivity,  $\rho$ , is a more complex quantity than the emissivity and the absorptivity. This is because  $\rho$  depends on the angle of the reflected energy in addition to the angle of the incident energy. For the most general case we have  $\rho''_{\lambda}(\lambda, \theta, \phi, \theta_r, \phi_r, T)$ .  $(\theta, \phi)$  is the direction from which the incident radiation comes and  $(\theta_r, \phi_r)$  is the direction in which the reflected energy goes.

### 5.4.4 Relationships between the Radiation Properties

There are several equations which can be used to relate the different radiation properties for a surface, depending on whether we want to study directional spectral values or study total and/or hemispherical values. It is important to understand these relationships so that we are able to determine how properties for use in building applications can be found. In this context we need to describe two terms that often are used in radiation heat transfer. These are gray surfaces and diffuse surfaces. A surface is termed directional gray if the directional spectral properties do not depend on wavelength. Further, a surface is termed diffuse spectral if the directional spectral properties do not depend on direction. The following relations exist between the absorptivity and the emissivity:

1.  $\alpha'_{\lambda}(\lambda, T, \theta, \phi) = \epsilon'_{\lambda}(\lambda, T, \theta, \phi)$  is the most general form of Kirchoff's law, which is the name used for the relations between the emissivity and the absorptivity. This relation can be used without restrictions for conditions of thermodynamic equilibrium.
2.  $\alpha'(T, \theta, \phi) = \epsilon'(T, \theta, \phi)$  holds if the surface is directional-gray or if the incident radiation has a spectral distribution that is proportional to the radiation from a blackbody at the same temperature as the surface. The last requirement is usually not fulfilled for practical problems.
3.  $\alpha_{\lambda}(\lambda, T) = \epsilon_{\lambda}(\lambda, T)$  is valid for diffuse-spectral surfaces or if the incident radiation does not depend on direction. The assumption of diffuse incident radiation is one that is often justified in the calculation of radiative transfer between surfaces of an enclosure.
4.  $\alpha(T) = \epsilon(T)$  is valid for diffuse-gray surfaces, or if the surface is directional-gray and the incident radiation is independent of angle, or if the surface is diffuse-spectral with incident radiation that has a spectral distribution that is proportional to the radiation from a blackbody at the same temperature as the surface.

If we consider an opaque surface we have the following relations between emissivity, absorptivity and reflectivity:

- $\alpha'_{\lambda}(\lambda, T, \theta, \phi) + \rho'_{\lambda}(\lambda, T, \theta, \phi) = 1$ , where the spectral directional-hemispherical reflectivity is considered. This means that we consider the energy incident from  $(\theta, \phi)$  and reflected into the hemisphere. Substituting the emissivity for the absorptivity we get  $\varepsilon'_{\lambda}(\lambda, T, \theta, \phi) + \rho'_{\lambda}(\lambda, T, \theta, \phi) = 1$ .
- Studying the total-directional energy we get  $\alpha'(T, \theta, \phi) + \rho'(T, \theta, \phi) = 1$ . And if we have the situation described in item 2 above we get  $\varepsilon'(T, \theta, \phi) + \rho'(T, \theta, \phi) = 1$ .
- For the spectral-hemispherical situation we get  $\alpha_{\lambda}(\lambda, T) + \rho_{\lambda}(\lambda, T) = 1$ . If we replace the absorptivity with the emissivity we get  $\varepsilon_{\lambda}(\lambda, T) + \rho_{\lambda}(\lambda, T) = 1$ , assuming that the conditions in item 3 above are satisfied.
- Finally we have  $\alpha(T) + \rho(T) = 1$  which can be written like  $\varepsilon(T) + \rho(T) = 1$  if we have the situation stated in item 4 above.

## 5.5 Thermophysical Properties of Aluminum Surfaces

To perform accurate numerical calculations of heat transfer in aluminum sections we need accurate values of the conductivity, emissivity and specific heat capacity (transient calculations) of the materials used in the sections. This section presents the emissivity of aluminum surfaces and other materials used in aluminum facade systems and frame sections. These values are from both theoretical considerations based on classical electromagnetic theory and measured emissivity values from the literature. This also includes a section on conductivity and the specific heat capacity of selected materials.

### 5.5.1 Radiative Properties by Classical Electromagnetic Theory

Radiative properties calculated from classical electromagnetic theory are limited to surfaces that are smooth, clean and reflect the incident radiation in a specular fashion, so-called ideal surfaces. Most real surfaces do not comply with these restrictions. This can be due to surface impurities and contamination, surface roughness, and crystal-structure modifications by surface working. The theory is also invalid for frequencies in the order of molecular vibrational frequencies. This restricts the results to wavelengths longer than the visible spectrum. However, a study of the emissivity from classical electromagnetic theory can still provide some valuable

information, at least for comparison with experimental results. When limited experimental data are available, extrapolation to other wavelengths and angles may be possible.

Before listing some of the equations, we need to describe some of the constants used. These are refractive index,  $n$ , complex refractive index,  $\bar{n} = n - i\kappa$ , and the extinction coefficient  $\kappa$ . The refractive index measure the bending of an electromagnetic wave when passing from one medium into another, and is equal to the speed of electromagnetic waves in vacuum divided by the speed of electromagnetic waves in the medium of interest.  $\kappa$  is a measure of the rate of diminution of transmitted electromagnetic waves via scattering and absorption for a medium. Further we need to describe what is meant by a dielectric medium. This is a nonconducting material, its electrical resistance approaches infinity, and the extinction coefficient is equal to zero. In addition to dielectrics we have materials with finite conductivity. For these materials the extinction coefficient is different from zero. For an ideal conductor with zero resistivity the electric field will be zero everywhere inside the material. Such a material will totally reflect the electromagnetic wave that strikes it. Then the extinction coefficient  $\kappa$  is large.

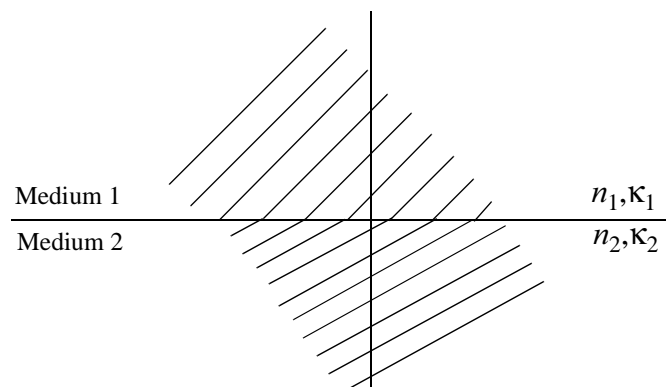


**Figure 5.3.** Wave incident on interface between two media.

From electromagnetic theory we find equations for the directional-hemispherical (reflection from one direction  $\theta$  into the hemisphere) spectral specular reflectivities for each of the polarization directions for the incident electromagnetic waves on the surface. The reflectivities are independent of  $\phi$ . The term specular means that a wave incident from the direction  $\theta$  (from the normal to the surface) will be reflected into an angle equal to the angle of incidence,  $\theta_r = \theta$ , rotated about the normal to the interface through a circumferential angle of  $\pi$ . Further, both  $n$  and  $\kappa$  generally depend on wavelength. However, the subscript  $\lambda$  is dropped to simplify the notation in the following equations. Also, due to lack of available spectral optical properties, the

**Table 5.1.** Refractive index  $n$  and extinction coefficient  $\kappa$  of metallic aluminum and aluminum oxide, and calculated  $\epsilon'_n$ .

Description	$\lambda$ [ $\mu\text{m}$ ]	$n$	$\kappa$	$\epsilon'_n$ <sup>a</sup>
Metallic aluminum <sup>b</sup>	5.00	8.67	48.6	0.0141
	10.00	25.3	89.8	0.0116
	20.00	60.7	147	0.0096
	30.00	94.2	199	0.0077
Aluminum oxide ( $\text{Al}_2\text{O}_3$ ) <sup>c</sup>	10.00	0.907	0.003	0.9976
	20.00	1.674	1.002	0.8212
	30.30	3.985	0.125	0.6410

a. Calculated from  $\epsilon'_n = 1 - \rho'_n$  where  $\rho'_n$  is the average of Eq. (5.18) and Eq. (5.19).

b. From Smith et al. (1985).

c. From Gervais (1991).

spectral value of the reflectivity and emissivity is often used for their total values (Siegel and Howell 1992). In Figure 5.3 we see an electromagnetic wave incident on an interface between two media. In our case, medium 1 is usually air (with  $n_1 - i\kappa_1 \approx 1$ ) and medium 2 is some kind of building material, like polyamide (nylon) or aluminum, both with a finite resistance. Typical values of  $n$  and  $\kappa$  for a metal (aluminum) and an insulator (aluminum oxide) are shown in Table 5.1 together with the calculated emissivity.

For ideal dielectrics ( $\kappa \rightarrow 0$ ) the directional-hemispherical spectral specular reflectivities are (Siegel and Howell 1992)

$$\rho'_{\parallel}(\theta) = \left\{ \frac{(n_2/n_1)^2 \cos \theta - [(n_2/n_1)^2 - \sin^2 \theta]^{1/2}}{(n_2/n_1)^2 \cos \theta + [(n_2/n_1)^2 - \sin^2 \theta]^{1/2}} \right\}^2, \text{ and} \quad (5.8)$$

$$\rho'_{\perp}(\theta) = \left\{ \frac{[(n_2/n_1)^2 - \sin^2 \theta]^{1/2} - \cos \theta}{[(n_2/n_1)^2 - \sin^2 \theta]^{1/2} + \cos \theta} \right\}^2. \quad (5.9)$$

The reflectivity of unpolarized incident radiation is equal to the average of Eq. (5.8) and Eq. (5.9) and for radiation at normal incidence ( $\theta = 0$ ) we get

$$\rho'_n = \left( \frac{n_2 - n_1}{n_2 + n_1} \right)^2 = \left\{ \frac{(n_2/n_1) - 1}{(n_2/n_1) + 1} \right\}^2. \quad (5.10)$$

After the reflectivity has been evaluated, the directional spectral emissivity can be found from  $\varepsilon'(T, \theta, \phi) + \rho'(T, \theta, \phi) = 1$ , when the body is opaque. Due to invariance with  $\phi$  we get  $\varepsilon'(T, \theta) = 1 - \rho'(T, \theta)$ . Integration of  $\varepsilon'(\theta)$  over the hemisphere can be carried out to find  $\varepsilon$

$$\begin{aligned} \varepsilon = & \frac{1}{2} - \frac{(3n+1)(n-1)}{6(n+1)^2} - \frac{n^2(n^2-1)^2}{(n^2+1)^3} \ln\left(\frac{n-1}{n+1}\right) + \frac{2n^3(n^2+2n-1)}{(n^2+1)(n^4-1)} \\ & - \frac{8n^4(n^4+1)}{(n^2+1)(n^4-1)} \ln n \end{aligned}, \quad (5.11)$$

where  $n = n_2 / n_1$ . The normal emissivity can be found from Eq. (5.10)

$$\varepsilon'_n = 1 - \left( \frac{n-1}{n+1} \right)^2 = \frac{4n}{(n+1)^2}, \quad (5.12)$$

again with  $n = n_2 / n_1$ . Based on Eq. (5.11) and Eq. (5.12) we find the ratio between  $\varepsilon$  and  $\varepsilon'_n$ . This ratio can for example be used to calculate  $\varepsilon$  when only  $\varepsilon'_n$  is known (extrapolation). A typical graph of the directional emissivity for an insulator is shown in Figure 5.4.

For materials where  $\kappa \neq 0$  (for most materials) we have the following relations for radiation incident from air or vacuum (Siegel and Howell 1992)

$$\rho'_{\parallel}(\theta) = \frac{(n\gamma - \alpha/\cos\theta)^2 + (n^2 + \kappa^2)\alpha - n^2\gamma^2}{(n\gamma + \alpha/\cos\theta)^2 + (n^2 + \kappa^2)\alpha - n^2\gamma^2} \text{ and} \quad (5.13)$$

$$\rho'_{\perp}(\theta) = \frac{(n\beta - \cos\theta)^2 + (n^2 + \kappa^2)\alpha - n^2\beta^2}{(n\beta + \cos\theta)^2 + (n^2 + \kappa^2)\alpha - n^2\beta^2}, \quad (5.14)$$

where

$$\alpha^2 = \left( 1 + \frac{\sin^2\theta}{n^2 + \kappa^2} \right)^2 - \frac{4n^2}{n^2 + \kappa^2} \left( \frac{\sin^2\theta}{n^2 + \kappa^2} \right), \quad (5.15)$$

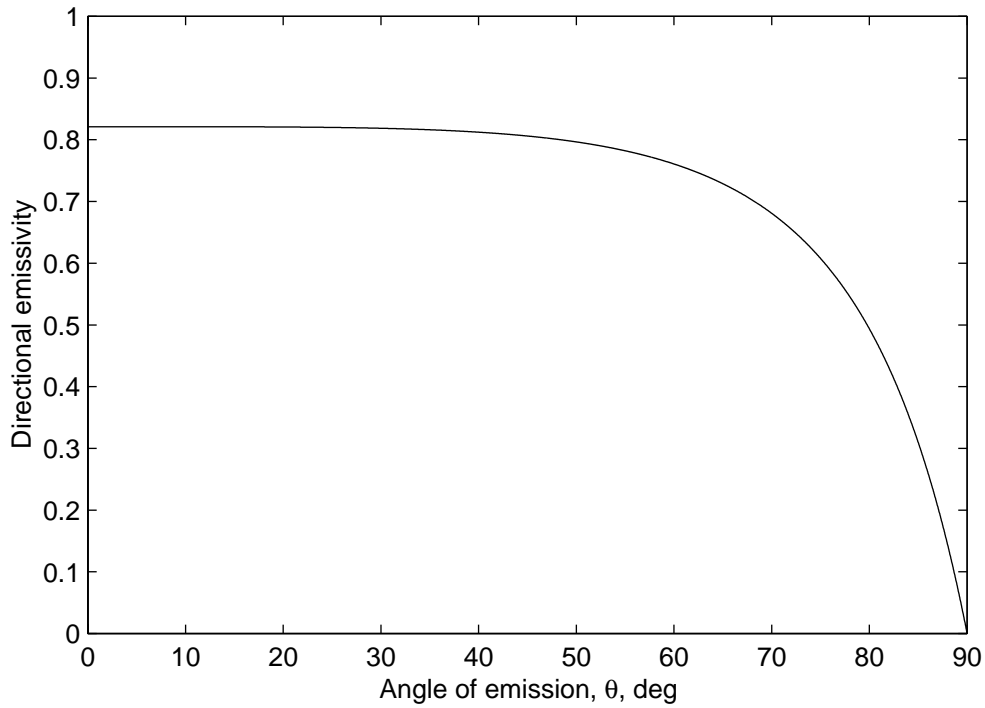


**Figure 5.4.** Typical curve for the directional emissivity of an insulator.

$$\beta^2 = \frac{n^2 + \kappa^2}{2n^2} \left( \frac{n^2 - \kappa^2}{n^2 + \kappa^2} - \frac{\sin^2 \theta}{n^2 + \kappa^2} + \alpha \right), \text{ and} \quad (5.16)$$

$$\gamma = \frac{n^2 - \kappa^2}{n^2 + \kappa^2} \beta + \frac{2n\kappa}{n^2 + \kappa^2} \left( \frac{n^2 + \kappa^2}{n^2} \alpha - \beta^2 \right)^{1/2}. \quad (5.17)$$

For metals the above relations simplify to (since the  $\sin^2 \theta$  term can be neglected relative to  $n^2 + \kappa^2$  for large  $\kappa$ )

$$\rho'_{\parallel}(\theta) = \frac{(n \cos \theta - 1)^2 + (\kappa \cos \theta)^2}{(n \cos \theta + 1)^2 + (\kappa \cos \theta)^2} \text{ and} \quad (5.18)$$

$$\rho'_{\perp}(\theta) = \frac{(n - \cos \theta)^2 + \kappa^2}{(n + \cos \theta)^2 + \kappa^2}. \quad (5.19)$$

From these equations we find the normal emissivity for unpolarized radiation into air or vacuum, using  $\varepsilon'(T, \theta) = 1 - \rho'(T, \theta)$  and the average of Eq. (5.18) and Eq. (5.19) to find  $\rho'(T, \theta)$ ,

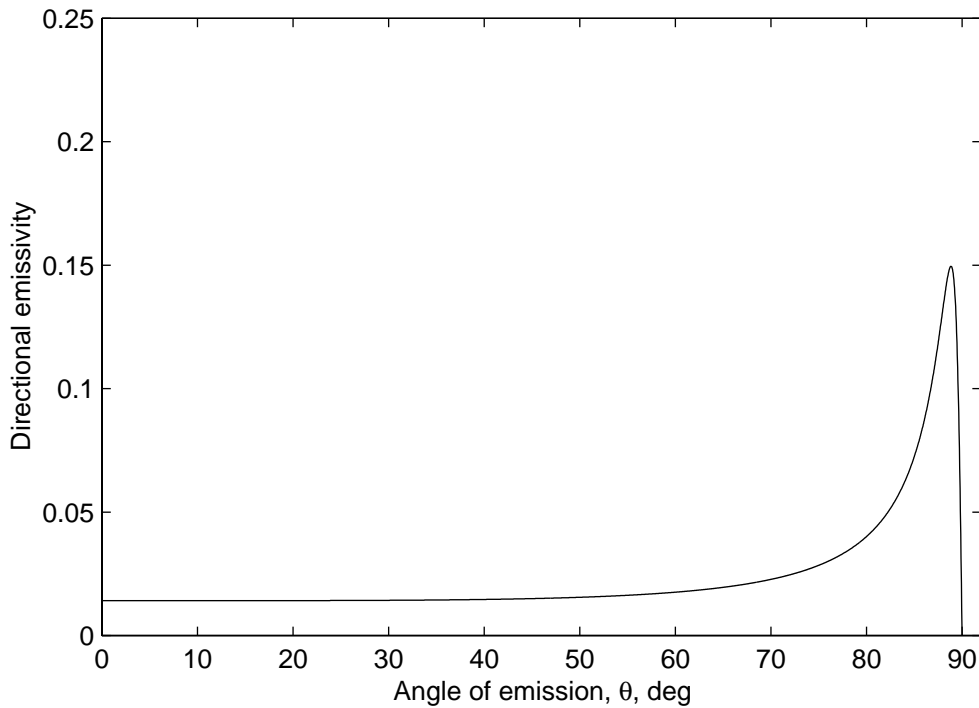


**Figure 5.5.** Typical curve for the directional emissivity of a metal.

$$\epsilon'_n = \frac{4n}{(n+1)^2 + \kappa^2}. \quad (5.20)$$

A typical graph of the directional emissivity for a metallic surface is shown in Figure 5.5. As opposed to the curve for the insulator we see that  $\epsilon'(\theta)$  increases as  $\theta$  approaches  $90^\circ$  before it drops to zero, whereas for the insulator there is no such increase in  $\epsilon'(\theta)$ .

### 5.5.2 Emissivity of Selected Materials Relevant for Aluminum Frames

In this section we present the emissivity of aluminum, aluminum alloys, treated aluminum surfaces, and other materials relevant for heat transfer in aluminum window frames, found in the literature.

Table 5.2 shows emissivity values found in two textbooks on heat transfer (Siegel and Howell 1992 and Mills 1995). Further, Table 5.3 reports emissivity values from Touloukian and Dewitt (1970), Touloukian and Dewitt (1972), and Touloukian et al. (1972). The first reference deals with radiative properties of metallic elements and alloys, the second with radiative properties of nonmetallic solids, and the last with radiative properties of coatings. All three books are a collection of radiative properties from different sources. Spectral values of the normal emissivity

for some relevant surfaces were also available from some of these books, but the wavelength range (1 - 10  $\mu\text{m}$ ) and temperature range (461 - 805 K) are not adequate for our applications.

**Table 5.2.** Emissivity of selected aluminum surfaces.

Description	Surface temperature [K]	Emissivity
Aluminum foil, as received	300	0.05 <sup>a</sup>
Aluminum foil, bright dipped <sup>b</sup>	300	0.03 <sup>a</sup>
Aluminum alloy 6061, as received <sup>b</sup>	300	0.04 <sup>a</sup>
Aluminum, hard-anodized <sup>b</sup>	300	0.80 <sup>a</sup>
Aluminum, soft-anodized <sup>b</sup>	300	0.76 <sup>a</sup>
Black enamel paint, heated 1000 hr. at 650 K <sup>b</sup>	300	0.80 <sup>a</sup>
Black epoxy paint <sup>b</sup>	300	0.87 <sup>a</sup>
White epoxy paint <sup>b</sup>	300	0.85 <sup>a</sup>
Aluminum, bright foil <sup>c</sup>	295	0.04 <sup>d</sup>
Aluminum, polished plate <sup>c</sup>	373	0.095 <sup>d</sup>
Aluminum, heavily oxidized <sup>c</sup>	370-810	0.20-0.33 <sup>d</sup>

a. Total-hemispherical emissivity.

b. From Mills (1995). Exact type of surface treatment and measurement method are not given.

c. From Siegel and Howell (1992). Exact type of surface treatment and measurement method for each value is not given. Linear interpolation can be used when temperatures and emissivities both have ranges.

d. Total-normal emissivity.

One source investigated the spectral dependence of directional emissivity ( $\theta = 25^\circ$ ,  $\phi = 2\pi$ ). The substance was sandblasted aluminum alloy 1100, nominal composition (99.0 min. Al). This was for wavelengths from 1 to 20  $\mu\text{m}$  and for a surface temperature of 306 K. They found that the emissivity decreased from about 0.6 to 0.1 when the wavelength increased from 1  $\mu\text{m}$  to 20  $\mu\text{m}$ .

Some emissivity values were also found in some other articles and handbooks. These are noted in Table 5.4. In addition three articles are described below; the first article deals with emissivity as function of direction, and the others with emissivity as function of thickness of anodizing film and for different electrolytes, respectively.

**Table 5.3.** Emissivity of selected aluminum surfaces from Touloukian and Dewitt (1970, 1972) and Touloukian et al. (1972).

Description	Surface temperature [K]	Type	Emissivity w/ (error)
Hand polished plate (0.2 in. thick)	227-282	Hemispherical-total	0.06 ( $\pm 3\%$ )
Foil, two years of exposure to salt and moisture at the seashore	311	Normal-total	0.10
Alloy 6061-T6 <sup>a</sup> , buffed	302	Hemispherical-total	0.0506, 0.0500, 0.0506 (< 7.7%)
Alloy 6061 <sup>a</sup> , as received	278	Hemispherical-total	0.04
Alloy 6061 <sup>a</sup> , sandblasted (120 size grit)	278	Hemispherical-total	0.41 (10%)
Alodined 7075-T6 <sup>b</sup> , substrat sandblasted	293	Hemispherical-total	0.234
Alodined 7075-T6 <sup>b</sup> , substrat alclad	259	Hemispherical-total	0.117
Alodined 7075-T6 <sup>b</sup> , substrat smooth and unclad	273 307 313	Hemispherical-total	0.100 0.091 0.091
Alloy 7075-T6 <sup>b</sup> , Martin Hardcoate anodized	217 242 285 313	Hemispherical-total	0.790 0.848 0.869 0.856
Epoxy on aluminum substrate	253 263 270	Hemispherical-total	0.73 0.71 0.73
1199 aluminum anodized for 10 min. in sulfuric acid, coating thickness 8.4 $\mu\text{m}$ . Polished in phosphoric/nitric acid bath for 2 min at 364 K	338	Hemispherical-total	0.68
1199 aluminum anodized for 15 min. in sulfuric acid, coating thickness 9.5 $\mu\text{m}$ . Polished in electrolytic fluoboric acid bath.	339	Hemispherical-total	0.69

**Table 5.3.** Emissivity of selected aluminum surfaces from Touloukian and Dewitt (1970, 1972) and Touloukian et al. (1972).

Description	Surface temperature [K]	Type	Emissivity w/ (error)
Anodized aluminum	296	Hemispherical-total	0.842 ( $\pm 5\%$ )
	343		0.830 ( $\pm 5\%$ )
	394		0.812 ( $\pm 5\%$ )
Anodized aluminum, layer of carbon electro-phoretically deposited into the pores of the surface	294	Hemispherical-total	0.890 ( $\pm 5\%$ )
	393		0.932 ( $\pm 5\%$ )

a. Nominal composition (1.0 Mg, 0.6 Si, 0.25 Cr, 0.25 Cu, Al balance).

b. Nominal composition (5.6 Zn, 2.5 Mg, 1.6 Cu, 0.3 Cr, Al balance).

**Table 5.4.** Emissivity of selected aluminum surfaces.

Description	Surface temperature [K]	Type	Emissivity
6061-T6 aluminum alloy (25 $\mu\text{m}$ thick film of boehmite, $\text{Al}_2\text{O}_3 \cdot \text{H}_2\text{O}$ ) <sup>a</sup>	“Room temperature”	Hemispherical-total	0.911-0.934
6061-T6 aluminum alloy ( $\text{Al}_2\text{O}_3$ coating). Same as above but after dehydration <sup>a</sup>	“Room temperature”	Hemispherical-total	0.884-0.891
Aluminum, polished <sup>b</sup>	373	Normal-total	0.095
Aluminum, heavily oxidized <sup>b</sup>	366	Normal-total	0.2
Aluminum oxide <sup>b</sup>	550	Normal-total	0.63
Aluminum, polished <sup>c</sup>	323-773	Hemispherical-total	0.04-0.06
Aluminum, rough surface <sup>c</sup>	293-323	Hemispherical-total	0.06-0.07
Aluminum, strongly oxidized <sup>c</sup>	328-773	Hemispherical-total	0.2-0.3

a. From Kollie et al. (1990). Dehydration of boehmite is known to occur above 565 K.

b. From VDI-Wärmeatlas (1997).

c. From Lide (1993) (Handbook of Chemistry and Physics)

De Silva and Jones (1986) studied the directional-total emissivity ( $\theta = 10^\circ$  to  $80^\circ$ ) of some metals, solar absorbers and dielectrics. In agreement with classical electromagnetic theory they found that the emissivity of metals increases with the angle from the normal to the surface. Particularly, for aluminum they found that the emissivity increased from approximately 0.04 for  $\theta = 10^\circ$  to 0.11 for  $\theta = 80^\circ$ . These investigations were for surfaces at 368 K.

Kohara and Niimi (1996) studied the spectral emissivity of anodized aluminum as a function of anodizing time and thickness of the anodizing film. They started with specimens of the aluminum alloy 1050-O. The specimens were anodized in a sulfuric acid bath at 20-30 °C for 1-150 minutes with direct current at constant voltages of 20-30 V. They used a Fourier transform infrared spectrophotometer to measure the emissivity in the spectral range from 5  $\mu\text{m}$  to 20  $\mu\text{m}$ . Kohara and Niimi found that anodizing influenced the spectral emissivity of aluminum most above  $\lambda = 7 \mu\text{m}$ . When the anodizing time increased from 2 - 10 minutes (corresponding to an increase in anodizing film thickness from approximately 1  $\mu\text{m}$  to 5  $\mu\text{m}$ ) the emissivity above  $\lambda = 7 \mu\text{m}$  increased from approximately 0.1 to 0.85. Below  $\lambda = 7 \mu\text{m}$  the emissivity increased from 0.1 to 0.2 for the same increase in anodizing time. For anodizing times above 20 minutes (film thickness above 10  $\mu\text{m}$ ) the emissivity was relatively constant like 0.9 above  $\lambda = 7 \mu\text{m}$  and 0.2 below  $\lambda = 7 \mu\text{m}$ .

Pavlovic and Ignatiev (1986) investigated the emissivity of anodic oxide coatings on aluminum prepared from solutions of phosphoric, chromic and sulfuric acid. The aluminum specimen had a purity of 99.8 %. They found that the emissivity increased from  $\epsilon = 0.06$  for a film thickness of 0.5  $\mu\text{m}$  to  $\epsilon = 0.8$  for a film thickness of 4  $\mu\text{m}$  and above (till 16  $\mu\text{m}$ ) for films formed in sulfuric acid. For chromic acid they found that the emissivity increased from  $\epsilon = 0.06$  for film thickness of 0.5  $\mu\text{m}$  to  $\epsilon = 0.75$  for a film thickness of 3.5  $\mu\text{m}$ . Phosphoric acid gave an increase in emissivity from  $\epsilon = 0.06$  for film thickness of 0.5  $\mu\text{m}$  to  $\epsilon = 0.25$  for a film thickness of 2  $\mu\text{m}$ . Maximum film thickness was reached after an oxidation time of 30 minutes for all samples. Pavlovic and Ignatiev explained the difference in emissivity due to the microstructural differences in the oxide films.

According to EAA (1995) anodized aluminum for use in building applications is supposed to have a minimum average thickness of 5, 10, 15, 20 or 25  $\mu\text{m}$ , depending on class. The classes are named by class 5 to class 25. Aluminum in the classes 5 and 10 is sufficient for indoor use while anodized aluminum in the classes 15 till 25 can be used outdoors. National standards and type of atmosphere should be checked before choosing the thickness class.

**Table 5.5.** Density,  $\rho$ , specific heat capacity,  $c$ , and conductivity,  $\lambda_k$ , of selected solids.

Description	$T$ [K]	$\rho$ [kg/m <sup>3</sup> ]	$c$ [J/kgK]	$\lambda_k$ [W/mK]
Pure aluminum <sup>a</sup>	300	2702	903	237
Aluminum oxide, Al <sub>2</sub> O <sub>3</sub> , alumina <sup>a</sup>	300	3970	765	36
Polyamide (nylon) <sup>a</sup>	300	1140	1670	0.24
Polyethylene, high density <sup>a</sup>	300	960	2090	0.33
Polyvinylchloride <sup>a</sup>	300	1714	1050	0.092
Aluminum alloy 6061-T4 <sup>b</sup>	298			154
Aluminum alloy 6061-T6 <sup>b</sup>	298			167
Aluminum alloy 6063-O <sup>b</sup>	298			217
Aluminum alloy 6063-T6 <sup>b</sup>	298			200

a. From Mills (1995).

b. From TAA (1994). These values are averaged for various sizes, product forms and methods of manufacturer and may not be representative of any particular product or size.

### 5.5.3 Material Properties of Selected Materials

In Table 5.5 we present the density, specific heat capacity and conductivity of aluminum, some of its alloys and some other materials relevant for heat transfer calculations on aluminum window frames. Values for other materials can be found in CEN (1998) or general textbooks like Mills (1995) and Kreith and Bohn (1997). The table shows that the conductivity of aluminum ranges from 154 to 237 W/mK, for the aluminum alloy 6061-T4 and pure aluminum, respectively. For the aluminum alloy usually found in window frames, the aluminum alloy 6061-T6, a conductivity of 167 W/mK is noted, and that is close to the value prescribed in CEN (1998), which is 160 W/mK.

## 5.6 Sensitivity Study

Studying the emissivity of anodized aluminum sections we find that the emissivity can vary from 0.68 for polished anodized surfaces to 0.934 for a 6061-T6 aluminum alloy with a 25  $\mu\text{m}$  thick film of boehmite. Here we will check how much different emissivities can influence the U-value of frame sections. This is important for knowing how accurate we need to determine the emissivity of materials used in window frames. Two frame sections with internal cavities are examined. The first, shown in Figure 5.6, is a simple hypothetical section for which the simplified

equations for heat transfer in a cavity can be assumed to be approximately right. Section number two, shown in Figure 5.7, is an actual window frame from WICONA Bausysteme GmbH (Wicona 1998). We note that due to the complexity of the complex window frame there are some small differences between the simulated frame and the frame shown in Figure 5.7. Heat flow through the frames is simulated with the steady state finite element program THERM 2.1a (Finlayson et al. 1998). Air cavities are simulated according to CEN (1998), as described in Chapter 2 and Chapter 3. In addition simulations with an improved view-factor radiation model (included in THERM) are performed to see if the type of radiation model influence the U-value significantly.

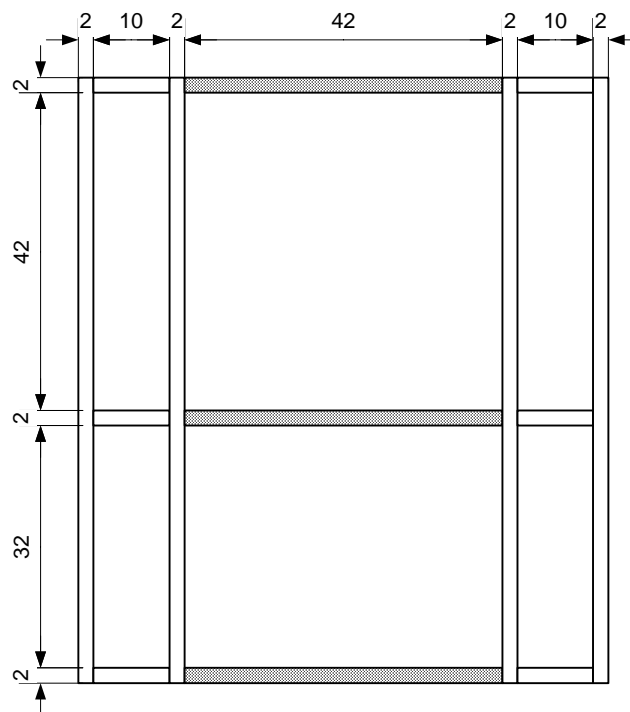


**Figure 5.6.** Simple frame section. Aluminum profiles are separated by thermal breaks of polyamide.

During the simulations the internal and external surface heat resistances were set to  $0.13 \text{ m}^2\text{K/W}$  and  $0.04 \text{ m}^2\text{K/W}$ , respectively. According to CEN (1998) we are to use an emissivity of 0.9 when no other information is available. Thus, this value is assigned to all materials, except for aluminum. For aluminum the emissivity is varied between 0.1 and 0.9. Strictly speaking, the surface heat resistances vary when the emissivity varies, however here these were fixed to limit the number of parameters. Also, the exterior surfaces of a window frame almost always have some sort of treatment, either painted or anodized, so the emissivity is close to 0.9 and therefore

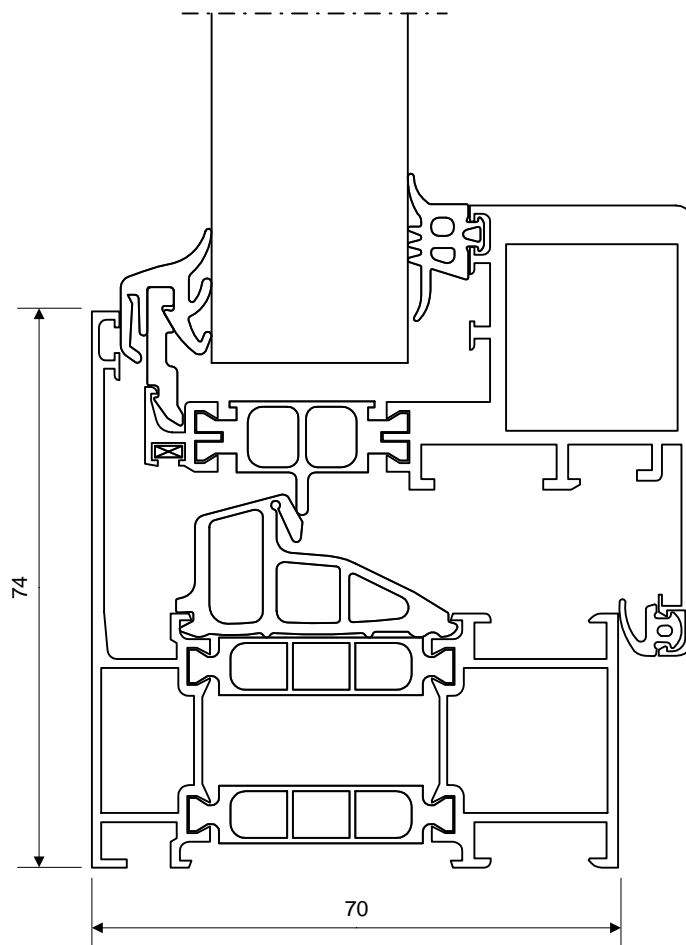


**Figure 5.7.** Window frame section from WICONA Bausysteme GmbH (Wicona 1998b)

the surface resistances used still are correct. Thus, it is the emissivity of aluminum facing internal cavities that is changed. The material properties used for the solid materials were found in CEN (1998) and are noted in Table 5.6.

When using the equivalent conductivity method, the temperatures of the warm and cold walls in in frame cavities have to be set manually. The wall temperatures are used to find the conductive and radiative heat transfer coefficients, see Eq. (3.27) and Eq. (3.29). However, these temperatures are not known in advance. One approach is therefore to use a fixed temperature difference,  $\Delta T = T_H - T_C$ , for all simulations. But each simulation with a different emissivity will undoubtedly give a new and different temperature distribution in the sections.  $\Delta T$  may therefore change from emissivity to emissivity, and then lead to a possible change in the convection heat transfer coefficient. Leaving  $\Delta T$  unchanged would give us the U-value resulting from the emissivity change alone, but not necessary the right U-value. Therefore, an iterating process was per-

**Table 5.6.** Conductivity of the materials used for the frame sections.

Description	Material	Conductivity [W/(mK)]
Aluminum profile	Aluminum	160
Thermal break	Polyamide (nylon)	0.25
Gasket	Buthyl rubber	0.24
“Glazing”	Extruded polystyrene	0.035

formed to arrive at the right equivalent conductivity. First, the wall temperatures are guessed, and after the first simulation the temperatures of the cavity walls are updated. This process is repeated until the values of  $T_H - T_C$  from two consecutive runs are smaller than  $0.4\text{ }^\circ\text{C}$ , and the temperatures themselves from two consecutive runs not change more than  $0.2\text{ }^\circ\text{C}$ . For surfaces where the temperature varied we used the mean temperature. For the complex frame section, to limit the number of cavities for which we had to change the temperature, we did not change the wall temperatures for the smallest cavities. For these cavities the wall temperatures were set equal to the values found after the first run. This approach gave a total number of 18 cavities for which we changed the temperatures. For the simple section the temperatures of all cavities were modified.

To find the U-value of the complex aluminum window frame the glazing was replaced by an insulation panel and the U-value calculated according to Eq. (2.14). Because the simple section was not completed by an insulation panel, as described in Chapter 2, the U-value was found from

$$U = \frac{Q_{tot}}{(T_i - T_e) \cdot L_{proj}}, \quad (5.21)$$

where  $Q_{tot}$  is the integrated heat flux across the indoor boundary.

The results are noted in Table 5.7. For both frames we see that the U-value changes more with emissivity when the CEN (1998) radiation model is used than when the view-factor radiation model is employed. This may be because the view-factor model takes radiation from all surfaces in the cavity into account while the CEN model only considers heat transfer from two opposite warm and cold surfaces. Also, relevant for the complex frame, surfaces blocking some of the radiation are considered when using the view-factor based model. The table also shows that the variation in the U-value due to differences in the emissivity is largest for the simple section.

**Table 5.7.** Results from the simulation of U-value for two different frame sections.

Emissivity	$U$ [W/m <sup>2</sup> K], simple section	$U$ [W/m <sup>2</sup> K] frame section	$U$ [W/m <sup>2</sup> K], simple section	$U$ [W/m <sup>2</sup> K] frame section
	CEN (1998) radiation model		View-factor based radiation model	
0.10	1.624	1.714	1.911	1.914
0.20	1.715	1.771	2.006	1.945
0.70	2.266	2.047	2.464	2.052
0.79	2.389	2.094	2.551	2.067
0.80	2.404	2.100	2.562	2.069
0.81	2.418	2.105	2.572	2.072
0.90	2.553	2.155	2.663	2.099

The initial question was how accurately the emissivity of aluminum needs to be determined, in order to report reliable U-values. Is it enough to separate between the values of 0.9 and 0.2 that are used for treated and untreated aluminum, respectively, or is higher accuracy needed? Looking at the results where the emissivity is changed between 0.79 and 0.81, we find only smaller differences for both sections and radiation models. At most the difference in the U-value is 0.029 W/m<sup>2</sup>K. Changing the emissivity between 0.8 and 0.9 the difference in U-value at most is 0.149, and varying the emissivity between 0.7 and 0.9 the difference at most is 0.287 W/m<sup>2</sup>K. If we consider a window of total area 1 m<sup>2</sup> where the frame area is 40 % of the total area, a difference in emissivity of 0.2 (from 0.7 to 0.9) may change the total window U-value of about 0.1 W/m<sup>2</sup>K (assuming that the glazing and linear thermal transmittance are equal for both cases). Thus, it may be worthwhile quantifying the emissivity in intervals of 0.1, but further accuracy is not necessary when U-values are determined.

Based on the current results, we also note that in addition to the differences in the U-value caused by the changes in emissivity, there also are differences in the frame U-values caused by the use of the two radiation models. For the simple and complex frames these differences in the U-value at most are 0.287 and 0.200, respectively. The maximum deviation occurs for  $\epsilon = 0.1$ .

## 5.7 Conclusions

This chapter has presented the basic properties used when calculating heat transfer by radiation. Further, this chapter presented emissivity values found from the use of electromagnetic theory, and emissivity values of aluminum surfaces with different treatments, found in the literature.

The emissivity values used for aluminium surfaces when calculating the thermal transmittance of window frames, 0.2 for untreated and 0.9 for treated surfaces, seems reasonable when a conservative approach is used. That is, the emissivity values used in rating fenestration products are the ones that are expected after years of use and wear.

A study of how sensitive the numerical calculations are to different values of the emissivity was also included. By performing a sensitivity study we found that an increase in emissivity from 0.7 to 0.9, increased the U-value of a simple hypothetical window frame by about 0.3 W/m<sup>2</sup>K at most. For a complex window frame the U-value increased by about 0.1 W/m<sup>2</sup>K for the same change in emissivity. By using a view-factor based radiation model to calculate the radiation heat transfer we find that the differences in U-value are even smaller. Thus, taking into account that a window frame only occupies a small part of the total window system, we find that an accuracy of 0.1 is sufficient when measuring the emissivity of aluminum surfaces, for use in calculations of window frame U-values.



# Chapter 6

## Conclusions

Based on the work presented in Chapters 2 to 5 and in Papers I to IV, the following conclusions can be drawn:

1. The CEN (1998) natural convection coefficient, which is supposed to be used for vertical frames, compares well to correlations suitable for high aspect ratio glazing cavities ( $W/L$  large). The ASHRAE (1996) and ISO (2000a) natural convection correlations for simulation of natural convection heat transfer in frame cavities are usable for cavities having a low,  $H/L < 0.5$ , or a high,  $H/L > 5$ , vertical aspect ratio. In the interpolation area,  $0.5 < H/L < 5$ , the correlation should be improved.
2. The CFD program FLUENT (Fluent 1998) was able to model combined natural convection and heat transfer in window frames with internal cavities well enough for generally good agreement between simulated and measured surface-temperature results. Thus, CFD simulations were performed to study convection effects in the internal cavities of window frames.
3. Although more investigations are needed, it seems that a cavity having an interconnection of less than about 7 mm can be split into two separate cavities.
4. Traditional software codes, simulating only conduction heat transfer and using equivalent conductivities for air cavities, give results that compare well with results from fluid flow simulations. This is provided that the air cavities are divided and that the correct convection heat-transfer correlations are used for the internal cavities of the window frames. Thus for vertical frame sections correlations that are usable for vertical air cavities have to be used and likewise for horizontal sections. Two-dimensional CFD and conduction simulations show that temperature contours deviate mostly within the internal air cavities of the frames.
5. It seems reasonable the use the assumption that convection in a complete window frame with joined, open internal cavities can be modeled by separating the horizontal and vertical cavi-

ties; this approach yields reasonably accurate predictions for the mean U-value of entire frame sections. Accurate modeling of corner regions will still require joining horizontal and vertical cavities.

6. CFD simulations of natural convection in three-dimensional cavities with a high vertical aspect ratio ( $H/L = 20, 40, \text{ and } 80$ ) and a low horizontal aspect ratio ( $W/L = 0.2, 0.5, 1, 2, \text{ and } 5$ ), the typical enclosure found in vertical aluminum window frames, show that cavities with a horizontal aspect ratio larger than 5 can be considered as two-dimensional with respect to heat transfer rates (to an accuracy of about 4 %). But, for cavities with a lower horizontal aspect ratio separate correlations should be used to quantify heat transfer rates. Paper III presents such correlations.
7. The normal spectral emissivity of an anodized aluminium window frame profile was measured, and the normal total emissivity was calculated. It was shown that the emissivity is fairly constant (between 0.834 and 0.856) for exterior parts of the anodized profile and for surfaces facing the thermal break cavity. Large variation was found for the all-aluminum internal cavities. The normal total emissivity varied between 0.055 and 0.82. However, because of the large conductivity of aluminum, this variation is not expected to influence heat transfer much, with regard to thermal transmittance simulations.
8. Based on the measurements of spectral normal emissivity and emissivity values found in the literature, the emissivity values used for aluminium surfaces when calculating the thermal transmittance of window frames, 0.2 for untreated and 0.9 for treated surfaces, seem reasonable if a conservative approach is used. That is, the emissivity values used in rating fenestration products are the ones that are expected over the entire service life of the frames. But since such values are rare and also since measurements, which also are used to rate window products and are supposed to give similar/equivalent results as the simulations, are performed on new products it is recommended that the emissivity of the material at fabrication time should be used instead of the emissivity expected over the entire service lifetime. Thus, for untreated aluminum an emissivity of 0.05 is recommended. Separate emissivity values should be used for calculation of U-values that are to be valid after years of use and wear.
9. Since an anodic coating is probably not needed inside thermal break cavities some sort of action could be performed to keep those untreated, when aluminum frames are anodized. If such actions are carried out manufacturers can use an emissivity of 0.2 (conservative value)

instead of 0.9 when calculating the thermal transmittance. If not an emissivity of 0.9 should be used.



## Chapter 7

### Suggestions for Further Work

In this thesis focus has been put on three-dimensional natural convection effects in window frames with internal cavities, and natural convection effects in complex horizontal window frames. One of the conclusions is that traditional two-dimensional heat-conduction simulation tools can still be used with good accuracy when calculating the window frame thermal transmittance. Still, models for transforming air cavities to solids by the use of an equivalent conductivity require more research. Further studies should be performed on when to divide frame cavities that have small throats or interconnections. Different two- and three-dimensional cavities of various shapes should be studied.

The correlations used in ASHRAE (1996) and ISO (2000a) to calculate the convective heat transfer coefficient for cavities with aspect ratios,  $H/L$ , between 0.5 and 5, are based on interpolation. It has been shown, by comparison with other results, that this interpolation can give wrong Nusselt numbers for some Rayleigh numbers and aspect ratios. Therefore a new correlation should be found for this intermediate aspect ratio range.

Laminar flow was assumed when the correlations for natural convection in three-dimensional cavities with a high vertical aspect ratio and a low horizontal aspect ratio were developed. Correlations should also be found for turbulent flow. Experimental validations of the numerical simulations should be performed.

Emissivities of window-frame materials (and also other building materials) that are usable over the entire service life should be measured. The emissivity of new frame materials should also be measured.

Condensation is a problem for some glazings, especially for the bottom part of the glazings. It should be investigated whether the natural convection effects taking place in window frames with internal cavities increase the condensation problem of glazings.

Most of the studies of heat transfer effects in fenestration systems have focused on windows manufactured for residential buildings. Research should be conducted to check if the current heat transfer models are accurate for fenestration systems used in commercial buildings.

# References

Akiyama, M. and Q.P. Chong. 1997. Numerical analysis of natural convection with surface radiation in a square enclosure. *Numerical Heat Transfer, Part A*, Vol. 31, pp. 419-433.

Arnold, J.N., D.K. Edwards and I. Catton. 1977. Effect of tilt and horizontal aspect ratio on natural convection in a rectangular honeycomb. *Journal of Heat Transfer. Transactions of the ASME*, Vol. 99, pp. 120-122.

ASHRAE 1996. *Draft BSR/ASHRAE Standard 142P - Standard method for determining and expressing the heat transfer and total optical properties of fenestration products*. Atlanta: American Society of Heating, Refrigerating and Air-conditioning Engineers Inc.

ASHRAE 1997. *1997 ASHRAE Handbook, fundamentals*. Atlanta: American Society of Heating, Refrigerating and Air-conditioning Engineers Inc.

Batchelor, G.K. 1954. Heat transfer by free convection across a closed cavity between vertical boundaries at different temperatures. *Quarterly Applied Mathematics*, Vol. 12, pp. 209-233.

Balaji, C. and S.P. Venkateshan. 1993. Interaction of surface radiation with free convection in a square cavity. *International Journal of Heat and Fluid Flow*, Vol. 14, pp. 260-267.

Balaji, C. and S.P. Venkateshan. 1994. Correlations for free convection and surface radiation in a square cavity. *International Journal of Heat and Fluid Flow*, Vol. 15, pp. 249-251.

Behnia, M., J.A. Reizes, and G. de Vahl Davis. 1990. Combined radiation and natural convection in a rectangular cavity with a transparent wall and containing a non-participating fluid. *International Journal for Numerical Methods in Fluids*, Vol. 10, pp. 305-325.

Bejan, A. and C.L. Tien. 1978. Laminar Natural convection in horizontal cavity with different end temperatures. *Journal of Heat Transfer. Transactions of the ASME*, Vol. 100, 641-647.

Berkovsky, B.M. and V.K. Polevikov. 1977. Numerical study of problems on high-intensive free convection. In: *Heat transfer and turbulent buoyant convection* (D.B. Spalding and N. Afgan, editors), Vol. II, pp. 443-455. Washington: Hemisphere Publishing Corporation.

BKS 2000. *Byggedetaljeblad 533.102. Vinduer. Typer og funksjoner*. Oslo: Norwegian Building Research Institute.

Blomberg, T. 1991. *Heat2. A heat transfer PC-program*. Lund: Lund University.

Branchaud, T.R., D. Curcija, and W.P. Goss. 1998. Local heat transfer in open frame cavities of fenestration systems. In: *Thermal performance of the exterior envelopes of buildings VII*. Atlanta: American Society of Heating, Refrigeration and Air-Conditioning Engineers.

Carpenter, S.C. and A.G. McGowan. 1989. Frame and spacer effects on window U-value. *ASHRAE Transactions*, Vol. 95, pp. 604-608.

Carpenter, S.C. and A. McGowan. 1998. Three-dimensional heat transfer effects in building components. *ASHRAE Transactions*. Vol. 104, pp. 1070-1076.

CEN 1996. *prEN 12519 - Doors and windows - Terminology*. Brussels: European Committee for Standardization.

CEN 1997. *EN 673 - Glass in building - Determination of thermal transmittance (U value) - Calculation method*. Brussels: European Committee for Standardization.

CEN 1998. *prEN ISO 10077-2 - Thermal performance of windows, doors and shutters - Calculation of thermal transmittance - Part 2: Numerical method for frames*. Brussels: European Committee for Standardization.

CEN 2000. *EN ISO 10077-1 - Thermal performance of windows, doors and shutters - Calculation of thermal transmittance - Part 1: Simplified method*. Brussels: European Committee for Standardization.

CEN 2001a. *prEN ISO 10077-2 - Thermal performance of windows, doors and shutters - Calculation of thermal transmittance - Part 2: Numerical method for frames*. Brussels: European Committee for Standardization.

CEN 2001b. *prEN 12412-2 - Thermal performance of windows, doors and shutters - Determination of thermal transmittance by hot box method - Part 2: Frames*. Brussels: European Committee for Standardization.

Claesson, J. and C.-E. Hagentoft. 1994. *Basic building physics, mathematical modelling*. Lund: Department of building technology and mathematical physics, University of Lund.

Curcija, D. 1992. *Three-dimensional finite elements model of overall, night time heat transfer through fenestration systems*. Ph.D. dissertation. Massachusetts: Department of Mechanical and Industrial Engineering, University of Massachusetts Amherst.

Curcija, D. and W.P. Goss. 1993. Two-dimensional natural convection over the isothermal indoor fenestration surface - finite element numerical solution. *ASHRAE Transactions*, Vol. 99, pp. 274-287.

Dascalaki, E., M. Santamouris, C.A. Balaras, and D.N. Asimakopoulos. 1994. Natural convection heat transfer coefficients from vertical and horizontal surfaces for building applications. *Energy and Buildings*, Vol. 20, pp. 243-249.

de Vahl Davis, G. and I.P. Jones. 1983. Natural convection in a square cavity: A comparison exercise. *International Journal for Numerical Methods in Fluids*, Vol. 3, pp. 227-248.

de Vahl Davis, G. 1983. Natural convection of air in a square cavity: A bench mark numerical solution. *International Journal for Numerical Methods in Fluids*, Vol. 3, pp. 249-264.

De Silva, A.A. and B.W. Jones. 1986. The directional-total emittance at 368 K of some metals, solar absorbers and dielectrics. *Journal of Physics D. Applied Physics*, Vol. 20, pp. 1102 - 1108.

EAA 1995. *Bestimmungen für das Gütezeichen für anodisch erzeugte Oxidschichten auf Aluminium-Halbzeug in der Architektur*. Zürich: QUALANOD.

Eckert, E.R.G. and W.O. Carlson. 1961. Natural convection in an air layer enclosed between two vertical plates with different temperatures. *International Journal of Heat and Mass Transfer*, Vol. 2, pp. 106-120.

Edwards, D.K., I. Catton, and J.N. Arnold. 1978. *Studies of heat transfer in thermally driven flows* (Rep No. UCLA-Eng-7828). Los Angeles: University of California.

ElSherbiny, S.M., G.D. Raithby, and K.G.T. Hollands. 1982a. Heat transfer by natural convection across vertical and inclined air layers. *Journal of Heat Transfer. Transactions of the ASME*, Vol. 104, pp. 96-102.

ElSherbiny, S.M., K.G.T. Hollands, and G.D. Raithby. 1982b. Effects of thermal Boundary conditions on natural convection in vertical and inclined air layers. *Journal of Heat Transfer. Transactions of the ASME*, Vol. 104, pp. 515-520.

Enermodal 1995. *FRAMEplus toolkit, version 4.0*. Kitchener, Ontario: Enermodal Engineering.

Finlayson, E., R. Mitchell, D. Arasteh, C. Huizenga, and D. Curcija. 1998. *Therm 2.0: Program description. A PC program for analyzing the two-dimensional heat transfer through building products*. Berkeley: University of California.

Fluent 1998. *FLUENT 5 User's Guide*. Lebanon: Fluent Incorporated.

Fusegi, T. and J.M. Hyun. 1994. Laminar and transitional natural convection in an enclosure with complex and realistic conditions. *International Journal of Heat and Fluid Flow*, Vol. 15, pp. 258-268.

Fusegi, T., M. Hyun, K. Kuwahara, and B. Farouk. 1991. A numerical study of three-dimensional natural convection in a differentially heated cubical enclosure. *International Journal of Heat and Mass Transfer*, Vol. 34, pp. 1543-1557.

Gebhart, B., Y. Jaluria, R.L. Mahajan, and B. Sammakia. 1988. *Buoyancy-induced flows and transport*. New York: Hemisphere Publishing Corporation.

Gervais, F. 1991. The optical properties aluminium oxide. In: *Handbook of Optical Constants of Solids II* (E.D. Palik, editor), pp. 761-775. San Diego: Academic Press Inc.

Griffith, B., E. Finlayson, M. Yazdanian, and D. Arasteh. 1998. The Significance of bolts in the thermal performance of curtain-wall frames for glazed facades. *ASHRAE Transactions*, Vol. 104, pp. 1063-1069.

Hallé, S., M.A. Bernier, A. Patenaude, and R. Jutras. 1998. The combined effect of air leakage and conductive heat transfer in window frames and its impact on the Canadian energy rating procedure. *ASHRAE Transactions*, Vol. 104, pp. 176-184.

Hanssen, S.O., J.V. Thue, Ø. Skarstein, F.O. Gjerstad, and V. Novakovic (1996). ENØK i bygninger - Effektiv energibruk, håndbok for planlegging, gjennomføring og oppfølging (In Norwegian). Oslo: Universitetsforlaget.

Haustermans, L. 2000. *Heat transfer in aluminium window frame profiles. Computer modelling and hot box measurements*. Master of Science Thesis. Leuven: Departement Burgerlijke Bouwkunde, Katholieke Universiteit Leuven.

Henkes, R.A.W.M. and C.J. Hoogendoorn. 1995. Comparison exercise for computations of turbulent natural convection in enclosures. *Numerical Heat Transfer, Part B*, Vol. 28, pp. 59-78.

Hollands, K.G.T. and L. Konicek. 1973. Experimental study of the stability of differentially heated inclined air layers. *International Journal of Heat and Mass Transfer*, Vol. 16, pp. 1467-1475.

Hollands, K.G.T. 1973. Natural convection in horizontal thin-walled honeycomb panels. *Journal of Heat Transfer. Transactions of the ASME*, Vol. 95, pp. 439-444.

Hollands, K.G.T., T.E. Unny, G.D. Raithby, and L. Konicek. 1976. Free convective heat transfer across inclined air layers. *Journal of Heat Transfer. Transactions of the ASME*, Vol. 98, pp. 189-193.

Hoogendoorn, C.J. 1986. Natural convection in enclosures. *Proceedings of the 8th International Heat Transfer Conference*, Vol. 1, pp. 111-120.

Hsieh, S.-S. and C.-Y. Wang. 1994. Experimental study of three-dimensional natural convection in enclosures with different working fluids. *International Journal of Heat and Mass Transfer*, Vol. 37, pp. 2687-2698.

ISO 1994. *ISO 10292 - Glass in building - Calculation of steady state U values (thermal transmittance) of multiple glazing*. Geneva: International Organization for Standardization.

ISO 1995. *ISO 10211-1 - Thermal bridges in building construction - Heat flows and surface temperatures - Part 1: General calculation methods*. Geneva: International Organization for Standardization.

ISO 1996. *ISO 6946 - Building components and building elements - Thermal resistance and thermal transmittance - Calculation method*. Geneva: International Organization for Standardization.

ISO 2000a. *ISO/DIS 15099 - Thermal performance of windows, doors and shading devices - Detailed calculations*. Geneva: International Organization for Standardization.

ISO 2000b. *ISO/FDIS 12567. Thermal performance of windows and doors - Determination of thermal transmittance by hot box method*. Geneva: International Organization for Standardization.

- Jonsson, B. 1985. *Heat transfer through windows. During the hours of darkness with the effect of infiltration ignored*. Document D13:1985. Stockholm: Swedish Council for Building Research.
- Kim, D.M. and R. Viskanta. 1984. Study of the effects of wall conductance on natural convection in differently oriented square cavities. *Journal of Fluid Mechanics*, Vol. 144, pp. 153-176.
- Kohara, S. and Y. Niimi. 1996. Infrared radiation properties of anodized aluminum. *Materials Science Forum*, Vol. 217-222, pp. 1623-1628.
- Kollie, T.G., F.J. Weaver, and D.L. McElroy. 1990. Evaluation of a commercial, portable, ambient-temperature emissometer. *Review of Scientific Instruments*, Vol. 61, pp.1509-1517.
- Korpela, S.A., Y. Lee, and J.E. Drummond 1982. Heat transfer through a double pane window. *Journal of Heat Transfer. Transactions of the ASME*, Vol. 104, pp. 539-544.
- Kreith, F. and M.S. Bohn. 1997. *Principles of heat transfer*. Boston: PWS Publishing Company.
- Kuyper, R.A., T.H. van der Meer, C.J. Hoogendoorn, and R.A.W.M. Henkes. 1993. Numerical study of laminar and turbulent natural convection in an inclined square cavity. *International Journal of Heat and Mass Transfer*, Vol. 36, pp. 2899-2911.
- Lartigue, B., S. Lorente, and B. Bourret. 2000. Multicellular natural convection in a high aspect ratio cavity: experimental and numerical results. *International Journal of Heat and Mass Transfer*, Vol. 43, pp. 3157-3170.
- Le Puetrec, Y. and G. Lauriat. 1990. Effects of heat transfer at the side walls on natural convection in cavities. *Journal of Heat Transfer. Transactions of the ASME*, Vol. 112, pp. 370-378.
- Lee, Y. and S.A. Korpela. 1983. Multicellular natural convection in a vertical slot. *Journal of Fluid Mechanics*, Vol. 126, pp. 91-121.
- Leong, W.H., K.G.T. Hollands, and A.P. Brunger. 1998. On a physically-realizable benchmark problem in internal natural convection. *International Journal of Heat and Mass Transfer*, Vol. 41, pp. 3817-3828.
- Lide, D.R. 1993. *Handbook of Chemistry and Physics*, 73<sup>RD</sup> edition. Florida: CRC Press.
- Linthorst, S.J.M. 1985. *Natural convection suppression in solar collectors*. Ph.D. thesis. Delft: Applied Physics Department, Delft University of Technology.
- Mills, A.F. 1995. *Heat and mass transfer*. Chicago: Richard D. Irwin Inc.
- Mitchell, R., C. Kohler, D. Arasteh, E. Finlayson, C. Huizenga, D. Curcija, and J. Carmody. 2000. THERM 2.1 NFRC simulation manual. Berkeley: Lawrence Berkeley National Laboratory.
- NBC 1969. Norwegian building code (in Norwegian). *Forskrifter om bygg av 1. august 1969*. Oslo: GRØNDAHL & SØN.

- NBC 1987. Norwegian building code (in Norwegian). *Byggeforskrift av 27. mai 1987 nr. 458 med endringer, sist av 21. desember 1988 nr. 1144*. Oslo: GRØNDAHL & SØN.
- NBC 1997. Norwegian building code (in Norwegian). *Forskrift om krav til byggverk og produkter til byggverk. Tekniske forskrifter til plan- og bygningsloven av 14. juni 1985 nr. 77*.
- Ostrach, S. 1972. Natural convection in enclosures. In: *Advances in heat transfer* (J.P. Hartnett and T.F. Irvine Jr, editors), Vol. 8, pp. 161-227. New York: Academic Press.
- Ostrach, S. 1988. Natural convection in enclosures. *Journal of Heat Transfer*, Vol. 110, pp. 1175-1190.
- Pavlovic, T. and A. Ignatiev. 1986. Optical and microstructural properties of anodically oxidized aluminum. *Thin solid films*, Vol. 138, pp. 97-109.
- Raithby, G.D., K.G.T. Hollands and T.E. Unny. 1977. Analysis of heat transfer by natural convection across vertical fluid layers. *Journal of Heat Transfer. Transactions of the ASME*, Vol. 99, pp. 287-293.
- Raithby, G.D. and K.G.T. Hollands. 1985. Natural convection. In: *Handbook of heat transfer fundamentals, Second Edition* (W.M. Rohsenow, J.P. Hartnett. and E.N. Ganic, editors), pp. 6.1-6.94. New York: McGraw-Hill Book Company.
- Raithby, G.D. and K.G.T. Hollands. 1998. Natural convection. In: *Handbook of heat transfer, Third edition* (W.M. Rosenhow, J.P. Hartnett. and Y.I. Cho, editors), pp. 4.1-4.99. New York: McGraw-Hill Book Company.
- Roth, H. 1998. *Comparison of thermal transmittance calculation methods based on ASHRAE and CEN/ISO standards*. Master of Science Thesis. Massachusetts: Department of Mechanical and Industrial Engineering, University of Massachusetts Amherst.
- Schrey, A.-C., R.A. Fraser, and P.F. de Abreu. 1998. Local heat transfer coefficients for a flush-mounted glazing unit. *ASHRAE Transactions*, Vol. 104, pp. 1207-1221.
- Sen, S. and A. Sarkar. 1995. Effects of variable property and surface radiation on laminar natural convection in a square enclosure. *International Journal of Numerical Methods in Heat and Fluid Flow*, Vol. 5, pp. 615-627.
- Shewen, E., K.G.T. Hollands, and G.D. Raithby. 1996. Heat transfer by natural convection across a vertical air cavity of large aspect ratio. *Journal of Heat Transfer. Transactions of the ASME*, Vol. 118, pp. 993-995.
- Shiralkar, G.S. and C.L. Tien. 1981. A numerical study of laminar natural convection in shallow cavities. *Journal of Heat Transfer. Transactions of the ASME*, Vol. 103, pp. 226-231.
- Siegel, R. and J.R. Howell. 1992. Thermal radiation heat transfer. New York: Taylor and Francis.
- Smart, D.R., K.G.T. Hollands, and G.D. Raithby. 1980. Free convection heat transfer across rectangular-celled diathermanous honeycombs. *Journal of Heat Transfer. Transactions of the ASME*, Vol. 102, pp. 75-80.

Smith, D.Y., E. Shiles, and M. Inokuti. 1985. The optical properties of metallic aluminium. In: *Handbook of Optical Constants of Solids* (E.D. Palik, editor), pp. 369-406. Orlando: Academic Press Inc.

Standaert P. 1984. Thermal evaluation of window frames by the finite difference method. In: *Proceedings of Windows in Building Design and Maintenance*. Stockholm: Swedish Council for Building Research.

Svendsen, S., K. Duer, and P. Noyé. 2000. *Calculating the heat transfer coefficient of frame profiles in aluminum*. Sagsrapport SR-0023. Lyngby: Department of Buildings and Energy, Technical University of Denmark.

TAA 1994. *Aluminum Design Manual 1994*. Washington: The Aluminum Association Inc.

Tian, Y.S. and T.G. Karayiannis. 2000. Low turbulence natural convection in an air filled square cavity. Part I: the thermal and fluid flow fields. *International Journal of Heat and Mass Transfer*, Vol. 43, pp. 849-866.

Touloukian, Y.S. and D.P. DeWitt. 1970. *Thermal radiative properties, vol. 7, metallic elements and alloys*. Thermophysical Properties Research Center of Purdue University, Data Series. Plenum Publishing.

Touloukian, Y.S. and D.P. DeWitt. 1972. *Thermal radiative properties, vol. 8, nonmetallic solids*. Thermophysical Properties Research Center of Purdue University, Data Series. Plenum Publishing.

Touloukian, Y.S., D.P. DeWitt, and R.S. Hernicz. 1972. *Thermal radiative properties, vol. 9, coatings*. Thermophysical Properties Research Center of Purdue University, Data Series. Plenum Publishing.

VDI-Wärmeatlas 1997. *VDI-Wärmeatlas, Berechnungsblätter für den Wärmeübergang*. VDI-Gesellschaft Verfahrenstechnik und Chemie-ingenieurwesen. Springer.

Wicona 1998a. *WICTEC Profile, Beschläge, Zubehör. Program 98/99*. Ulm: WICONA Bausysteme GmbH.

Wicona 1998b. *WICLINE/WICSTYLE/WICSLIDE Profile, Beschläge, Zubehör. Program 98/99*. Ulm: WICONA Bausysteme GmbH.

Wright, J. 1996. A correlation to quantify convective heat transfer between vertical window glazings. *ASHRAE Transactions*, Vol. 102, pp. 940-946.

Yin, S.H., T.Y. Wung, and K. Chen. 1978. Natural convection in an air layer enclosed within rectangular cavities. *International Journal of Heat and Mass Transfer*, Vol. 21, pp. 307-315.

Zhao, Y., D. Curcija, and W.P. Goss. 1997. Prediction of the multicellular flow regime of natural convection in fenestration glazing cavities. *ASHRAE Transactions*, Vol. 103.

Zhao, Y. 1998. *Investigation of heat transfer performance in fenestration system based on finite element methods*. Ph.D. dissertation. Massachusetts: Department of Mechanical and Industrial Engineering, University of Massachusetts Amherst.

Zhong, Z.Y., K.T. Yang, and J.R. Lloyd. 1985. Variable property effects in laminar natural convection in a square enclosure. *Journal of Heat Transfer. Transactions of the ASME*, Vol. 107, pp. 133-138.

# Paper I

Three-Dimensional Conjugate Computational Fluid Dynamics Simulations of Internal Window Frame Cavities Validated Using Infrared Thermography

*ASHRAE Transactions* 2001, Vol. 107, Pt. 2

Arild Gustavsen, Brent T. Griffith, and Dariush Arasteh



# Three-Dimensional Conjugate Computational Fluid Dynamics Simulations of Internal Window Frame Cavities Validated Using Infrared Thermography

Arild Gustavsen,<sup>\*</sup> Brent T. Griffith,<sup>+</sup> and Dariush Arasteh<sup>+</sup>

---

## ABSTRACT

*This paper studies the effectiveness of one commercial Computational Fluid Dynamics (CFD) program for simulating combined natural convection and heat transfer in three dimensions for air-filled cavities similar to those found in the extruded frame sections of windows. The accuracy of the conjugate CFD simulations is evaluated by comparing results for surface temperature on the warm side of the specimens to results from experiments that use infrared (IR) thermography to map surface temperatures during steady-state thermal tests between ambient thermal chambers set at 0 and 20 °C. Validations using surface temperatures have been used in previous studies of two-dimensional simulations of glazing cavities with generally good results. Using the techniques presented and a non-contact infrared scanning radiometer we obtained surface temperature maps with a resolution of 0.1 °C and 3 mm and an estimated uncertainty of  $\pm 0.5$  °C and  $\pm 3$  mm. Simulation results are compared to temperature line and contour plots for the warm side of the specimen. Six different cases were studied, including a simple square section in a single vertical cavity and two four-sided frame cavities as well as more complex H- and U-shaped sections. The conjugate CFD simulations modeled the enclosed air cavities, the frame section walls, and the foam board surround panel. Boundary conditions at the indoor and outdoor air/solid interface were modeled using constant surface heat-transfer coefficients with fixed ambient-air temperatures. In general, there was good agreement between the simulations and experiments although the accuracy of the simulations is not explicitly quantified. We conclude that such simulations are useful for future evaluations of natural convection heat transfer in frame cavities.*

---

<sup>\*</sup> Department of Building and Construction Engineering, Norwegian University of Science and Technology, Alfred Getz v. 3, N-7491 Trondheim, Norway.

<sup>+</sup> Building Technologies Department, Environmental Energy Technologies Division, Ernest Orlando Lawrence Berkeley National Laboratory, Berkeley CA, USA.

## INTRODUCTION

Considerable research effort has been made during recent decades on improving calculation and measurement procedures for predicting the thermal performance of building envelope components such as windows, doors, and walls (see e.g. ElSherbiny et al. 1982, Wright and Sullivan 1994, Shewen et al. 1996, Griffith et al. 1998, Carpenter and McGowan 1998 and Larsson et al. 1999). This research has resulted in some standardized methods of measuring and calculating the thermal performance of building components and in new computer simulation programs that can be used on a routine basis (e.g. Finlayson et al. 1998 and EE 1995). These computer programs can often substitute for more expensive experiments; however, to be sure that these programs accurately predict the thermal properties, it is necessary to validate them using results from physical tests and research simulations.

Historically, the thermal performance parameter of interest has been the thermal transmittance or U-factor because it is used to size the loads that a building heating and cooling system must address. Thus, the traditional method of verifying computer programs is to compare calculated U-factors with measured values. This way of validating the computer programs makes use of one single aggregate parameter (total heat flow), and therefore does not offer scientists sufficient detail to verify that calculations are correct. Relying only on the thermal transmittance coefficient means that temperature gradients on the surface of the specimen not are taken into account.

Another way of verifying the accuracy of computer simulations of heat transfer is to compare them to measured results for surface temperature. Using infrared (IR) thermography allows the researchers to gather many temperature data for the surface of a specimen. Scientists using the traditional approach could use thermocouples to gather temperature data, but this approach does not give temperature data with the high spatial resolution as infrared thermography data. Both the U-factors and the infrared thermography approaches have been used previously to verify computer codes and computer simulations (see e.g. Carpenter and Elmahdy 1994, Sullivan et al. 1996, and Griffith et al. 1998).

In this study we assess the usefulness of a commercially available Computational Fluid Dynamics (CFD) computer program for simulating geometries typically found in buildings, such as window frames with internal cavities (e.g., aluminum and vinyl frame sections). The simulations modeled combine fluid flow and heat transfer in three dimensions inside cavities similar to those found in a vinyl frame section. A previous investigation of conjugate CFD models that compared results for two-dimensional models of glazing cavities to infrared

thermographic measurements showed generally good agreement (Sullivan et al. 1996). Both in that study and in the current one, conjugate CFD techniques were used to model an enclosed air cavity, and the warm side and cold side surfaces were modeled using constant heat-transfer coefficients and a fixed ambient-air temperature. Measured data were collected using infrared thermography to map surface temperatures on the warm side of specimens during steady-state thermal tests between 0 and 20 °C.

## SPECIMENS

Six different frame cavity specimens were measured and modeled. Although each specimen can be thought of as either a complete window frame or a component of a complete window frame, the sections used were not actual window frames but rather standard and custom vinyl extrusions. The sizes of the profiles in cross section were chosen to span the range of internal cavity sizes generally found in window frames. The simple shapes of the profiles were chosen to limit the complexity of the CFD model, and to allow us to better understand the natural convection effects found in the experiments and simulations. Because the maximum reasonable size of a specimen that can be tested in the Infrared Thermography Laboratory (IRLab) at Lawrence Berkeley National Laboratory (LBNL) is approximately 0.9 m by 0.9 m, we used specimens with a maximum area of 0.8 m by 0.8 m. This size limitation helped to ensure homogenous boundary conditions across the full width of the specimen. Polyvinyl chloride (PVC) was used to form the cavities so that larger temperature gradients could develop on the surface compared to those that would be found with a higher-conductivity frame material such as aluminum.

The specimens are listed in Table 1 along with their dimensions and testing orientation. The Rayleigh numbers listed in Table 1 are maximums that were calculated based on the size of the inner cavity for the extreme case where the temperature difference is 20 °C. Figure 1 diagrams the cross sections of the different frame geometries; from left to right we see the one-inch section, two-inch section, the two-inch H-section and the two-inch U-section.

Table 1. Specimen descriptions

Description	1-inch square frame 	2-inch square frame 	Vertical, 2-inch section 	Vertical, 2-inch H-section 	Vertical 2-inch U-section 	Horizontal 2-inch U-section 
Orientation during test	entire frame	entire frame	vertical	vertical	vertical	horizontal
Overall height (mm)	800	800	800	640	580	49.8
Overall width (mm)	800	800	50.8	49.8	49.8	580
Outer size of cross-section (mm)	25.4	50.8	50.8	49.8	49.8	49.8
Outer depth of frame section (mm)	25.4	50.8	50.8	48.4	50.8	50.8
Wall thickness (mm)	2.0	2.0	2.0	2.0	2.0	2.0
Size of inner cavity (maximum length in heat flow direction) (mm)	21.4	46.8	46.8	44.4	46.8	46.8
H/L aspect ratio	37.2 / 1	17.0 / 1	17.1	14.4	12.4	0.98
W/L aspect ratio	1 / 37.2	1 / 17.0	1	N/A	N/A	N/A
Maximum Rayleigh number, $Ra_{max}$	$2.4 \times 10^4$	$2.5 \times 10^5$	$2.5 \times 10^5$	$2.2 \times 10^5$	$2.5 \times 10^5$	$2.5 \times 10^5$

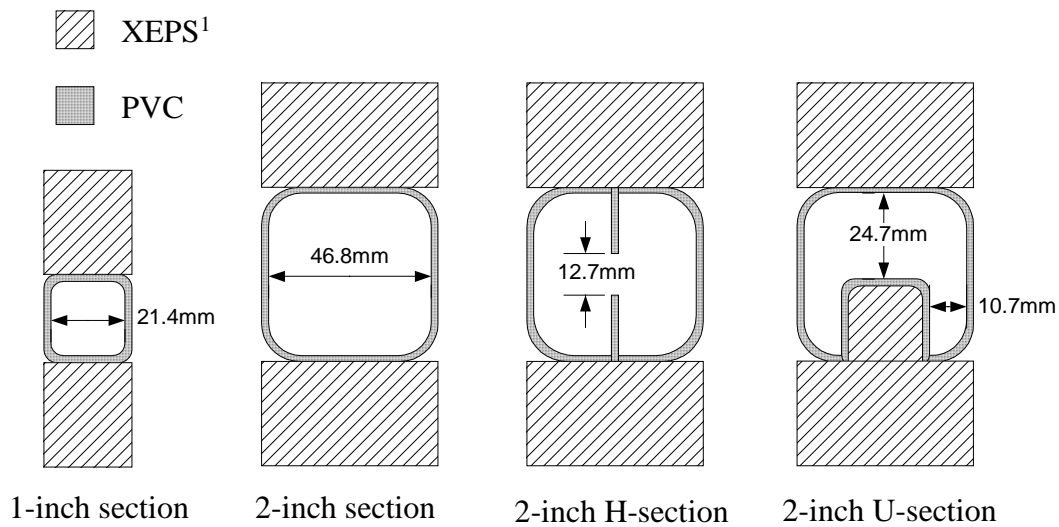


Figure 1. Schematic of cross sections for one-inch, two-inch, two-inch H and two-inch U-section specimens.

### Specimen Mounting

The specimens were mounted in foam board surround panels for thermal testing. The CFD simulation focused on only the frame cavities, so the mounting was designed to match the boundary conditions of the model rather than the configuration found in a real window.

<sup>1</sup> XEPS = extruded polystyrene

The one-inch specimen was mounted in 25.4-mm-thick extruded polystyrene (XEPS) foam board, and the two-inch-thick specimens were mounted in 50.8-mm-thick XEPS. Figure 2 shows how the frame sections were sealed to the surround panel to eliminate air infiltration. On the warm side of the test specimen, the small cavity created by the rounded edge of the frame section was filled with silicone sealant to make the surface flat. On the cold side, the joint was sealed using pressure-sensitive vinyl tape that was carefully applied to limit pockets of trapped air. The square frames were assembled much like complete window frames with a continuous air cavity around all four sides, as shown in Figure 3. Instead of a glazing unit, the frames were filled with XEPS of the same thickness as the profiles themselves. The area covered by each frame was 0.8 m by 0.8 m. For the three vertical tests, single lengths of a frame section were mounted vertically so that the long axis of the cavity was oriented parallel to gravity and perpendicular to heat flow. For the horizontal test, a single length of the frame section was mounted horizontally so that the long axis of the cavity was oriented perpendicular to gravity and perpendicular to heat flow. The warm-side surface of each specimen was painted to ensure a uniform surface emittance of 0.9. Location markers (thin aluminum strips, 3 mm by 50 mm) were attached to the surface of the surround panel to allow us to identify locations in the infrared images so we could relate image pixels to spatial coordinates.

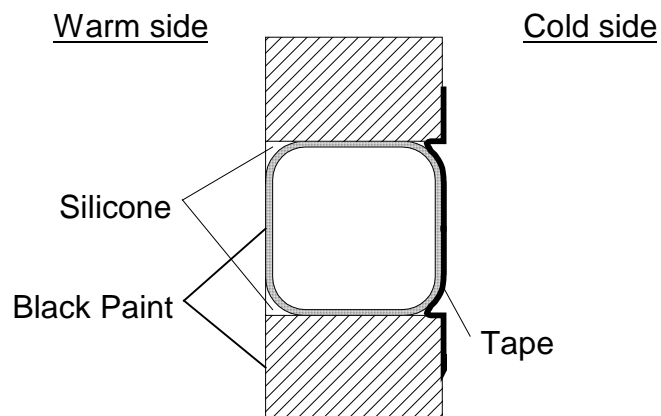


Figure 2. Schematic of air sealing techniques for thermal testing.

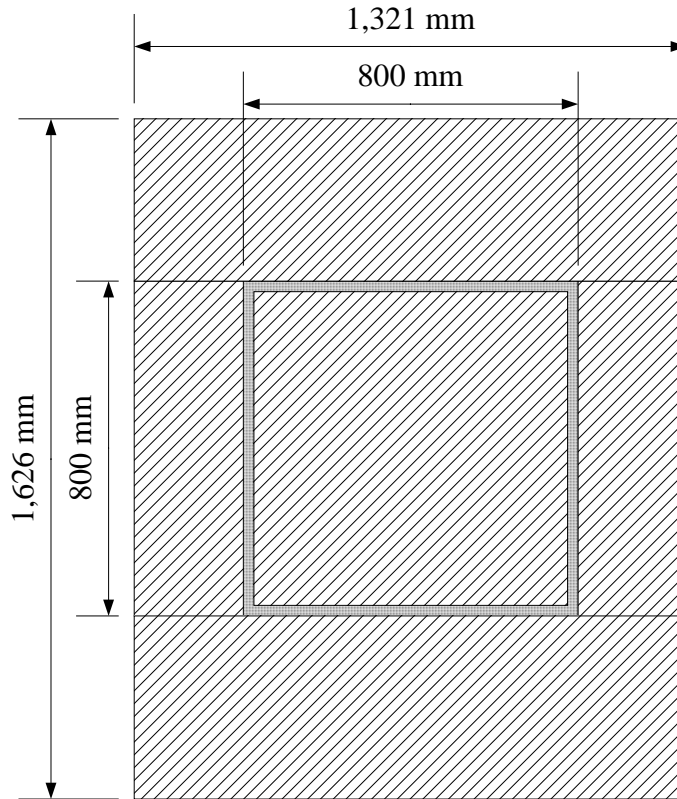


Figure 3. Mounting of entire frame specimen in the XEPS surround panel; the figure is drawn for the dimensions of the one-inch square frame specimen.

## EXPERIMENTS

Thermal testing gathered measured data to compare to the results of simulations. Infrared thermography was used because this technique can collect, in a non-invasive fashion, surface temperature data with high spatial resolution. The equipment and procedures used to conduct these measurements at the IRLab have previously been described in the literature (Griffith and Arasteh 1999, Türlér et al. 1997, and Griffith et al. 1995). A summary is provided here for completeness.

### IR Box

The main apparatus used in the IRLab for thermal testing is the IR box, which generates steady-state heat flow through the test specimen. A specimen is mounted between a warm chamber (the thermography chamber) and a climate chamber, as shown in Figure 4. The climate chamber is used to simulate cold outdoor conditions, and the thermography chamber simulates normal indoor conditions. The IR box is similar to an ordinary hot box used to measure U-factor (described in ISO 1994) except that there is no baffle in the

thermography chamber. The baffle is removed so the IR imager can have a full view of the test specimen. The opening between the climate chamber and the thermography chamber is 1.2 m by 1.2 m.

**Thermal Conditions**

In the climate chamber the air flow is upward and parallel to the test specimen’s surface, with a baffle placed 10 cm from the surface of the test specimen. The entire air flow is routed through ducts that have nearly constant cross-section size and rounded corners where the wind changes direction (see Figure 4). The absolute air speed is about 3.0. m/s but depends on chamber operation and specimen geometry.

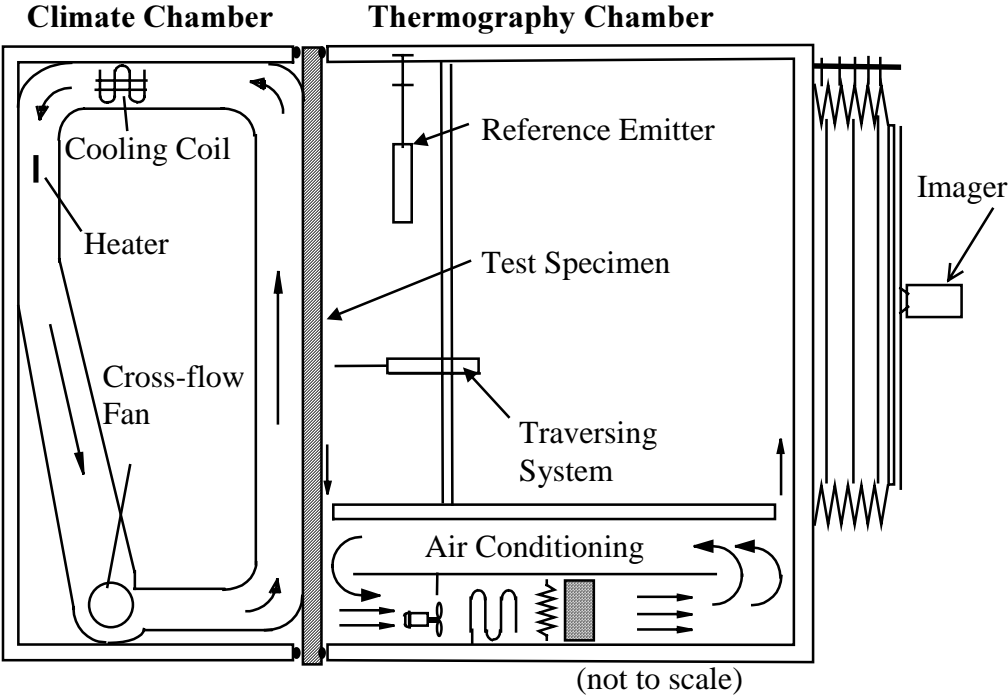


Figure 4. Figure of IR box used to generate steady-state heat flow through test specimen

The thermography chamber allows an IR imager to measure the surface temperature of the specimen while air temperature and velocity are controlled and measured on the warm side of the specimen under uniform thermal radiation conditions. The thermography chamber’s outer size is 1.4 m wide and 2.1 m high; the depth can vary from 0.9 to 4.2 m; bellows is used to vary the depth of the chamber, and the full depth is used to capture a full-size image of a test specimen. Air circulation is controlled in a recirculation zone within the chamber subfloor. A 50-mm-wide slot runs across the entire width of the subfloor at the edge beneath the specimen creating an air sink that drains cooler air running off the specimen into

the subfloor. At the opposite edge of the subfloor, a 40-mm-wide output slot introduces conditioned air at low velocity to the warm chamber.

During our experiments, we used ISO conditions (ISO 1998); the warm side bulk air temperature was controlled at 20 °C, and the cold-side bulk air temperature was controlled at 0 °C. Separate experiments were performed to characterize the performance of the IR box for the rates of surface heat transfer. A special test specimen, known as a calibrated transfer standard (CTS), was used to directly measure the rates of surface heat transfer or film coefficients. Although the exact film coefficients during a given test depend on the specimen, the CTS technique has been adopted to characterize and adjust the operation of a specific thermal test facility (ASTM 1199). A CTS is a large-area heat flux transducer that consists of two sheets of glass sandwiching an expanded polystyrene (EPS) foam core. The CTS used here measures 914 mm high by 610 mm wide and 23.1 mm thick. It is instrumented with 12 pairs of thermocouples situated at the interface between foam and glass that are used to measure the temperature difference across the foam. The thermal conductivity of the foam is characterized separately so that the total heat flow through the specimen can be determined. From the total heat flow and the conductivity of the glass, the surface temperatures at the interfaces between glass and air are determined. Overall surface heat transfer coefficients are then determined using averaged values for surface temperatures, the total heat flow, and the bulk air temperatures. See the test method (ASTM 1199) for a more complete description of the data reduction methods. The overall surface heat-transfer coefficient for the cold side was measured at  $26 \pm 5 \text{ W/m}^2\text{K}$ . The overall surface heat-transfer coefficient for the warm side was measured at  $7.9 \pm 0.4 \text{ W/m}^2\text{K}$ .

## Data Acquisition

The environmental chambers are controlled and monitored by a computer-based data acquisition system. Data noted include air temperature and velocity, specimen surface temperature, and relative humidity. These data are used to ensure stable environmental conditions. The computer-based system can also be used to measure the surface temperature in the more traditional way by means of thermocouples attached directly to the specimen. This added measurement technique is useful for measuring the temperature on the back side of the specimen (the side of the specimen facing the climate chamber) and also to verify the thermal imaging results. A traversing system can be used for measurement of air temperature and velocity.

## Infrared Measurements

The thermal imager captures test specimen surface temperature data on the warm side of the specimen and is mounted either inside or outside the chamber. A typical measurement setup is shown in Figure 5. A reference emitter and a background mirror are used to achieve uncertainties of about  $\pm 0.5$  °C (Griffith and Arasteh 1999). The measurement and calculation procedures are described below.

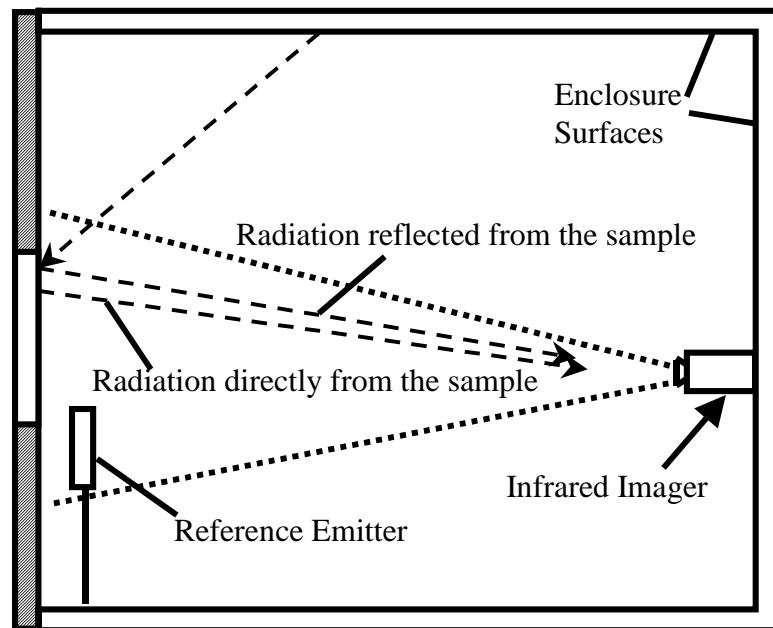


Figure 5. A typical thermography setup

## Determining Surface Emissivity

The emissivity of the samples being measured is important in IR thermography because it has a direct bearing on the strength and spectral distribution of radiation leaving the surface which is the item being measured and in turn being interpreted to estimate surface temperature. Emissivity values found in standard tables are not employed because they might be different from the value found within the spectral range of the imager. Thus, the emissivity of a sample is measured in a separate experiment, in which the sample is compared to another material with a known emissivity,  $e_{ref}$ . Thin samples from both materials are mounted on an isothermal plate that has a temperature 10 to 20 °C above or below the background temperature to insure high contrast between the radiation from the specimens and from the background. Next, the background compensation in the infrared imager software (Bales 1993) is turned off by setting the emissivity to 1.0. Both samples are then imaged simultaneously. Readings are averaged both over time and space to find the equivalent

blackbody temperature of the sample,  $T_{e=1,smpl}$  [K], and the equivalent blackbody temperature of the known reference material,  $T_{e=1,ref}$  [K]. Also, an equivalent blackbody temperature,  $T_{back}$  [K], for the background environment is found by using a background mirror (which reflects the background radiation). The emissivity of the sample,  $e_{smpl}$ , is then calculated from (Griffith and Arasteh 1999):

$$e_{smpl} = \frac{T_{e=1,smpl}^4 - T_{back}^4}{T_{e=1,ref}^4 - T_{back}^4} \cdot e_{ref} \quad (1)$$

## Determining the Infrared Temperature

The temperature of the specimen is found by averaging a number of consecutive IR images, usually 16, giving us  $T_{e=1}$  [K]. The subscript  $e = 1$  is a result of setting the emissivity to 1 in the thermography software before taking the images. Each image can consist of 1,024 by 768 data points (the usual resolution is about 500 by 500), and each point represents the temperature of a given point on the surface of the test specimen. Two types of views are possible: close-ups showing only parts of the specimen in the picture and complete shots with the entire specimen in one picture. Once the specimen has been measured, we attach a background mirror to it and capture and average a new set of 16 images, giving us  $T_{back}$  [K] (still with the emissivity set to 1). The background mirror is used to correct the previously measured temperature for background radiation. The mirror is kept small to lessen the effect of reduced surface emissivity on the overall thermal situation. From the above procedure we calculate the infrared specimen temperature  $T_{IR}$  [K] (Türler et al. 1997)

$$T_{IR} = \left( \frac{T_{e=1}^4 - (1 - e_{surf}) \cdot T_{back}^4}{e_{surf}} \right)^{1/4}, \quad (2)$$

where  $e_{surf}$  is the previously measured emissivity of the sample. If the camera had been perfectly calibrated and no drift was expected with time,  $T_{IR}$  could be the final result. However, the uncertainty of using the above approach is normally  $\pm 2$  °C; therefore, we use a reference emitter to increase our accuracy (see next paragraph). The IR temperature can be calculated point by point (using values of  $T_{back}$  and  $T_{e=1}$  from the same location) or by using a mean value of the background temperature,  $T_{back}$ , for the entire sample. The type of approach used is determined by the complexity of the specimen surface.

## Correcting the Infrared Temperature Using a Reference Emitter

To correct for drift and uncertainties in the infrared imager, we use a reference emitter. The reference emitter is a temperature-controlled device with a known surface emissivity. During each measurement, the reference emitter is situated near the specimen being measured and within the field of view of the infrared imager. The reference emitter is kept relatively in focus while the imager is focused on the test specimen. The infrared temperature of the reference emitter,  $T_{IR,ref}$ , is compared to a direct contact measurement,  $T_{DC,ref}$ , and the deviation is used to scale the infrared results for the test specimen,  $T_{IR,smpl}$ , to find the temperature  $T$ :

$$T = T_{IR,smpl} - (T_{IR,ref} - T_{DC,ref}) \quad . \quad (3)$$

The reference emitter is designed and placed so that its presence interferes minimally with air temperature and flow along the specimen.

## NUMERICAL CALCULATIONS

A commercial computational fluid dynamics (CFD) program was used for the numerical part of this study (Fluent 1998). This program is for modeling fluid flow and heat transfer in complex geometries and uses a control-volume-based technique to solve the governing equations.

### Mathematical Model

The governing equations for the system can be written using different notations. Here, we write the equations for a transient, three-dimensional and incompressible problem. In Table 1, we see that the maximum Rayleigh number,  $Ra_{max}$ , for the vertical, one-inch section is close to the laminar/turbulence limit. Flow changes from laminar to turbulent near  $Ra = 2 \times 10^4$  for two-dimensional cavities where  $H/L = 40$  (Yin et al. 1978). However, the temperature difference between the internal walls of the cavity is likely to be smaller than 20 °C, which is the temperature difference used for calculating the maximum Rayleigh number, so the real Rayleigh number is lower. In addition, the turbulence limit is probably higher than  $Ra = 2 \times 10^4$  for a three-dimensional vertical square cavity than for a two-dimensional cavity because of the added restriction imposed on the flow by the narrowness of the cavity. We therefore assume laminar flow. Further we omit viscous dissipation and only consider transport of "one gas," air. We assume that all air properties are constant (that is, the conductivity,  $k$ , specific heat capacity,  $c_p$ , and dynamic viscosity,  $\mu$ , are constant). We also assume that the density,  $\rho$ ,

is constant, except in the buoyancy term in the  $y$ -momentum equation where we use the Boussinesq approximation. The equation for conservation mass can be written as

$$\frac{\partial \rho}{\partial t} + \frac{\partial}{\partial x}(\rho u) + \frac{\partial}{\partial y}(\rho v) + \frac{\partial}{\partial z}(\rho w) = 0 \quad , \quad (4)$$

where  $u$ ,  $v$ , and  $w$  are the velocities in the  $x$ ,  $y$ , and  $z$  directions, respectively, and  $t$  is the time variable. The momentum equations take the following form:

$$\begin{aligned} \frac{\partial u}{\partial t} + \frac{\partial}{\partial x}(\rho uu) + \frac{\partial}{\partial y}(\rho vu) + \frac{\partial}{\partial z}(\rho wu) \\ = -\frac{\partial p}{\partial x} + \frac{\partial}{\partial x}\left(\mu \frac{\partial u}{\partial x}\right) + \frac{\partial}{\partial y}\left(\mu \frac{\partial u}{\partial y}\right) + \frac{\partial}{\partial z}\left(\mu \frac{\partial u}{\partial z}\right) \end{aligned} \quad (5)$$

$$\begin{aligned} \frac{\partial v}{\partial t} + \frac{\partial}{\partial x}(\rho uv) + \frac{\partial}{\partial y}(\rho vv) + \frac{\partial}{\partial z}(\rho wv) \\ = -\frac{\partial p}{\partial y} + \frac{\partial}{\partial x}\left(\mu \frac{\partial v}{\partial x}\right) + \frac{\partial}{\partial y}\left(\mu \frac{\partial v}{\partial y}\right) + \frac{\partial}{\partial z}\left(\mu \frac{\partial v}{\partial z}\right) - \rho g \beta (T - T_r) \end{aligned} \quad (6)$$

$$\begin{aligned} \frac{\partial w}{\partial t} + \frac{\partial}{\partial x}(\rho uw) + \frac{\partial}{\partial y}(\rho vw) + \frac{\partial}{\partial z}(\rho ww) \\ = -\frac{\partial p}{\partial z} + \frac{\partial}{\partial x}\left(\mu \frac{\partial w}{\partial x}\right) + \frac{\partial}{\partial y}\left(\mu \frac{\partial w}{\partial y}\right) + \frac{\partial}{\partial z}\left(\mu \frac{\partial w}{\partial z}\right) \end{aligned} \quad (7)$$

for the  $x$ ,  $y$ , and  $z$  directions, respectively. We calculate the buoyancy (or thermal expansion) coefficient,  $\beta$ , from  $\beta = 1/T_m$ ;  $g$  is gravity in the  $y$  direction, and  $p$  is static pressure. The expression for thermal expansion coefficient  $\beta$  is based on the perfect gas assumption. The energy equation can be written

$$\begin{aligned} \rho c_p \frac{\partial T}{\partial t} + \rho c_p \frac{\partial}{\partial x}(uT) + \rho c_p \frac{\partial}{\partial y}(vT) + \rho c_p \frac{\partial}{\partial z}(wT) \\ = \frac{\partial}{\partial x}\left(k \frac{\partial T}{\partial x}\right) + \frac{\partial}{\partial y}\left(k \frac{\partial T}{\partial y}\right) + \frac{\partial}{\partial z}\left(k \frac{\partial T}{\partial z}\right) + S_h \end{aligned} \quad (8)$$

$T$  is the air temperature, and  $S_h$  is an energy source that can be a result of radiation. In solid regions, the CFD program calculates conduction heat transfer from

$$\rho c_p \frac{\partial T}{\partial t} = \frac{\partial}{\partial x}\left(k \frac{\partial T}{\partial x}\right) + \frac{\partial}{\partial y}\left(k \frac{\partial T}{\partial y}\right) + \frac{\partial}{\partial z}\left(k \frac{\partial T}{\partial z}\right) + q''' \quad . \quad (9)$$

We use the Discrete Transfer Radiation Model (DTRM) to calculate radiation heat transfer inside the internal air cavities. This model assumes that a single ray can approximate the radiation leaving a surface element in a certain range of solid angles (see Figure 6), and that the surfaces are diffuse gray. The accuracy of the model is mainly limited by the number of rays traced and the computational grid. At each radiation face, rays are fired at discrete values of the zenith and azimuth angles. To cover the radiating hemisphere,  $\theta$  and  $\phi$  are varied from 0 to  $\pi/2$  and 0 to  $2\pi$ , respectively. Thus, the ray tracing technique used in DTRM can provide a prediction of radiation heat transfer between surfaces without the use of explicit view-factor calculations.

The radiation intensity approaching a point on a wall surface is integrated to yield the incident radiation heat flux,  $q_{in}$ , as

$$q_{in} = \int_{\mathbf{s} \cdot \mathbf{n} > 0} I_{in} \mathbf{s} \cdot \mathbf{n} d\Omega \quad , \quad (10)$$

where  $\Omega$  is the hemispherical solid angle,  $I_{in}$  is the intensity of the incoming ray,  $\mathbf{s}$  is the ray direction vector, and  $\mathbf{n}$  is the normal pointing out of the domain. The net radiation heat flux from the surface,  $q_{out}$ , is computed as a sum of the reflected portion of  $q_{in}$  and the emissive power of the surface

$$q_{out} = (1 - \varepsilon_w) q_{in} + \varepsilon_w \sigma T_w^4 \quad , \quad (11)$$

where  $T_w$  is the surface temperature of the point  $\mathbf{P}$  on the surface, and  $\varepsilon_w$  is the wall emissivity.

In our model we use three types of boundary conditions, the heat flux boundary condition (at adiabatic boundaries), the symmetry boundary condition and the convective heat transfer boundary condition. The CFD program assumes zero flux of all quantities across a symmetry boundary. That is, there is no convective flux and no diffusion flux across a symmetry plane: the normal velocity component at the symmetry plane is zero and the normal gradients of all flow variables are zero at the symmetry plane. For the convective boundary condition, the heat flux to the wall is calculated from

$$q'' = h_f (T_w - T_f) + q''_{rad} = h_{ext} (T_{ext} - T_w) \quad , \quad (12)$$

where  $h_f$  and  $h_{ext}$  are the fluid and external (warm and cold sides) heat transfer coefficients;  $T_w$ ,  $T_f$ , and  $T_{ext}$  are the wall, fluid, and external heat sink temperatures; and  $q''_{rad}$  is the radiative heat flux.

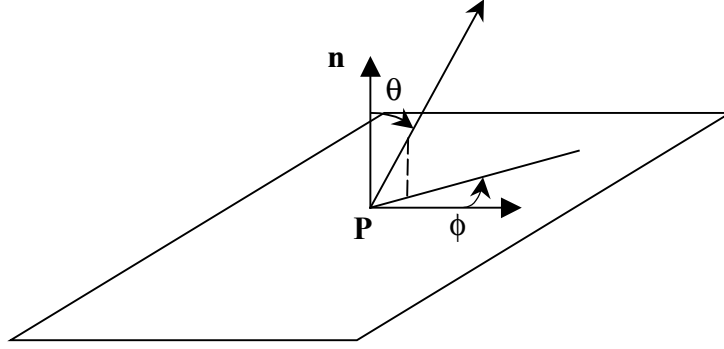


Figure 6. Angles  $\theta$  and  $\phi$  define the hemispherical solid angle about a point  $P$  on a boundary face.

## Numerical Method

The CFD program uses a control-volume-based technique to convert the governing equations above to algebraic equations that can be solved numerically (Fluent 1998). The control-volume technique consists of integrating the governing equations about each control volume, which yields discrete equations that conserve each quantity on a control-volume basis. That is, the complete geometry is divided into small control volumes for which the discretized equations are solved. We used the program's segregated solver with double precision to solve the discretized equations. The segregated solver solves the different equations sequentially. After discretization, the conservation equation for a general variable  $\phi$  at cell  $P$  can be written as

$$a_p \phi_p = \sum_{nb} a_{nb} \phi_{nb} + b \quad , \quad (13)$$

where the subscript  $nb$  refers to neighbor cells,  $a_p$  and  $a_{nb}$  are the linearized coefficients for  $\phi_p$  and  $\phi_{nb}$ , and  $b$  is the source term. These equations are solved using a Gauss-Seidel linear equation solver in conjunction with an algebraic multigrid method.

The discrete values are stored for the center of each cell. However, when solving the equations, we also need face values for the variables in the convection terms. For the energy and momentum variables, these are found by using the QUICK (Quadratic Upstream Interpolation for Convective Kinetics) scheme. In addition the CFD program uses central differences to approximate the diffusion terms and SIMPLEC (Semi-Implicit Method for Pressure-Linked Equations Consistent) to couple the interaction between pressure and velocity. The CFD program also has to use a pressure-interpolation scheme to find the pressure values at the cell faces. This is necessary because the program stores the pressure values in the cell centers just as it does for the rest of the variables. We chose to use the

PRESTO (PREssure Staggering Option) scheme, which is like the staggered grid approach described by Patankar (1980). The PRESTO scheme is recommended for buoyancy flows and hexahedral meshes. Because the equations are non-linear, we use relaxation for some of the variables to avoid divergence.

Convergence is determined by checking the scaled residuals (Fluent 1998)

$$R^\phi = \frac{\sum_{cells P} \left| \sum_{nb} a_{nb} \phi_{nb} + b - a_p \phi_p \right|}{\sum_{cells P} \left| a_p \phi_p \right|}, \quad (14)$$

and ensuring that they are less than  $10^{-5}$  for all variables except for the energy equation in which the residuals have to be less than  $10^{-6}$ .

## Material Properties and Boundary Conditions

The material properties and the boundary conditions used during the numerical simulations are shown in Tables 2 and 3. Air properties were calculated at 10 °C. Surface film coefficients were selected from CEN (1998); note that these values are within the uncertainty ranges of the results obtained for the test chambers from measurements using a 13-mm foam core CTS.

Table 2. Material properties used in the computer simulations

Material	Emissivity	Thermal conductivity, (W/m-K)
PVC	0.9	0.17
Painted XEPS	0.9	0.03

Table 3. Boundary conditions used in the computer simulations

Surface	Temperature (°C)	Total surface film coefficient (W/m <sup>2</sup> -K)
Warm Side	20	7.69
Cold Side	0	25

## MEASUREMENT AND SIMULATION CONSIDERATIONS

Because it is not practical to simulate every subtlety of the specimens, differences between the specimens and the computer models invariably arise. Characteristics of the experiments that were not directly modeled include: the use of silicone to seal and flatten the warm side surface, the presence of paint on the warm-side surface, and the use of vinyl tape on the cold-side to form an air seal between the specimen and the surround panel. For the difference between the simulated and measured profiles, we also know that silicone has about the same conductivity as PVC.

In Figure 1 we see that the edges of the frame sections are round; however, in the simulations we used square, orthogonal angles at these edges. The effect of this simplification was tested in a separate two-dimensional simulation that compared models with rounded (as tested) and square edges. We found that the total heat transfer through the different configurations changed by 0.2% and that the surface temperature data deviated by a maximum of 0.4 °C. The biggest difference in temperature was found right above the place where the simplification in edge shape was made. For the other places the difference was much smaller.

Symmetry boundary conditions were also used where possible to reduce the number of computational cells and to reduce computation time. Such an assumption could lead to exclusion of particular effects or modification of the "real" solution, but, as we will see later, this approach does not seem to have introduced additional error. The results section notes where the symmetry boundary condition was used.

## SENSITIVITY OF NUMERICAL PROCEDURE AND GRIDDING

We chose a hexahedral mesh for discretization of the different geometries. To ensure that the resolution in the discretization of the geometry was high enough, some grid sensitivity tests were performed. Some of these were not performed on the final geometries but on simpler sections that represent one part of the more complex geometries. This approach was chosen to limit the simulation time (some of the complete sections took several days to simulate). One test was performed on a two-dimensional high-aspect-ratio cavity ( $A = H/L = 40$ ) with two vertical isothermal walls separated by two horizontal adiabatic walls. We varied the grid density (using an equispaced grid, the same as used inside the air cavities in the frame models) both in the heat flow direction and in the vertical direction. We found that a mesh consisting of 25 nodes in the heat-flow direction and 200 nodes in the vertical direction was sufficient. Further refinement only resulted in minor changes in the Nusselt number (a mesh with  $45 \times 450$  nodes resulted in a change of Nusselt number by 1%). Using a mesh with  $25 \times 200$  nodes within the vertical part of the one-inch square frame, also results in a grid aspect ratio of 4.4, which is less than the suggested maximum value of 5 (Fluent 1998). One test was also performed on a three-dimensional, horizontal, two-inch section. The number of nodes was increased both within the solid materials and in the air cavity. The refinement resulted in a change of only 0.3% in the total heat-transfer through the test specimen. The boundary conditions in this test were identical to the boundary conditions in the final simulations.

We also tried to increase the number of rays traced in the radiation heat-transfer algorithm and found that doubling the number of rays in both directions only changed the

total heat transfer by 0.2% (with the other parameters left constant). Thus, for the radiation analysis, we used four separate  $\theta$  and  $\phi$  divisions in all the final simulations.

For high-aspect-ratio cavities such as those typically found in glazing, it is known that secondary (multicellular) flow can exist (see e.g. Zhao et al. 1997 or Wright and Sullivan 1994). Therefore we first wanted to check whether the CFD program was capable of simulating such a flow even though secondary flow does not necessarily exist for cavities with a low width ( $W$ ) to length ( $L$ ) aspect ratio. In Table 1 we see that the vertical aspect ratio of our samples ranges from approximately 17 to 37 and that the Rayleigh number can be within the multicellular regime (Zhao et al. 1997). Two different two-dimensional cases were tested, one cavity with an aspect ratio of 20 and another with an aspect ratio of 40. Both were simulated with a Rayleigh number of  $10^4$ , known to produce secondary flow. Multicellular flow resulted in both cases. The Nusselt numbers,  $Nu_{A=20} = 1.404$  and  $Nu_{A=40} = 1.256$ , were also close to what other investigators have found. ElSherbiny et al. (1982) found 1.404 and 1.240, respectively. In our simulations the cavity had two isothermal sidewalls separated by two horizontal adiabatic walls.

## RESULTS

The data from our experiments and simulations can be presented in several ways. Here, we look at both the temperature along vertical lines and the surface temperature in two-dimensional contour plots. The different line plot figures include schematics of the locations on the samples where the temperature data were collected. The absolute uncertainties in the measured data for Figures 7 through 12 are estimated to be  $\pm 0.5$  °C for temperature and  $\pm 3$  mm for the distance. Table 3 shows the number of nodes, number of iterations and final residuals for each simulated case. Additional details related to each case are noted below.

Table 3. Simulation summary. The table shows number of nodes, number of iterations, and sum of residuals in the final solution. For the two-inch square frame we did not find a steady-state solution, and used a transient solution procedure.

Description	Number of nodes	Energy residual	Momentum residual	Continuity residual
1-inch square frame	868,992	$2.6532 \times 10^{-9}$	$1.7090 \times 10^{-6}$	$9.8472 \times 10^{-6}$
2-inch square frame	868,992	N/A	N/A	N/A
Vertical, 2-inch section	238,000	$1.90 \times 10^{-10}$	$> 4.28 \times 10^{-8}$	$9.85 \times 10^{-6}$
Vertical, 2-inch H-section	310,320	$1.27 \times 10^{-10}$	$> 4.26 \times 10^{-8}$	$9.99 \times 10^{-6}$
Vertical, 2-inch U-section	506,440	$6.99 \times 10^{-6}$	$> 3.86 \times 10^{-10}$	$7.56 \times 10^{-8}$
Horizontal, 2-inch U-section	506,440	$7.02 \times 10^{-6}$	$> 4.18 \times 10^{-5}$	$1.53 \times 10^{-4}$

### Line Plots of Surface Temperature

Figure 7 shows the surface temperature along a line down the middle of the vertical, two-inch cavity. The vertical axis shows the distance from the bottom of the profile; 0 mm is at the bottom of the profile, and 800 mm is at the top. Above and below the specimen, data are plotted for the temperature of the foam surround panel in which the frame section was mounted. The horizontal axis shows the surface temperature in °C. The IR data were determined by averaging some data points on each vertical level to reduce the noise level in the data. However, because the temperature varies in the horizontal direction, the number of data points averaged were kept to a minimum (about 3 data points, equal to a length of approximate 5 millimeters). For the CFD simulation, a symmetry boundary condition was used along the middle of the PVC section.

Figure 8 shows the temperature of the middle part of the 640-mm-long two-inch H-section mounted vertically. The horizontal axis shows the temperature in degrees Celsius, and the vertical axis shows the location on the specimen surface in millimeters. The co-ordinate 0 is set to be at the bottom of the section. A symmetry boundary condition was used in the numerical simulation.

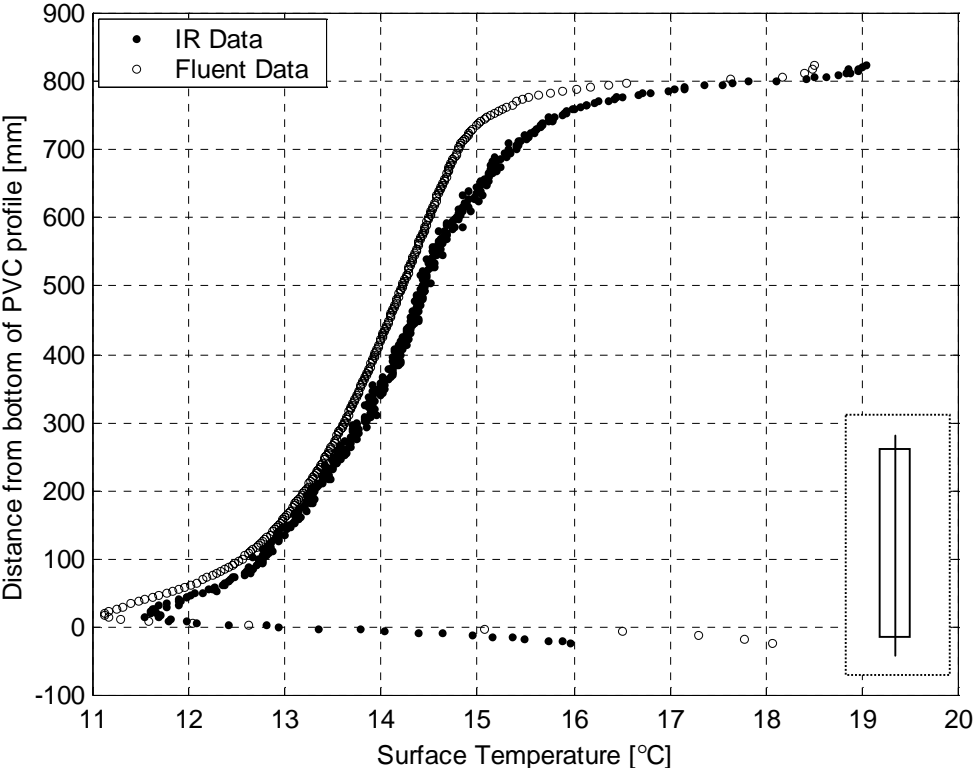


Figure 7. Surface temperature of vertical, two-inch cavity; experimental uncertainty is estimated to  $\pm 0.5$  °C (Griffith and Arasteh 1999).

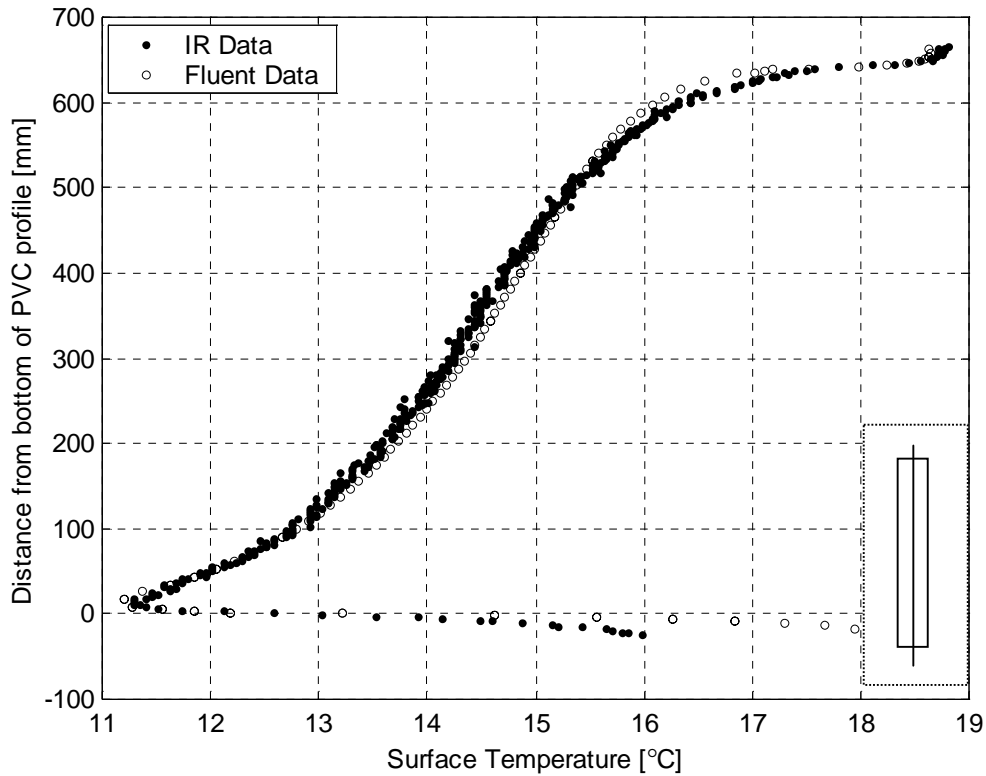


Figure 8. Surface temperature of the vertical, two-inch H-section; experimental uncertainty is estimated to  $\pm 0.5$  °C (Griffith and Arasteh 1999).

### Contour Plots of Surface Temperature

In Figure 9 we see contour plots of the surface temperature of the vertical, two-inch U-section shown to the right in Figure 1. The 580-mm-long profile was mounted vertically with the open part to the left. The vertical axis shows the accumulated distance from the bottom of the profile and the horizontal axis the distance from the left edge of the specimen. The units on both axes are millimeters. The plot to the left shows thermography results, and the plot to the right shows CFD results. The separate color bar to the right shows the relation between gray scale and temperature in degrees Celsius. In the numerical simulations for these sections, the scaled energy residuals did not decrease to  $10^{-6}$  but stopped at  $7 \times 10^{-6}$ . However, we still assume a converged solution because the heat transfer through the specimen converged to a constant level.

In Figure 10 we see the results for the same section described above but this time horizontally mounted with the open part of the cavity on the top. The dimensions on both axes are millimeters, and the lower left corner of the specimen has the co-ordinate (0,0). In the CFD simulation for this test specimen, we found that the residuals oscillated somewhat. That is the energy residual reduced to  $7 \times 10^{-6}$ , continuity to  $1.5 \times 10^{-4}$ , and the scaled x-, y-, and

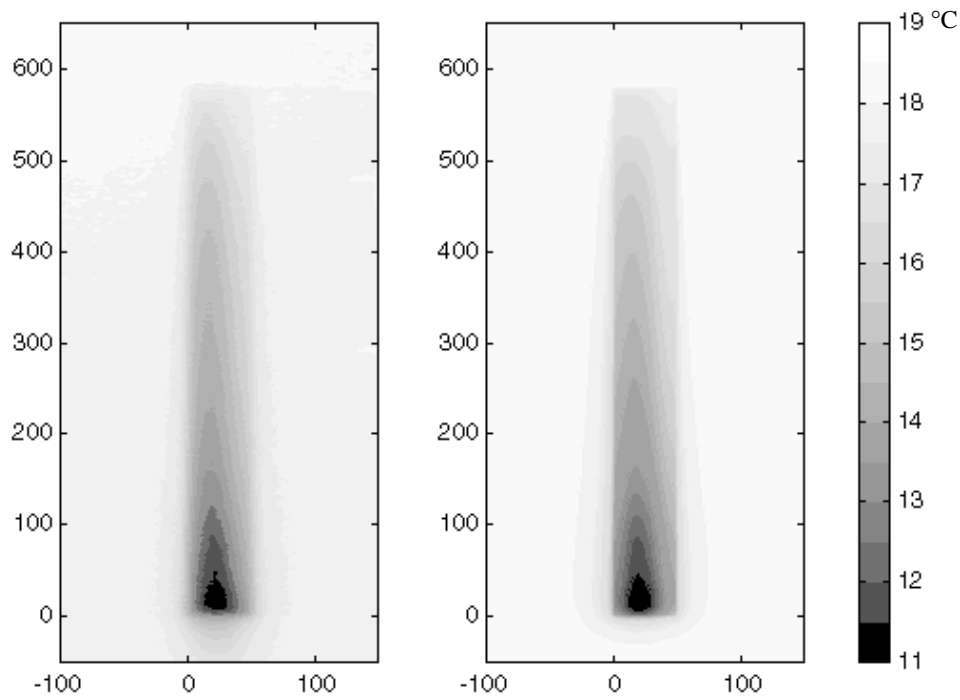


Figure 9. Contour plot of surface temperature for the two-inch U-section mounted vertically with the open side on the left. The plot on the left is from infrared measurements, and the plot on the right is from CFD simulations. The units for the horizontal and vertical axes are both millimeters. Experimental uncertainty is estimated to  $\pm 0.5$  °C (Griffith and Arasteh 1999).

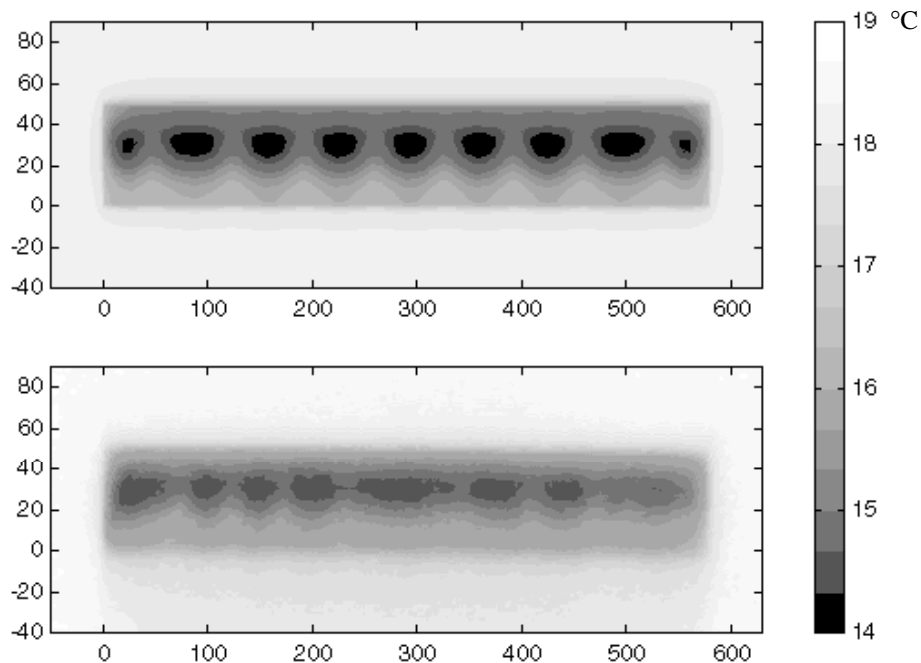


Figure 10. Surface temperature of the two-inch U-section mounted horizontally with the open side on the top; the top plot is from simulations, and the bottom is measured. Experimental uncertainty is estimated to  $\pm 0.5$  °C (Griffith and Arasteh 1999).

z-velocity residuals to less than  $5 \cdot 10^{-5}$ . The total heat flux through the test specimen and the XEPS panel varied between 11.7 and 11.9 W/m<sup>2</sup>K. Because no transient studies were conducted in the experimental part of this work, we did not pursue a transient numerical solution either (at this stage). The results were still included to show that such a flow pattern can exist within horizontal window frame geometries.

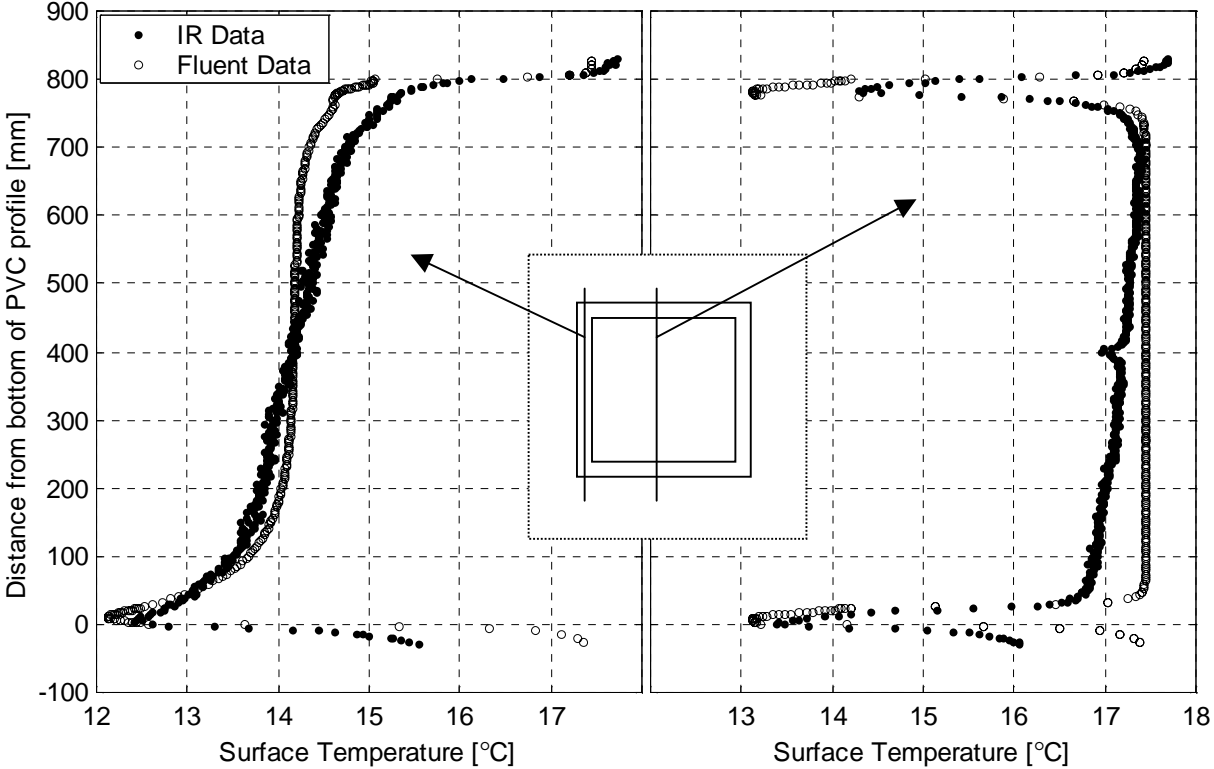


Figure 11. Surface temperature of the one-inch square frame; the left graphs show the temperature along the middle of the vertical part of the complete frame. The right graphs show the temperature along a vertical line down the middle of the frame. Experimental uncertainty is estimated to  $\pm 0.5$  °C (Griffith and Arasteh 1999).

### The One-Inch and Two-Inch Square Frames

Figures 11 and 12 show the temperature along different lines on the warm surfaces of the one-inch and two-inch square frames, respectively. In both the figures, the left graphs show the temperature along the middle of the vertical part of the complete frame. The graphs to the right show the temperature along a vertical line down the middle of the frames. The horizontal axis shows the temperature in degrees Celsius, and the vertical axis shows the distance from the bottom of the frame in millimeters. Symmetry boundary conditions were used for both sections. We had problems finding a converged solution for the two-inch square frame. After switching to a transient solution procedure, we found that the warm-side surface

temperature in the bottom corner not did change more than 0.01 °C, well within the uncertainty range of our experiments. The air temperature inside the cavity, in the bottom corner, oscillated between 4.64 and 5.28 °C. The heat flux through the frame seemed to converge against 46.56 W/m<sup>2</sup>.

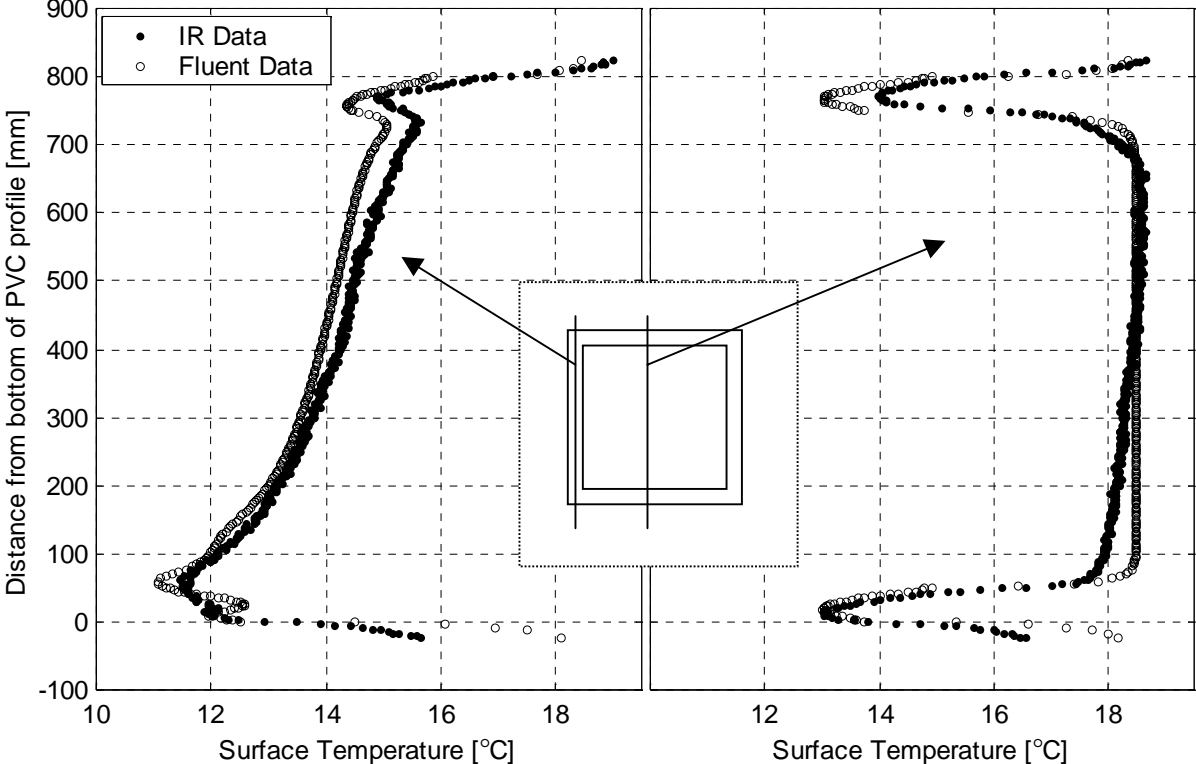


Figure 12. Surface temperature of the two-inch square frame; the left graphs show the temperature along the middle of the vertical part of the complete frame. The right graphs show the temperature along a vertical line down the middle of the frame. Experimental uncertainty is estimated to  $\pm 0.5$  °C (Griffith and Arasteh 1999).

## DISCUSSION

### Surface Temperature of Frame Sections

Both for the vertical, two-inch cavity, Figure 7, and the vertical, two-inch H-section, Figure 8, we see that there is good agreement between the results from the simulations and the experiments. Except for at the XEPS foam panel, the difference is less than the 0.5 °C uncertainty in the infrared measurements. For the foam panel we see that the CFD program predicts lower temperatures at the top than we found in the experiments. The most likely reason for this is that the foam panel over the test specimen does not have as low a temperature as required to create as high a convection heat-transfer coefficient as used in the

simulations. Thus, at the top, the total heat-transfer coefficient for the foam is less in the experiment than in the simulation. However, below the test specimen the situation is the opposite. We see that the temperature measured in the experiment is lower than the temperature generated by the simulation. This phenomenon is generally expected, arising from the use of fixed surface heat-transfer coefficients although, in reality, the convective portion of the total varies locally.

We also find good agreement between the measured and calculated temperatures for the vertical two-inch U-section shown in Figure 9. Just as for the cases discussed above, we find that the biggest difference is between the temperature on the XEPS foam panel below the sample.

Both the experimental and simulation results show an interesting and complex surface temperature pattern for the horizontal two-inch U-section (Figure 10). There appears to be a multicellular flow that the CFD simulation has done a fairly good job of predicting, as shown by the fairly good agreement in the scale and number of air-flow cells. There are three possible reasons for the difference between the numerical simulations and the IR thermography results. The first reason might be that there are differences between the simulated and the measured profile; the measured section had rounded corners and did not have perfectly equal dimensions throughout the length of the section. The second reason for the difference between the simulated and measured section might be transient behavior, and the third reason might be that the boundary conditions were different.

### Surface Temperature of One-Inch and Two-Inch Square Frame

There is more discrepancy between the measured data and the numerical data for the four-sided frames than for the other sections, especially for the upper part of the frames and for the foam insert. The experimental results show that the surface temperature of the foam insert decreases with decreasing distance from the bottom edge (valid for both frames). This is probably a result of variation in surface heat-transfer coefficient with height. An inconstant heat-transfer coefficient is probably also the reason for the temperature difference between the experimental and simulation results for the upper part of the frames. However, for the rest of the specimens, the agreement between the experiment and simulation results is good.

## CONCLUSION

We conclude that conjugate CFD simulations are useful for evaluating natural convection heat transfer in frame cavities. The CFD program was able to model combined

natural convection and heat transfer well enough for generally good agreement between simulated and measured surface-temperature results. Results for all three vertical cavity cases agreed within the measurement uncertainty. The horizontal U-section specimen displayed a complex multi-cellular flow; although some discrepancies between the measured results and the numerical simulations can be found, the simulation was able to produce a qualitative temperature pattern that matches the measurements. The four-sided frames showed the largest deviations between measurements and simulations.

Based on this work, we conclude that CFD simulations can be used to study convection effects in the internal cavities of window frames. To further increase the accuracy of these simulations, fluid flow would need to be simulated at the warm side and cold side surfaces of the frame sections. However, for the moment, because of the computer resources that such three-dimensional problems require, simulating both external and internal flows will likely be limited to two-dimensional models, especially for the complex realistic geometries found in real window frames.

Future research will study these and additional CFD results more in detail, seeking more insight into the convection effects that arise in complete window frames in contrast to those found in single vertical and horizontal cavities. A study of ways in which the conduction heat-transfer software tools in use today can be used to calculate the thermal performance of window frames with reasonable accuracy will also be performed.

## ACKNOWLEDGMENTS

This work was supported by Hydro Aluminum and the Assistant Secretary for Energy Efficiency and Renewable Energy, Office of Building Technology, State and Community Programs, Office of Building Systems of the U.S. Department of Energy under Contract No. DE-AC03-76SF00098.

## REFERENCES

- ASTM 1199. *ASTM C 1199, Standard test method for measuring the steady state thermal transmittance of fenestration systems using hot box methods*. Annual Book of ASTM Standards, Vol. 04.06. Philadelphia: American Society for Testing and Materials.
- Bales 1993. *The BSI TIP, Thermal image processor, Operator's manual*. Bales Scientific Inc., Walnut Creek Calif., USA.

- Carpenter, S.C. and A.H. Elmahdy. 1994. Thermal performance of complex fenestration systems. *ASHRAE Transactions* 100(2): 1179-1186.
- Carpenter, S.C. and A. McGowan. 1998. Three-dimensional heat transfer effects in building components. *ASHRAE Transactions* 104(1B): 1070-1076.
- CEN 1998. *prEN ISO 10077-2 - Thermal performance of windows, doors and shutters - Calculation of thermal transmittance - Part 2: Numerical method for frames*. Brussels: European Committee for Standardization.
- ElSherbiny, S.M., G.D. Raithby, and K.G.T. Hollands. 1982. Heat transfer by natural convection across vertical and inclined air layers. *Journal of Heat Transfer. Transactions of the ASME* 104, 96-102.
- EE (Enermodal Engineering). 1995. *FRAMEplus toolkit, version 4.0*. Kitchener, Ontario: Enermodal Engineering.
- Finlayson, E., R. Mitchell, D. Arasteh, C. Huizenga, and D. Curcija. 1998. *THERM 2.0: Program description. A PC program for analyzing the two-dimensional heat transfer through building products*. Berkeley, Calif.: University of California.
- Fluent 1998. *FLUENT 5 User's Guide*. Fluent Incorporated, Lebanon, UK.
- Griffith, B.T. and D. Arasteh. 1999. Buildings research using infrared imaging radiometers with laboratory thermal chambers. In *Proceedings of the thermosense XXI conference* (D.H. LeMieux. and J.R. Snell, editors). Vol. 3700: 502-513. The International Society for Optical Engineering.
- Griffith, B., D. Curcija, D. Türlér, and D. Arasteh. 1998. Improving computer simulations of heat transfer for projecting fenestration products: Using radiation view-factor models. *ASHRAE Transactions* 104(1B), 845-855.
- Griffith, B.T., F. Beck, D. Arasteh, and D. Türlér. 1995. Issues associated with the use of infrared thermography for experimental testing of insulated systems. In: *Thermal performance of the exterior envelopes of buildings VI*. Atlanta: American Society of Heating, Refrigeration and Air-Conditioning Engineers.
- ISO 1994. *ISO 8990 - Thermal insulation - Determination of steady-state thermal transmission properties - Calibrated and guarded hot box*. Geneva: International Organisation for Standardisation.

- ISO 1998. *Draft Standard ISO/DIS 12567 - Thermal performance of doors and windows - Determination of thermal transmittance by hot box method*. Geneva: International Organisation for Standardisation.
- Larsson, U., B. Moshfegh, and M. Sandberg. 1999. Thermal analysis of super insulated windows (numerical and experimental investigations). *Energy and Buildings* 29, 121-128.
- Patankar, S.V. (1980). *Numerical heat transfer and fluid flow*. Washington, D.C.: Hemisphere.
- Shewen, E., K.G.T. Hollands, and G.D. Raithby. 1996. Heat transfer by natural convection across a vertical air cavity of large aspect ratio. *Journal of Heat Transfer. Transactions of the ASME* 118, 993-995.
- Sullivan, H. F., J.L. Wright, and R.A. Fraser. 1996. Overview of a project to determine the surface temperatures of insulated glazing units: Thermographic measurement and two-dimensional simulation. *ASHRAE Transactions* 102(2): 516-522.
- Türler, D., B.T. Griffith, and D. Arasteh. 1997. Laboratory procedures for using infrared thermography to validate heat transfer models. In: *Insulation materials: Testing and applications*, third volume, ASTM STP 1320. (R.S. Graves and R.R. Zarr, editors). Philadelphia: American Society for Testing and Materials.
- Wright, J.L. and H.F. Sullivan. 1994. A two-dimensional numerical model for natural convection in a vertical, rectangular window cavity. *ASHRAE Transactions* 100: 1193-1206.
- Yin, S.H., T.Y. Wung, and K. Chen. 1978. Natural convection in an air layer enclosed within rectangular cavities. *International Journal of Heat and Mass Transfer* 21: 307-315.
- Zhao, Y., D. Curcija, and W.P. Goss. 1997. Prediction of the Multicellular Flow Regime of Natural Convection in Fenestration Glazing Cavities. *ASHRAE Transactions* 103(1): 1009-1020.

## Paper II

Natural Convection Effects in Three-Dimensional Window Frames with Internal Cavities

*ASHRAE Transactions* 2001, Vol. 107, Pt. 2

Arild Gustavsen, Brent T. Griffith, and Dariush Arasteh



# Natural Convection Effects in Three-Dimensional Window Frames with Internal Cavities

Arild Gustavsen,<sup>\*</sup> Brent T. Griffith<sup>+</sup> and Dariush Arasteh<sup>+</sup>

---

## ABSTRACT

*This paper studies three-dimensional natural convection effects in window frames with internal cavities. Infrared (IR) thermography experiments, computational fluid dynamics (CFD) simulations, and calculations with traditional software for simulating two-dimensional heat conduction were conducted. The IR thermography experiments mapped surface temperatures during steady-state thermal tests between ambient thermal chambers set at 0 and 20 °C. Using a non-contact infrared scanning radiometer and an external referencing technique, we were able to obtain surface temperature maps with a resolution of 0.1 °C and 3 mm and an estimated uncertainty of  $\pm 0.5$  °C and  $\pm 3$  mm using. The conjugate CFD simulations modeled the enclosed air cavities, frame section walls, and foam board surround panel. With the two-dimensional heat conduction simulation software, we used correlations to model heat transfer in the air cavities. For both the CFD simulations and the conduction simulation software, boundary conditions at the external air/solid interface were modeled using constant surface heat-transfer coefficients with fixed ambient air temperatures.*

*Different cases were studied, including simple, four-sided frame sections (with one open internal cavity), simple vertical sections with a single internal cavity, and horizontal sections with a single internal cavity. The sections tested in the Infrared Thermography Laboratory (IR lab) at Lawrence National Laboratory (LBNL) were made of PVC. Both PVC and thermally broken aluminum sections were modeled. Based on the current investigations, it appears that the thermal transmittance or U-factor of a four-sided section can be found by calculating the average of the thermal transmittance of the respective single horizontal and vertical sections. In addition, we conclude that two-dimensional heat transfer simulation software agrees well with CFD simulations if the natural convection correlations used for the internal cavities are correct.*

---

<sup>\*</sup> Department of Building and Construction Engineering, Norwegian University of Science and Technology, Alfred Getz v. 3, N-7491 Trondheim, Norway.

<sup>+</sup> Building Technologies Department, Environmental Energy Technologies Division, Ernest Orlando Lawrence Berkeley National Laboratory, Berkeley CA, USA.

## INTRODUCTION

Natural convection in glazing cavities has been an international research topic for many years. Convection heat-transfer correlations have been determined both from experiments (e.g. Shewen et al. 1996 and ElSherbiny et al. 1982) and numerical simulations (e.g. Zhao 1998 and Lee and Korpela 1983). In simulations, a two-dimensional situation usually is assumed and can be justified because of the extensive width of the glazing cavities. The convection heat-transfer correlations that have emerged from experiments also only consider two-dimensional cavities. In contrast, heat transfer in window frames with internal cavities has not received much attention. Only few researchers (e.g., Haustermans 2000 and Griffith et al. 1998) have reported effects resulting from the natural convection in such frames. Griffith et al. (1998) studied the significance of bolts on the thermal performance of curtain-wall frames, but did not focus on the natural convection effects in the internal cavities in detail. Haustermans (2000) measured the thermal performance of two types of thermally broken aluminum window frames with internal cavities in a guarded hot box. Complete (four-sided) window frames, single vertical and single horizontal sections were tested. Haustermans (2000) found that, for U-factor calculation purposes, a four-sided frame could be regarded as an assembly of independent vertical and horizontal frame sections. By comparing U-factors, he found that CFD simulations of single horizontal and vertical sections agreed well with experimental results. Simulations with traditional two-dimensional heat-conduction simulation software also gave U-factors that agreed well with his experimental results if the correct air cavity natural convection correlations were used. However, Haustermans did not study specimen surface temperatures in detail. Surface-temperature studies are important for insight about window frame corner effects and about how natural convection effects in internal cavities develop.

Some researchers will probably claim that each horizontal and vertical portion of a window frame can be approximated in two dimensions. Horizontal sections, because of their width, could be modeled in two dimensions with some accuracy, but for vertical sections, which have narrow cavities, three-dimensional effects are expected. Furthermore, information about entire window frames with internal cavities is lacking and merits research.

This paper looks at different effects that result from natural convection in the internal cavities of thermally broken aluminum window frames and PVC window frames. This is a follow-up paper to the work done by an earlier paper by the same authors (Gustavsen et al. 2001), which discusses validation of window frame cavity CFD simulations by infrared (IR) thermography experiments. As in the investigations for the previous report, the work done for

this paper is based on IR thermography experiments and numerical simulations with the computational fluid dynamics (CFD) program FLUENT (Fluent 1998). In addition, we performed numerical simulations with a more traditional two-dimensional conduction heat transfer program, THERM 2.0 (Finlayson et al. 1998). Different simple frame configurations were studied.

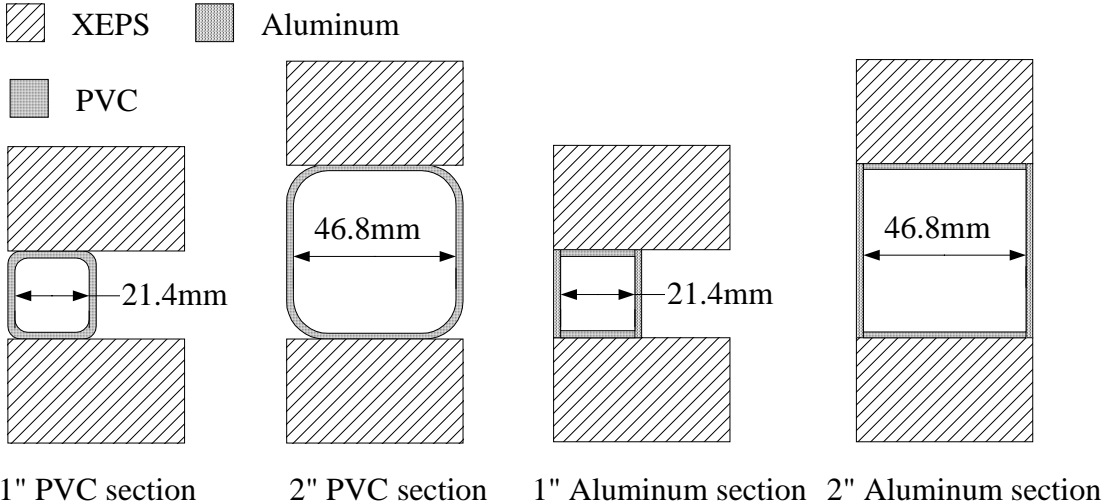


Figure 1. Cross section of the measured PVC profiles and the modeled thermally broken aluminum profiles mounted in two-inch-thick (50.8-mm) extruded polystyrene panel (XEPS).

## METHODOLOGY

### Window Frame Geometries

Although each specimen studied can be thought of either as a complete window frame or as a component of a complete window frame, the sections we used were not actual window frames but rather standard and custom vinyl (polyvinyl chloride, PVC) extrusions and thermally broken aluminum sections. The cross sections of the specimens are shown in Figure 1. The sections were mounted in extruded polystyrene (XEPS). Complete (four-sided) window frame sections, and horizontal and vertical sections were studied. When we refer to four-sided sections, we mean a configuration like the one shown in Figure 2. These sections have open internal cavities so that air can flow freely from the vertical sections to the horizontal sections and vice versa. The horizontal sections were mounted as shown in Figure 3 to get similar natural convection effects on the warm side as for the four-sided sections. Because the focus of this work is on the window frame rather than on a complete window with glazing, we used XEPS to fill the window frame sections. Different profile sizes were

chosen to represent the range of sizes usually found in window frames with internal cavities. Window frames found in actual buildings have several internal cavities; however, we chose the described configuration so that we could determine which cavity caused convection effects when we analyzed the warm-surface temperature data from the experiments. Another reason for choosing simple sections was that we wanted to limit the complexity of the CFD model.

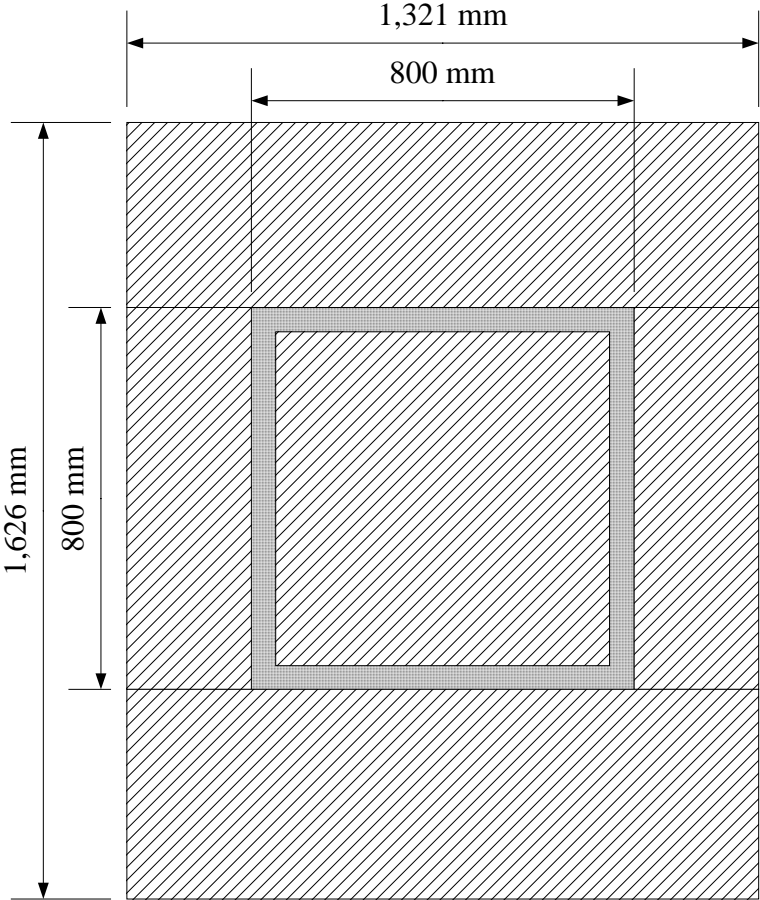


Figure 2. Mounting of four-sided frame specimen in the XEPS surround panel. The figure is drawn for the dimensions of the two-inch (50.8-mm) frame specimen.

In the experiments, PVC was used for the cavities to allow larger temperature gradients to develop on the surface than would result with a higher-conductivity material such as aluminum. Because of the use of PVC and the manufacturing process followed, the edges of the profiles were rounded, as shown for the two sections to the left in the Figure 1. In the simulations, however, we modeled the PVC sections with orthogonal corners. Other characteristics of the physical experiments that not were directly modeled include: the use of silicone to seal and flatten the warm-side surface of the sections, the presence of paint on the

warm-side surface, and the use of vinyl tape on the cold side to form an air seal between the specimen and the surround panel. Thermally broken aluminum frames were also modeled [these were not tested in the Infrared Thermography Laboratory (IR lab)]. The aluminum frames had the same dimensions as the PVC sections. The only difference is that the warm and the cold sides of the specimen were aluminum instead of PVC, as shown for the two sections to the right in Figure 1. The conductivity of the thermal break was set to be the same as the conductivity of PVC. The reader is referred to Gustavsen et al. (2001) for a more thorough description of specimen preparation and mounting and a discussion of the differences between the tested specimens and the modeled specimens. The different specimens used in this paper are listed in Table 1 along with their sizes, aspect ratios and other important properties.

**Experiments**

The experimental part of this work was conducted at the Infrared Thermography Laboratory (IR lab) at Lawrence Berkeley National Laboratory (LBNL). The IR lab consists

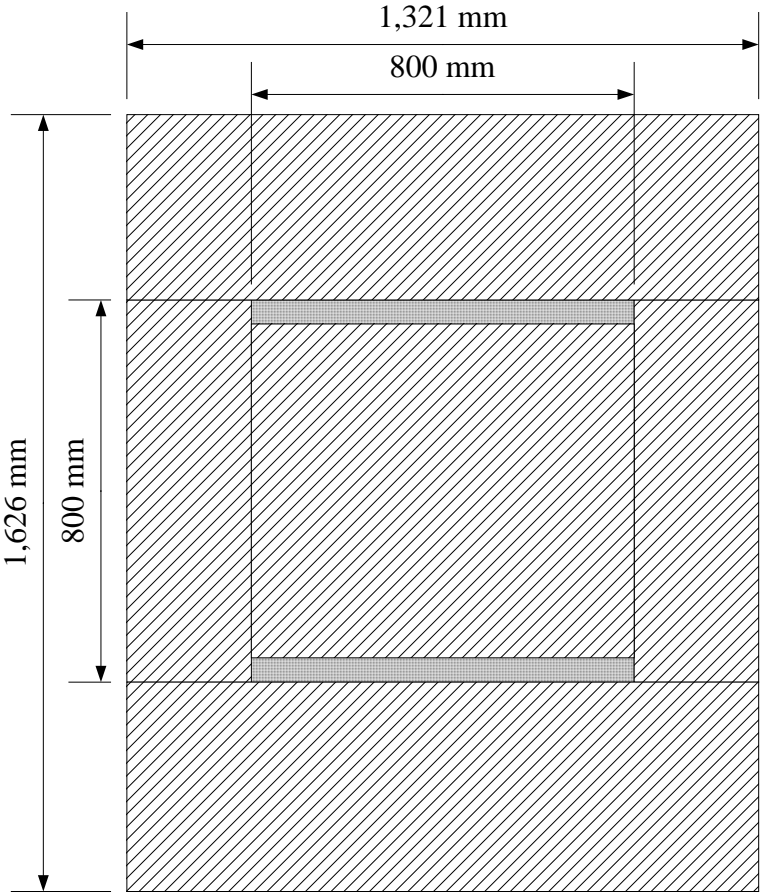


Figure 3. Mounting of the two horizontal specimens in the XEPS surround panel; the figure is drawn for the dimensions of the two-inch (50.8-mm) PVC profiles.

Table 1. Specimen descriptions;  $H/L$  and  $W/L$  are based on the inner height  $H$ , inner length  $L$ , and inner width  $W$ . The maximum Rayleigh number,  $Ra_{max}$ , is calculated from  $\Delta T = 20$  °C, inner length  $L$  of the cavity in the heat-flow direction, and air properties at mean temperature  $T_m = 10$ °C.

Description	1-Inch Square Frame 	Vertical, 1-Inch Section 	Horizontal, 1-Inch Section 	2-Inch Square Frame 	Vertical, 2-Inch Section 	Horizontal, 2-Inch Section 
Orientation during test	entire frame	vertical	horizontal	entire frame	vertical	horizontal
Overall height (mm)	800	800	25.4	800	800	800
Overall width (mm)	800	25.4	800	800	50.8	50.8
Outer size of cross section (mm)	25.4	25.4	25.4	50.8	50.8	50.8
Outer depth of frame section (mm)	25.4	25.4	25.4	50.8	50.8	50.8
Wall thickness (mm)	2.0	2.0	2.0	2.0	2.0	2.0
Size of inner cavity (maximum length in heat-flow direction) (mm)	21.4	21.4	21.4	46.8	46.8	46.8
$H/L$ aspect ratio	37.2 / 1	37.4	1	17.0 / 1	17.1	1
$W/L$ aspect ratio	1 / 37.2	1	37.4	1 / 17.0	1	17.1
Maximum Rayleigh number, $Ra_{max}$	$2.4 \times 10^4$	$2.4 \times 10^4$	$2.4 \times 10^4$	$2.5 \times 10^5$	$2.5 \times 10^5$	$2.5 \times 10^5$

of an IR box in which a steady state heat flow is created through specimens mounted between a climate chamber and a thermography chamber. The climate chamber is used to simulate outside conditions with a given temperature and air velocity across the face of the specimen. The thermography chamber is used to maintain stable conditions on the warm side of the test specimen. The IR box differs from a traditional hot box because there is no baffle in front of the specimen in the thermography chamber. The baffle is omitted to allow for an unobstructed view of the test specimen. An infrared imager with a detector sensitive to thermal radiation in the wavelength interval 8-12  $\mu\text{m}$  is used to capture temperature data. A detailed discussion of IR thermography and the external referencing technique used are thoroughly presented elsewhere (Griffith et al. 1995 and 1999, and Türler et al. 1997) and thus will not be described in detail here. Below, we give only a short summary of the boundary conditions.

In our experiment we used ISO (ISO 1998) conditions; that is, the warm-side bulk air temperature was controlled to 20 °C, and the cold-side bulk air temperature was controlled to 0 °C. Separate experiments, using a calibrated transfer standard (CTS), characterized the performance of the IR box for rates of surface heat transfer. The overall surface heat-transfer

coefficient for the cold side was measured at  $26 \pm 5 \text{ W/m}^2\text{K}$ . The overall surface heat-transfer coefficient for the warm side was measured at  $7.9 \pm 0.4 \text{ W/m}^2\text{K}$ .

## Computer Simulations

We used the computational fluid dynamics program FLUENT (Fluent 1998) and the two-dimensional conduction heat transfer program THERM 2.0 (Finlayson et al. 1998) for the numerical simulations described in this paper. The CFD program uses a control-volume-based technique to convert the governing equations to algebraic equations that can be solved numerically. The method will not be described in detail; only salient features pertinent to this investigation will be presented. Readers interested in the numerical method are referred to Fluent (1998) and textbooks, i.e. Patankar (1980) or Versteeg and Malalasekera (1995), that describe this technique. THERM 2.0 uses a finite-element approach to solve the governing equations in two dimensions. Correlations are used to model convection heat transfer in air cavities, and view factors or fixed radiation coefficients can be used to calculate radiation heat transfer.

In the CFD program, our conjugate heat transfer problem involves solution of three-dimensional energy, momentum, and continuity equations on a hexahedral mesh. Air flow is assumed to be incompressible. Viscous dissipation is not addressed, and all thermo-physical properties are assumed to be constant except for the buoyancy term of the y-momentum equation where the Boussinesq approximation is assumed. In Table 1, we see that the maximum Rayleigh number,  $Ra_{max}$ , for the vertical, one-inch section is close to the laminar/turbulence limit. Flow changes from laminar to turbulent near  $Ra = 2 \times 10^4$  for two-dimensional cavities where  $H/L = 40$  (Yin et al. 1978). However, the temperature difference between the internal walls of the cavity is likely to be smaller than  $20 \text{ }^\circ\text{C}$ , which is the temperature difference used for calculating the maximum Rayleigh number, so the real Rayleigh number is lower. In addition, the turbulence limit is probably higher than  $Ra = 2 \times 10^4$  for a three-dimensional vertical square cavity than for a two-dimensional cavity because of the added restriction imposed on the flow by the narrowness of the cavity. Because we also know that laminar flow simulations performed using FLUENT compared well with IR thermography (Gustavsen et al. 2001), we assumed laminar flow for the simulations in this paper. Radiation heat transfer was included in the simulations by use of the Discrete Transfer Radiation Model (DTRM), which relies on a ray-tracing technique to calculate surface-to-surface radiation. The internal cavity walls are assumed to be diffuse gray, and the fluid (air) does not interact with the radiative process. SIMPLEC (Semi-Implicit Method for Pressure-

Linked Equations Consistent) was used to model the interaction between pressure and velocity. The energy and momentum variables at cell faces were found by using the QUICK (Quadratic Upstream Interpolation for Convective Kinetics) scheme. In addition, FLUENT uses central differences to approximate the diffusion terms and relies on the pressure interpolation scheme PRESTO (PREssure Stagging Option) to find the pressure values at the cell faces. PRESTO is similar to the staggered grid approach described by Patankar (1980). Convergence is determined by checking the scaled residuals and ensuring that they are less than  $10^{-5}$  for all variables except for the energy equation in which the residuals have to be less than  $10^{-6}$ .

The material properties and the boundary conditions used in the simulations are given in Tables 2 and 3, respectively. As we see in Table 2, the emissivity of aluminum was set to 0.9, like the emissivity of PVC, so that both sections would have the same radiation properties; this value is close to what we find for anodized aluminum.

Table 2. Material Properties used in the computer simulations.

Material	Emissivity	Thermal conductivity, W/mK
Aluminum	0.9	160
PVC	0.9	0.17
Painted XPS	0.9	0.03

Table 3. Boundary conditions used in the computer simulations.

	Temperature, °C	Total surface film coef., W/m <sup>2</sup> K
Warm Side	20	7.69
Cold Side	0	25

## RESULTS

We studied several properties and effects, including warm-side surface temperatures, corner effects, complex flow patterns, and heat-transfer rates. Most of the figures of surface temperature also show schematically the locations on the frame sections where the temperature data were collected. For the heat-transfer calculations, we compared three-dimensional CFD simulations and traditional conduction heat-transfer simulations.

### Surface Temperature Plots

Figure 4 shows the warm-side surface temperatures along a line down the middle of the one-inch square frame and the pair of one-inch horizontal profiles, which are one-inch versions of the specimens shown in Figures 2 and 3, respectively. Both data sets are from IR thermography experiments. The vertical axis shows the accumulated distance from the lower

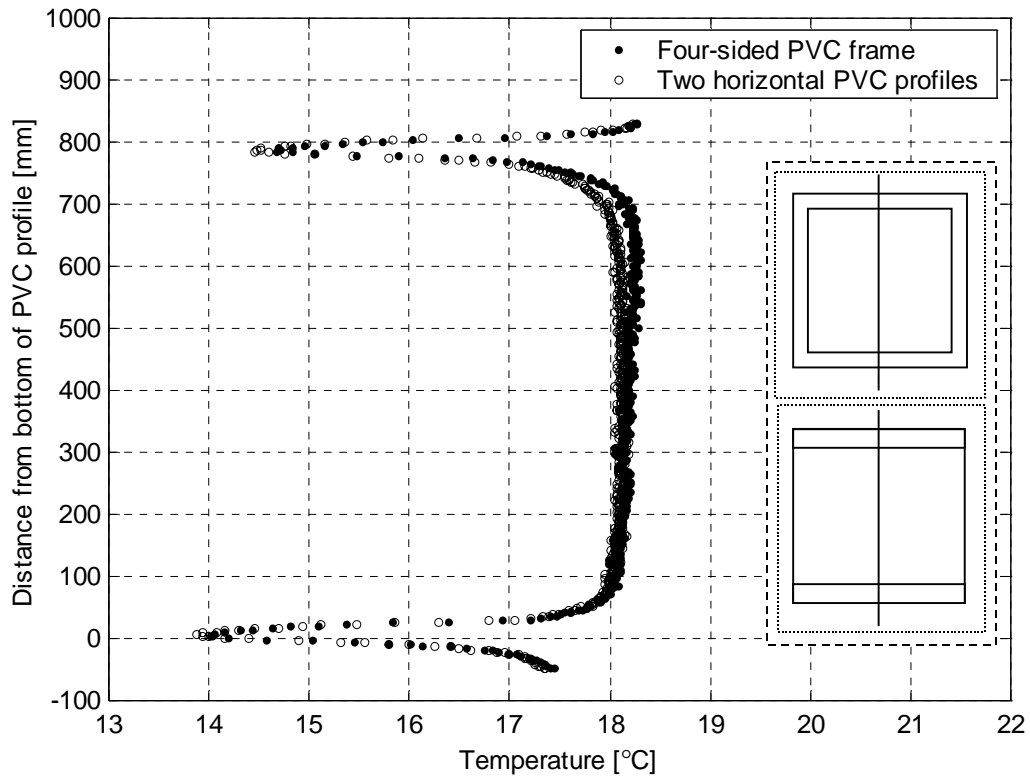


Figure 4. Surface temperatures down the middle of one-inch square frame compared to the temperatures down the middle of the two one-inch horizontal PVC profiles; experimental uncertainty is estimated to  $\pm 0.5$  °C (Griffith and Arasteh 1999).

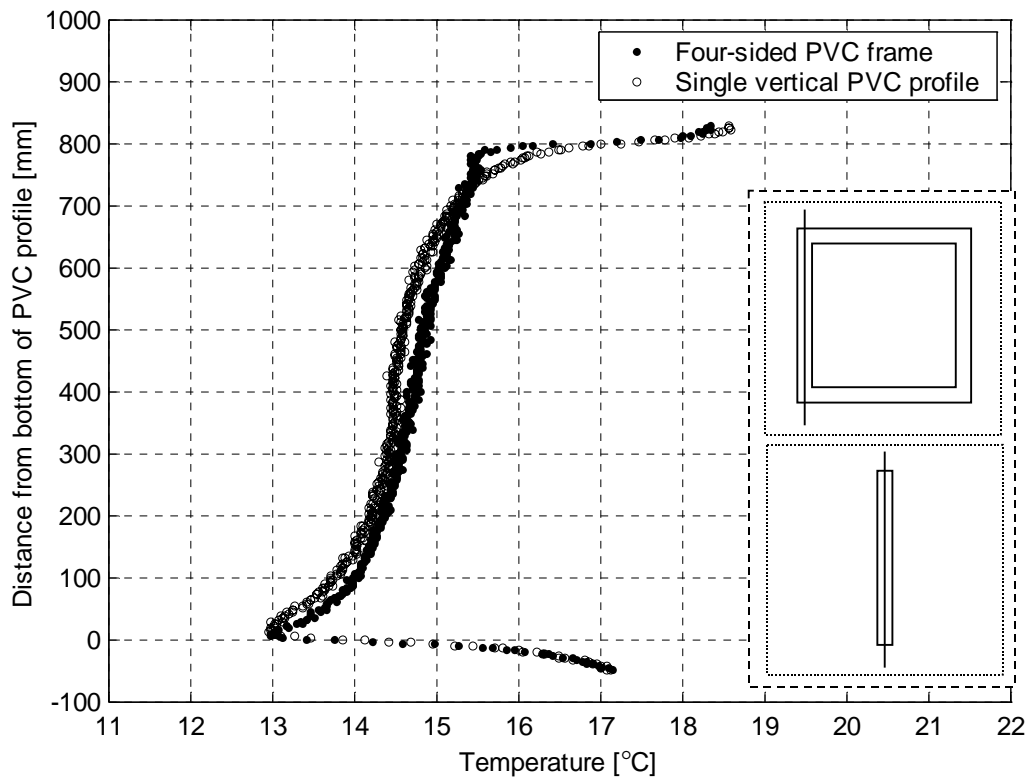


Figure 5. Temperature along the vertical part of the four-sided one-inch PVC frame compared to the surface temperatures of a single vertical one-inch PVC profile; experimental uncertainty is estimated to  $\pm 0.5$  °C (Griffith and Arasteh 1999).

edge of the bottom profile in millimeters. The lower profile extends from 0 to 25.4 mm and the upper profile from 774.6 to 800 mm. Outside these areas, data are plotted for the temperature of the foam surround panel in which the specimens were mounted. The horizontal axis shows the surface temperature in degrees Celsius, °C. The IR data were averaged on each vertical level to reduce noise.

In Figure 5 we see the temperature down the middle of the vertical part of the one-inch square frame compared to the temperature down the middle of a single one-inch vertical profile. The horizontal axis shows the surface temperature in °C, and the vertical axis shows the accumulated distance from the bottom edge of the frame section and the single PVC profile. The bottom edge of the profiles is 0 mm; 800 mm is on the top. Data were averaged on each vertical level to reduce noise; however, because the temperature varies in the horizontal direction, the number of data points averaged was kept to a minimum.

Figure 6 shows a line plot of the temperature along the middle of the lower left horizontal part (the corner region) of the one-inch square frame compared to the temperature along the middle of one single horizontal PVC profile (mounted in the configuration of two

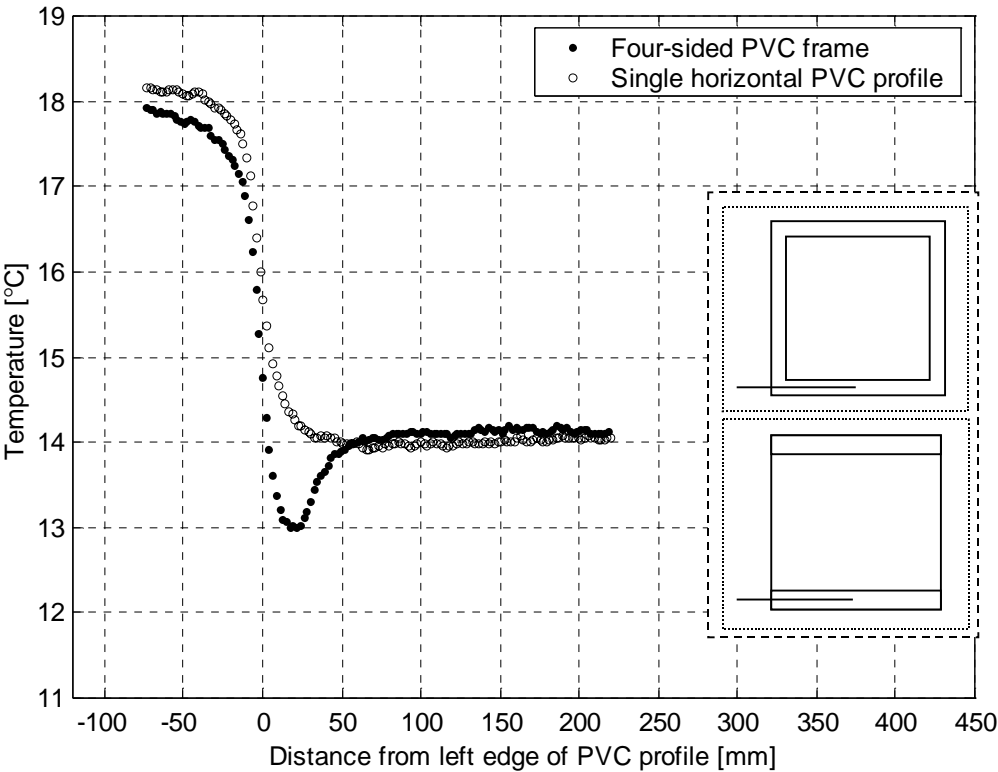


Figure 6. Temperatures along the left lower horizontal part of the four sided one-inch PVC frame compared to the surface temperatures along a line of the lowest one-inch profile in the configuration made up of two separate horizontal profiles; experimental uncertainty is estimated to  $\pm 0.5$  °C (Griffith and Arasteh 1999).

horizontal profiles shown in Figure 3). The horizontal axis shows the distance from the left edge of the PVC profiles in millimeters, and the vertical axis shows the temperature in °C.

Figures 7, 8, and 9 show the same temperature line plots for the two-inch frame and profile sections as are shown in Figures 4, 5, and 6 for the one-inch sections. In Figure 7, which show surface temperatures down the middle of the two-inch square frame compared to the temperatures down the middle of the two two-inch horizontal PVC profiles, the lower PVC section extends from 0 to 50.8 mm, and the upper PVC section extends from 749.2 to 800 mm.

Figure 10 compares surface temperatures for the one-inch thermally broken aluminum specimens. The left graph shows the surface temperatures along the top and bottom horizontal parts of the four-sided one-inch frame (the corner regions) compared to the surface temperatures along the middle of a single horizontal profile. The horizontal axis shows the distance from the left edge of the thermally broken aluminum profiles in millimeters. The vertical axis shows the surface temperatures in °C. The right graph compares the temperatures along the middle of one vertical part of the four-sided frame to the surface temperatures of the middle of the single vertical one-inch section. The vertical axis shows the

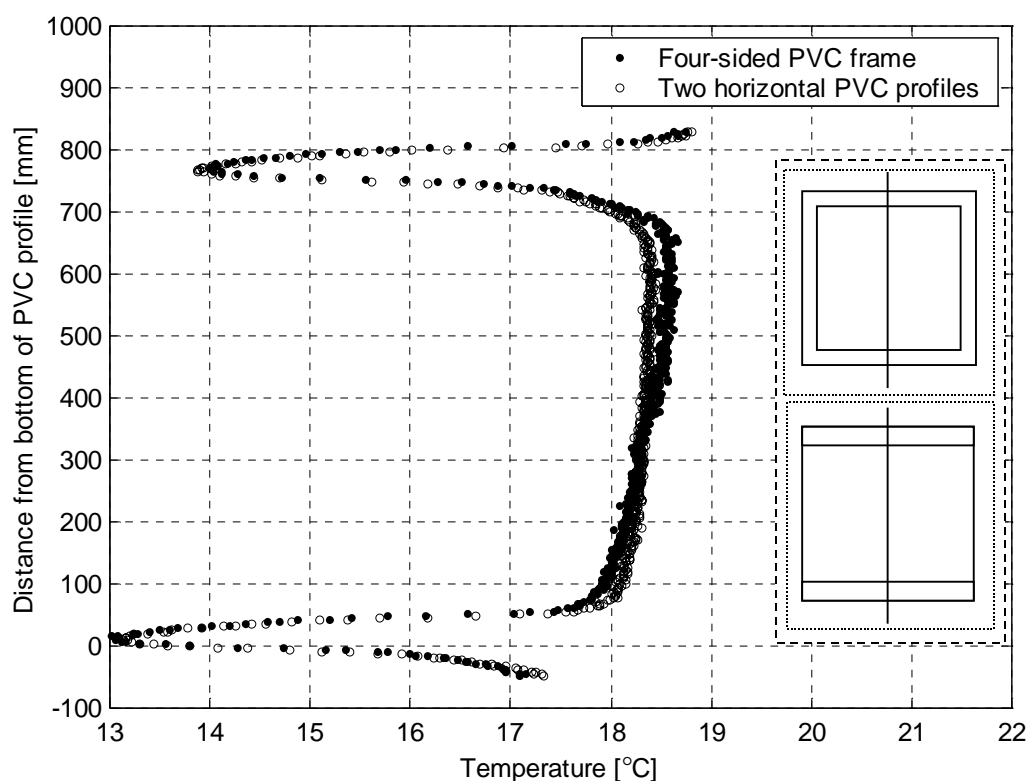


Figure 7. Surface temperatures down the middle of the two-inch square frame compared to the temperatures along the middle of the configuration made up of two two-inch horizontal profiles. Experimental uncertainty is estimated to  $\pm 0.5$  °C (Griffith and Arasteh 1999).

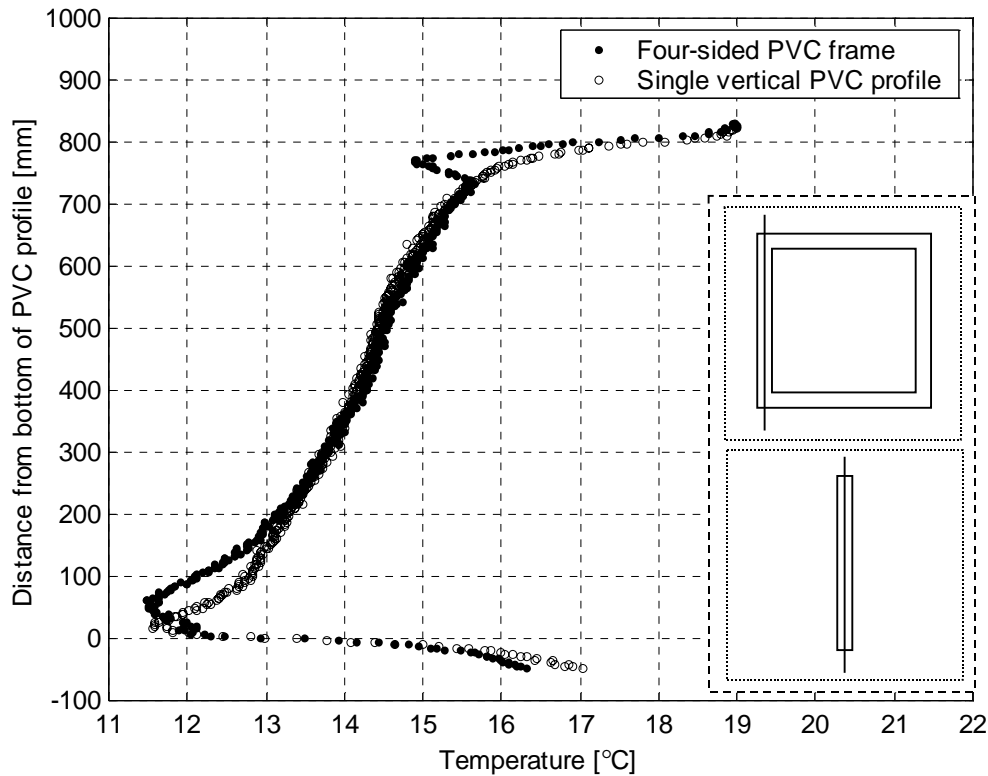


Figure 8. Temperatures along the vertical part of the four-sided two-inch PVC frame compared to the surface temperatures of a single vertical two-inch PVC profile; experimental uncertainty is estimated to  $\pm 0.5$  °C (Griffith and Arasteh 1999).

distance from the bottom of the profile; the bottom of the profile is at 0 millimeters, and the top is at 800 millimeters. The horizontal axis shows the surface temperatures in °C. We do not have similar plots for the two-inch thermally broken aluminum frame because that section did not converge using a stationary solution procedure and a transient solution procedure was too time consuming.

### Complex Flow

From studies on natural convection in glazing cavities we know that secondary flow may appear for certain geometries and boundary conditions (see e.g. Zhao et al. 1997 or Wright and Sullivan 1994). In Figure 11, we see the indoor surface temperatures of a two-dimensional model of the one-inch vertical PVC frame compared to the surface temperatures of the middle of the three-dimensional one-inch vertical PVC frame. Both data sets are from CFD simulations. The horizontal axis shows the surface temperatures in °C and the vertical axis the accumulated distance from the bottom edge of the PVC sections in millimeters. Secondary flow was not observed for the vertical two-inch frame.

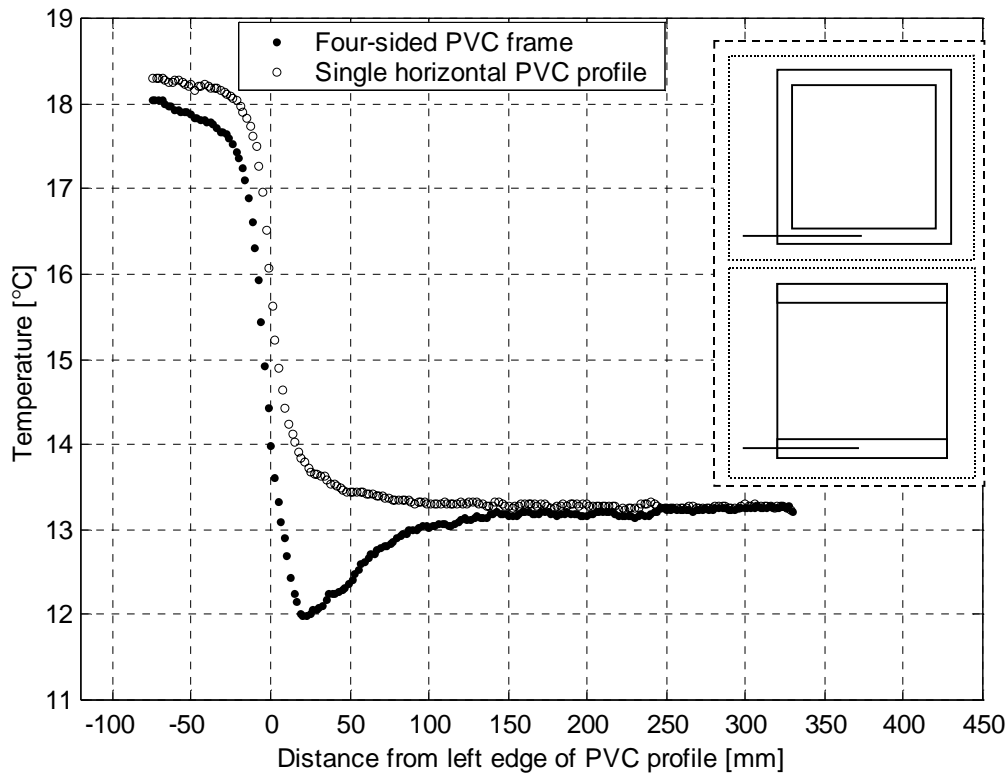


Figure 9. Temperatures along the left lower horizontal part of the four-sided two-inch PVC frame compared to the surface temperatures along the middle of the lowest two-inch profile in the configuration made up of two separate horizontal profiles. Experimental uncertainty is estimated to  $\pm 0.5$  °C (Griffith and Arasteh 1999).

## U-Factors

Table 4 summarizes the U-factor calculations for the different PVC frame sections; Table 5 summarizes similar results for thermally broken aluminum frames. Both tables include simulation results from FLUENT and THERM. No experimental results are included because we did not measure the heat-transfer rates through the specimens. For the THERM simulations, we used correlations to calculate convection and radiation heat transfer in the air cavities. Correlations from both ASHRAE 142P (ASHRAE 1996) and ISO/DIS 10077-2 (CEN 1998) were tested. We note that the heat convection correlations in the *proposed* ISO 15099 (ISO 1999) are the same for air cavities in frames as the correlations used in ASHRAE 142P and that the radiation correlation for air cavities used in ASHRAE 142P is in fairly good agreement with the correlation proposed in ISO 15099 for  $H/L > 1$  (Roth 1998).

For the FLUENT simulations symmetry boundary conditions were used to reduce the number of computational cells and to reduce computation time. To ensure that the resolution in the discretization of the geometry was high enough, some grid sensitivity tests were performed. Some of these were not performed on the final geometries but on simpler sections

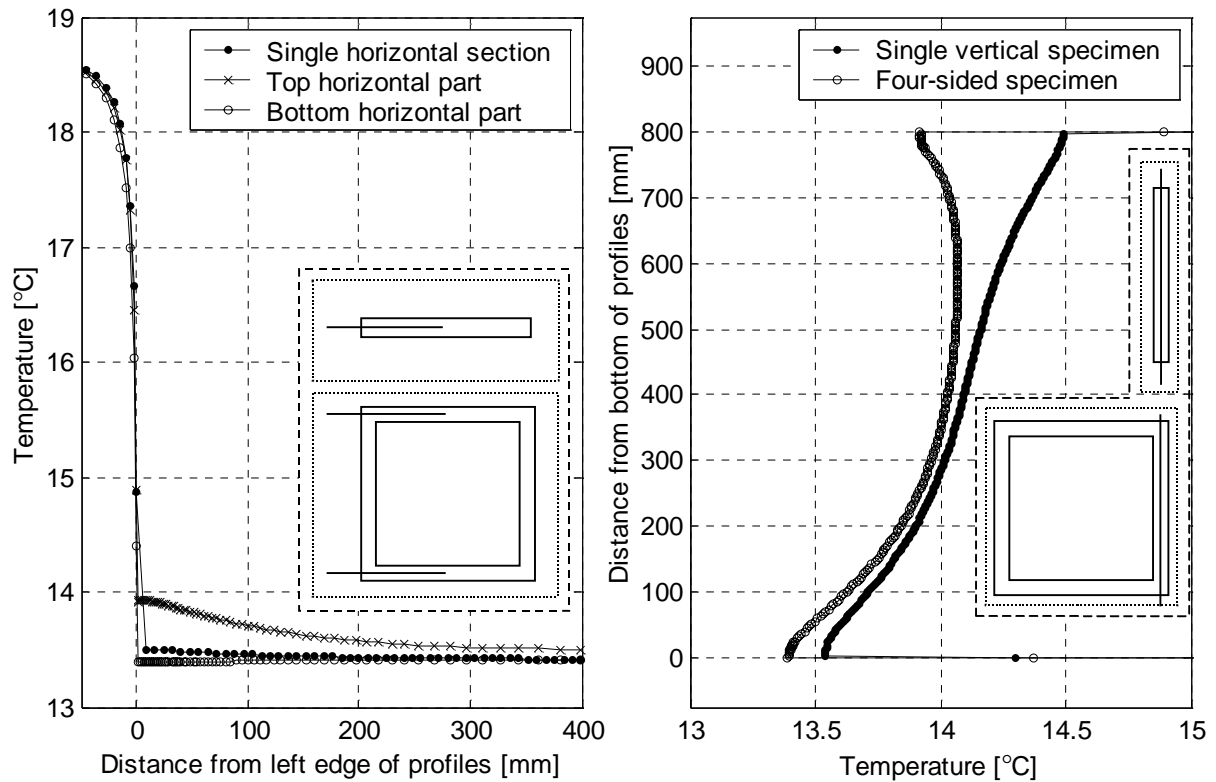


Figure 10. This figure compares surface temperatures for the one-inch thermally broken frames. The left graph shows the temperatures along the top and bottom horizontal parts of the four-sided one-inch frame compared to the surface temperatures along the middle of the single horizontal profile. The right graph compares the temperatures along the vertical part of the four-sided frame to the surface temperatures of the single vertical one-inch profile.

that represent one part of the more complex geometries. For instance, for a two-dimensional cavity with an aspect ratio of  $H/L = 40$  we found that an equispaced mesh of  $25 \times 200$  was sufficient (a mesh with  $45 \times 450$  nodes resulted in a change of Nusselt number by 1%). One test was also performed on a three-dimensional, horizontal, two-inch section. The number of nodes was increased both within the solid materials and in the air cavity. The refinement resulted in a change of only 0.3% in the total heat-transfer through the test specimen. The boundary conditions in this test were identical to the boundary conditions in the final simulations. We also tried to increase the number of rays traced in the radiation heat-transfer algorithm and found that doubling the number of rays in both directions only changed the total heat transfer by 0.2% (with the other parameters left constant). For the THERM simulations, we verified the influence of mesh density on U-factor for all sections by successively refining the mesh.

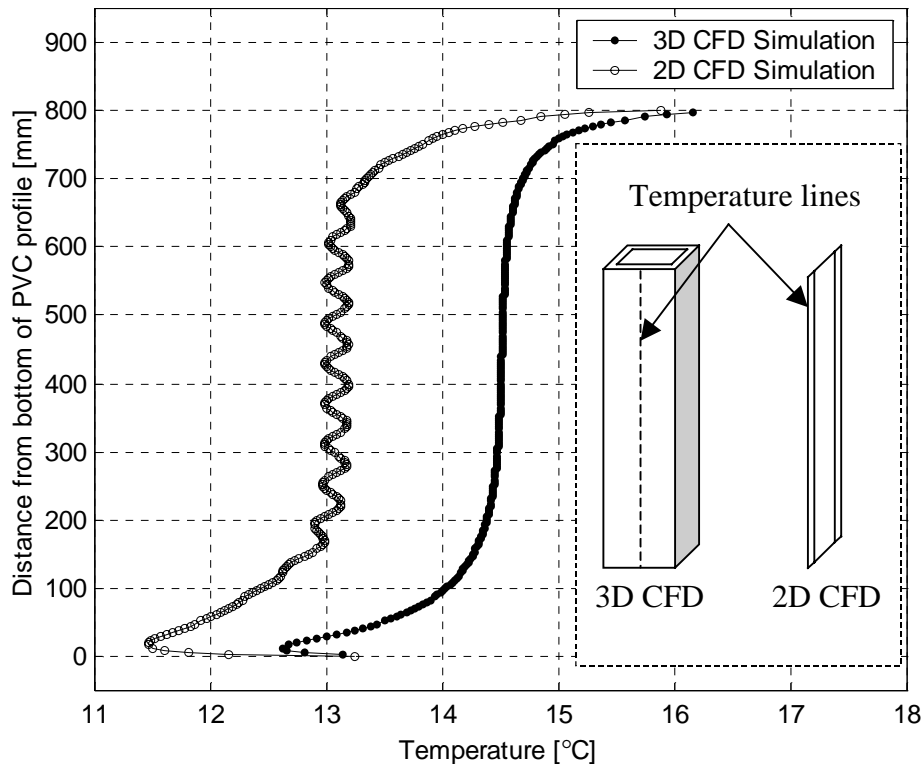


Figure 11. Temperature distribution on the middle of the indoor side of the vertical three-dimensional PVC frame and a two-dimensional model of the PVC frame.

For both the FLUENT and THERM simulations, the U-factor was determined by calculating the heat flow through the warm side of the specimen and dividing that by the surface area and difference between the external and internal air temperatures. The temperatures on the internal wall surfaces in the cavity used for calculating the convection and radiation effects from the correlations in THERM were determined through several simulations and then adjusting the surface temperature.

Table 4. Results for different simulations of PVC window frame sections from the CFD program FLUENT and the conduction heat-transfer program THERM.

Simulation Description (PVC Sections)	1-Inch Sections, U-Factor, W/m <sup>2</sup> K	2-Inch Sections, U-Factor, W/m <sup>2</sup> K
2D Section, ASHRAE (THERM)	2.29	2.53
2D Section, CEN (THERM)	2.16	2.19
3D Horizontal Section (FLUENT CFD)	2.34	2.40
3D Vertical Section (FLUENT CFD)	2.12	2.24
3D Four-Sided Frame (FLUENT CFD)	2.24	2.33 <sup>1</sup>

<sup>1</sup> This case did not converge using a stationary solution procedure. This is the value toward which the heat flow seems to converge, if the problem runs for a long time using a transient solution procedure.

Table 5. Results for different simulations of thermally broken aluminum window frame sections from the CFD program FLUENT and the conduction heat transfer program THERM.

Simulation Description (Aluminum Sections)	1-Inch Sections, U-Factor, W/m <sup>2</sup> K	2-Inch Sections, U-Factor, W/m <sup>2</sup> K
2D Section, ASHRAE (THERM)	2.46	2.65
2D Section, CEN (THERM)	2.31	2.27
3D Horizontal Section (FLUENT CFD)	2.52	2.56
3D Vertical Section (FLUENT CFD)	2.28	2.38
3D Four-Sided Frame (FLUENT CFD)	2.42	N/A

## DISCUSSION

In this discussion we analyze the differences between four-sided and single vertical and horizontal frame sections. We are interested in determining the limitations of treating a complete (four-sided) window frame with internal cavities as it were made up of simple jamb sections; that is, dividing the complete frame into its separate parts and simulating them by themselves instead of simulating the complete frame or using simple THERM/NFRC or CEN models.

### Surface Temperature

Figures 4 through 9 compares the surface temperatures of four-sided sections with those of single vertical and horizontal sections. All of these figures are based on results from the IR lab only; no CFD results are included. From Figures 4 and 7, we see that the temperatures of the middle of the four-sided frames compare well with the temperatures of the middle of the horizontal profiles. This means that the temperature differences between the upper and lower profiles of the four-sided PVC sections are not a result of cold air flowing to the bottom profile but rather of natural convection effects on the warm side, changing from top to bottom. For the CFD simulations, which used a constant surface heat-transfer coefficient, we found that the warm-side surface temperature for the four-sided PVC frame sections was the same at the middle of the top and bottom profiles (edge/corner effects are discussed below).

For the vertical sections, shown in Figures 5 and 8, there is somewhat more discrepancy between the surface temperatures of a single section and of a four-sided section. For the two-inch profiles, this difference is mostly limited to the area near the top and bottom of the frames (the corner regions); for the middle parts of the sections, the shapes of the temperature curves are almost identical. For the one-inch sections, there is a smaller difference overall, but the shapes of the curves seem to be a little different. This difference

might be a result of local variation in the cold side convection effects caused by the difference in overhanging XEPS, see Figure 1.

For the thermally broken aluminum sections we have only CFD results. Figure 10 compares the surface temperatures of different one-inch specimens. We find that there are smaller temperature gradients on the surfaces for these specimens than for the PVC sections. This is a result of the high conductivity of aluminum. This high conductivity is probably also the reason for the temperatures being higher on the top horizontal part of the four-sided section than on the bottom. This temperature difference is not only limited to the edges but persists throughout the profiles. The high conductivity also prevents the local surface temperature effects (local maximum and minimum values) like those we find on the PVC sections.

### Corner Effects for PVC Sections

From Figure 6, we see that the corner region of the one-inch four-sided PVC frame specimen extends about 60 mm into the horizontal part of the bottom frame, which also is what we find from the CFD simulations. Figure 9 shows that for the two-inch four-sided PVC frame, the corner region extends to about 250 mm, which is the same as what we find from the CFD simulation. For the top horizontal profile in the four-sided frames (not shown in any of the figures), these distances are about the same.

### U-factors

Because heat-transfer simulations are usually performed to generate U-factors for use in rating window frames, it is useful to compare our CFD simulations with the usual way of calculating window frame U-factors, by using conduction analysis software. Table 4 shows calculated U-factors for all PVC frames, and Table 5 shows U-factors for thermally broken aluminum frames. By studying the CFD results only, we find that there is a difference of about  $0.2 \text{ W/m}^2\text{K}$  between the horizontal and vertical profile U-factors. A difference between horizontal and vertical profiles is also anticipated from natural convection correlation studies that show that the Nusselt number is higher for square cavities than for cavities with a high aspect ratio (see, e.g., Raithby and Hollands, 1998). The CFD simulations also seem to indicate that the U-factor of a complete (or four-sided) window frame can be found by calculating the average of the horizontal and vertical profile U-factors. This agrees with the recent findings of Haustermans (2000), who measured in a guarded hot box the U-factors of real thermally broken aluminum window frames with internal cavities. These experiments

measured both four-sided window frames and single vertical and horizontal sections. Haustermans (2000) also tried to close the internal cavities of four-sided thermally broken aluminum frames; he found that closing the internal cavities at the corners had no significant influence on the U-factor.

Looking at the results from THERM, which used correlations to simulate the natural convection and radiation effects inside the cavities, we find that results differed depending on which correlations we used. Comparing the results from ASHRAE and CEN, we find that the ASHRAE correlations give higher U-factors than the CEN correlations. Further, we find that ASHRAE U-factors compare well with the results of the three-dimensional horizontal sections simulated with FLUENT, and the CEN U-factors compare well with the results of the vertical three-dimensional profiles simulated with FLUENT. The THERM simulations are two-dimensional. Thus, the simulated cases look like the specimens shown in Figure 1. Therefore, we would expect the U-factors from the THERM simulations to lie closest to the horizontal CFD result, as the ASHRAE correlation results do. However, as reported by Gustavsen (1999), the CEN correlation for natural convection more closely resembles natural convection in high-aspect-ratio cavities than in square cavities. Therefore, the result we found, in which the CEN U-factor is closer to the U-factor from the vertical frame CFD simulations, is also to be expected.

## Treatment of Window Frames in Components

Modeling an entire window frame with internal cavities is a complex task and may require substantial computer resources and simulation time. Therefore, it is helpful to investigate whether frame cavities can be modeled at separate vertical and horizontal cavities even when they may be joined to make a continuous cavity in a four-sided frame.

Above, we studied warm-side surface temperatures of various frame sections using IR thermography and found that, except at the corner regions, the top and bottom parts of the four-sided PVC frames have similar surface temperature patterns. That is, the surface temperatures of the top and bottom profiles would be the same if the warm side surface natural convection effects were constant along the frame section. In addition, the surface temperatures of the vertical parts of the four-sided PVC sections compared well to the surface temperature of the single vertical PVC sections, excluding corner regions. However, the discrepancies in temperature patterns for the thermally broken aluminum specimens are larger, and not only limited to small corner regions. Therefore, complete four-sided window frames will have to be simulated to find local temperature effects. However, if we look at the

U-factor results it seems reasonable to assume that the U-factor of a complete window frame can be found by calculating the average of the respective horizontal and vertical parts. This appears to be valid for both PVC frames and thermally broken aluminum frames.

## Heat transfer

Most correlations used today for finding the thermal performance (U-factor) of window frames are based on two-dimensional studies (both radiation and natural convection correlations). However, for vertical three-dimensional window frames, two-dimensions cannot be presumed without errors in the final U-factor. These errors are a result of the small width-to-length aspect ratio of the internal frame cavities. Figure 11, for instance, shows that the secondary flow that exist in a two-dimensional,  $W/L \rightarrow \infty$ , cavity does not exist in a three-dimensional cavity where  $W/L = 1$ . The possible lack of secondary flow and the constraint imposed on the air flow in the cavity by the added vertical walls in a real three-dimensional cavity will probably decrease natural convection effects.

## CONCLUSIONS

Based on our experiments and numerical simulations of heat flow through simple window frame sections we draw the following conclusions:

1. Infrared thermography can be used to accurately measure the surface temperatures of window frames with internal cavities; these data can be used to compare natural convection effects in four-sided window frames with convection effects found in single vertical and horizontal window frames.
2. CFD tools are useful for evaluating natural convection in the internal cavities of window frames.
3. Although more investigations are needed, especially for more realistic frame sections (and those with glazing), it is reasonable to proceed using the assumption that convection in a complete window frame with joined, open internal cavities can be modeled by separating horizontal and vertical cavities; this approach yield reasonably accurate predictions for the mean U-factor of entire frame sections. Accurate modeling of corner regions will still, however, require joining horizontal and vertical cavities.
4. Traditional heat-conduction simulation tools, like THERM, can still be used with good accuracy when calculating window frame U-factors. This statement is valid if the

correct convection heat-transfer correlations are used for the internal cavities of the window frames, keeping the orientation of the frames in mind.

## FUTURE RESEARCH

This work was conducted to extend our insight into heat transfer in window frame sections with internal cavities. Here, we only consider simple frame sections with one internal cavity. In practice, however, different effects are highly coupled, so, to get more information about window frames with internal cavities, we need to consider variable heat-transfer coefficients for the surfaces (or model air flow at the surface), and to consider more realistic frames with more than one internal cavity, window frames with glazing, and frame sections with irregular (not rectangular) cavities. Finally, further investigation is needed to determine accurate correlations for natural convection in air enclosures with a high vertical aspect ratio ( $H/L > 5$ ) and a low horizontal aspect ratio ( $W/L \sim 1$ ).

## ACKNOWLEDGMENTS

This work was supported by Hydro Aluminum and the Assistant Secretary for Energy Efficiency and Renewable Energy, Office of Building Technology, State and Community Programs, Office of Building Systems of the U.S. Department of Energy under Contract No. DE-AC03-76SF00098.

## REFERENCES

- ASHRAE 1996. *Draft BSR/ASHRAE Standard 142P - Standard method for determining and expressing the heat transfer and total optical properties of fenestration products*. Atlanta: American Society of Heating, Refrigerating and Air-conditioning Engineers, Inc.
- CEN 1998. *Draft prEN ISO 10077-2 - Thermal performance of windows, doors and shutters - Calculation of thermal transmittance - Part 2: Numerical method for frames*. Brussels: European Committee for Standardization.
- ElSherbiny, S.M., G.D. Raithby, and K.G.T. Hollands. 1982. Heat transfer by natural convection across vertical and inclined air layers. *Journal of Heat Transfer. Transactions of the ASME* 104: 96-102.

- Finlayson, E., R. Mitchell, D. Arasteh, C. Huizenga, and D. Curcija. 1998. *THERM 2.0: Program description. A PC program for analyzing the two-dimensional heat transfer through building products*. Berkeley: California: University of California.
- Fluent 1998. *FLUENT 5 User's Guide*. Lebanon, UK: Fluent Incorporated.
- Griffith, B.T. and D. Arasteh. 1999. Buildings research using infrared imaging radiometers with laboratory thermal chambers. In: *Proceedings of the thermosense XXI conference*. (D.H. LeMieux. and J.R. Snell, editors). Vol. 3700: 502-513. The International Society for Optical Engineering.
- Griffith, B.T., F. Beck, D. Arasteh, and D. Türler. 1995. Issues associated with the use of infrared thermography for experimental testing of insulated systems. In: *Thermal performance of the exterior envelopes of buildings VI*. Atlanta: American Society of Heating, Refrigeration and Air-Conditioning Engineers.
- Griffith, B., E. Finlayson, M. Yazdanian, and D. Arasteh. 1998. The Significance of bolts in the thermal performance of curtain-wall frames for glazed facades. *ASHRAE Transactions* 104(1B):, 1063-1069.
- Gustavsen, A., B.T. Griffith, and D. Arasteh. 2001. Three-dimensional conjugate computational fluid dynamics simulations of internal window frame cavities validated using infrared thermography. *ASHRAE Transactions* 207(2).
- Gustavsen, A. 1999. Comparison of Nusselt number correlations for convection heat transfer in a cavity. In: *Proceedings of the 5th symposium on building physics in the Nordic countries*, Vol. 1: 201-208. Göteborg, Sweden: Chalmers University of Technology.
- Haustermans, L. 2000. *Heat transfer in aluminium window frame profiles. Computer modelling and hot box measurements*. Master of Science Thesis. Leuven, Belgium: Departement Burgerlijke Bouwkunde, Katholieke Universiteit Leuven.
- ISO 1999. *Draft Standard ISO 15099 - Thermal Performance of Windows, Doors and Shading Devices - Detailed Calculations*. Geneva, Switzerland: International Organisation for Standardisation.
- ISO 1998. *Draft Standard ISO/DIS 12567 - Thermal performance of doors and windows - Determination of thermal transmittance by hot box method*. Geneva, Switzerland: International Organisation for Standardisation.

- Lee, Y. and S.A. Korpela. 1983. Multicellular natural convection in a vertical slot. *Journal of Fluid Mechanics* 126: 91-121.
- Patankar, S.V. 1980. *Numerical heat transfer and fluid flow*. Washington, D.C.: Hemisphere.
- Raithby, G.D. and K.G.T Hollands. 1998. Natural convection. In: *Handbook of heat transfer*, 3d ed. (W.M. Rosenhow, J.P. Hartnett. and Y.I. Cho, editors). pp. 4.1-4.99. New York: McGraw-Hill.
- Roth, H. 1998. *Comparison of thermal transmittance calculation methods based on ASHRAE and CEN/ISO standards*. Master of Science Thesis. Massachusetts: Department of Mechanical and Industrial Engineering, University of Massachusetts Amherst.
- Shewen, E., K.G.T. Hollands, and G.D. Raithby. 1996. Heat transfer by natural convection across a vertical air cavity of large aspect ratio. *Journal of Heat Transfer. Transactions of the ASME* 118: 993-995.
- Türler, D., B.T. Griffith, and D. Arasteh. 1997. Laboratory procedures for using infrared thermography to validate heat transfer models. In: *Insulation materials: Testing and applications*, 3d vol., ASTM STP 1320 (R.S. Graves. and R.R. Zarr, editors). American Society for Testing and Materials.
- Versteeg, H.K. and W. Malalasekera, 1995. *An introduction to computational fluid dynamics. The finite volume method*. Essex, England: Addison Wesley Longman Limited.
- Wright, J.L. and H.F. Sullivan. 1994. A two-dimensional numerical model for natural convection in a vertical, rectangular window cavity. *ASHRAE Transactions* 100(2): 1193-1206.
- Yin, S.H., T.Y. Wung, and K. Chen. 1978. Natural convection in an air layer enclosed within rectangular cavities. *International Journal of Heat and Mass Transfer* 21: 307-315.
- Zhao, Y., D. Curcija, and W.P. Goss. 1997. Prediction of the Multicellular Flow Regime of Natural Convection in Fenestration Glazing Cavities. *ASHRAE Transactions* 103(1): 1009-1020.
- Zhao, Y. 1998. *Investigation of heat transfer performance in fenestration system based on finite element methods*. Ph.D. dissertation. Massachusetts: Department of Mechanical and Industrial Engineering, University of Massachusetts Amherst.

## Paper III

Numerical Simulation of Natural Convection in Three-dimensional Cavities  
with a High Vertical Aspect Ratio and a Low Horizontal Aspect Ratio

Arild Gustavsen and Jan Vincent Thue



# Numerical Simulation of Natural Convection in Three-dimensional Cavities with a High Vertical Aspect Ratio and a Low Horizontal Aspect Ratio

Arild Gustavsen\* and Jan Vincent Thue  
Department of Building and Construction Engineering, Norwegian University  
of Science and Technology, Alfred Getz v. 3, N-7491 Trondheim, Norway

---

## ABSTRACT

This paper studies the effect of the horizontal aspect ratio on heat flow through cavities with a high vertical aspect ratio. The cavities studied have vertical aspect ratios of 20, 40, and 80 and horizontal aspect ratios ranging from 0.2 to 5. Simulations of two-dimensional cavities are also included. The simulations show that three-dimensional cavities with a horizontal aspect ratio larger than five can be considered as being two-dimensional cavities to within 4 % when considering heat transfer rates. Nusselt number correlations for the different horizontal aspect ratios are included. Complex multicellular flow is studied for one of the cavities.

## NOMENCLATURE

$a$	coefficient in discretized equation
$b$	source term in discretized equation
$c_p$	specific heat at constant pressure
$g$	gravitational acceleration
$H$	height of air cavity
$k$	thermal conductivity
$L$	length separating isothermal plates
$Nu$	Nusselt number
$n_x, n_y, n_z$	number of computational cells in the $x$ -, $y$ - and the $z$ -directions
$p$	air pressure
$Pr$	Prandtl number

---

\* Corresponding author. Tel.: +47 73 59 68 58; fax +47 73 59 46 37; e-mail: Arild.Gustavsen@bygg.ntnu.no

$Ra_L$	Rayleigh number, $gc_p\beta\Delta T\rho^2L^3/(\mu k)$
$R^\phi$	sum of residuals for variable $\phi$
$t$	time
$T$	temperature
$u, v, w$	velocity components in the x-, y- and z-directions
$x, y, z$	Cartesian coordinates
$W$	width of air cavity

#### *Greek symbols*

$\alpha$	thermal diffusivity
$\beta$	thermal expansion coefficient
$\phi$	variable in discretized equation
$\mu$	air viscosity
$\rho$	air density
$\tau$	time constant

#### *Subscripts*

$C$	cold
$H$	hot
$m$	mean value
$nb$	neighbor control volume
$P$	refers to control volume P
$r$	reference

## INTRODUCTION

Natural convection in vertical enclosures has been extensively studied numerically and experimentally. The practical aim has usually been to relate the heat transfer across the cavity to the temperature difference between the vertical sidewalls and the Rayleigh number. The main reason for the interest in this problem is that many engineering problems can be simplified to this geometry. These include the cooling of electronic equipment, airflow in rooms, and heat transfer through building sections. Among building sections, glazing cavities (i.e. in double pane windows) have received a lot of attention. Reviews of natural convection effects in general and natural convection correlations that have emerged from some of these

studies can be found in Raithby and Hollands [1]. Natural convection in enclosures is reviewed by e.g. Ostrach [2] and Hoogendoorn [3]. Zhao et al. [4] and Wright and Sullivan [5] review natural convection in glazing cavities and fenestration systems.

When researchers are searching for heat transfer correlations for natural convection in glazing cavities the typical geometry studied is a three-dimensional enclosure with large height,  $H$ , and width,  $W$ , and a small length,  $L$ , separating two isothermal panes. The other walls are either adiabatic or have a linear temperature profile. The vertical aspect ratio,  $H/L$ , usually ranges from 5 to 110, and in the experiments the horizontal aspect ratio,  $W/L$ , is usually larger than 5. Researchers often study a two-dimensional cavity in numerical simulations because of the large width of glazing cavities. Correlations that have emerged from these studies, and are used when rating fenestration products, only include the vertical aspect ratio  $H/L$  as a parameter, not  $W/L$ .

Some researchers have reported effects due to the width,  $W$ , of the cavity. ElSherbiny et al. [6] experimentally studied the effect of  $W/L$  for a cavity where  $H/L$  was held constant to 5. The heat transfer was measured along a strip (200 mm wide) lying midway between the two perfectly conducting edges (the total width,  $W$ , of the plates were 635 mm). For  $8 \times 10^3 < Ra_L < 2 \times 10^5$  the maximum difference between  $Nu$  for  $W/L = 5$  and  $Nu$  for  $W/L = 7.5$  was about 4.3 %. The corresponding difference in  $Nu$  for  $W/L = 7.5$  and  $Nu$  for  $W/L = 15$  was about 3 %. Outside this  $Ra_L$  range the differences in  $Nu$  caused by changes in  $W/L$  were negligible. Fusegi et al. [7] compared the overall Nusselt number for a three-dimensional cubical enclosure with the overall Nusselt number for the square two-dimensional enclosure. Their study was numerical and the walls were assumed to be adiabatic. They found that the Nusselt number for the three-dimensional cube was smaller than for the two-dimensional square for  $Ra_L < 10^5$ . The difference was about 8 % at most. At  $Ra_L = 10^6$  the difference was about 2 %.

Commercial façades, windows and door systems made today often include PVC sections or thermally broken aluminum sections. These have internal cavities. In the horizontal parts of such systems the two-dimensional correlations can be used with good approximation, because of the large width of the cavities. However in the vertical sections the width separating the lateral walls is small, more of the same order as the length separating the plates orthogonal to the heat flow direction. That is  $W/L \approx 1$  and  $H/L \approx 40 - 110$ . This paper studies the effect of  $W/L$  on the Nusselt number of cavities with high vertical aspect ratio for different Rayleigh numbers.

## MATHEMATICAL MODEL

The problem under consideration is shown in Figure 1. The flow domain is the interior of the three-dimensional cavity. The length  $L$  of the cavity separates two isothermal walls, one at a high temperature  $T_H$  and the other at a low temperature  $T_C$ . The other walls are adiabatic, although in the numerical simulations we used a symmetry condition at  $z = W/2$ . The interior of the cavity is filled with air.  $T_H$  is set equal to 293.15 K and  $T_C$  equal to 273.15, resulting in a mean temperature,  $T_m$ , of 283.15. Thus, the overheat ratio becomes  $\delta = (T_H - T_C)/T_C = 0.073$ . The small value of  $\delta$ , is less than 0.1 and allows the use of the Boussinesq approximation (see Zhong et al. [8]). The conductivity,  $k$ , specific heat capacity,  $c_p$ , coefficient of thermal expansion,  $\beta$ , and dynamic viscosity,  $\mu$ , are assumed to be constant and are evaluated at  $T_m$ . The Rayleigh number is changed by varying the pressure  $p$ , and the ideal gas law is then used to evaluate the density,  $\rho$ , at  $T_m$  and  $p$ .

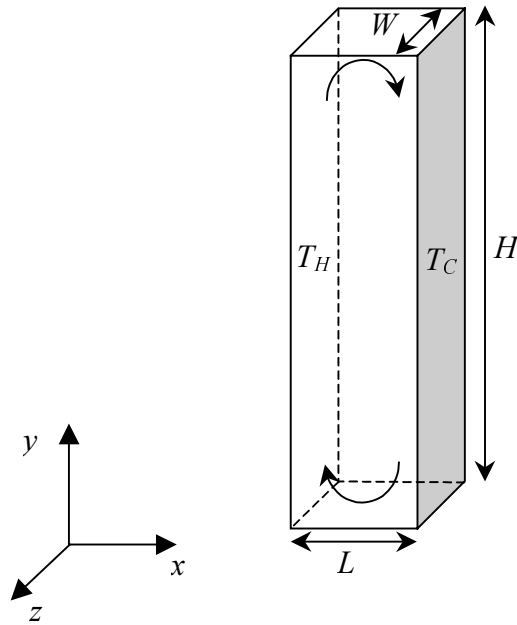


Figure 1 Schematic representation of cavity problem. The plates parallel to the page, and the top and bottom sides are adiabatic.

We used the commercial computational fluid dynamics (CFD) program FLUENT for the solution of the equations in this study (Fluent [9]). The governing equations for the system can be written using different notations. Here, we write the equations for a transient, three-dimensional, incompressible and laminar problem. We omit viscous dissipation and only consider the transport of one gas, air. The governing equations become

$$\frac{\partial \rho}{\partial t} + \rho \frac{\partial u}{\partial x} + \rho \frac{\partial v}{\partial y} + \rho \frac{\partial w}{\partial z} = 0 \quad (1)$$

$$\frac{\partial u}{\partial t} + \rho \frac{\partial}{\partial x}(uu) + \rho \frac{\partial}{\partial y}(vu) + \rho \frac{\partial}{\partial z}(wu) = -\frac{\partial p}{\partial x} + \frac{\partial}{\partial x}\left(\mu \frac{\partial u}{\partial x}\right) + \frac{\partial}{\partial y}\left(\mu \frac{\partial u}{\partial y}\right) + \frac{\partial}{\partial z}\left(\mu \frac{\partial u}{\partial z}\right) \quad (2)$$

$$\begin{aligned} \frac{\partial u}{\partial t} + \rho \frac{\partial}{\partial x}(uv) + \rho \frac{\partial}{\partial y}(vv) + \rho \frac{\partial}{\partial z}(wv) \\ = -\frac{\partial p}{\partial y} + \frac{\partial}{\partial x}\left(\mu \frac{\partial v}{\partial x}\right) + \frac{\partial}{\partial y}\left(\mu \frac{\partial v}{\partial y}\right) + \frac{\partial}{\partial z}\left(\mu \frac{\partial v}{\partial z}\right) - \rho g\beta(T - T_r) \end{aligned} \quad (3)$$

$$\frac{\partial u}{\partial t} + \rho \frac{\partial}{\partial x}(uw) + \rho \frac{\partial}{\partial y}(vw) + \rho \frac{\partial}{\partial z}(ww) = -\frac{\partial p}{\partial z} + \frac{\partial}{\partial x}\left(\mu \frac{\partial w}{\partial x}\right) + \frac{\partial}{\partial y}\left(\mu \frac{\partial w}{\partial y}\right) + \frac{\partial}{\partial z}\left(\mu \frac{\partial w}{\partial z}\right) \quad (4)$$

where Equation (1) is the equation for the conservation of mass and Equations (2)-(4) are the momentum equations for the  $x$ -,  $y$ -, and  $z$ -directions, respectively. The energy equation can be written

$$\rho c_p \frac{\partial T}{\partial t} + \rho c_p \frac{\partial}{\partial x}(uT) + \rho c_p \frac{\partial}{\partial y}(vT) + \rho c_p \frac{\partial}{\partial z}(wT) = \frac{\partial}{\partial x}\left(k \frac{\partial T}{\partial x}\right) + \frac{\partial}{\partial y}\left(k \frac{\partial T}{\partial y}\right) + \frac{\partial}{\partial z}\left(k \frac{\partial T}{\partial z}\right). \quad (5)$$

As stated above, the boundary conditions for the walls separating the isothermal walls are adiabatic. Previous researchers found that the difference between using an adiabatic and a linear temperature boundary condition on the top and bottom walls in two-dimensional studies was small for aspect ratios higher than  $H/L = 20$  (see e.g. Raithby and Wong [10]). However, that conclusion will probably not be the same considering the boundary condition of the other two walls (parallel to the  $x$ - $y$  plane in Figure 1). In this study we limit our attention to adiabatic walls only, except for the two isothermal walls. Thus, the boundary conditions can be written:

$$T = T_H \quad \text{at} \quad x = 0 \quad , \quad (6)$$

$$T = T_C \quad \text{at} \quad x = L \quad , \quad (7)$$

$$\frac{\partial T}{\partial y} = 0 \quad \text{at} \quad y = 0 \quad \text{and} \quad y = H \quad , \quad (8)$$

$$\frac{\partial T}{\partial z} = 0 \quad \text{at} \quad z = 0 \quad \text{and} \quad z = W \quad , \quad (9)$$

and

$$u = v = w = 0 \quad \text{at} \quad x = 0, x = L, y = 0, y = H, z = 0, \quad \text{and} \quad z = W \quad . \quad (10)$$

## NUMERICAL SCHEME AND METHOD OF SOLUTION

### Numerical Procedure

The CFD program uses a control-volume-based technique to convert the governing equations above to algebraic equations that can be solved numerically (Fluent [9]). The control volume technique consists of integrating the governing equations about each control-volume, which yield discrete equations that conserve each quantity on a control volume basis. That is, the complete geometry is divided into small control-volumes for which the discretized equations are solved. We used the program's segregated solver with double precision to solve the discretized equations. The segregated solver solves the different equations sequentially. After discretization, the conservation equation for a general variable  $\phi$  at cell  $P$  can be written as

$$a_p \phi_p = \sum_{nb} a_{nb} \phi_{nb} + b \quad (11)$$

where the subscript  $nb$  refers to neighbor cells,  $a_p$  and  $a_{nb}$  are the linearized coefficients of  $\phi_p$  and  $\phi_{nb}$ , and  $b$  is the source term. These equations are solved using a Gauss-Seidel linear equation solver in conjunction with an algebraic multigrid method.

The discrete values are stored at the center of each cell. However, when solving the equations, we also need face values for the variables in the convection terms. For the energy and momentum variables, these are found by using the QUICK (Quadratic Upstream Interpolation for Convective Kinetics) scheme. In addition, the CFD program uses central differences to approximate the diffusion terms and SIMPLER (Semi-Implicit Method for Pressure-Linked Equations Consistent) to couple the interaction between pressure and velocity. Fluent uses a pressure-interpolation scheme to find the pressure values at the cell faces. This is necessary because the program stores the pressure values in the cell centers just as it does for the rest of the variables. We decided to use the PRESTO (PREssure Staggering Option) scheme, which is like the staggered grid approach described by Patankar [11]. The PRESTO scheme is recommended for buoyancy flow and hexahedral meshes. Because the equations are non-linear we use relaxation for some of the variables to avoid divergence.

When solving the equations we experienced that a stationary solution procedure did not work for all cases and that not all problems had a stationary solution. That is, for most cases we found a stationary solution by using a stationary solution procedure, for other cases we found a stationary solution by using a transient approach, and for even other cases we did not find a

stationary solution at all. Convergence, when using the stationary solver, is determined by checking the scaled residuals (Fluent [9])

$$R^\phi = \frac{\sum_{cells P} \left| \sum_{nb} a_{nb} \phi_{nb} + b - a_P \phi_P \right|}{\sum_{cells P} |a_P \phi_P|} \quad (12)$$

and ensuring that they were less than  $10^{-5}$  for all variables except for the energy equation in which the residuals have to be less than  $10^{-6}$ . When this is not achieved we switch to a transient 1<sup>st</sup>-order implicit solver. Then convergence is determined by monitoring the heat flux through the warm side of the enclosure and the air temperature in the middle of the cavity. If these quantities converge toward a constant level we conclude that the problem has a stationary solution, and if not there is no stationary solution. If the last case arises we let the simulation run for a period of time and then report the time average of the Nusselt number.

### Grid Sizing and Sensitivity

Table 1 shows a list of the various geometries studied with information about the mesh density used. Further, Figure 2 shows the mesh for one of the enclosures,  $H/L = 20$  and  $W/L = 2$ . From the figure we see that we use equispaced grid spacing in the vertical direction ( $y$ -direction), except near the top and bottom walls where boundary-layer-meshing is employed. In the other directions we use gradual meshing with thinner control volumes close to the walls. The selection of mesh density was based on several considerations. We wanted to limit the number of mesh nodes to limit the computational time, but still be sure that our calculations were accurate. By looking at work by other researchers we found that Wright and Sullivan [12] used  $25 \times 200$  at  $H/L = 40$ , Ramanan and Korpela [13] used a  $32 \times 256$  grid at  $H/L > 17.5$ , and that Korpela et al. [14] used  $17 \times 65$  at  $10 < H/L < 20$ . Raithby and Wong [10] used a maximum of  $10 \times 66$ ,  $14 \times 98$  and  $18 \times 98$  for cavities with aspect ratios of 20, 40 and 80, respectively. A common feature of all of these studies is that they were two-dimensional and that they used an equispaced mesh. In a more recent study Lartigue et al. [15] found that approximately 30 000 grid nodes were necessary to obtain a grid independent solution for their two-dimensional cavity with an aspect ratio  $H/L = 40$ , however they do not say how the nodes were distributed. Most of the numerical three-dimensional simulations performed are for cubes or geometries close to the cube geometry (see e.g. Leong et al. [16], Fusegi et al. [7], or Ozoe et al. [17]). The selected mesh density, shown in Table 1, reflects some of the previous studies mentioned above and a mesh density study performed for some of the studied geometries. For instance for  $(H/L, W/L) = (20, 5)$  we found that a refinement of

the mesh from  $(nx,ny,nz) = (25,108,33)$  to  $(35,148,48)$  resulted in a change of the average Nusselt number of 0.3% at  $Ra = 10^5$ . For  $(H/L,W/L) = (40,1)$  we found that a refinement of the mesh from  $(25,208,12)$  to  $(35,288,27)$  resulted in a change of the average Nusselt number of 0.1 % at  $Ra = 1.42 \times 10^4$ . Another requirement, fulfilled with the mesh used, is that at least one computational node is inside the boundary layer.

Table 1. Aspect ratios and mesh resolution  $(nx,ny,nz)$  of the studied specimens (symmetry boundary condition was employed in the  $z$ -direction). The last row shows the mesh density for the two-dimensional simulations.

$H/L \backslash W/L$	20	40	80
0.2	(25,108,12)	(25,208,12)	(25,408,12)
0.5	(25,108,12)	(25,208,12)	(25,408,12)
1	(25,108,12)	(25,208,12)	(25,408,12)
2	(25,108,13)	(25,208,13)	(25,408,13)
5	(25,108,33)	(25,208,33)	(25,408,33)
N/A (2D, $W/L \rightarrow \infty$ )	(25,108)	(25,208)	(25,408)

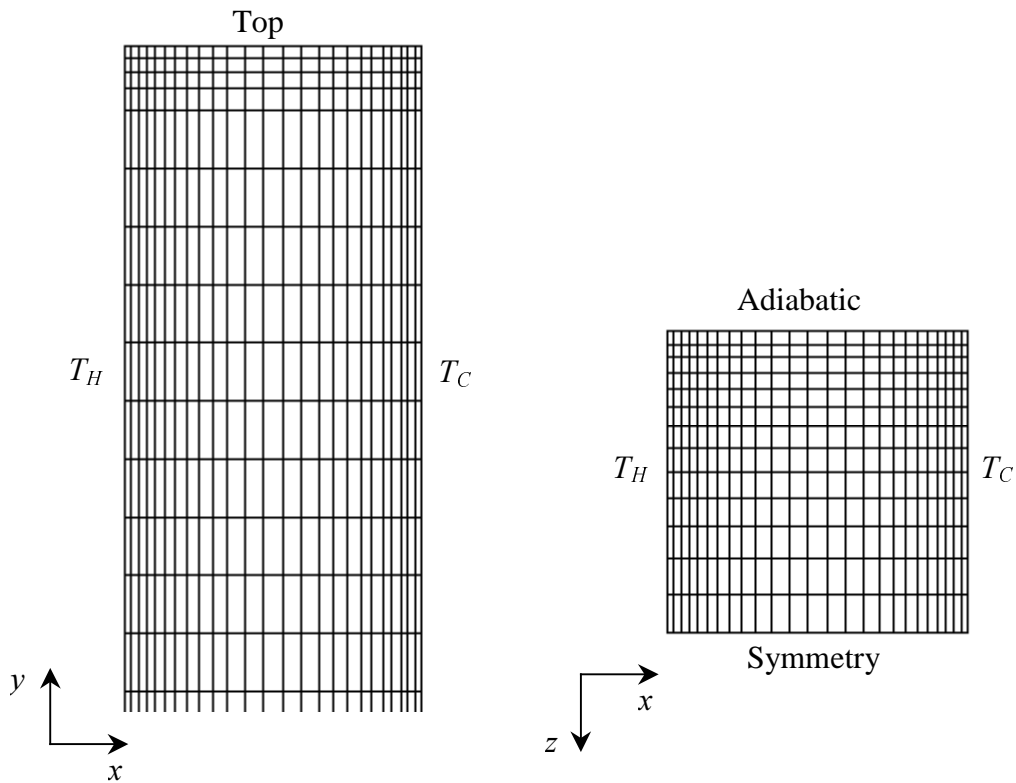


Figure 2. Different views of the mesh for a cavity where  $H/L = 20$  and  $W/L = 2$ . The mesh density is  $(nx,ny,nz) = (25,108,13)$ . The left-hand figure shows the upper part of the cavity and the right-hand figure a cross section parallel to the  $x$ - $z$  plane.

As shown in Figure 2 we use a symmetry boundary condition at  $z = W/2$  to limit the number of computational cells. This is a significant assumption, however, we still pursued using this assumption to limit the computational time. The significance of this assumption on the average Nusselt number was checked for two cavities and is discussed in the results and discussion section.

## RESULTS AND DISCUSSION

### Comparison with Previous Results

For high aspect ratio cavities like those typically found in glazing cavities it is known that secondary flow (multicellular flow) can exist (see Lartigue et al. [15], Zhao et al. [18], Wright and Sullivan [12] or Korpela et al. [14]). Therefore we want to check if the CFD program is capable of simulating such a flow, even though secondary flow does not necessarily exist for cavities with a low width-to-length aspect ratio.

Table 2. Comparison of average Nusselt numbers for two-dimensional cavities

H/L	Ra	Present study (numerical)	Zhao [19] (numerical)	Raithby and Wong [10] (numerical)	ElSherbiny et al. [6] (experimental)
20	$1 \times 10^3$	1.022	1.027	1.02	1.008
	$1 \times 10^4$	1.404 <sup>a</sup>	1.419	1.37	1.404
	$1 \times 10^5$	2.710	2.668	2.66	2.971
40	$1 \times 10^3$	1.011	1.010	1.01	1.000
	$5 \times 10^3$	1.093	1.088	N/A	1.034
	$1 \times 10^4$	1.256 <sup>a</sup>	1.272	1.19	1.240
80	$1 \times 10^3$	1.006	1.003	1.01	1.000
	$5 \times 10^3$	1.047	1.036	N/A	1.018

Two different two-dimensional cases that are known to produce secondary flow were tested (see Zhao et al. [18]), one cavity with an aspect ratio of 20 and another with an aspect ratio of 40. Both were simulated with a Rayleigh number of  $10^4$ . We got multicellular flow for both cases. Table 2 compares the average Nusselt number for both these cavities and also for a cavity with an aspect ratio of  $H/L = 80$  to results from Zhao [19], Raithby and Wong [10], and ElSherbiny et al. [6]. Other Rayleigh numbers are also included. We see that our results compare well to the other researchers' results. In our simulations the cavities had two

---

<sup>a</sup> Secondary (multicellular) flow

isothermal sidewalls separated by two horizontal adiabatic walls, the same as Zhao (1998) and Raithby and Wong [10]. ElSherbiny et al. [6] studied a cavity with two isothermal walls separated by perfectly conducting walls.

### Effect of Symmetry Boundary Condition

As stated previously, we decided to use a symmetry boundary condition at  $z = W/2$  when simulating the cavities. Here we test how this assumption influences the final average Nusselt number and also if it changes the temperature and velocity distribution in the cavity. Two cavities were tested at  $Ra = 10^4$ , one which was found not to experience secondary flow,  $H/L = 20$  and  $W/L = 1$ , and another which was found to have secondary flow,  $H/L = 20$  and  $W/L = 5$ . The number of nodes used for the complete version of the first cavity,  $H/L = 20$  and  $W/L = 1$ , were  $(nx,ny,nz) = (25,108,24)$ , and the number of nodes used for the complete version of the second cavity,  $H/L = 20$  and  $W/L = 5$ , were  $(nx,ny,nz) = (25,108,66)$ . For the first enclosure we found that the Nusselt number of the symmetry-boundary-condition cavity was  $Nu = 1.26910$ , and that the Nusselt number of the complete cavity, not using a symmetry boundary condition, was  $Nu_c = 1.26896$ . In addition to the good agreement between the Nusselt numbers we found that the temperature and velocity magnitude along a vertical line in the middle of each cavity overlapped.

We did not find a stationary solution for the other case,  $H/L = 20$  and  $W/L = 5$ . Therefore, to be able to check the influence of the symmetry boundary condition, we decided to use a transient solution approach and monitor heat flux through the warm side of the enclosure and air temperature in the middle of the cavity. The initial temperature in the cavity was set to 273.15 K, and the air velocity to 0 m/s in all directions. We set the time step,  $\Delta t$ , to 0.02 s. The specific time step was chosen from calculating the time constant,  $\tau$ , and dividing that by 10, an approach suggested by Fluent [9]. The time constant was calculated from (Fluent [9])

$$\tau = \frac{L}{U} \sim \frac{L^2}{\alpha} (\text{Pr } Ra)^{-1/2} = \frac{L}{\sqrt{g\beta\Delta TL}} \quad (13)$$

We let the simulation run for 60 seconds, and found that the temperature in the middle of the cavity overlapped throughout that period of time. The heat flux curves experienced the same shape, however they were shifted somewhat relative to each other. That is, the symmetry case gave a little higher heat flux through the cavity than the complete case. This difference in heat flux only results in a difference in the Nusselt number of 1 % (this might be different for other

cavities and Rayleigh numbers). Therefore, we decided to continue using the symmetry boundary condition.

### Nusselt Number for Three-dimensional Cavities

Table 3 shows the average Nusselt number as function of the Rayleigh number,  $Ra$ , the horizontal aspect ratio,  $W/L$ , and the vertical aspect ratio,  $H/L$ . Results for two-dimensional cavities are also included. Footnotes note when multicellular or transient flow appears and if we use a transient solution procedure. For some of the cavities we see that the results are included for low horizontal aspect ratios,  $W/L \leq 1$ , but not for high horizontal aspect ratios and the two-dimensional cases. The reason for this is that Yin et al. [20] report transition to turbulent flow for two-dimensional cavities close to and above the last reported  $Ra$ , and that we did not find a stationary solution for these cases. Results are reported for  $W/L \leq 1$  because here we find stationary solutions. Also, previous two-dimensional numerical studies of Nusselt numbers tend to diverge from experimental results when the Rayleigh number gets close to the turbulent transition zone (we can also see this in Table 2). We cannot say whether the 3D simulations compare to experiments at high Rayleigh numbers for cavities with a low horizontal aspect ratio because no experimental results exist for such cases.

Table 3 shows that all two-dimensional cavities have a stationary solution, even though for some of the cavities we have to use a transient solution procedure. However, this does not mean that there necessarily exists a stationary solution for three-dimensional cavities at the same Rayleigh numbers. From the table we see that for the cavities with a vertical aspect ratio of  $H/L = 20$  we do not find a stationary solution for  $W/L = 5$  at  $Ra = 1 \times 10^4$  and  $2 \times 10^4$ . For cavities with an aspect ratio of  $H/L = 40$  we find similar results for  $W/L = 5$  at  $Ra = 1 \times 10^4$  and  $1.42 \times 10^4$ , and for  $W/L = 2$  at  $Ra = 1.42 \times 10^4$ . Whether this is because the flow becomes turbulent at lower Rayleigh numbers within these cavities or because the flow only becomes transient it is difficult to say. We did not search for particular or repeating patterns in the transient results. The only three-dimensional cavity for which we find a stationary multicellular flow is the cavity with a vertical aspect ratio of  $H/L = 20$  and a horizontal aspect ratio of  $W/L = 2$  at  $Ra = 2 \times 10^4$ . This case is studied in detail below.

Figure 3 displays data for the  $H/L = 20$  cavity graphically, and compares the data to the correlation of ElSherbiny et al. [6]. The vertical axis shows the Nusselt number and the horizontal axis the Rayleigh number. Different symbols are used for the various horizontal aspect ratios. Figure 4 is a diagram of the data for the  $H/L = 40$  cavity. We see that the

agreement between the correlations of ElSherbiny et al. [6] and our data is good for  $Ra$  less or equal to  $10^4$ . For higher  $Ra$ , our Nusselt numbers tend to be smaller, also for the two-dimensional cavity. This is similar to what other investigators have found (see e.g. Zhao et al. [4]), comparing two-dimensional numerical results to the experimental results of ElSherbiny et al. [6]. Considering the difference between two-dimensional and three-dimensional results we do not find a large difference between the  $W/L = 5$  cavity and our two-dimensional simulations. For  $H/L = 20$  we find that the maximum difference is 2.5 %, and for  $H/L = 40$  we find a maximum difference of 3.7 %. For both cavities the maximum difference is found for a

Table 3. The calculated values of average Nusselt numbers,  $Nu$ .  $W/L = \infty$  indicates a two-dimensional cavity.

$H/L$	$Ra$	$W/L$					
		$\infty$	5	2	1	0.5	0.2
20	$1 \times 10^3$	1.022	1.020	1.017	1.012	1.005	1.001
	$2 \times 10^3$	1.062	1.056	1.049	1.037	1.018	1.002
	$5 \times 10^3$	1.186	1.173	1.154	1.124	1.072	1.011
	$1 \times 10^4$	1.404 <sup>a</sup>	1.369 <sup>a,b</sup>	1.326	1.269	1.169	1.037
	$2 \times 10^4$	1.698 <sup>a,c</sup>	1.671 <sup>a,b</sup>	1.617	1.532	1.359	1.100
	$5 \times 10^4$	2.237 <sup>c</sup>	2.196	2.136	2.037	1.823	1.295
	$1 \times 10^5$	2.710	2.670	2.612	2.506	2.291	1.606
40	$1 \times 10^3$	1.011	1.010	1.008	1.006	1.003	1.000
	$2 \times 10^3$	1.031	1.028	1.024	1.018	1.009	1.001
	$5 \times 10^3$	1.093	1.086	1.077	1.062	1.036	1.006
	$1 \times 10^4$	1.256 <sup>a</sup>	1.210 <sup>a,b</sup>	1.164	1.135	1.084	1.019
	$1.42 \times 10^4$	1.354 <sup>a,c</sup>	1.335 <sup>a,b</sup>	1.236 <sup>a,b</sup>	1.196	1.125	1.031
	$2 \times 10^4$			1.416 <sup>a</sup>	1.279	1.181	1.050
	$5 \times 10^4$				1.650	1.460	1.148
80	$1 \times 10^3$	1.006	1.005	1.004	1.003	1.001	1.000
	$2 \times 10^3$	1.015	1.014	1.012	1.009	1.004	1.000
	$5 \times 10^3$	1.047	1.043	1.038	1.031	1.018	1.003
	$1 \times 10^4$				1.067	1.042	1.009
	$2 \times 10^4$				1.140	1.090	1.025
	$5 \times 10^4$				1.353	1.233	1.074
	$1 \times 10^5$				1.654	1.464	1.154

<sup>a</sup> Secondary (multicellular) flow

<sup>b</sup> The simulation did not converge. The Nusselt number noted is the time average, found from letting the simulation run for a period of time using a transient solution procedure.

<sup>c</sup> The case converged against a constant value of heat flow through the cavity and a constant temperature in the middle of the cavity using a transient solution procedure.

Rayleigh number of  $10^4$ . Because of the small difference, it seems reasonable to treat three-dimensional cavities with horizontal aspect ratios,  $W/L$ , larger than 5 as two-dimensional cavities, considering Nusselt number predictions. However, when studying flow velocity pattern, and local temperature effects the third dimension needs to be taken into account. When the horizontal aspect ratio is equal to 2 and lower, we find that the difference between the two-dimensional and the three-dimensional cavities is larger than 5 %. It seems that similar conclusions can be drawn for the  $H/L = 80$  cavities, although we have little data.

### Nusselt Number Correlations

An attempt was made to find a simple equation that can correlate all the data, however the resulting equation was not accurate enough. Therefore we decided to correlate the data to one equation at each horizontal aspect ratio,  $W/L$ . Interpolation can then be used at intermediate  $W/L$ . The equation chosen is

$$Nu = \left[ 1 + (a \cdot Ra^b)^c \right]^{1/c}, \quad (14)$$

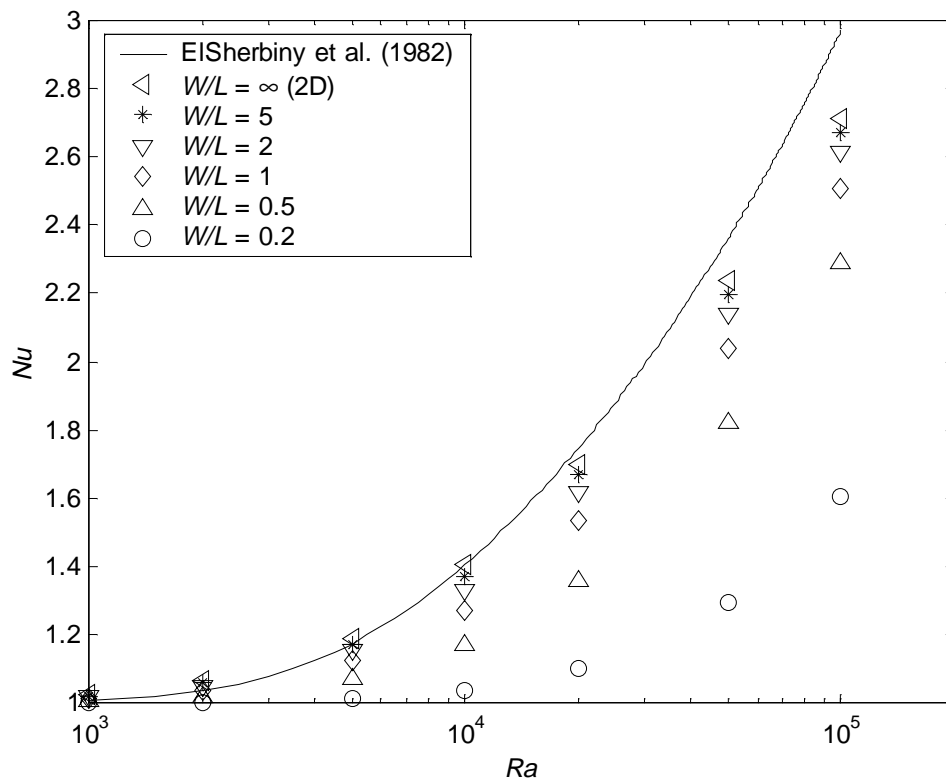


Figure 3. Average Nusselt number plotted as function of the Rayleigh number,  $Ra$ , for different horizontal aspect ratios,  $W/L$ . The vertical aspect ratio,  $H/L$ , is equal to 20.

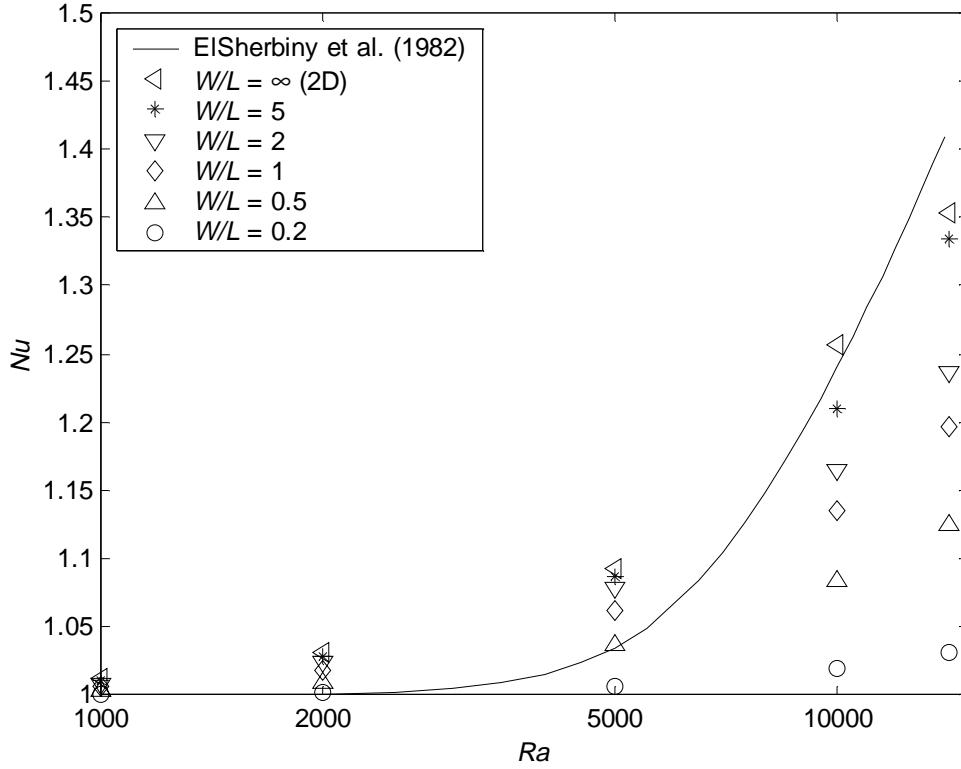


Figure 4. Average Nusselt number plotted as function of the Rayleigh number,  $Ra$ , for different horizontal aspect ratios,  $W/L$ . The vertical aspect ratio,  $H/L$ , is equal to 40.

where  $a$ ,  $b$  and  $c$  are constants. The equation is based on a correlation suggested by ElSherbiny et al. [6]. Table 4 shows correlation coefficients for different horizontal aspect ratios,  $W/L$ . For the  $H/L = 20$  cavity the equation should only be used within the bounds formed by the maximum and minimum values of  $Ra$  and  $W/L$  in Table 3. For the  $H/L = 40$  cavity the correlation is valid for  $0.2 \leq W/L \leq 5$  and  $1 \times 10^3 \leq Ra \leq 1.42 \times 10^4$ . For  $H/L = 20$  the data agree with Equation (14), when using the coefficients in Table 4, to within 1.4 % (maximum deviation) and with a standard deviation of 0.0220. For  $H/L = 40$  the respective data are 0.5 % and 0.0054.

### Multicellular Flow in a Three-Dimensional Cavity

Above we noted that we got stationary multicellular flow for the  $(H/L, W/L) = (40, 2)$  cavity at  $Ra = 2 \times 10^4$ . In Figures 5 through 9 we visualize the temperature and flow pattern in this cavity.

Figure 5 shows the temperature contours at five  $z$ -locations. From the diagrams we see that the shape of the isotherms changes depending on the  $z$  position. Figure 6 shows  $x$ -,  $y$ -, and  $z$ -velocity contours at different heights,  $y$ , in the cavity. Figures 7, 8, and 9 also display velocity

contours, however now for planes that are parallel to the  $y$ - $z$  plane (see Figure 1). Figure 7 is a diagram of the  $x$ -velocity contours, Figure 8 displays  $y$ -velocity contours, and Figure 9 shows  $z$ -velocity contours. The separate colour bar to the right of each diagram shows the relation between the gray scale and velocity. Because we used a symmetry boundary condition in the simulations, each diagram in Figures 6 through 9 is made by mirroring data around the symmetry plane. The figures show a complex flow. Not only do we see secondary flow in the  $x$ -direction (between the isothermal walls), but also in the other directions.

Table 4. Correlation coefficients

H/L	W/L	a	b	c
20	0.2	0.0018	0.5752	2.22561
	0.5	0.0328	0.3683	4.0544
	1	0.0449	0.3493	3.7586
	2	0.0750	0.3086	5.5801
	5	0.0721	0.3143	4.7615
40	0.2	0.0013	0.5907	2.5163
	0.5	0.0061	0.4922	2.6166
	1	0.0074	0.4895	2.5053
	2	0.0111	0.4599	2.6705
	5	0.0038	0.5852	2.5197

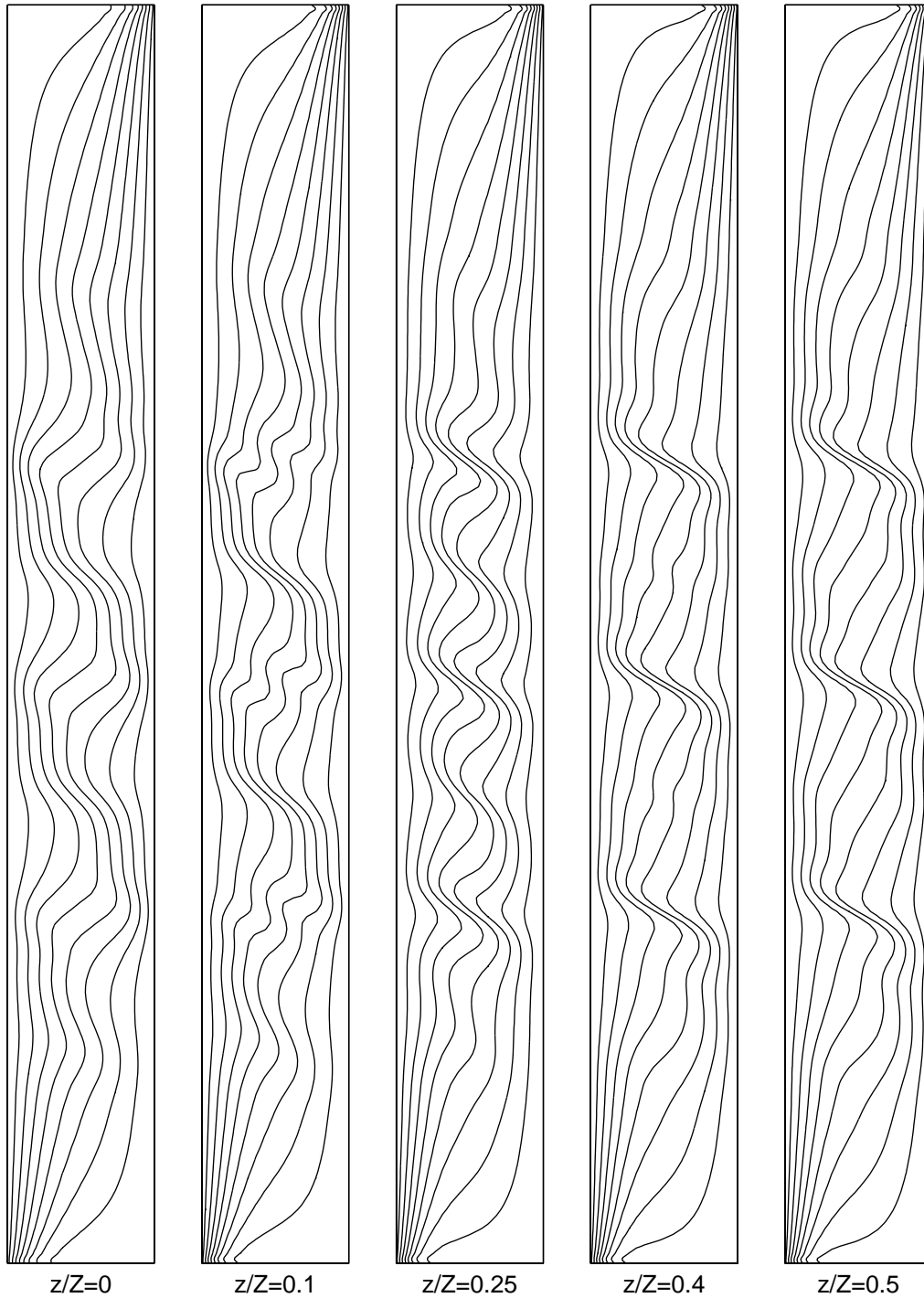


Figure 5. Temperature contours at different places in the  $(H/L, W/L) = (40, 2)$  cavity. Each plane is parallel to the  $x$ - $y$ -plane in Figure 1.  $Z$  is the total width of the cavity. The figures are stretched in the  $x$ -direction.

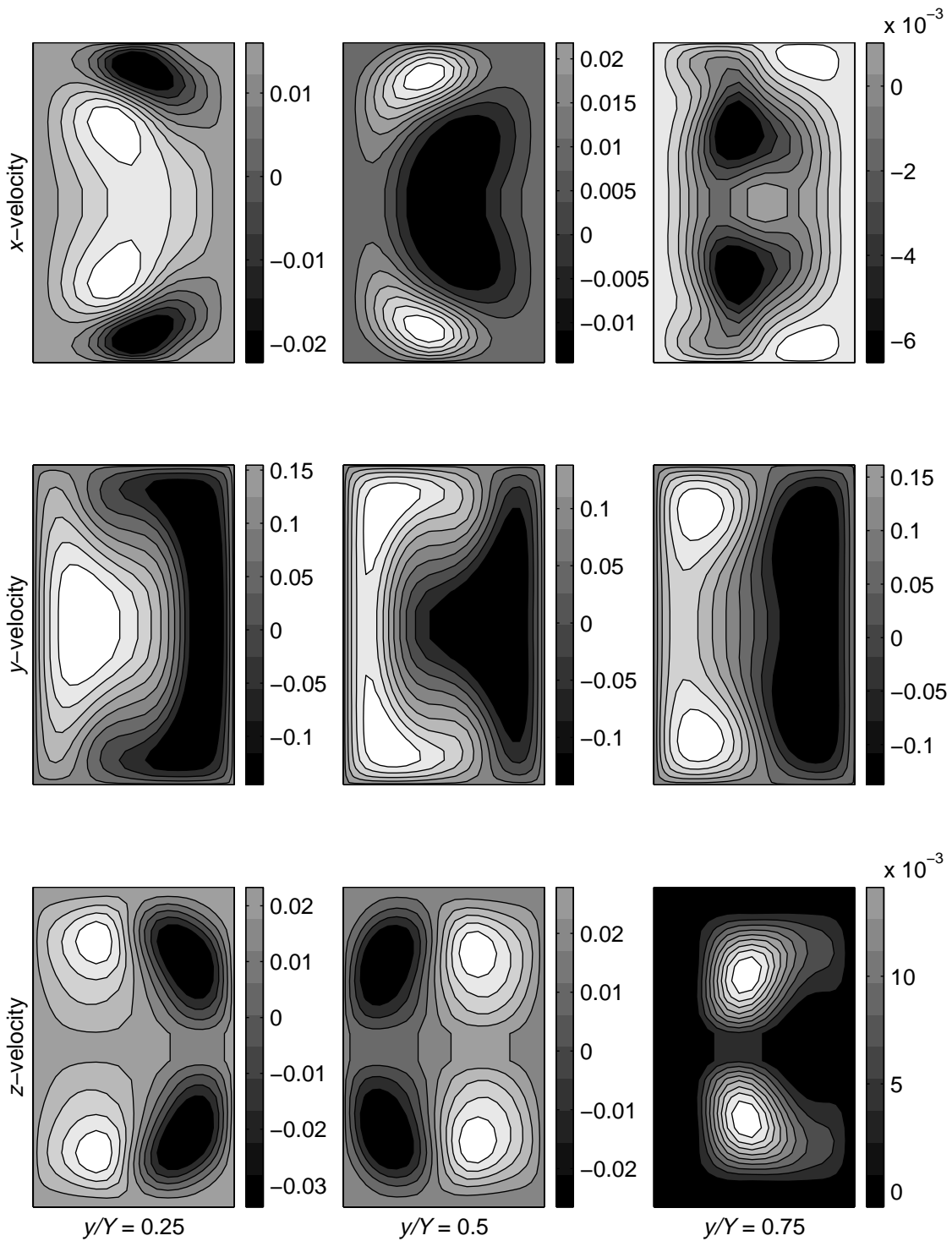


Figure 6. Velocity (m/s) contours at different heights in the  $(H/L, W/L) = (40, 2)$  cavity. Each plane is parallel to the  $x$ - $z$ -plane in Figure 1.  $Y$  is the total height of the cavity. The warm side of the cavity is to the left, the  $x$ -vector is pointing from left to right, the  $y$ -vector is pointing out of the page, and the  $z$ -vector is pointing from top to bottom. The figures are not in the correct scale.

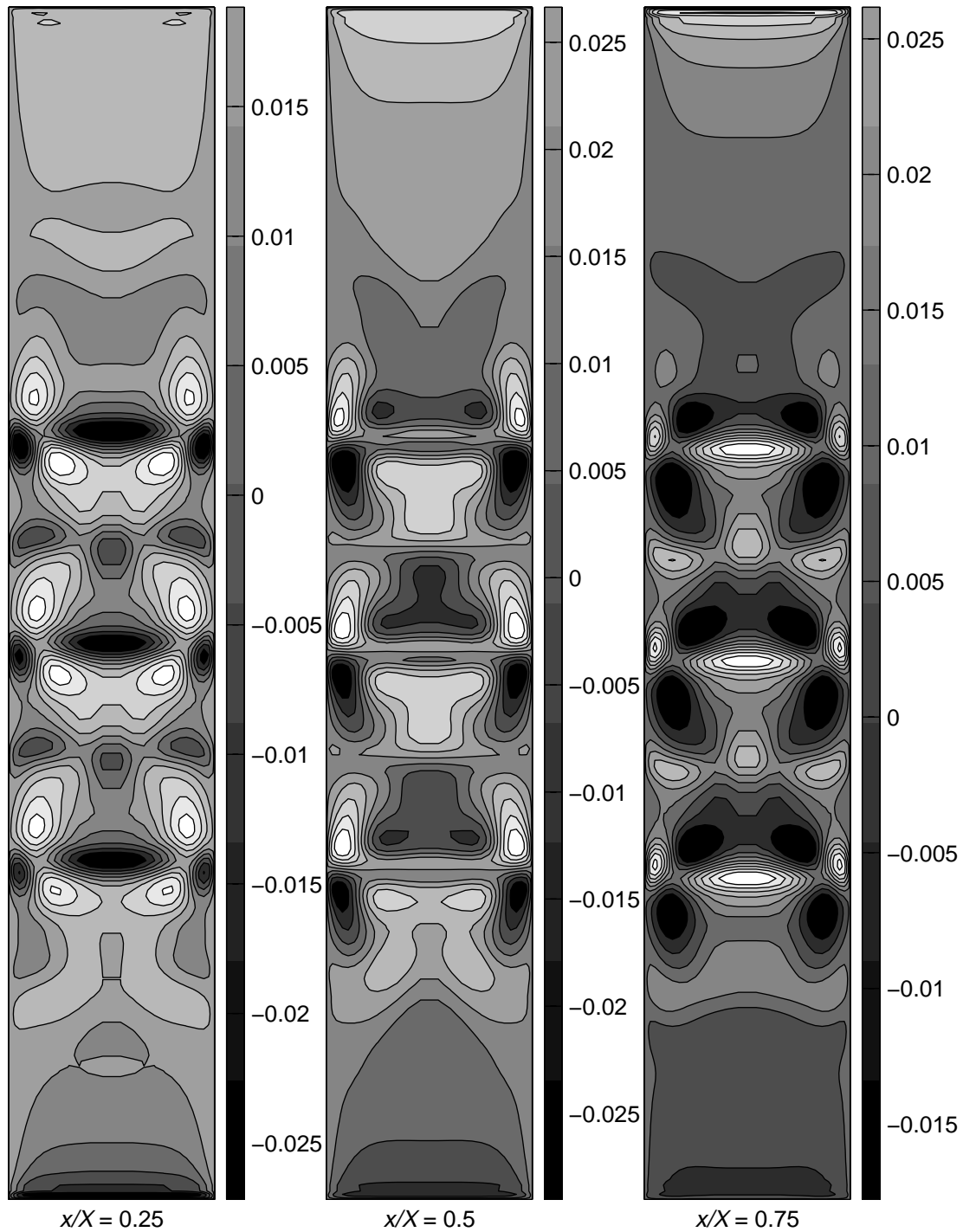


Figure 7.  $x$ -velocity contours (m/s) for different planes in the  $(H/L, W/L) = (40, 2)$  cavity. Each plane is parallel to the  $y$ - $z$ -plane in Figure 1.  $X$  is the total length of the cavity. The  $x$ -vector is pointing into the page, the  $y$ -vector is pointing from bottom to top, and the  $z$ -vector is pointing from left to right. The figures are not in the correct scale.

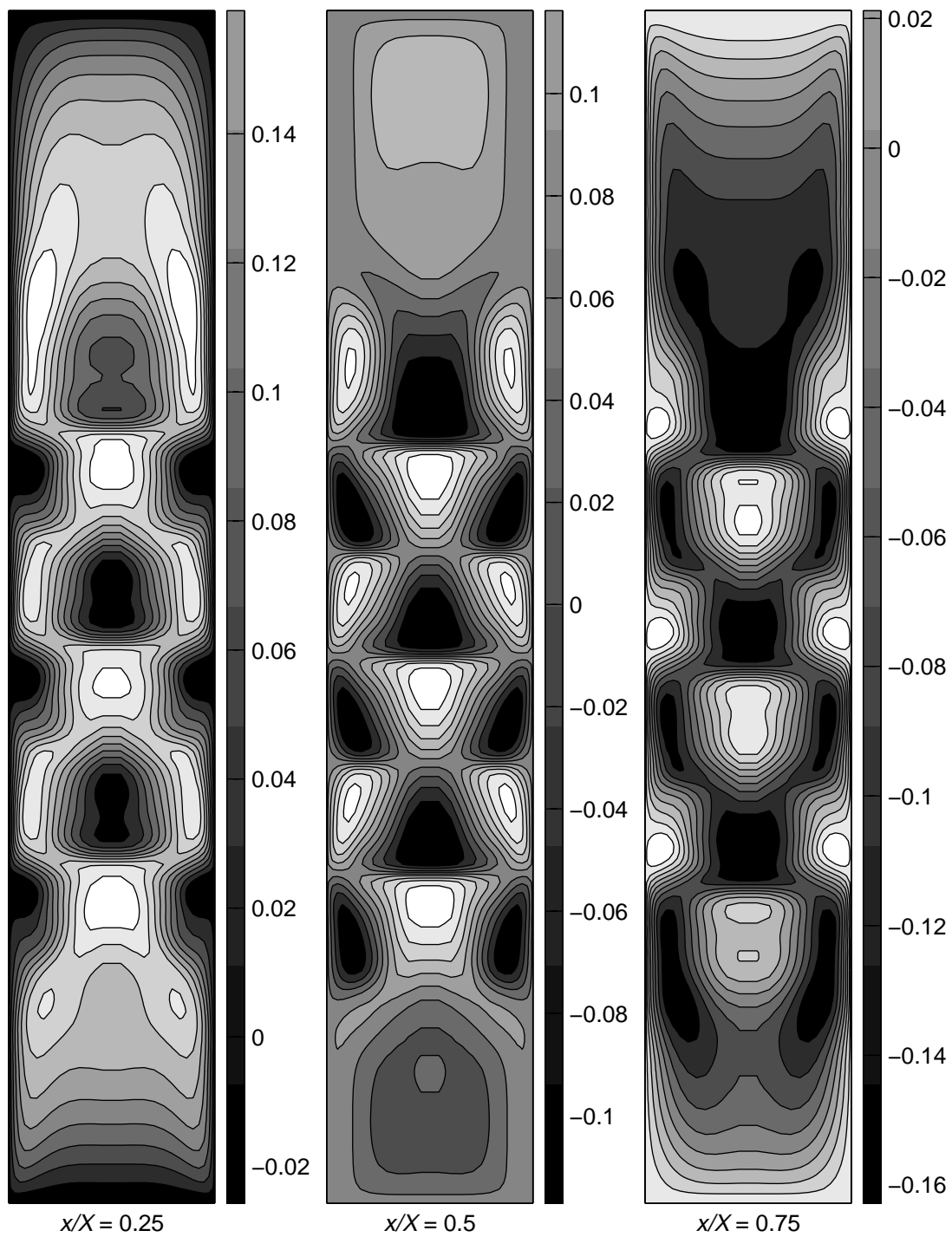


Figure 8.  $y$ -velocity contours (m/s) at different planes in the  $(H/L, W/L) = (40, 2)$  cavity. Each plane is parallel to the  $y$ - $z$ -plane in Figure 1.  $X$  is the total length of the cavity. The  $x$ -vector is pointing into the page, the  $y$ -vector is pointing from bottom to top, and the  $z$ -vector is pointing from left to right. The figures are not in the correct scale.

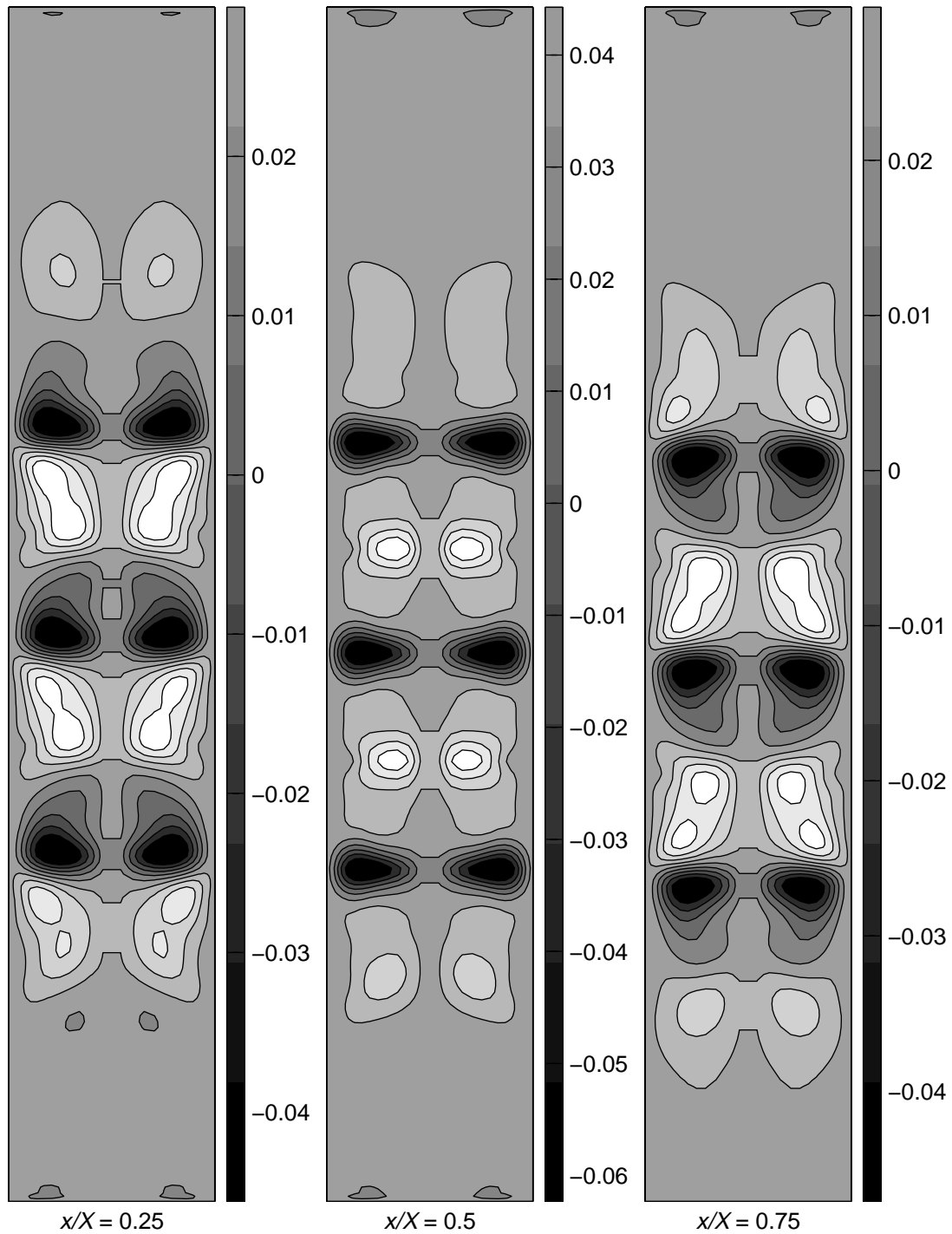


Figure 9.  $z$ -velocity contours (m/s) at different planes in the  $(H/L, W/L) = (40, 2)$  cavity. Each plane is parallel to the  $y$ - $z$ -plane in Figure 1.  $X$  is the total length of the cavity. The  $x$ -vector is pointing into the page, the  $y$ -vector is pointing from bottom to top, and the  $z$ -vector is pointing from left to right. The figures are not in the correct scale.

## CONCLUSIONS

Natural convection in three-dimensional enclosures with a vertical aspect ratios of 20, 40, and 80 and horizontal aspect ratios between 5 and 0.2 were simulated. The cavities had two opposite isothermal and four adiabatic walls. Nusselt numbers were found for Rayleigh numbers ranging from  $10^3$  to  $10^5$ . The simulations show that cavities with a horizontal aspect ratio larger than 5 can be considered as two-dimensional cavities with respect to heat transfer rates (to an accuracy of about 4 %). However, the cavities need to be simulated in all three dimensions when studying velocity and temperature pattern. Stationary results for two-dimensional cavities do not automatically mean that there are stationary solutions for three-dimensional cavities. Results for one cavity show that the flow gets complex when multicellular flow appears in a three-dimensional cavity. Nusselt number correlations are presented at different horizontal aspect ratios, and we suggest interpolation to get Nusselt numbers for intermediate aspect ratios. Future research should try to verify the complexity of the flow in three-dimensional cavities and extend the Rayleigh number range for the correlations.

## ACKNOWLEDGMENTS

This work was supported by Hydro Aluminum.

## REFERENCES

1. G. D. Raithby and K. G. T. Hollands, Natural convection. In: *Handbook of heat transfer, Third edition*. (Edited by W.M. Rosenhow, J.P. Hartnett. and Y.I. Cho), Chap. 4. McGraw-Hill (1998).
2. S. Ostrach, Natural convection in enclosures, *Journal of Heat Transfer Transactions of the ASME* **110**, 1175-1190 (1988).
3. C. J. Hoogendoorn, Natural convection in enclosures, *Proceedings of the Eighth International Heat Transfer Conference*, Vol. 1, pp. 111-120. Hemisphere, Washington D.C. (1986).
4. Y. Zhao, D. Curcija and W. P. Goss, Convective heat transfer correlations for fenestration glazing cavities: A review, *ASHRAE Transactions* **105** (1999).

5. J. L. Wright and H. F. Sullivan, Natural convection in sealed glazing units: A review, *ASHRAE Transactions* **95**, 592-603 (1989).
6. S. M. ElSherbiny, G. D. Raithby and K. G. T. Hollands, Heat transfer by natural convection across vertical and inclined air layers, *Journal of Heat Transfer Transactions of the ASME* **104**, 96-102 (1982).
7. T. Fusegi, M. Hyun, K. Kuwahara and B. Farouk, A numerical study of three-dimensional natural convection in a differentially heated cubical enclosure, *International Journal of Heat and Mass Transfer* **34**, 1543-1557 (1991).
8. Z. Y. Zhong, K. T. Yang and J. R. Lloyd, Variable property effects in laminar natural convection in a square enclosure, *Journal of Heat Transfer Transactions of the ASME* **107**, 133-138 (1985).
9. Fluent, *Fluent 5 User's Guide*. Fluent Incorporated, Lebanon, UK. (1998).
10. G. D. Raithby and H. H. Wong, Heat transfer by natural convection across vertical air layers, *Numerical Heat Transfer* **4**, 447-457 (1981).
11. S. V. Patankar, *Numerical heat transfer and fluid flow*. Hemisphere, Washington, D.C. (1980).
12. J. L. Wright and H. F. Sullivan, A two-dimensional numerical model for natural convection in a vertical, rectangular window cavity, *ASHRAE Transactions* **100**, 1193-1206 (1994).
13. N. Ramanan and S. A. Korpela, Multigrid solution of natural convection in a vertical slot, *Numerical Heat Transfer, Part A* **15**, 323-339 (1989).
14. S. A. Korpela, Y. Lee and J. E. Drummond, Heat transfer through a double pane window, *Journal of Heat Transfer Transactions of the ASME* **104**, 539-544 (1982).
15. B. Lartigue, S. Lorente and B. Bourret, Multicellular natural convection in a high aspect ratio cavity: experimental and numerical results, *International Journal of Heat and Mass Transfer* **43**, 3157-3170 (2000).

16. W. H. Leong, K. G. T. Hollands, and A. P. Brunger, On a physically-realizable benchmark problem in internal natural convection, *International Journal of Heat and Mass Transfer* **41**, 3817-3828 (1998).
17. H. Ozoë, T. Okamoto, S. W. Churchill and H. Sayama, Natural convection in doubly inclined rectangular boxes, *Proceedings of the Sixth International Heat Transfer Conference*, Vol. 2, pp. 293-298. Toronto, Canada (1978).
18. Y. Zhao, D. Curcija and W. P. Goss, Prediction of the multicellular flow regime of natural convection in fenestration glazing cavities, *ASHRAE Transactions* **103** (1997).
19. Y. Zhao, Investigation of heat transfer performance in fenestration system based on finite element methods, Ph.D. Thesis, University of Massachusetts, Amherst, Massachusetts (1998).
20. S. H. Yin, T. Y. Wung and K. Chen, Natural convection in an air layer enclosed within rectangular cavities, *International Journal of Heat and Mass Transfer* **21**, 307-315 (1978).



## Paper IV

Spectral Emissivity of Anodized Aluminum and the Thermal Transmittance of Aluminum Window Frames

*Nordic Journal of Building Physics*, submitted

Arild Gustavsen and Paul Berdahl



# Spectral Emissivity of Anodized Aluminum and the Thermal Transmittance of Aluminum Window Frames

SUBMITTED: June 2001.  
REVISED: XXX.  
PUBLISHED: XXX.

*Arild Gustavsen, University Lecturer,  
Department of Building and Construction Engineering  
Norwegian University of Science and Technology  
N-7040 Trondheim, Norway;  
email: [Arild.Gustavsen@bygg.ntnu.no](mailto:Arild.Gustavsen@bygg.ntnu.no)  
<http://www.bygg.ntnu.no/batek/personal/gustavsen/>*

*Paul Berdahl, Physicist,  
Heat Island Group  
Environmental Energy Technologies Division  
Ernest Orlando Lawrence Berkeley National Laboratory  
Berkeley, CA 94720, USA;  
email: [PHBerdahl@lbl.gov](mailto:PHBerdahl@lbl.gov)*

**KEYWORDS:** *Spectral emissivity, Anodized aluminum, Masking tape, Fenestration, Window frames, Thermal transmittance.*

## **SUMMARY:**

*This paper studies the normal spectral emissivity of an anodized aluminum window frame profile, an untreated aluminum profile, and some masking tapes. The normal spectral emissivity is measured in the wavelength interval from 4.5 to 40  $\mu\text{m}$  (wavenumbers 2222  $\text{cm}^{-1}$  to 250  $\text{cm}^{-1}$ ). Total emissivity values are also reported. Specimens are cut both from the edge and from the middle of the six-meter long anodized aluminum profile. Specimens facing the internal cavities (thermal break cavity and all aluminum cavity) are measured. The masking tapes are of the types used in measurements of thermal transmittance (U-value) of window frames. It is shown that the normal total emissivity is fairly constant (between 0.834 and 0.856) for exterior parts of the anodized profile and for surfaces facing the thermal break cavity. The normal total emissivity of the all-aluminum internal cavities is found to vary between 0.055 and 0.82. For two of the tapes measured, the normal spectral emissivity is found to be fairly independent of wavelength for wavelength between 6.5 and 40  $\mu\text{m}$ .*

## 1. Introduction

Heat transfer in building sections is a combined process involving conduction, convection and radiation. Conduction takes place in solid materials while convection and radiation takes place both at the exterior surfaces of building sections and in the internal cavities of building sections. Radiation heat transfer depends on the emissivity of building sections, the temperature differences between the surfaces within building sections, and on the temperature differences between the exterior faces of building sections and the exterior environment. Since the temperature difference usually not can be controlled to reduce heat transfer through building sections the emissivity is the parameter that needs to be reduced to minimize radiation heat transfer effects.

When calculating the thermal transmittance (or  $U$ -value) of aluminum window frames the usual approach, although not explicitly stated, is to use the emissivity of the material that is expected after years of use and wear rather the emissivity value at fabrication time. This leads to use of a low emissivity ( $\epsilon = 0.2$ ) for metallic surfaces and a high emissivity ( $\epsilon = 0.9$ ) for treated (e.g. anodized or painted) aluminum surfaces (Mitchell et al. 2000). This applies both to exterior parts of aluminum profiles and interior surfaces of the cavities. Generally the emissivity of aluminum will depend on oxide layer thickness. Polished aluminum (not oxidized) can have a hemispherical total emissivity as low as 0.04 (Touloukian and Dewitt 1970). However, aluminum exposed to the environment will grow an oxide layer. This layer protects the aluminum beneath the oxide layer from further oxidation. Touloukian and Dewitt (1970) reports that an aluminum foil exposed to the salt and moist environment at the seashore for two years get a normal total emissivity of 0.1. Handbooks (see e.g. VDI-Wärmeatlas 1997 or Lide 1993) report that heavily oxidized aluminum has a hemispherical total emissivity of 0.2. Thus, an emissivity of 0.2 is used for untreated aluminum window profiles when  $U$ -value calculations are performed.

To increase the thickness of the oxidation layer beyond the thickness that natural oxidation in air is able to produce, aluminum window profiles are anodized. This is done to increase the corrosion resistance, and also sometimes to get a surface with the desired surface finish. The anodizing process consists of placing aluminum profiles in acid-based electrolyte and letting an electric current pass through it. According to the European Aluminium Association (EAA 1995) the oxide layer of anodized aluminum should have a minimum average thickness of 5, 10, 15, 20 or 25  $\mu\text{m}$  when used in buildings. An aluminum oxide thickness of 5 or 10  $\mu\text{m}$  is

sufficient for indoor use while oxide thicknesses of 15 to 25  $\mu\text{m}$  can be used outdoor. Emissivity values of anodized aluminum are often reported in textbooks, but little is said about the thickness of the oxide coating. Mills (1995) for instance reports that hard anodized aluminum has a hemispherical total emissivity of 0.8 and that soft anodized aluminum has a hemispherical total emissivity of 0.76, both at about 300 K. Tolukian & Dewitt (1972) report that anodized aluminum at 296 K has a hemispherical total emissivity of 0.842. Further, Kohara and Niimi (1996) found that the normal spectral emissivity of aluminum alloy 1050-O<sup>1</sup> with oxide layers (anodized in sulfuric acid) with thicknesses between 5 and 16  $\mu\text{m}$  was approximately equal to 0.9 for wavelengths between 7 and 20  $\mu\text{m}$ . Below 7  $\mu\text{m}$  the normal emissivity was close to 0.2. Thinner oxide layers resulted in lower emissivities. The emissivity of oxide layers between 16 and 20  $\mu\text{m}$  thick were reported for the discrete wavelengths 10 and 20  $\mu\text{m}$ , and was found to be quite constant, close to 0.9. Their experiments were carried out at 300 °C. Thus, anodized aluminum profiles used in building frames complying with EAA (1995) seem to require an emissivity of 0.9 when *U*-value calculations are to be performed.

The wavelength range of interest when calculations of heat transfer in building sections are performed is about 5 to 70  $\mu\text{m}$  (see Figure 1). About 98% of the energy emitted from a blackbody at  $T = 283\text{ K}$  is within this wavelength interval. However, a narrower wavelength interval can also be studied, and the result will still be quite accurate. In this paper the wavelength interval studied is from 4.5 to 40  $\mu\text{m}$ . About 93 % of the energy emitted from a blackbody at  $T = 283\text{ K}$  is within this wavelength interval. Aluminum window frame profiles consist of external and internal surfaces (inside frame cavities) and are often six meters long when they are anodized. This paper studies how this influences the normal spectral emissivity of the interior cavities of one commercially available anodized aluminum profile. The emissivities of some other materials like mask tape are also reported. These are measured since such tapes often are used in hotbox experiments performed to measure the thermal transmittance of windows. A discussion on the difference between the emissivity used in calculations of thermal transmittance and actually present in experiments is also included.

---

<sup>1</sup> This alloy consists of minimum 99.5% Al, maximum 0.05% of each of Cu, Mg, Mn, V, and Zn, and maximum 0.4% Fe, maximum 0.25% Si, and maximum 0.03% Ti.

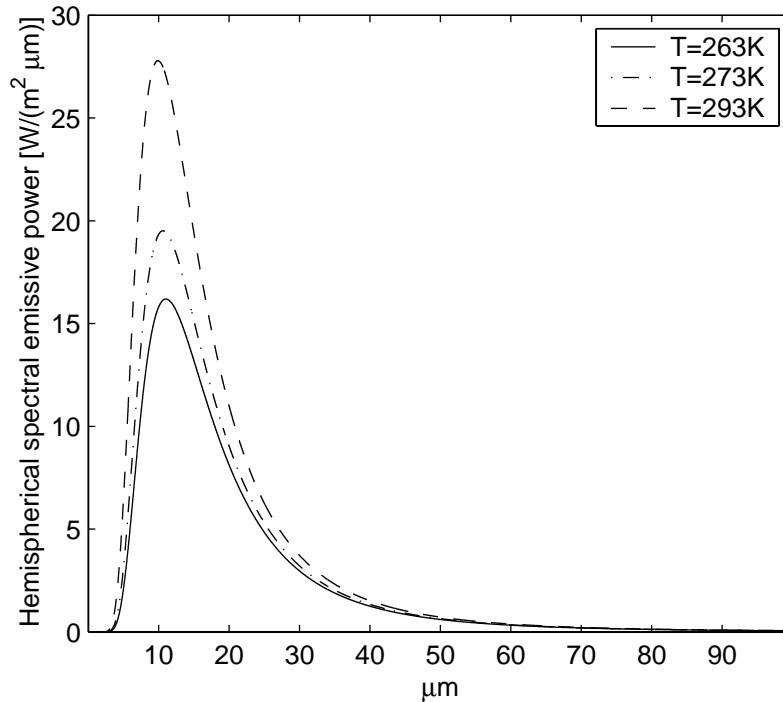


Figure 1. The figure shows the spectral distribution of emissive power for some temperatures relevant for heat transfer in building sections calculated from Planck's law.

## 2. Experimental Procedure

The anodized samples were cut from a regular factory made aluminum profile with the shape shown in Figure 2. The aluminum profiles were of the alloy 6061-T6, which often is used for building applications. This alloy consists of 98% Al, 0.04 - 0.35% Cr, 0.15 - 0.4% Cu, maximum 0.7% Fe, 0.8 - 1.2% Mg, maximum 0.15% Mn, 0.4 - 0.8% Si, maximum 0.15% Ti, and maximum 0.25% Zn. These aluminum profiles are made for use in aluminum window frames and are fabricated in sections that are six meters long. The aluminum profiles are anodized in their full length while attached to the polyamide thermal break. The aluminum sections also receive a water bath treatment (95 - 100 °C) after the anodizing process. This is done to seal the open pores present in the oxide layer after anodizing. According to the factory the profile has an exterior oxide layer of 20 μm. The surfaces did not get a surface treatment besides that received from the factory.

The tested samples were cut from different parts of the anodized aluminum profile and had a surface area of approximately 15 by 20 mm<sup>2</sup> and were 1.5 to 2 mm thick. An aluminum sheet and a sample cut from an extruded untreated profile were also tested. The last sample was also of the 6061-T6 alloy. Table 1 lists the aluminum samples tested. The material description column in the table includes information about from where on the anodized

aluminum profile the samples were cut. *Edge* means that the sample was cut from one of the two edges of the profile, and *middle* means that the sample was cut 2.5 meter from one edge. *External* notes that the sample is from the exterior part of the profile and *internal* means that the sample was facing an internal cavity. In addition, *Al* or *br.* (*br.* = break, meaning thermal break) are attached to the label *internal*. *Al* means an internal cavity completely surrounded by aluminum, and *br.* means that the sample was facing the thermal break cavity. The other materials tested are listed in Table 2. These are tapes that often are used when experimental testing of fenestration products are performed.

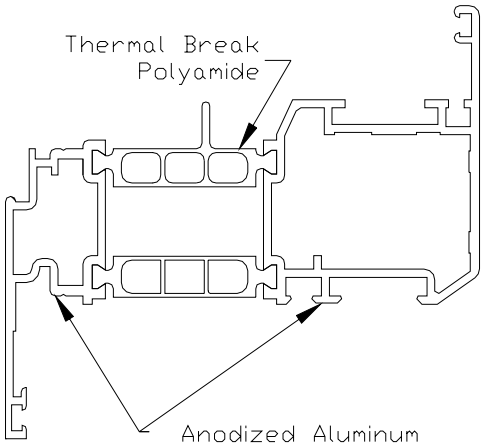


Figure 2. Figure of anodized aluminum profile from which the tested specimens were cut.

Table 1. The table shows the name of the different samples and where on the six-meter long profile the samples were cut.

Material Description (Label)	Appearance	Sample Number
Anodized Al, edge, external	diffuse aluminum	1
Anodized Al, edge, internal Al	diffuse aluminum	2
Anodized Al, edge, internal br.	diffuse aluminum	3
Anodized Al, middle, external	diffuse aluminum	4
Anodized Al, middle, internal Al	partly bright aluminum	5
Anodized Al, middle, internal br.	diffuse aluminum	6
Untreated extruded Al	partly bright aluminum	7
Parsec Thermo-Brite Al sheet	bright aluminum	8

Table 2. The table shows the name of the non-aluminum samples tested.

Material Description (Label)	Appearance	Sample Number
Nashua 357 gray tape	gray	9
Red Permacel P-34 masking tape	red	10
Tartan 5140 masking tape	paper	11
Scotch 231 3-712 masking tape	paper	12

The normal spectral emissivity of the specimens was measured with a Fourier transform infrared (or FTIR) spectrometer (BRUKER IFS 28) fitted with an input port and an emission adapter (A 540/7). This experimental arrangement has the advantage that the spectral emissivity of diffusely scattering samples can be measured, in contrast with techniques in which emissivity is determined from specular spectral reflectance measurements, based on Kirchhoff's law. The emission adapter consists of a heated temperature-controlled sample mount inside a housing that has a central 12-mm diameter aperture. Specimens are attached to the sample mount with a high conductivity adhesive (Dupont Conductor Composition 4929N) to eliminate the problem of poor thermal contact. This procedure ensures that the temperature of the sample is close to the temperature of the sample mount. The sample mount also has a reference material attached to it against which the emission from the measured samples is compared. The spectral emissivity of the reference material was determined in a separate set of experiments with a blackbody cavity at several temperatures, procedures not discussed further here. Based on the known emissivity of the reference material we find the emissivity of the samples by comparing the emission spectra from the reference material to that of the sample

$$\epsilon'_{\lambda,n,sampl}(\lambda) = \frac{e'_{\lambda,n,sampl}(\lambda) \cdot \epsilon'_{\lambda,n,ref}(\lambda)}{e'_{\lambda,n,ref}(\lambda)} \quad (1)$$

Here,  $\epsilon'_{\lambda,n,sampl}(\lambda)$  is the normal spectral emissivity of the sample and  $\epsilon'_{\lambda,n,ref}(\lambda)$  is the normal spectral emissivity of the reference material.  $e'_{\lambda,n,sampl}(\lambda)$  and  $e'_{\lambda,n,ref}(\lambda)$ , the radiative emissions from the sample and the reference material, are measured in two consecutive experiments. The spectral emissivity of the sample is then reported. Throughout the experiments the sample mount was kept at 71 °C (344 K). The temperature range of interest for heat transfer in building sections is primary from -20 °C to 30 °C. However, previous research has shown that the emissivity of anodized aluminum is fairly constant for temperatures lower than 71 °C. According to Touloukian et al. (1972) the hemispherical total emissivity of anodized aluminum is reduced by 0.012 (from 0.842 to 0.830) when the temperature increases from 23 to 70 °C. The measured emissivity values will therefore represent the emissivity for the desired temperature range well. The absolute accuracy of the measurements with the FTIR spectrometer depends on the accuracy with which the reference material was calibrated, and is estimated to be  $\pm 0.05$  units. The measurements are reproducible to within  $\pm 0.01$  units or better.

Some samples were also measured with a Devices & Services (D&S) Model AE Emissometer. The D&S Emissometer is a comparative device requiring calibration with two reference materials, one having an emissivity of 0.06 and another having an emissivity of 0.88. The detector outputs voltage that is linear with the emittance to within  $\pm 0.01$  units (D&S 1979). The detector portion of the instrument is heated to 82 °C so that the sample does not need to be heated. The samples can therefore be measured at room temperature. After calibration a measurement takes place by placing the sample and the high emissivity reference sample at a heat sink. The heat sink is used to maintain constant temperature. Then, voltages are measured for the high emissivity reference sample and the sample. The detector is placed over each for 60-90 seconds, until the reading becomes steady. The sample emissivity,  $\epsilon_{\text{sampl}}$ , can then be calculated from the measured voltages according to

$$\epsilon_{\text{sampl}} = V_{\text{sampl}} \cdot \frac{\epsilon_{hi}}{V_{hi}}, \quad (2)$$

where  $\epsilon_{hi}$  is the emissivity of the high emissivity reference material (0.88), and  $V_{\text{sampl}}$  and  $V_{hi}$  are the measured voltage with the detector placed over the sample and the high emissivity material, respectively. Kollie et al. (1990) found that the repeatability of the D&S Emissometer is  $\pm 0.008$  and that the uncertainty is  $\pm 0.014$ . They also found that the value measured with the emissometer probably is the total hemispherical emissivity, not the normal emissivity.

### 3. Results and Discussion

First in this section we will present the normal spectral emissivity for the different samples. Second, total emissivities will be calculated from the spectral data. Third, some of the total values calculated from spectral data will be compared to the hemispherical total values from the D&S emissometer. At last, a discussion on the use of an emissivity of 0.2 for shiny metallic surfaces in calculations of the thermal transmittance will be discussed.

#### 3.1 Normal Spectral Emissivity of Anodized and Untreated Aluminum

Figures 3 through 5 shows the normal spectral emissivity of the samples cut from the six-meter long anodized aluminum profile shown in Figure 2. The horizontal axis shows the wavenumber,  $\nu$ , with respective wavelengths,  $\lambda$ , in brackets, and the vertical axis shows the normal spectral emissivity. The wavenumber range displayed is from 2222  $\text{cm}^{-1}$  to 250  $\text{cm}^{-1}$ , or from 4.5  $\mu\text{m}$  to 40  $\mu\text{m}$ , in wavelengths. (Wavenumber is merely the inverse of wavelength,

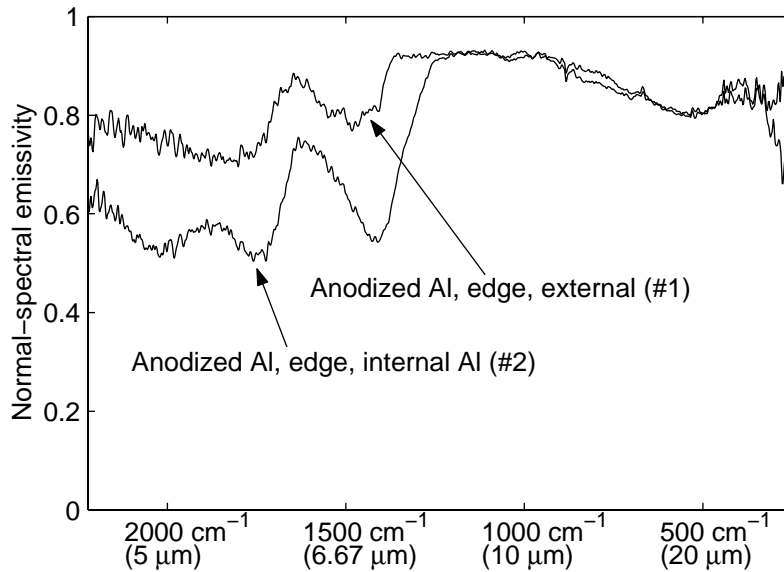


Figure 3. The figure shows the normal spectral emissivity of anodized aluminum for samples number 1 and 2. Results for wavelengths from 4.5 to 40  $\mu\text{m}$  are plotted. The uncertainty in the measurement is estimated to  $\pm 0.05$  units.

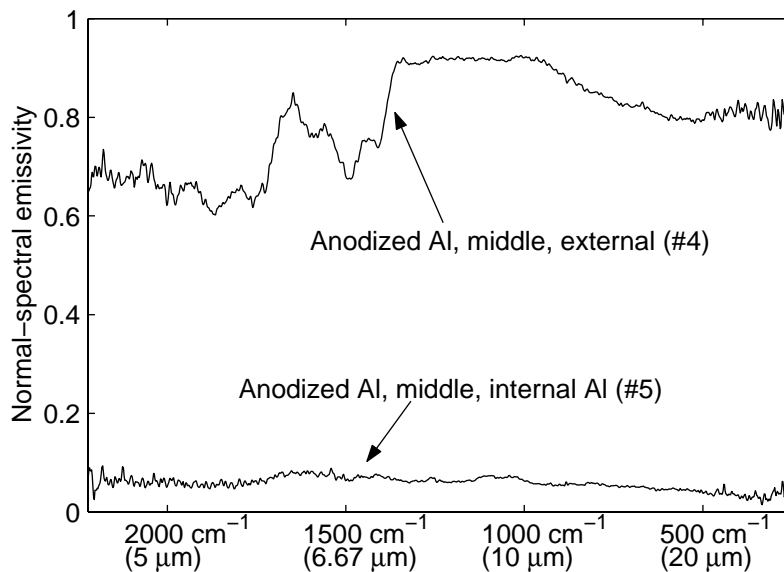


Figure 4. The figure shows the normal spectral emissivity of anodized aluminum for samples number 4 and 5. Data for wavelengths from 4.5 to 40  $\mu\text{m}$  are plotted. The uncertainty in the measurement is estimated to  $\pm 0.05$  units.

expressed in the  $\text{cm}^{-1}$  units popular in FTIR spectrometry.) For all figures 32 spectra were averaged. A qualitative idea of the noise present in the long- and short-wavelength portions of the spectra can be obtained from the lower curves in Figures 4 and 6, which are otherwise rather featureless. The figures show that, except for the aluminum samples that face a cavity only surrounded by aluminum, there only are small differences between the measured emissivities of the anodized aluminum profile. That is, the spectral emissivities of samples 1,

3, 4, and 6 show similar behavior and have approximately the same magnitude. The graph for sample number 2, the anodized sample from the edge of the profile and facing an aluminum cavity, also shows a similar behavior, but its magnitude is somewhat lower for smaller wavelengths, and for the longest wavelengths. For all the samples mentioned above (1, 2, 3, 4, and 6) the diagrams display a steep change in emissivity near approximately  $1300\text{ cm}^{-1}$ . This is similar to what was found by Kohara and Niimi (1996). However, in their experiments the emissivity was even lower ( $\sim 0.2$ ) for wavenumbers higher than  $1300\text{ cm}^{-1}$ . The difference may be attributed to the fact that the anodized aluminum profiles were submerged in water at  $98\text{ }^{\circ}\text{C}$  to close the open pores in the aluminum oxide layer, and that the samples measured by Kohara and Niimi (1996) did not receive that treatment (or that their experiments were carried out at  $300\text{ }^{\circ}\text{C}$ ). We note that water has a strong absorption feature near  $1600\text{ cm}^{-1}$ , which correlates with a maximum appearing in our emission spectra. Thus emission from water is at least a partial explanation for the higher emissivity observed above  $1300\text{ cm}^{-1}$ . The spectral emissivity of sample number 5, the anodized sample from the middle of the profile and facing an aluminum cavity, is low (less than 0.1) for all wavelengths. The emissivity being that low could partly be anticipated from the brighter look of the sample, however, a larger value was still expected because the surface was diffuse. An explanation for this low emissivity may be that there is no anodic coating on the surface. Instead it looks diffuse because it is rough. The slightly increased emittance (compared to the untreated sample, see below) may therefore be due to the roughness. If there was a coating present, some spectral variation would be expected (like for sample number 8). The reason for this low emissivity (and for lack of anodic coating) may be that, during the anodizing process, the ions in the solution are attracted to the tube and can not flow all the way to the center. Figure 6 shows that the emissivity of the untreated extruded aluminum sample is fairly constant ( $\sim 0.05$ ) for all the wavelengths plotted. When calculating heat transfers in building sections scientists often assume that surfaces are gray. That is, the emissivity of the surfaces is assumed not to depend on wavelength. From the figures we see that all emissivity spectra depend on wavelength, but that constant levels of  $\epsilon$  can be found for some of the samples within limited wavelength intervals.

### **3.2 Normal Spectral Emissivity of Selected Materials**

Figure 6 displays the normal spectral emissivity of an aluminum sheet. As expected the aluminum sheet has a low emissivity. The aluminum sheet is also measured with D&S emissometer, and was mainly included for comparison with that (see below).

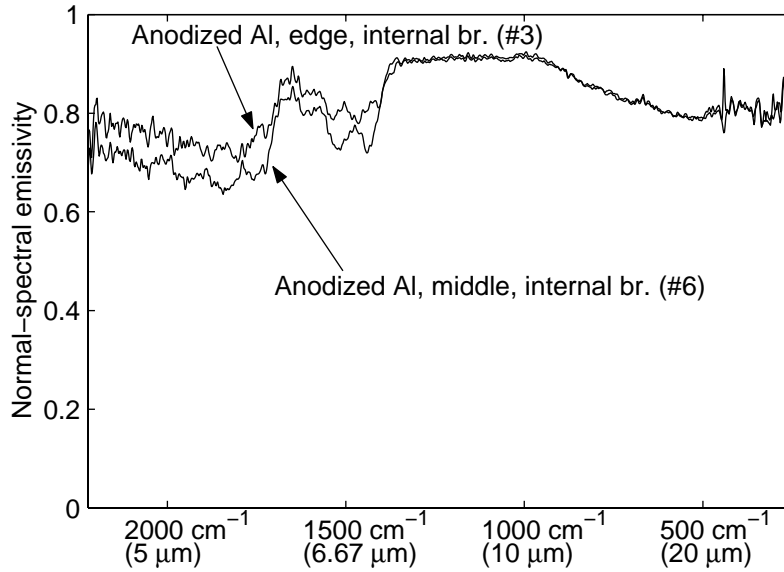


Figure 5. The figure shows the normal spectral emissivity of anodized aluminum for samples number 3 and 6. Results for wavelengths from 4.5 to 40  $\mu\text{m}$  are plotted. The uncertainty in the measurement is estimated to  $\pm 0.05$  units.

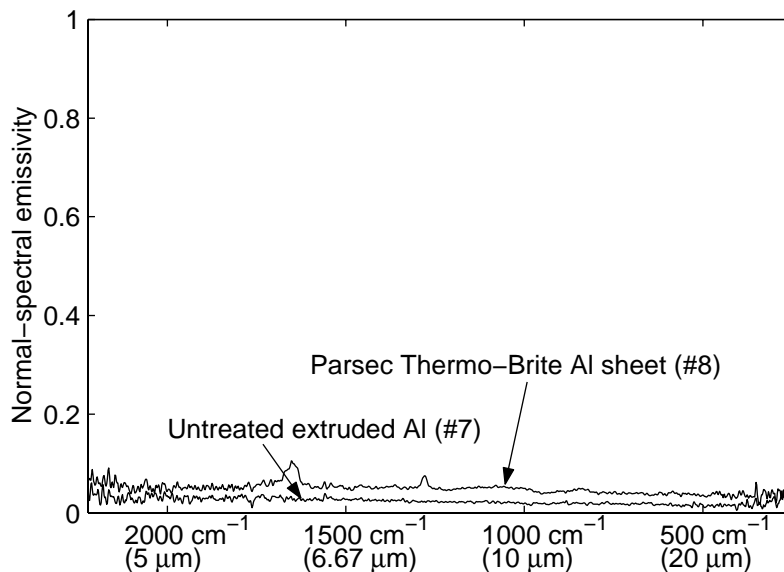


Figure 6. The diagram shows the normal spectral emissivity of untreated extruded aluminum and an aluminum sheet (samples number 7 and 8). Results for wavelengths from 4.5 to 40  $\mu\text{m}$  are plotted. The uncertainty in the measurement is estimated to  $\pm 0.05$  units.

The tapes measured in the FTIR spectrometer are often used in experiments performed to find the thermal transmittance of building sections. In those experiments the tapes are often assumed to have a total emissivity close to 0.9. Figures 7 and 8 show that this also is the case for three of the tapes (samples 10, 11 and 12), if we limit our study to wavenumbers less than  $1700\text{ cm}^{-1}$  (or wavelengths larger than approximately  $6\text{ }\mu\text{m}$ ). For larger wavenumber ( $\nu >$

1700  $\text{cm}^{-1}$ ) the emissivity is lower, however when total emissivities are to be studied this will not contribute much to the final value because most of the energy emitted is for wavenumbers larger than 1700  $\text{cm}^{-1}$  (see below). The Nashua 357 gray tape has a lower emissivity than the other tapes. This lower emissivity may be due to some aluminum pigment in the gray tape. A second possibility is that the tape is quite thick (like 1 mm) and that the temperature of the tape's surface has fallen slightly below the heat sink temperature.

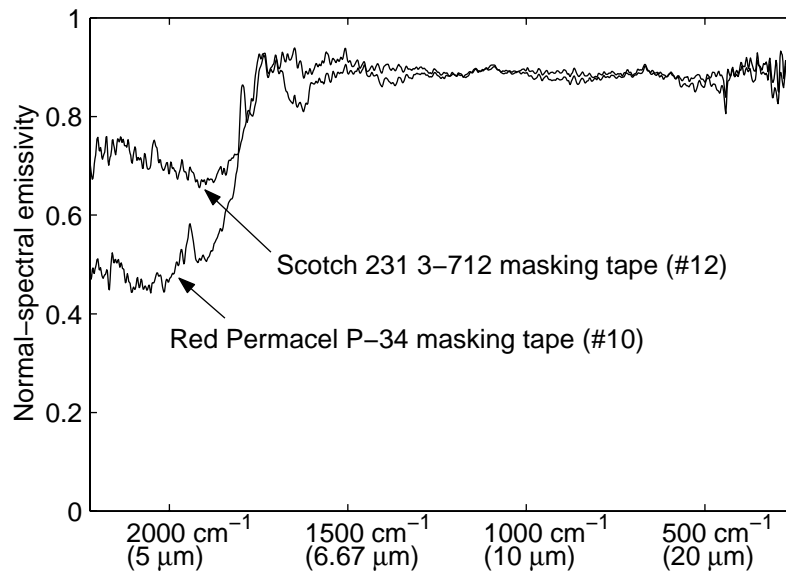


Figure 7. The figure shows the normal spectral emissivity of two types of masking tapes (samples number 10 and 12). Data for wavelengths from 4.5 to 40  $\mu\text{m}$  are plotted. The uncertainty in the measurement is estimated to  $\pm 0.05$  units.

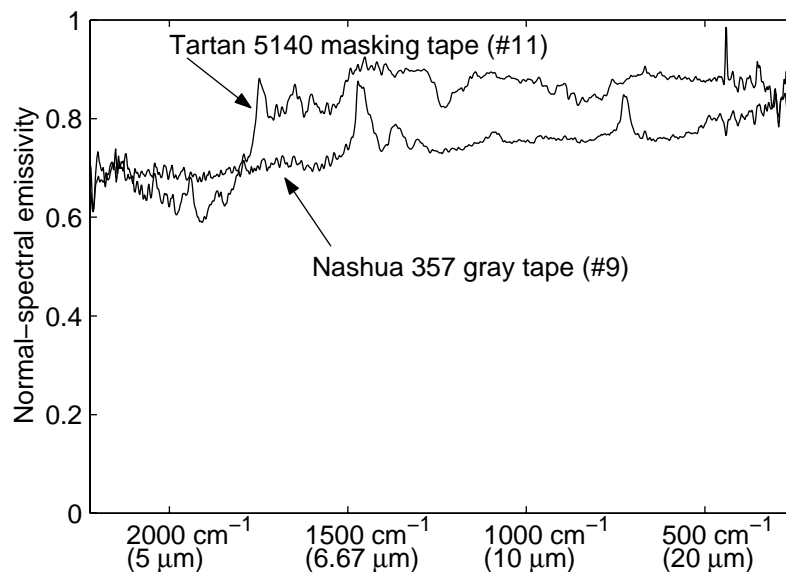


Figure 8. The figure shows the normal spectral emissivity of two types of tapes (samples number 9 and 11). Data for wavelengths from 4.5 to 40  $\mu\text{m}$  are plotted. The uncertainty in the measurement is estimated to  $\pm 0.05$  units.

### 3.3 Total Emissivity Values

When calculations of heat transfer in building sections are performed the hemispherical total emissivity is used, under the assumption that the surfaces are diffuse gray. Diffuse signifies that the directional emissivity does not depend on direction and gray signifies that the emissivity does not depend on wavelength. The aluminum samples could not be tested in the D&S emissometer because only smaller pieces could be cut from the anodized aluminum section. The D&S emissometer was therefore only used for measuring two samples, and these could then be compared to results from the FTIR spectrometer. The materials tested with both instruments were the Scotch masking tape (sample number 12) and the Parsec Thermo-Brite Al sheet (sample number 8). Table 3 shows the results from this comparative test. The results from the FTIR spectrometer were averaged over the wavelength interval 4.5 to 40  $\mu\text{m}$  according to (based on Siegel & Howell 1992)

$$\epsilon'_n = \frac{\int_{4.5\mu\text{m}}^{40\mu\text{m}} \epsilon'_{\lambda,n}(\lambda, T) \cdot e'_{\lambda b,n}(\lambda, T) d\lambda}{\int_{4.5\mu\text{m}}^{40\mu\text{m}} e'_{\lambda b,n}(\lambda, T) d\lambda}, \quad (3)$$

where  $e'_{\lambda b,n}$  is the blackbody emissive power in vacuum, and  $\epsilon'_{\lambda,n}(\lambda, T)$  is the measured spectral emissivity.  $e'_{\lambda b,n}$  is found from Planck's law, and were evaluated at  $T = 344 \text{ K}$  ( $71 \text{ }^\circ\text{C}$ ). The integrals were numerically solved using the trapezoidal rule (Press et al. 1992). Theoretically the lower and upper integration limits should be 0 and  $\infty$ , respectively, however, below 4.5  $\mu\text{m}$  and above 40  $\mu\text{m}$  the surfaces emit little energy. That is also why the spectral emissivity gets noisy close to 4.5 and 40  $\mu\text{m}$  in Figures 3 through 8. When looking at the results in Table 3 we must remember that D&S emissometer measures hemispherical emissivity while the FTIR spectrometer measures normal emissivity. Still, we find good agreement between the different instruments (within the uncertainty of the instruments).

*Table 3. The table shows results from emissivity measurements made on adhesive tape and aluminum sheet. The FTIR spectrometer results are averaged in the wavelength interval from 4.5 to 40  $\mu\text{m}$  (wavenumbers from 2222 to 250  $\text{cm}^{-1}$ ). The D&S emissometer column reports the hemispherical emissivity while the FTIR spectrometer column shows the normal emissivity.*

<b>Material Description (Label)</b>	<b>D&amp;S Emissometer</b>	<b>FTIR Spectrometer</b>
Parsec Thermo-Brite Al sheet (#8)	0.036	0.045
Scotch 231 3-712 masking tape (#12)	0.898	0.877

Table 4 shows the normal total emissivities calculated from Equation (3). Overall the emissivity of the anodized profile is fairly constant (0.834-0.856) for surfaces facing the exterior and the thermal break cavity (samples number 1,3,4 and 6). These emissivities also compare well to previous results. Tolukian & Dewitt (1972) e.g. report hemispherical total emissivities of 0.842 and 0.830 at 296 and 343 K, and Tolukian et al. (1972) report an hemispherical total emissivity 0.869 at 285 K for anodized aluminum. For the two samples that face a cavity completely surrounded by aluminum (samples number 2 and 5) the normal total emissivity varies from 0.055 to 0.820. Thus, ideally an average emissivity of about 0.44 should be assigned for thermal transmittance calculations, assuming that the emissivity depends linearly with profile length between these two emissivity limits and that a window frame is made up of equal parts of frames with the different treatments. However, if a conservative approach should be chosen, an emissivity of 0.9 should be used in calculations. Also, in  $U$ -value calculations the differences in emissivity within cavities completely surrounded by aluminum will not make to much of a difference in the final  $U$ -value result, because there only will be a small temperature difference across the cavity, and therefore little radiation heat transfer. The measured normal total emissivity of untreated extruded aluminum being 0.020 is low compared to other sources. Siegel & Howell (1992) for instance report a normal total emissivity of 0.04 at 295 K for a bright aluminum foil. The total emissivities of the masking tapes (samples number 10, 11 and 12) are close to the often-used value 0.9.

*Table 4. The table shows normal total emissivities calculated based on the FTIR spectrometer results. The spectral emissivities are averaged in the wavelength interval from 4.5 to 40  $\mu\text{m}$  (wavenumbers from 2222 to 250  $\text{cm}^{-1}$ ).*

<b>Material Description (Label)</b>	<b>Normal Total Emissivity (FTIR)</b>
Anodized Al, edge, external (#1)	0.856
Anodized Al, edge, internal Al (#2)	0.820
Anodized Al, edge, internal br. (#3)	0.844
Anodized Al, middle, external (#4)	0.834
Anodized Al, middle, internal Al (#5)	0.055
Anodized Al, middle, internal br. (#6)	0.837
Untreated extruded Al (#7)	0.020
Nashua 357 gray tape (#9)	0.765
Red Permacelel P-34 masking tape (#10)	0.870
Tartan 5140 masking tape (#11)	0.861

### 3.4 Emissivity Issues in Calculation and Measurement of Thermal Transmittance of Aluminum Window Frames

As noted in the introduction, an emissivity of 0.2 is used for untreated aluminum surfaces when the thermal transmittance of aluminum window frames is calculated, even though the emissivity of untreated aluminum is closer to 0.05 when the sections are new. The reason for this is that the calculated  $U$ -value should be representative for the window frame after years of use and wear, after which the untreated aluminum frames may oxidize and the emissivity increase to about 0.2. However, the use of 0.2 instead of 0.05 in the simulations may be questioned. The reason for this is that when measurements are performed for rating fenestration products they are performed on new products. Thus, when measurements and simulations are compared, two different aluminum sections in reality are compared; one with an emissivity of 0.05 (the measured) and another where the emissivity is 0.2 (the simulated). Since both approaches are equally valid according to international standards (see CEN 2001a and CEN 2001b), the manufacturers in practice can choose whether to get a good (measured frame  $U$ -value,  $\varepsilon = 0.05$ ) or poor (simulated frame  $U$ -value,  $\varepsilon = 0.2$ ) thermal transmittance, a result which not is desirable.

When experiments are used to verify simulations, the experimental  $U$ -value usually is lower than the simulated value. Haustermans (2000) studied heat transfer in a quite simple thermally broken aluminum frame. The aluminum profile had no surface treatment. Thus, an emissivity of 0.05 should be representative for the aluminum parts of the frame. Both simulations and measurements were performed. The frame had mostly rectangular cavities and the used cavity models can therefore be assumed to be right (air cavities are simulated as solid material and an equivalent conductivity is assigned to the cavity that incorporates both radiation and convection). He used an emissivity of 0.2 for the internal cavities and found that measured thermal transmittance was slightly smaller than the simulated. Svendsen et al. (2000) compare simulated  $U$ -values with a measured  $U$ -value, and even when they use detailed radiation models for the internal cavities (with metallic surfaces having an emissivity of 0.2) and divide complex air cavities to better represent the air convection effects, they find that the measured  $U$ -value, being  $2.5 \text{ W/m}^2\text{K}$ , is smaller than the calculated  $U$ -value,  $2.89 \text{ W/m}^2\text{K}$ . Svendsen et al. (2000) also say that much lower values for emissivity could be assigned in the simulations, but that values which are ensured correct over the entire service life of the frame at the moment not are available, and therefore use  $\varepsilon = 0.2$ . We feel that even when such emissivity values will be available, the emissivity values of new materials should

be used, two ensure that experimental and simulated  $U$ -values can be expected to be equal. A separate set of material data should be used for calculation of thermal transmittances that are valid over the service life period of a product. National norms can refer to these procedures (and material data) when requirements are formulated. Another reason for using the emissivity of the new material instead of the service life emissivity is that also glazings and other building materials are rated based on new material properties. Little is known about how material properties change with time, weathering and use. Thus, further efforts should be put on measuring emissivity and other material properties that are correct over the entire service life of window frame materials and building materials in general.

#### **4. Conclusions**

This paper reports the normal spectral and normal total emissivity of different parts of a six-meter long anodized aluminum profile. It is shown that the normal total emissivity is fairly constant (between 0.834 and 0.856) for exterior parts of the anodized profile and for surfaces facing the thermal break cavity. These are the parts of the aluminum profile that are most important for heat flow calculations through window frames. Large variation is shown for the all-aluminum internal cavities. The normal total emissivity is found to vary between 0.055 and 0.82, however, because of the large conductivity of aluminum this variation is not expected to influence heat transfer much. With respect to thermal transmittance simulations it is recommended that the emissivity of the material at fabrication time should be used instead of the emissivity expected over the entire service life of the section. This is because measurements, which also are used to rate window products and are supposed to give similar/equivalent results as the simulations, are performed on new products.

Further research should be conducted to find the emissivity of aluminum surfaces that have received other treatments, as for instance painted aluminum profiles. Painted profiles often receive an initial anodizing treatment to increase the adhesion between the paint and the aluminum profile, and an oxide layer may therefore be present in frame cavities (and increase the emissivity) even if there is no paint there. It is questionable whether the thickness of this treatment is thick enough to increase the emissivity. Aluminum frames exposed to the environment should also be measured, to find emissivity values that are representative for the section over the service life period.

## 5. Acknowledgements

This work was supported by Hydro Aluminum. P. B. was supported by the Assistant Secretary for Energy Efficiency and Renewable Energy, Building Technologies, of the U. S. Department of Energy under contract No. DE-AC03-76SF00098.

## 6. List of Symbols

$e$	emissive power	$\text{W m}^{-2} \mu\text{m}^{-1} \text{sr}^{-1}$
$T$	temperature	K
$U$	thermal transmittance	$\text{W m}^{-2} \text{K}^{-1}$
$V$	voltage	V

### Greek

$\varepsilon$	emissivity	-
$\lambda$	wavelength	m
$\nu$	wavenumber	$\text{cm}^{-1}$

### Subscripts

$hi$	refers to high emissivity
$n$	normal
$ref$	reference material
$sampl$	sample
$\lambda$	spectral quantity

### Superscripts

'	directional quantity
---	----------------------

## 7. References

CEN (2001a). *prEN ISO 10077-2 - Thermal performance of windows, doors and shutters - Calculation of thermal transmittance - Part 2: Numerical method for frames*, European Committee for Standardization, Brussels, Belgium.

CEN (2001b). *prEN 12412-2 - Thermal performance of windows, doors and shutters - Determination of thermal transmittance by hot box method - Part 2: Frames*, European Committee for Standardization, Brussels, Belgium.

D&S (1979). *Emissometer model AE operating instructions*. Devices & Services Co., Dallas, TX.

EAA (1995). *Bestimmungen für das Gütezeichen für anodisch erzeugte Oxidschichten auf Aluminium-Halbzeug in der Architektur*, QUALANOD, Zürich.

- Haustermans, L. (2000). *Heat transfer in aluminium window frame profiles. Computer modelling and hot box measurements*, Master of Science Thesis, Departement Burgerlijke Bouwkunde, Katholieke Universiteit Leuven. Leuven, Belgium.
- Lide, D.R. (1993). *Handbook of Chemistry and Physics, 73<sup>RD</sup> edition* (Lide, D.R., editor), CRC Press.
- Kohara, S. and Niimi, Y. (1996). Infrared radiation properties of anodized aluminum, *Materials Science Forum*, Vol. 217-222, 1623-1628.
- Kollie, T.G., Weaver, F.J. and McElroy, D.L. (1990). Evaluation of a commercial, portable, ambient-temperature emissometer, *Review of Scientific Instruments*, Vol. 61, 1509-1517.
- Mills, A.F. 1995. *Heat and mass transfer*, Richard D. Irwin Inc, Chicago, USA.
- Mitchell, R., Kohler, C, Arasteh, D., Finlayson, E., Huizenga, C., Curcija, D. and Carmody, J. (2000). *THERM 2.1 NFRC simulation manual*, Ernest Orlando Lawrence Berkeley National Laboratory, Berkeley CA, USA.
- Press, W.H., Teukolsky, S.A., Vetterling, W.T. and Flannery, B.P. (1992). *Numerical recipes in C, the art of scientific computing, second edition*, Cambridge University Press, New York NY, USA.
- Siegel, R. and Howell, J.R. (1992). *Thermal radiation heat transfer*, Taylor&Francis, Washington DC, USA.
- Svendsen, S., Duer, K. and Noyé P. (2000). *Calculating the heat transfer coefficient of frame profiles in aluminum*, Sagsrapport SR-0023, Department of Buildings and Energy, Technical University of Denmark.
- Touloukian, Y.S. and DeWitt, D.P. (1970). *Thermal radiative properties, vol. 7, metallic elements and alloys*, Thermophysical Properties Research Center of PurDue University, Data Series, Plenum Publishing.
- Touloukian, Y.S. and DeWitt, D.P. (1972). *Thermal radiative properties, vol. 8, nonmetallic solids*, Thermophysical Properties Research Center of PurDue University, Data Series, Plenum Publishing.

Touloukian, Y.S., DeWitt, D.P. and Hemicz R.S. (1972). *Thermal radiative properties, vol. 9, coatings*, Thermophysical Properties Research Center of PurDue University, Data Series, Plenum Publishing.

VDI-Wärmeatlas (1997). *VDI-Wärmeatlas, Berechnungsblätter für den Wärmeübergang*, VDI-Gesellschaft Verfahrenstechnik und Chemie-ingenieurwesen, Springer.